

**A STUDY OF PREMIXED, SHOCK-INDUCED  
COMBUSTION WITH APPLICATION TO  
HYPERVELOCITY FLIGHT**

A Thesis  
Presented to  
The Academic Faculty

by

Erik Lee Axdahl

In Partial Fulfillment  
of the Requirements for the Degree  
Doctor of Philosophy in the  
School of Aerospace Engineering

Georgia Institute of Technology  
December 2013

Copyright © 2013 by Erik Lee Axdahl

**A STUDY OF PREMIXED, SHOCK-INDUCED  
COMBUSTION WITH APPLICATION TO  
HYPERVELOCITY FLIGHT**

Approved by:

Alan W. Wilhite, Advisor  
School of Aerospace Engineering  
*Georgia Institute of Technology*

Ajay Kumar  
Systems Analysis and Concepts  
Directorate (Ret.)  
*NASA Langley Research Center*

Timothy Lieuwen  
School of Aerospace Engineering  
*Georgia Institute of Technology*

Suresh Menon  
School of Aerospace Engineering  
*Georgia Institute of Technology*

Stephen Ruffin  
School of Aerospace Engineering  
*Georgia Institute of Technology*

Date Approved: 6 November 2013

*To those who mentor  
the next generation*

## ACKNOWLEDGEMENTS

Progress is not made in a vacuum, and therefore I am grateful to those who have helped and mentored me up to and during my graduate school years. My thesis advisor, Dr. Alan Wilhite, and I chanced to have a one-on-one conversation with each other during my first visit to Georgia Tech that cemented my resolve to begin my studies at NASA Langley Research Center through the National Institute of Aerospace. Since then, I have met and known many, including my wife, who have greatly affected my life. I thank Dr. Wilhite for providing this opportunity to me as well as his advice, direction, support, and conversations along the way.

I have been fortunate to have many mentors in my career to this point. Dr. Ajay Kumar has advised and worked very closely with me throughout the course of the work contained in this thesis. Even though work duties demanded much of him, he always found time every week to meet with me to talk about my research and give helpful direction. I look forward to working with him in the future. Other research mentors in my life have included Dr. Juan Cruz, Mr. Garry Qualls, Dr. Roger Arndt, and Dr. Martin Wosnik. All of these individuals have contributed substantially to the type of researcher I am today.

After I finished my Master's work and was a researcher without a home, it was the Hypersonic Airbreathing Propulsion Branch at NASA Langley that adopted me, first as a student and then as a civil servant. I have been proud to work with each and every individual in my branch, who have been able to provide great advice and a good medium of idea exchange through the course of this work. I look forward to working in this field with these people going forward.

I would also like to acknowledge all of my friends who have been a great source of

joy and camaraderie in my life.

I have unconditional gratitude for my family, including my parents Roanne and Lee. They have provided me lifelong support that I try to repay in my actions every day. My wife and best friend Rachel also deserves a very special acknowledgment for her partnership, support, and patience. Being a graduate student can be a grumpy, scatterbrained business, but she looked past all of that and decided to love me any-ways.

# TABLE OF CONTENTS

<b>DEDICATION</b> . . . . .	<b>iii</b>
<b>ACKNOWLEDGEMENTS</b> . . . . .	<b>iv</b>
<b>LIST OF TABLES</b> . . . . .	<b>x</b>
<b>LIST OF FIGURES</b> . . . . .	<b>xii</b>
<b>LIST OF SYMBOLS OR ABBREVIATIONS</b> . . . . .	<b>xxii</b>
<b>GLOSSARY</b> . . . . .	<b>xxv</b>
<b>SUMMARY</b> . . . . .	<b>xxvi</b>
<b>I INTRODUCTION</b> . . . . .	<b>1</b>
1.1 Motivation for Current Research (What is a Shcramjet and What Are its Challenges?) . . . . .	1
1.2 Background of PMSIC Technology . . . . .	6
1.3 Knowledge Gaps in the Literature . . . . .	11
1.4 Objectives and Contributions . . . . .	14
1.5 Dissertation Preview . . . . .	16
<b>II FOREBODY INJECTION AND MIXING</b> . . . . .	<b>17</b>
2.1 Numerical Framework and Approach . . . . .	20
2.2 Validation . . . . .	24
2.2.1 Transverse Injection into a Quiescent Medium . . . . .	25
2.2.2 Transverse Injection into a Supersonic Crossflow . . . . .	32
2.2.3 Axial injection into a Supersonic Coflow . . . . .	35
2.3 Modeling and Simulation . . . . .	43
2.3.1 Performance . . . . .	43
2.3.2 Flow Conditions . . . . .	45
2.3.3 Injector Geometries . . . . .	47
2.3.4 Computational Domain . . . . .	50
2.4 Mixing Results . . . . .	57

2.4.1	Flush Wall Injection . . . . .	57
2.4.2	Ramp Injection . . . . .	64
2.4.3	Strut Injection . . . . .	73
2.4.4	Injector Comparisons . . . . .	75
2.4.5	Effect of Turbulent Schmidt Number . . . . .	79
2.5	Chapter Summary . . . . .	81
<b>III AUTOIGNITION MITIGATION . . . . .</b>		<b>83</b>
3.1	Model Selection and Validation . . . . .	86
3.1.1	Chemical Model Selection via Ignition Delay . . . . .	86
3.1.2	Blunt-Body, Premixed, Shock-Induced Combustion . . . . .	91
3.2	Flow Simulation and Metrics of Performance . . . . .	104
3.2.1	Flow Conditions and Computational Domain . . . . .	104
3.2.2	Measurement of Oxygen Burning . . . . .	105
3.3	Baseline Simulations of Autoignition . . . . .	107
3.4	Autoignition Mitigation Strategies for Forebody Flows . . . . .	113
3.4.1	Overview of Wall Cooling Strategies . . . . .	113
3.4.2	Wall Transpiration . . . . .	117
3.4.3	Film Cooling . . . . .	119
3.5	Simulation of Transpiration and Film Cooling . . . . .	121
3.5.1	Simulation Matrix . . . . .	121
3.5.2	Results of Film Cooling . . . . .	123
3.5.3	Results of Wall Transpiration . . . . .	133
3.5.4	Effect of Turbulent Schmidt Number on Autoignition . . . . .	134
3.5.5	Effect of Chemical Model on Autoignition . . . . .	136
3.6	Chapter Summary . . . . .	139
<b>IV TWO-DIMENSIONAL COMBUSTOR CALCULATIONS . . . . .</b>		<b>143</b>
4.1	Modeling and Simulation . . . . .	144
4.1.1	Inflow Profiles . . . . .	144

4.1.2	Computational Domain and Methodology . . . . .	145
4.1.3	Performance Metrics . . . . .	146
4.2	Results and Discussion . . . . .	147
4.3	Chapter Summary . . . . .	155
<b>V</b>	<b>QUASI-1D SHOCK &amp; REACTION FRONT STABILITY . . . . .</b>	<b>158</b>
5.1	Derivation of the Quasi-1D Form of Equations . . . . .	163
5.1.1	Governing Equations . . . . .	163
5.1.2	Boundary and Initial Conditions . . . . .	169
5.2	Physical Modeling . . . . .	169
5.2.1	Nonequilibrium Chemistry . . . . .	170
5.2.2	Viscosity and Thermal Conductivity . . . . .	172
5.2.3	Diffusion Velocity . . . . .	173
5.2.4	Specific Heat, Enthalpy, Entropy, and Gibbs free energy . . . . .	175
5.3	Solution Methodology . . . . .	176
5.3.1	MacCormack's Method . . . . .	176
5.3.2	Numerical Damping . . . . .	177
5.3.3	Finite-Rate Chemistry . . . . .	178
5.4	Validation . . . . .	181
5.4.1	Stagnation Point Heat Transfer . . . . .	181
5.4.2	Thermodynamic Properties in the Shock Layer . . . . .	183
5.4.3	Qualitative Comparison to Experiment and Numerical Simulation . . . . .	184
5.4.4	Quantitative Reaction Front Oscillation Frequency . . . . .	190
5.4.5	Comparison to 1D Mechanism Models . . . . .	194
5.5	Effect of Equivalence Ratio on Stability . . . . .	196
5.6	Chapter Summary . . . . .	200
<b>VI</b>	<b>SUMMARY AND AVENUES OF FUTURE WORK . . . . .</b>	<b>202</b>
6.1	Summary of Contributions . . . . .	202
6.2	Avenues of Future Numerical Work . . . . .	205

6.2.1	Forebody Injector Design and Optimization . . . . .	205
6.2.2	Chemically Active Cooling . . . . .	209
6.2.3	Effect of Blunt Bodies and Non-Optimal Trajectories . . . . .	210
6.2.4	Integrated Analysis using Variable Geometry . . . . .	211
6.2.5	Further Development and Application of Quasi-1D Framework	212
6.3	Avenues of Future Experimental Work . . . . .	213
6.3.1	Hypervelocity Validation and Calibration Database . . . . .	213
6.3.2	Testing and Evaluation of Forebody Mixing Concepts . . . . .	213
<b>APPENDIX A — TAYLOR SERIES EXPANSION OF FLOW VARI-</b>		
<b>ABLES . . . . .</b>		<b>215</b>
<b>APPENDIX B — GRID METRICS AND COMPUTATIONAL DO-</b>		
<b>MAIN . . . . .</b>		<b>218</b>
<b>APPENDIX C — IDEAL FUEL-AIR CONDITIONS ON A HY-</b>		
<b>PERVELOCITY FOREBODY . . . . .</b>		<b>221</b>
<b>APPENDIX D — FINITE-RATE CHEMISTRY MODELS . . . . .</b>		<b>224</b>
<b>REFERENCES . . . . .</b>		<b>230</b>

## LIST OF TABLES

1	A capability summary of the VULCAN CFD code . . . . .	23
2	Freestream and flat plate conditions. Flat plate conditions are obtained by shocking the freestream flow through a 5 degree turning followed by a 6 degree turning. All cases use an air molar composition of 79% N <sub>2</sub> and 21% O <sub>2</sub> . . . . .	46
3	Fuel injector exit conditions. All cases use 100% H <sub>2</sub> at a static temperature of 390 K. . . . .	46
4	Injector geometry for flush-wall injection. All injectors have the same exit area. . . . .	47
5	Modified ramp cases. . . . .	49
6	Number of grid points full computational domain for each injector concept. . . . .	57
7	Number of grid points in the performance sampling region in each direction as well as total cells. . . . .	57
8	Maximum $y^+$ values along the wall for each flush-wall fuel injection concept. . . . .	58
9	Flush-wall injected fuel spilled at cowl closure as a percentage of the nominal fuel injection mass flow rate of 0.02639 kg/s. . . . .	64
10	Ramp injected maximum wall $y^+$ values. Legend: C(antilivered), W(edge), M(atched pressure), S(onic pressure) . . . . .	65
11	Ramp injected fuel spilled at cowl closure as a percentage of the nominal fuel injection mass flow rate of 0.02639 kg/s. Legend: C(antilivered), W(edge), M(atched pressure), S(onic pressure) . . . . .	73
12	Cases simulated for the Ruegg and Dorsey experiments are listed. All conditions are at 300 K with a spherical diameter of 20 mm . . . . .	94
13	Transpiration array conditions . . . . .	119
14	Film cooling conditions . . . . .	120
15	Coolant mass flow rates for each value of blowing parameter. . . . .	121
16	Simulation matrix for parallel film cooling cases with sonic injection. Checkmarks indicate cases that were run and x-marks indicate cases not run. . . . .	122

17	Simulation matrix for 10 <i>o</i> film cooling cases with sonic injection. Checkmarks indicate cases that were run and x-marks indicate cases not run.	122
18	Simulation matrix for 45 <i>o</i> film cooling cases with sonic injection. Checkmarks indicate cases that were run and x-marks indicate cases not run.	122
19	Simulation matrix for transpiration cooling cases with a porosity of 2%. Checkmarks indicate cases that were run and x-marks indicate cases not run. . . . .	123
20	Coefficients of fourth-order polynomial fits of reduced collision integrals. Integrals are expressed as $I(T^*) = a_0 + a_1T^* + a_2T^{*2} + a_3T^{*3} + a_4T^{*4}$	174
21	Comparison of Fay and Riddell with the QUIVR solution of heat flux for the validation case. . . . .	183
22	Selected Ruegg and Dorsey experimental conditions for a 20 mm diameter, spherical projectile fired into premixed, stoichiometric hydrogen/air.	186
23	Oscillation frequencies from experiment and numerical investigations.	193
24	An example summary of the pre- and post-mixed properties are shown for stoichiometric hydrogen-air flow at the Mach 12 point on a $q = 1500$ psf trajectory. . . . .	223

## LIST OF FIGURES

1	Staging altitudes and velocities for a vehicle with a first stage maximum speed of Mach 10 versus a vehicle with a maximum first stage speed of Mach 15. . . . .	2
2	A notional scramjet . . . . .	4
3	A notional shcramjet . . . . .	5
4	Technical challenges for a notional shcramjet. . . . .	6
5	A reproduced schematic of the concept analyzed by Dunlap, <i>et al.</i> [4] is shown. . . . .	7
6	A reproduced schematic of the concept analyzed by Sargent and Gross [5] is shown. . . . .	8
7	A reproduced schematic of the concept proposed by Rubins and Rhodes [8] is shown. . . . .	9
8	A reproduced schematic of the PMSIC experiment conducted by by Rubins and Rhodes [8] is shown. . . . .	9
9	A reproduced schematic of the concept proposed by Rubins and Bauer [9] is shown. . . . .	10
10	Studies involved in the present work and knowledge to be gained. . .	12
11	A schematic of the flow in the vicinity of an underexpanded transverse fuel injector in supersonic flow is shown. . . . .	18
12	The grid used for injection validation is shown with every fourth grid point drawn. For cases with crossflow, the flow originates from the upper right. . . . .	26
13	Injector detail for the validation grid with all grid points drawn. The injector topology consists of an H-grid near the center of the injector with a C-grid wrapped around it. . . . .	27
14	A plane bisecting the sonic jet is shown from the converged case of jet pressure ratio equal to 20. Parameters of the jet are shown, consisting of wavelength, $w$ , Mach disk diameter, $D_m$ , exit diameter, $D_e$ , and Mach disk standoff distance $x_m$ . . . . .	29
15	Normalized Mach disk diameter as a function of jet pressure ratio. Numerical results from Vulcan are compared against the results of Wilkes <i>et. al</i> [55] and Love <i>et. al</i> [56]. . . . .	30

16	Normalized Mach disk standoff distance as a function of jet pressure ratio. Numerical results from Vulcan are compared against the results of Wilkes <i>et. al</i> [55] and Love <i>et. al</i> [56]. . . . .	31
17	Normalized jet wavelength as a function of jet pressure ratio. Numerical results from Vulcan are compared against the results of Wilkes <i>et. al</i> [55] and Love <i>et. al</i> [56]. . . . .	32
18	The centerline hydrogen mass fraction field of a converged VULCAN case where $J = 4.75$ is shown compared to the analytical relation from Equation 3 with $m = 1$ , $n = 2.55$ . . . . .	34
19	The centerline hydrogen mass fraction field of a converged VULCAN case where $J = 16.35$ is shown compared to the analytical relation from Equation 3 with $m = 1.3$ , $n = 3$ . . . . .	34
20	Vertical displacement of the Mach disk midpoint as a function of dynamic pressure. . . . .	35
21	A schematic of the Waitz expansion ramp injector is shown (from [62]).	36
22	A photograph of the Waitz expansion ramp injector experimental apparatus is shown (from [62]). . . . .	37
23	The expansion ramp geometry of Waitz for the validation study is shown.	38
24	The computational grid for the validation study in the vicinity of the injector is shown. . . . .	38
25	Comparisons of maximum helium mass fraction as a function of normalized distance from the injector exit between experiment and numerical simulations at various turbulent Schmidt numbers. Lines are for visual aid only and do not imply a curve shape. . . . .	40
26	Experimental contours of helium mass fraction at normalized x coordinates of (a) 4, (b) 8, and (c) 13 from the injector exit are shown compared to numerical contours at normalized x coordinates of (d) 4, (e) 8, and (f) 13. . . . .	41
27	Numerically solved contours for helium mass fraction are shown for (a) - (c) $Sc_t = 0.25$ , (d) - (f) $Sc_t = 0.5$ , and (g) - (i) $Sc_t = 1.0$ . The columns sequentially show normalized x coordinates of 4, 8, and 13 from the injector exit. . . . .	42
28	A schematic of the stream thrust potential methodology. . . . .	45
29	The baseline forebody geometry used in this study is shown. . . . .	45
30	Notional geometry for flush wall injectors. . . . .	47
31	Side-, top-, and perspective-view geometry for modified ramp injectors.	49

32	Side- and top-view geometry for strut injector. . . . .	50
33	A side- and top-view schematic of the computational domain is shown. . . . .	51
34	The circular injector (green) is shown positioned in the portion of the computational domain where performance sampling occurs. . . . .	51
35	The wedge injector (green) is shown positioned in the portion of the computational domain where performance sampling occurs. . . . .	52
36	The diamond injector (green) is shown positioned in the portion of the computational domain where performance sampling occurs. . . . .	52
37	The stinger injector (green) is shown positioned in the portion of the computational domain where performance sampling occurs. . . . .	52
38	The unswept ramp (blue) injector is shown positioned in the portion of the computational domain where performance sampling occurs. . . . .	53
39	The strut injector (blue) is shown positioned in the portion of the computational domain where performance sampling occurs. . . . .	53
40	The computational grid in the vicinity of the circular injector (green) is shown. . . . .	54
41	The computational grid in the vicinity of the wedge injector (green) is shown. . . . .	54
42	The computational grid in the vicinity of the diamond injector (green) is shown. . . . .	55
43	The computational grid in the vicinity of the stinger injector (green) is shown. . . . .	55
44	The computational grid in the vicinity of the unswept ramp wedge injector (blue) is shown. . . . .	56
45	The computational grid in the vicinity of the strut injector (blue) is shown. . . . .	56
46	Contour plots of wall $y^+$ for the (a) full flowpath and (b) in the vicinity of the fuel injector. Flow is from the left to the right and hydrogen issues from the injector out of the page. . . . .	58
47	Contour plots of wall $y^+$ for the (a) full flowpath and (b) in the vicinity of the diamond fuel injector. Flow is from the left to the right and hydrogen issues from the injector out of the page. . . . .	59
48	Contour plots of wall $y^+$ for the (a) full flowpath and (b) in the vicinity of the diamond fuel injector. Flow is from the left to the right and hydrogen issues from the injector out of the page. . . . .	59

49	Contour plots of wall $y^+$ for the (a) full flowpath and (b) in the vicinity of the diamond fuel injector. Flow is from the left to the right and hydrogen issues from the injector out of the page. . . . .	60
50	Fence plots of hydrogen mass fraction for the flush-wall injection cases.	61
51	Performance of transverse injection concepts: (a) mixing efficiency versus $x$ , (b) stream thrust potential versus $x$ , and (c) stream thrust potential versus mixing efficiency. . . . .	62
52	Fuel equivalence ratio contours for the (a) circular, (b) diamond, (c) wedge, and (d) stinger injection case at $x = 0.1$ m and 0.713 m. Lines are plotted as $\phi = 0.1, 1, 2 \dots 7$ . Circular marker indicates vortex center.	64
53	Contour plots of wall $y^+$ for the full flowpath of the unswept ramp fuel injector with cavity at both a (a) pressure matched and (b) sonic pressure condition. Flow is from the left to the right and the ramp itself is blanked out. . . . .	65
54	Contour plots of wall $y^+$ for the full flowpath of the unswept ramp fuel injector with expansion wedge at both a (a) pressure matched and (b) sonic pressure condition. Flow is from the left to the right and the ramp itself is blanked out. . . . .	66
55	Contour plots of wall $y^+$ for the full flowpath of the swept ramp fuel injector with cavity at both a (a) pressure matched and (b) sonic pressure condition. Flow is from the left to the right and the ramp itself is blanked out. . . . .	66
56	Contour plots of wall $y^+$ for the full flowpath of the swept ramp fuel injector with expansion wedge at both a (a) pressure matched and (b) sonic pressure condition. Flow is from the left to the right and the ramp itself is blanked out. . . . .	67
57	Fence plots of hydrogen mass fraction for the ramp injection cases without the base expansion wedge. . . . .	68
58	Performance of ramp injection concepts for matched pressure: (a) mixing efficiency versus $x$ , (b) stream thrust potential versus $x$ , and (c) stream thrust potential versus mixing efficiency. Dashed lines indicate cases with the expansion wedge feature. . . . .	69
59	Stream traces that indicate flow arcing. . . . .	70
60	Performance of ramp injection concepts for sonic pressure: (a) mixing efficiency versus $x$ , (b) stream thrust potential versus $x$ , and (c) stream thrust potential versus mixing efficiency. Dashed lines indicate cases with the expansion wedge feature. . . . .	71

61	Fuel equivalence ratio contours for the swept and unswept ramp cases at $x = 0.21$ m and $0.713$ m. Lines are plotted as $\phi = 0.1, 1, 2 \dots 7$ . Circular marker indicates vortex center. . . . .	72
62	Contour plots of wall $y^+$ for the full flowpath of the strut injector. Flow is from the left to the right and the strut itself is blanked out. . . . .	74
63	Fence plot of hydrogen mass fraction for the strut injection case. . . . .	75
64	Performance of the strut injection concept: (a) mixing efficiency versus $x$ , (b) stream thrust potential versus $x$ , and (c) stream thrust potential versus mixing efficiency. . . . .	76
65	Fuel equivalence ratio contours for the strut injector case at $x = 0.16$ and $0.713$ m m. Lines are plotted as $\phi = 0.1, 1, 2 \dots 7$ . Circular marker indicates vortex center. . . . .	77
66	Performance of the best injection concepts: (a) mixing efficiency versus $x$ , (b) stream thrust potential versus $x$ , and (c) stream thrust potential versus mixing efficiency. . . . .	78
67	Comparisons of stream thrust potential versus mixing efficiency between the (a) stinger, (b) unswept ramp with wedge, and (c) strut injectors for $Sc_t = 0.25 - 1.0$ . . . . .	80
68	Notional diagram of wall transpiration. . . . .	84
69	Notional diagram of film cooling via a slot for both (a) tangential and (b) angled injection. . . . .	85
70	Comparing ignition delay time as a function of initial reactor temperature for a constant pressure of $2.0$ atm using different solvers. . . . .	89
71	Comparing ignition delay time as a function of initial reactor temperature for a constant pressure of $2.0$ atm using different chemical models. . . . .	90
72	Comparing ignition delay time as a function of initial reactor temperature for a constant pressure of $2.5$ atm using different chemical models. . . . .	91
73	Comparing ignition delay time as a function of initial reactor temperature for a constant pressure of $2.0$ atm using different reduced models from the Jachimowski mechanism. . . . .	92
74	The grid used in the validation study is shown with every tenth grid point normal to the surface and every third grid point tangential to surface. . . . .	93
75	(a) Numerical shadowgraph of a Mach 5, 20 mm spherically blunted projectile fired into $0.1$ atm quiescent H <sub>2</sub> -Air is shown and compared to the (b) experimental shadowgraph [96]. . . . .	95

76	(a) Numerical shadowgraph of a Mach 4.9, 20 mm spherically blunted projectile fired into 0.25 atm quiescent H <sub>2</sub> -Air is shown and compared to the (a) experimental shadowgraph [96]. . . . .	97
77	(a) Numerical shadowgraph solution of a Mach 4.8, 20 mm spherically blunted projectile fired into 0.5 atm quiescent H <sub>2</sub> -Air is shown and compared to the (b) experimental shadowgraph [96]. . . . .	98
78	A comparison is shown between shock and reaction front standoff distances for experiment and the present simulation at 0.1 atm. . . . .	99
79	A comparison is shown between shock and reaction front standoff distances for experiment and the present simulation at 0.25 atm. . . . .	100
80	A comparison is shown between shock and reaction front standoff distances for experiment and the present simulation at 0.5 atm. . . . .	100
81	Numerical shadowgraph for the Mach 4.47 projectile case with stoichiometric H <sub>2</sub> -air at 0.421 atm and 292 K ambient conditions. . . . .	101
82	Density contours on the stagnation streamline for the Mach 4.47 case are presented as a function of distance from the projectile nose and time. . . . .	102
83	Water mass fraction as a function of time at the projectile wall for the Mach 4.47 case. . . . .	103
84	The discrete Fourier transform taken of the wall water mass fraction for the Mach 4.47 case. . . . .	104
85	Top-level schematic of performance sampling region that spills oxygen (for a system where fuel is in excess). . . . .	106
86	Notional oxygen mass flow rates as a function of distance along sampling region with spilled and burned quantities indicated. . . . .	106
87	Stinger injector contours of (a) water production and (b) water mass fraction in the flow domain of interest. Flow is from the upper left to the lower right. . . . .	109
88	Mass flow rates of oxygen and combustion efficiency downstream of stinger without autoignition mitigation. . . . .	110
89	Strut injector contours of (a) water production and (b) water mass fraction in the flow domain of interest. Flow is from the upper left to the lower right. . . . .	112
90	Mass flow rates of oxygen and combustion efficiency downstream of strut without autoignition mitigation. . . . .	113

91	Unswept ramp injector contours of (a) water production and (b) water mass fraction in the flow domain of interest. Flow is from the upper left to the lower right. . . . .	114
92	Mass flow rates of oxygen and combustion efficiency downstream of strut without autoignition mitigation. . . . .	115
93	Global equivalence ratio as a function of blowing parameter . . . . .	117
94	Relative change in specific impulse as a function of blowing parameter	118
95	Schematic diagram of wall transpiration. . . . .	119
96	Schematic diagrams of film cooling via a slot for both (a) tangential and (b) angled injection. . . . .	120
97	Baseline, reacting flow without autoignition mitigation is shown as numerical shadowgraph overlaid with oxygen water mass fractions. . .	124
98	Changes in mass flow of oxygen burned for secondary hydrogen injection is shown. . . . .	125
99	Numerical shadowgraphs overlaid with water contours $Y_{H_2O} = 0.01, 0.02, \dots, 0.22$ for tangential film cooling with hydrogen. Coolant temperature of 100 K and $B = 20\%$ . . . . .	126
100	Numerical shadowgraphs overlaid with water contours $Y_{H_2O} = 0.01, 0.02, \dots, 0.22$ for tangential film cooling with hydrogen. The coolant temperature is 740 K and $B = 20\%$ . . . . .	126
101	Numerical shadowgraphs overlaid with water contours $Y_{H_2O} = 0.01, 0.02, \dots, 0.22$ for 10 degree film cooling with hydrogen. $B = 20\%$ and ambient temperatures of (a) 100 K and (b) 740 K are shown. . . . .	127
102	Numerical shadowgraphs overlaid with water contours $Y_{H_2O} = 0.01, 0.02, \dots, 0.22$ for 45 degree film cooling with hydrogen. The coolant temperature is 740 K and $B = 20\%$ . . . . .	127
103	Changes in mass flow of oxygen burned for secondary helium injection is shown. . . . .	129
104	Numerical shadowgraphs overlaid with water contours $Y_{H_2O} = 0.01, 0.02, \dots, 0.22$ for 10 degree film cooling with helium. $B = 15\%$ and ambient coolant temperatures of (a) 100 K and (b) 740 K are shown.	130
105	Changes in mass flow of oxygen burned for secondary nitrogen injection is shown. . . . .	132
106	Numerical shadowgraphs overlaid with water contours $Y_{H_2O} = 0.01, 0.02, \dots, 0.22$ for transpiration cooling with helium. Parameters $B = 20\%$ and $W = 25\%$ are shown. . . . .	133

107	Changes in mass flow of oxygen burned for secondary helium transpiration are shown. . . . .	134
108	Numerical shadowgraphs overlaid with water contours $Y_{H_2O} = 0.01, 0.02, \dots, 0.22$ for transpiration cooling with helium. $B = 20\%$ and patch sizings of (a) $W = 25\%$ and (b) $L = 50\%$ are shown. . . . .	135
109	Changes in mass flow of oxygen burned for tangential, secondary hydrogen and helium injection is shown. . . . .	137
110	Percent changes in mass flow of oxygen burned for tangential, secondary hydrogen and helium injection is shown. . . . .	138
111	Strut injector contours of (a) water production and (b) water mass fraction in the flow domain of interest using the Ó Conaire mechanism without hydrogen peroxide. Flow is from the upper left to the lower right. . . . .	140
112	Stinger injector contours of (a) water production and (b) water mass fraction in the flow domain of interest using the Ó Conaire mechanism without hydrogen peroxide. Flow is from the upper left to the lower right. . . . .	141
113	The grid used in the combustor study is shown with every fourth grid point plotted normal to the walls. . . . .	146
114	The grid used in the stability study is shown. . . . .	146
115	A notional trend of thrust potential versus distance in a combustor. . . . .	148
116	Contours of water mass fraction overlaid with lines of constant pressure for Mach numbers (a) 11, (b) 15, and (c) 20. . . . .	149
117	Thrust potential and combustion efficiency for the Mach 12 case. The shoulder of the geometry is where $x = 0$ . . . . .	151
118	Optimum combustor length and combustion efficiency at that point at different trajectory points. . . . .	153
119	Filled contours of water mass fraction superimposed with lines of constant pressure for the Mach 12 strut flowfield at $y =$ (a) 0, (b) 0.0172, and (c) 0.0345 m . . . . .	154
120	Filled contours of water mass fraction superimposed with lines of constant pressure for Mach numbers (a) 15, (a) 17, and (c) 20. . . . .	156
121	Reaction and shock front locations on the stagnation streamline as a function of time for the stable regime. . . . .	159
122	Reaction and shock front locations on the stagnation streamline as a function of time for the regular, unsteady regime. . . . .	160

123	Reaction and shock front locations on the stagnation streamline as a function of time for the large-disturbance, unsteady regime. . . . .	161
124	Schematic of the current state of the art for solving flow ahead of a blunted projectile. . . . .	161
125	Schematic of a new way for solving flow ahead of a blunted projectile.	162
126	The flow schematic and coordinate system for the quasi-1D equations are shown. . . . .	164
127	Comparison of the CHEMEQ algorithm and the CHEMEQ algorithm using $\alpha$ -QSS. [84] . . . . .	178
128	The solution of nondimensional heat flux as a function of distance from the wall is shown for a 63.5 mm projectile with $T_w = 3000$ K and traveling at $M_\infty = 5.72$ at an altitude of 35 km. . . . .	184
129	Comparison of QUIVR $\rho/\rho_{shock}$ result in shock layer compared to reference data. . . . .	185
130	Comparison of QUIVR $T/T_{shock}$ result in shock layer compared to reference data. . . . .	185
131	(a) Contours of water mass fraction on the stagnation streamline overlaid with contour lines of pressure as a function of non-dimensional time for Ruegg and Dorsey experiment Case 1. (b) An annotated experimental shadowgraph captured by Ruegg and Dorsey for the same conditions is shown for comparison. . . . .	187
132	(a) Contours of water mass fraction on the stagnation streamline overlaid with contour lines of pressure as a function of non-dimensional time for Ruegg and Dorsey experiment Case 2. The drawn contact discontinuity is approximated based on separate density contours. (b) An annotated experimental shadowgraph captured by Ruegg and Dorsey for the same conditions is shown for comparison. . . . .	188
133	(a) Contours of water mass fraction on the stagnation streamline overlaid with contour lines of pressure as a function of non-dimensional time for Ruegg and Dorsey experiment Case 3. (b) An annotated experimental shadowgraph captured by Ruegg and Dorsey for the same conditions is shown for comparison. . . . .	189
134	A detail view of density contours on the stagnation streamline as a function of time for Case 3 for the (a) QUIVR quasi-1D simulation and (b) high-fidelity, 2D simulation produced using VULCAN. Note that the computed results are non-dimensional in time while the high-fidelity plot is in seconds. . . . .	189

135	Reaction front oscillation frequency as a function of projectile velocity for experimental and numerical investigations. Note that frequencies are grouped due to FFT windowing. . . . .	192
136	Contour lines of (a) density on the stagnation streamline as a function of time for Ruegg and Dorsey experiment Case 2 and (b) 1D mechanism for the regular, unsteady regime by Matsuo (reproduced with permission). . . . .	195
137	Contour lines of (a) density on the stagnation streamline as a function of time for Ruegg and Dorsey experiment Case 3 and (b) 1D mechanism for the regular, unsteady regime by Matsuo and Fujii (reproduced with permission). . . . .	197
138	A detail view of the (a) stagnation streamline density contours from the present simulation (Case 3) compared to a (b) 1D sub-mechanism of the large-disturbance regime as proposed by Matsuo and Fujii [97] (reproduced with permission). . . . .	197
139	Filled contours of reaction front frequency as a function of projectile velocity and ambient pressure for (a) lean, (b) stoichiometric, and (c) rich equivalence ratios. The black line on the latter two plots indicate the Chapman-Jouget detonation velocity. . . . .	199
140	Notional $N^2$ diagram for the analysis framework along with example codes to be used in each node. . . . .	206
141	A hypervelocity trajectory at a constant dynamic pressure of 1500 psf is shown. . . . .	222

## LIST OF SYMBOLS OR ABBREVIATIONS

$\dot{m}$	Mass flow rate.
$\mathbf{M}, \mathbf{N}$	Flux vectors.
$\mathbf{Q}$	Source vector.
$\mathbf{U}$	State vector.
$A$	Area or forward reaction coefficient.
$a$	Local speed of sound.
$B$	Blowing parameter.
$b_f$	Exponential parameter for forward reaction rate.
$c$	Species concentration.
$C_f$	Forward reaction rate coefficient for Arrhenius equation.
$C_p$	Specific heat at constant pressure.
$d$	Dimension.
$D$	Diameter or damping term.
$D_t$	Turbulent mass diffusion.
$E$	Total energy.
$E_a$	Activation energy.
$e_{tb}$	Reaction third body efficiency.
$F$	Stream thrust potential.
$f_{int}$	Internal degrees of freedom.
$g$	Gibbs free energy.
$H$	Altitude or total enthalpy.
$h$	Sensible enthalpy.
$h_p$	Penetration height.
$H_{mid}$	Height of the midpoint of the Mach disk.
$I_{sp}$	Specific impulse.

$J$	Dynamic pressure ratio, $q_{inj}/q_1$ .
$k$	Local body curvature or reaction rate coefficient.
$k_B$	Boltzmann constant.
$K_c$	Equilibrium gas constant in terms of concentration.
$L_c$	Combustor length.
$Le$	Lewis number.
$M$	Mach number.
$m$	Molecular weight.
$n, s$	Normal and tangential coordinates.
$p$	Pressure.
$P$	Wall porosity.
$Pr$	Prandtl number.
$Pr_t$	Turbulent Prandtl number.
$q$	Dynamic pressure, $\rho v/2$ , or heat flux.
$R$	Sphere radius.
$r$	Local cylindrical radius.
$R_u$	Universal gas constant.
$Re_\infty$	Reynolds number based on freestream quantities.
$Sc$	Schmidt number.
$Sc_t$	Turbulent Schmidt number.
$T$	Temperature.
$t$	Time.
$v, u$	Normal and tangential velocity coordinates.
$V_\infty$	Freestream speed.
$w$	Jet wavelength.
$x, y, z$	Cartesian coordinates.
$Y$	Species mass fraction.

$\alpha$	Body angle measured from the stagnation streamline.
$\alpha_j$	Temperature exponent for forward reaction rate.
$\beta$	Non-dimensional height measured from the stagnation streamline.
$\chi$	Species mole fraction.
$\dot{\omega}_i$	Production rate of species $i$ .
$\epsilon$	Lennard-Jones energy of attraction.
$\epsilon_m$	Machine epsilon.
$\eta_c$	Combustion efficiency.
$\eta_m$	Mixing efficiency.
$\gamma$	Ratio of specific heats.
$\lambda$	Non-dimensional distance measured from the sphere center.
$\mu$	Dynamic viscosity.
$\nu_t$	Turbulent viscous diffusivity.
$\nu_{ij}$	Stoichiometric coefficient.
$\phi$	Mixture equivalence ratio.
$\Pi_{ij}$	Stress tensor.
$\rho$	Density.
$\tau_r$	Combustor residence time.

## GLOSSARY

<b>C/C</b>	Carbon/Carbon composite.
<b>CEA</b>	Chemical Equilibrium with Applications.
<b>CFL</b>	Courant-Friedrichs-Lewy.
<b>CMC</b>	Ceramic Matrix Composite.
<b>DAF</b>	Diagonalized Approximate Factorialization.
<b>DAKOTA</b>	Design Analysis Kit for Optimization and Terascale Applications.
<b>DDT</b>	Detonation-to-Deflagration Transition.
<b>ILU</b>	Incomplete LU factorialization.
<b>LARCK</b>	Langley Algorithm for Research in Chemical Kinetics.
<b>LDFSS</b>	Low Dissipation Flux Splitting Scheme.
<b>LES</b>	Large Eddy Simulation.
<b>MUSCL</b>	Monotone Upstream-centered Schemes for Conservation Laws.
<b>NASA</b>	National Aeronautics and Space Administration.
<b>NASP</b>	National AeroSpace Plane.
<b>NO-PLIF</b>	Planar Laser-Induced Fluorescence of Nitric Oxide.
<b>ODWE</b>	Oblique Detonation Wave Engine.
<b>OH-PLIF</b>	Planar Laser-Induced Fluorescence of OH.
<b>PMSIC</b>	Premixed, Shock-Induced Combustion.
<b>QUIVR</b>	QUasI-1d solVer with Reactions.
<b>RANS</b>	Reynolds-Averaged Navier Stokes.
<b>RAS</b>	Reynolds-Averaged Simulation.
<b>SCRAMJET</b>	Supersonic Combustion RAMJET.
<b>SHCRAMJET</b>	Shock-induced, supersonic Combustion RAMJET.
<b>TVD</b>	Total Variation Diminishing.
<b>VULCAN</b>	Viscous Upwind aLgorithm for Complex flow ANalysis.
<b>WMF</b>	Wall-Matching Function.

## SUMMARY

One of the current goals of research in hypersonic, airbreathing propulsion is access to higher Mach numbers. A strong driver of this goal is the desire to integrate a scramjet engine into a transatmospheric vehicle airframe in order to improve performance to low Earth orbit (LEO) or the performance of a semi-global transport. Airbreathing engines such as the scramjet have enhanced performance over non-airbreathing rockets due to the removed requirement of carrying oxidizer on board the vehicle. This advantage is reflected in enhanced efficiency in the form of specific impulse which translates to lower vehicle gross lift off weight when carrying the same size payload to orbit. Additional benefits potentially derived from a smaller, lighter vehicle include reduced cost, maintenance, and possibly improved reliability.

There are technical challenges for scramjets flying in the hypervelocity (Mach 10+) speed regime. The first issue is residence time of the fuel-air mixture in the combustor as the residence time decreases as the freestream velocity of the vehicle increases. The second issue is the internal heating loads experienced by the vehicle as velocity increases. In order to prevent vehicle materials from exceeding their design temperature limits, active cooling is often employed in scramjet designs. This active cooling may have a negative impact to efficiency if excess fueling is required.

The previously discussed problems encountered by scramjets at hypervelocity speeds have the potential to be alleviated by engines using premixed, shock-induced combustion (PMSIC). In this concept, the fuel is injected on the forebody of the vehicle upstream of the inlet. This allows the fuel and air to mix along the forebody instead of in the combustor. Once the mixture reaches the inlet, the flow is processed

through a shock wave of sufficient strength to induce combustion without the use of other ignition devices. Because the combustor only needs to support combustion and not mixing its length is reduced considerably, positively impacting the issues of combustor weight and heat loads. The burned gases then expand in the vehicle nozzle to produce thrust.

The goal of the research presented in this dissertation is to understand the flow mechanisms driving the performance and feasibility of a hypervelocity, shock-induced combustion ramjet (shcramjet). This dissertation presents a series of complementary studies simulating the physics of a shcramjet vehicle traveling at hypervelocity speeds. Regions of interest on the vehicle include the forebody, where injection and mixing must take place with low losses and without autoignition occurring. Another region is the inlet, where the presence of combustion instabilities must be evaluated. Optimization to maximize performance is not within the scope of this research. The design of a specific flight or ground test article is also not an objective of this research.

New knowledge for forebody mixing gained during the course of this research includes the comparative performance of the three primary classes of injection at forebody conditions relevant to hypervelocity flight. These classes include transverse, ramp, and strut injection. A technically defensible means of analyzing the performance of each concept was devised and consisted of the direct comparison of the loss-tracking metric as a function of mixing efficiency. This provided a valid means to identify injectors that perform the best given any particular level of mixing achieved. In doing so, a novel, pathfinding strut injector concept was identified as a superior performer relative to the other concepts studied. This concept will form the starting point for future studies in forebody injection.

The presence of autoignition in the mixing regions of the best performing injectors from the mixing study were also evaluated. During the course of the study it was found that transverse injection, an otherwise high-loss method of injection and mixing,

was characterized by extensive regions of autoignition due to shock wave generated by the fuel plume. The strut injector had two regions of ignition: a small midstream ignition zone due to the presence of shock waves and one at the wall due to the hot boundary layer. Attempts were made to mitigate the latter region using both film and transpiration cooling at the wall via a parametric study of coolant species and injector conditions. It was found that film cooling using either hydrogen or helium provided a significant amount of autoignition mitigation at the wall.

Shock-induced combustion in a constant area duct was simulated at conditions corresponding to freestream Mach numbers ranging from 10 to 20 at a constant dynamic pressure of 71,820 Pa (1500 psf). It was found that no instabilities were present in the flow in the vicinity of the shock wave or elsewhere. At each Mach number simulated, the optimum duct length that provided maximum stream thrust potential was extracted. Another study was conducted with shock-induced combustion of hydrogen/air ahead of a blunted projectile in a quasi-1D framework. As part of this study, the axisymmetric Navier-Stokes equations were reformulated in a form valid in the stagnation region of the projectile in order to significantly decrease the solution time. A new tool was developed and validated against experimental and numerical studies in the literature. It was then applied to parameter studies not yet undertaken in the literature due to the feasibility constraints associated with simulating a large number of axisymmetric simulations. In doing so, regions of instability were mapped out in a large velocity/pressure parameter space.

# CHAPTER I

## INTRODUCTION

### *1.1 Motivation for Current Research (What is a Scramjet and What Are its Challenges?)*

One of the current goals of research in hypersonic, airbreathing propulsion is access to higher Mach numbers. A strong driver for attaining this goal is the desire to integrate a scramjet engine<sup>1</sup> into a transatmospheric vehicle airframe in order to improve single stage or two stage performance to low Earth orbit [1]. Airbreathing engines such as the scramjet enjoy enhanced performance over non-airbreathing rockets due to the eliminated requirement of carrying oxidizer on board the vehicle. This advantage is reflected in enhanced efficiency (i.e.  $I_{sp}$ ) which translates to lower vehicle gross lift off weight when carrying the same sized payload to orbit [2]. Additional benefits potentially derived from a smaller, lighter vehicle include reduced cost, maintenance, and possibly improved reusability.

Scramjets are operationally limited to the atmospheric stage of flight due to requirement that the atmosphere provide the oxygen necessary for combustion. Transition to rocket mode to complete the flight to orbit occurs at the point in the trajectory where the air is too thin for scramjet operation or earlier in the trajectory due to other constraints. Because the subsequent pull-up stage is of lower efficiency, the staging Mach number is critical in defining the overall efficiency of the vehicle; the higher the staging Mach number the more efficient the overall vehicle. Figure 1 demonstrates the difference in staging flight velocity for a vehicle at Mach 10 versus one at Mach 15.

---

<sup>1</sup>Scramjet engines are characterized by a flowpath with ideally no moving parts and air compression accomplished by shock waves produced by the forebody and inlet of the vehicle. This will be discussed in more detail later.

The higher first stage maximum Mach number achieves 38% of the required kinetic energy to LEO versus 15% for the lower first stage maximum Mach number.

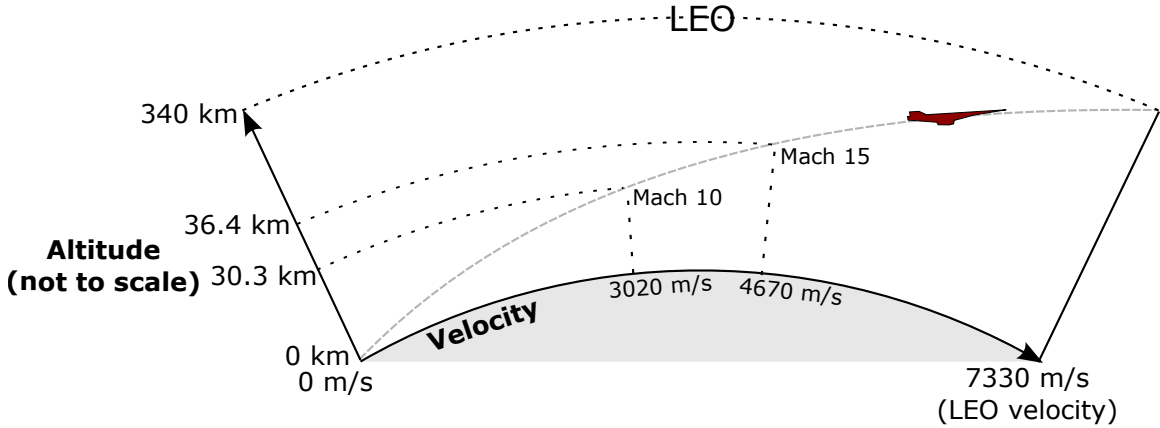


**Figure 1:** Staging altitudes and velocities for a vehicle with a first stage maximum speed of Mach 10 versus a vehicle with a maximum first stage speed of Mach 15.

There are technical challenges that scramjets face when attempting to fly in the hypervelocity<sup>2</sup> speed regime. The first issue is related to the residence time of the fuel-air mixture in the combustor. The residence time of the fuel within the combustor ( $\tau_r \approx L_c/V_\infty$ ) rapidly decreases as the freestream velocity of the vehicle increases. This severely limits the time available for fuel injection, fuel-air mixing, and burning within the combustor. While the combustor could be lengthened to compensate for decreasing residence time, doing so will create additional weight burdens on the vehicle as the combustor tends to be a significant weight component of the engine.

The second issue is related to the heating loads experienced by the vehicle. As velocity increases, the heating loads experienced by the external and internal surfaces of the vehicle become more harsh. In order to prevent vehicle materials from exceeding their design temperature limits, active cooling is often employed in scramjet designs.

Primary methods of active cooling are

<sup>2</sup>The term hypervelocity typically refers to Mach numbers above 10, which corresponds to velocities in excess of 3 km/s on 1000 to 2000 psf trajectories. In this velocity regime, stagnated regions will begin to exhibit oxygen dissociation [3].

1. Passing cryogenic hydrogen through channels below the flowpath surface
2. Injecting a film of hydrogen gas at the surface in the internal flowpath (so-called “film cooling”).

Both of these cooling methods provide lower surface temperatures with the first method preheating the fuel before it enters the combustor. As the vehicle velocity increases past a critical limit, however, a fuel system supplying near-stoichiometric hydrogen to the flowpath is no longer sufficient for cooling and an increase in fuel flow rate is necessary to keep the surfaces cool [2]. This causes two negative impacts. First, the excess fuel is wasted for lack of oxidizer with which to react. Second, vehicle specific impulse is negatively impacted by the increased fuel mass flow rate, reducing engine efficiency.

Attention is now given to the current concepts occupying the hypersonic and hypervelocity regimes of flight. The first is the supersonic combustion ramjet (i.e. scramjet), shown notionally in Figure 2. Because of the highly integrated nature of hypersonic propulsion, the term scramjet is typically used to describe not only the engine but the vehicle itself. However, here the discussion is limited to the engine only. The typical scramjet concept is a single, continuous flowpath ideally with no moving parts (e.g. no mechanical compressors or turbines). The incoming airflow is compressed on the forebody of the vehicle via a system of oblique shock waves that, for an ideal case, terminate at the shoulder of the inlet<sup>3</sup>. Once the compressed air passes into the fully enclosed flowpath, some concepts require the use of an isolator section that is characterized by a shock-train interacting with a growing boundary layer (e.g. a “dual-mode” scramjet). The isolator section provides the necessary time for the pressure rise demanded by the combustor so that inlet unstart does not occur.

---

<sup>3</sup>The shoulder is the point on the vehicle forebody where the flow experiences a local expansion. Two dimensional designs typically aim to terminate the cowl shock wave on the shoulder to minimize shock structures in the internal flowpath.

Once the air enters the combustor fuel is injected where it is then mixed with the air stream. Combustion occurs by igniting the mixture, for example with a silane-hydrogen pilot stream or through autoignition if the ambient conditions allow. The burned gas mixture then expands through the nozzle to create thrust.

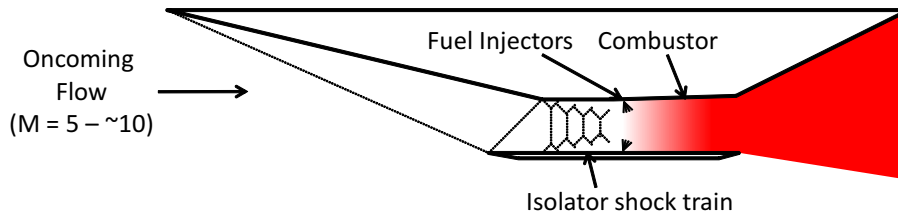


**Figure 2:** A notional scramjet

The previously discussed problems encountered by scramjets at hypervelocity speeds may be alleviated by engines using premixed, shock-induced combustion (PMSIC), shown notionally in Figure 3. In this concept, the fuel is injected on the forebody of the vehicle upstream of the inlet. This allows the fuel and air to mix along the forebody instead of in the combustor. Once the mixture reaches the inlet, the flow is processed through a shock wave of sufficient strength to induce combustion without the use of other ignition devices. Because the combustor only needs to support combustion and not injection and mixing, its length is reduced considerably, positively impacting the issues of combustor weight and heat loads. The burned gases then expand on the vehicle nozzle to produce thrust. Engines using PMSIC are called either shock-induced combustion ramjets (e.g. shcramjets) or oblique detonation wave engines (e.g. ODWEs, or wave engines). The distinction between the two is in the distance between the combustion front and the shock front inducing it: shcramjets typically have a measurable distance between the two while wave engines do not (i.e. the inducing shock wave is a detonation wave). The remainder of this proposal will use the term shcramjet to refer to an engine using PMSIC.

Although it addresses many of the problems faced by scramjets, the shcramjet concept encounters technical challenges of its own. These challenges are illustrated

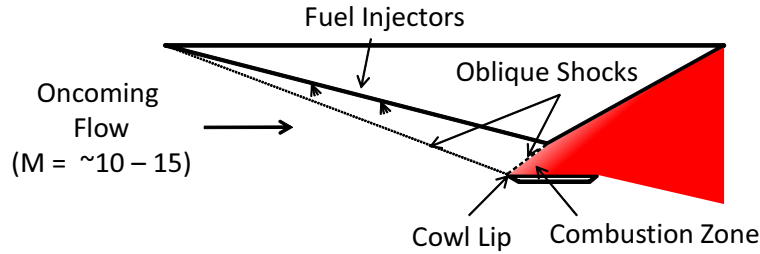


**Figure 3:** A notional scramjet

in Figure 4 and summarized as follows:

**Nonuniform forebody mixing** Fuel injected on the forebody of the vehicle must be able to mix effectively into a cross stream of very high Mach number (e.g. Mach 7-8 for a Mach 12 vehicle). The effect of high Mach numbers on vorticity and mixing of the fuel jet is not well understood. Additionally, uniform mixing is desired in order to allow even burning in the combustor of the scramjet.

**Boundary layer autoignition** As the injected fuel enters the hot forebody boundary layer there is a risk of autoignition of the resulting fuel-air mixture near the body. This would result in the generation of severe pressure drag, high wall heating, and significant fuel losses. Therefore, the prevention or mitigation of autoignition on the forebody is of high importance.

**Shock wave instability** It is possible for combustion instabilities to develop in the reaction zone due to interaction between the shock wave and the induced reaction front. This has been observed in fundamental studies of both blunt body and wedge-supported shock-induced combustion. Depending on the conditions of the oncoming flow, the system may either be completely stable or unstable with possibly large-amplitude behaviors. This can occur in a perfectly mixed system although non-uniformities in mixing may contribute to instability as well. Consequences of these instabilities may range from performance loss to engine unstart.

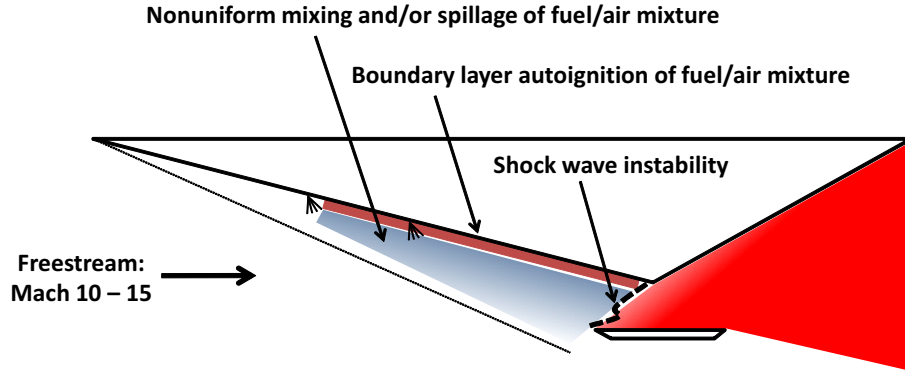


**Figure 4:** Technical challenges for a notional scramjet.

The goal of this research is to evaluate and understand the mechanisms driving the performance of a hypervelocity scramjet vehicle. The research presents a series of complementary studies that simulate the physics of a notional scramjet vehicle traveling at and above Mach 12. Regions of interest on the vehicle include the forebody, where injection and mixing must take place without autoignition, and the inlet-combustor, where combustion instabilities must be minimized to ensure predictable and uniform performance. These regions of interest on the vehicle will be studied individually with inflow boundary conditions traceable to hypervelocity freestream flight conditions. The objective of this study is a physics-based understanding of the performance drivers of the scramjet system; however, black-box optimization to maximize performance is not within the scope of this research. At the conclusion of this research, understanding of the physics driving hypervelocity vehicle performance will be enhanced, thus allowing an analyst to effectively design a scramjet flowpath.

## ***1.2 Background of PMSIC Technology***

This section provides orientation to the high-level background of PMSIC as related to the identification of cycle concepts using the technology and their benefits over the state-of-the-art of the time as well as today. While high-level system studies raise important questions (e.g. How can fuel be injected while minimizing losses? How

may fuel be prevented from burning in the vicinity of the injector?), it will be left to subsequent chapters of this dissertation to provide background and study to them.

Initial cycle analyses of the detonative ramjet originated in the 1950's and were limited to top-level parameter studies assuming ideal mixing and burning. Dunlap, *et al.* [4] evaluated the benefits of an airbreathing engine using wedge-stabilized, detonative combustion versus other, more conventional cycles. Their concept of such an engine is shown in Figure 5. Their analysis assumed perfectly mixed fuel and air upstream of the detonation location with no losses present except for those caused by the detonation wave. The authors brought up the possibility of an unstable detonation wave, concluding that a wedge centerbody would in all likelihood provide the necessary stabilization. They also bring up the possibility for fuel burning in the boundary layer in the vicinity of the fuel injectors. This issue persists today and motivates the current research. It was realized in their analysis, assuming ideal mixing and a fixed ignition temperature, that a hydrogen-fueled concept can realize similar performance to a conventional ramjet at higher Mach numbers. While the study suffered from drawbacks such as not understanding the autoignition properties of the fuels used, it was an important initial data point in the literature.

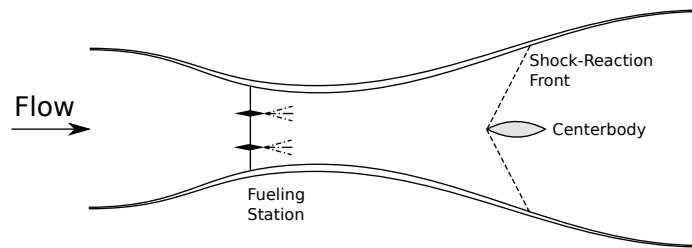


**Figure 5:** A reproduced schematic of the concept analyzed by Dunlap, *et al.* [4] is shown.

Soon after the Dunlap study, Sargent and Gross [5] published a study analyzing the detonation wave ramjet in further detail using hydrocarbon fuel. The study was derived from experimental results in plane and oblique detonation, reported by Gross [6, 7]. As with the Dunlap cycle, the engine concept was assumed to compress the

incoming air stream to a target supersonic velocity subject to varying inlet kinetic energy efficiencies. A representation of the engine analyzed by Sargent and Gross is shown in Figure 6. Assuming no losses from injection, uniform mixing, and complete combustion, the Isp, SFC, thermal efficiency, and exit to inlet area ratio were determined as a function of flight and detonation Mach numbers, inlet efficiency, and nozzle efficiency. The results indicated that compared to the subsonic burning ramjet, the detonation wave engine has lower fuel consumption at the cost of thermodynamic performance (which is a minor difference for some cases). The report also identified other salient points relating to the ODWE, for example shorter combustor lengths (due to reduced mixing and reaction length), lighter structure (due to lower static pressure), and lower heat loads (due to shorter lengths). The problem of fuel injection was also identified, an issue that persists today and motivates the current research. The need for variable geometry was also identified as a critical need.

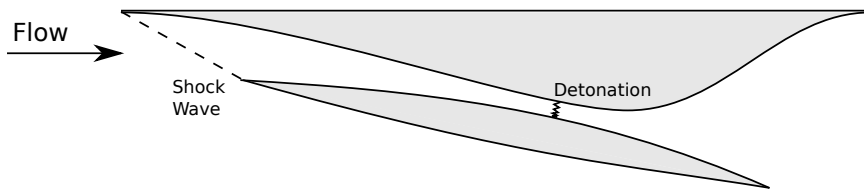


**Figure 6:** A reproduced schematic of the concept analyzed by Sargent and Gross [5] is shown.

Rubins and Rhodes [8] conducted experiments in premixed, shock-induced combustion at the Arnold Engineering Development Center in 1963 that were important pathfinding studies in the feasibility of the technology. Rather than relying on the creation of a detonation wave for combustion, an oblique shock was used to raise the temperature of a premixed fuel-air stream above the mixture’s autoignition temperature. In this sense, what they were proposing was not a “wave” engine, but a more general shock-induced combustion process. A flowpath using this technology is shown in Figure 7. The process shown differs from an oblique detonation in the sense that the reaction zone is no longer tightly coupled with the shock wave, the only purpose

of which is to increase the temperature of the fuel-air mixture.

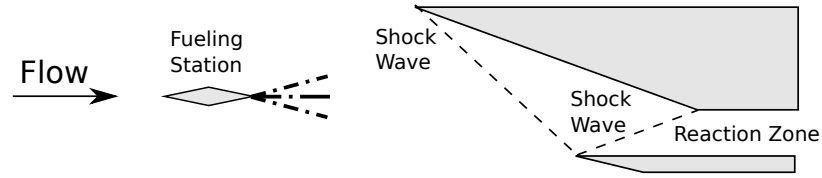


**Figure 7:** A reproduced schematic of the concept proposed by Rubins and Rhodes [8] is shown.

In order to test the concept, Rubins and Rhodes created an experiment that mixed fuel and air before the mixture was processed through an oblique shock supported by a  $28^\circ$  wedge. A schematic of the experiment is shown in Figure 8 with the upstream flow provided by a combustion-heated Mach 3 tunnel. The experiments showed that it is possible to control chemical reaction through the use of shock waves and demonstrated predictable behavior in the combustion process compared to theory. Similar to previous studies, Rubins and Rhodes identified the issue of fuel injection as a critical one moving forward.

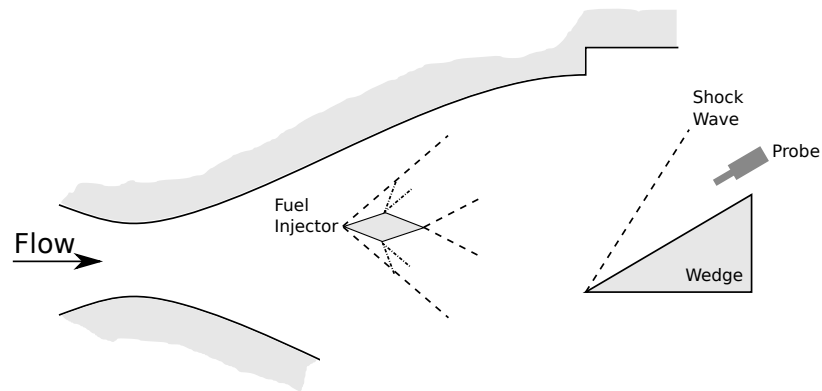


**Figure 8:** A reproduced schematic of the PMSIC experiment conducted by by Rubins and Rhodes [8] is shown.

Rubins and Bauer [9] made cycle calculations to evaluate the benefits of preinjection as applied to scramjet flowpaths—as sketched in Figure 9—in the Mach 9 to 22 range. Their study was distinct in that the concept studied had fuel injected on the

forebody of the vehicle during the compression cycle. While one proposal for ignition of the premixed fuel-air stream was via shock waves, it was only one of a handful of other options, for example the more conventional pilot flame/jet. The study was completely analytical in nature and identified key benefits of forebody injection, including improved fuel specific impulse due to lowered forebody wall friction (for a lighter-than-air fuel) and improved pressure recovery. Methods to limit forebody fuel ignition were also discussed, for example parallel fuel injection and the use of film cooling.

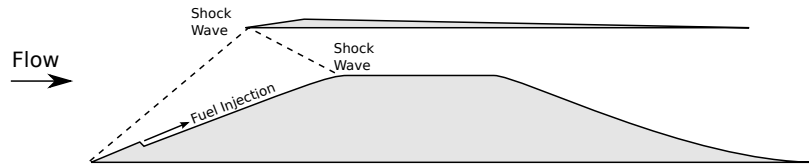


**Figure 9:** A reproduced schematic of the concept proposed by Rubins and Bauer [9] is shown.

Through the 1970’s, PMSIC research generally concentrated on unit studies of shock-induced combustion ahead of blunted projectiles and wedges [10, 11, 12] without much direct maturation of engine concepts using PMSIC. These intervening studies did provide important steps in understanding the physics of the phenomenon, as will be discussed in later chapters. As for the lack of further concepts using PMSIC, research focus most likely drifted away from the technology due to near-term challenges (e.g. forebody auto-ignition) and the fact that scramjet flight at low- to mid-hypersonic (i.e. 5 - 10) Mach numbers was and is realizable without premixing.

The period from the late 1970’s through the early 1990’s brought important studies toward the development of PMSIC technology. First, there were a number of systems studies [13, 14, 15, 2] that brought the concept of a transatmospheric vehicle using PMSIC engines into greater focus and showed their potential benefits over “traditional” scramjet engines. These detailed studies demonstrated an important pull case for the technology and remain important references for the quantitative systems

benefit of PMSIC. Second, the advent of the National AeroSpace Plane (NASP) concept was a milestone in the national drive toward developing an orbital access vehicle using airbreathing engines. Because the orbital access use case is an important one for PMSIC technology. Third, through the same time period, computational fluid dynamics experienced rapid improvements in capability and some of the first numerical simulations on PMSIC and its application to an engine were conducted [16, 17, 18, 19]. Many of these initial studies marked the beginning of long-lasting and geographically diverse research programs into the technology. Finally, experiments in PMSIC found some resurgence [20, 21] and further demonstrated the feasibility of the technology.

With the systems benefits of scramjet engines having been established, research in the physics of PMSIC has experienced renewed focus in the new millennium. Fundamental studies in blunt-body PMSIC have maintained attention in Japan and wedge-supported PMSIC has continued to be studied in the United States and elsewhere. In addition, research programs addressing systems issues related to PMSIC, for example fuel injection, has received attention by researchers in the United States, Canada, and Europe. While the background of this research will be outlined in future chapters, the fact that strong research programs exist to develop the technology for use in hypervelocity engines lends optimism for the future of the scramjet concept.

### ***1.3 Knowledge Gaps in the Literature***

While fundamental advances have been made in advancing the state of the art in PMSIC and its application to scramjet engines, the literature currently has several gaps that are open avenues for pathfinding research. Selected knowledge gaps are categorically summarized as follows:

**Forebody Injection/Mixing:** Few concepts have been studied in depth for forebody fuel injection in the hypervelocity regime. Recent studies have concerned the forebody injection of fuel using either a slot [22] or modified ramps

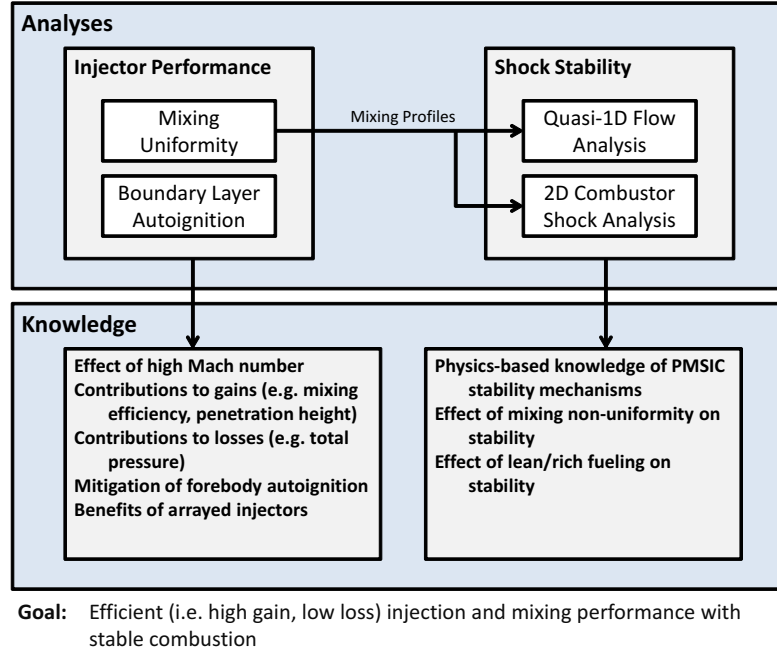


**Figure 10:** Studies involved in the present work and knowledge to be gained.

[23]. While a number of studies from the same research group have tackled the latter geometry in terms of characterizing its performance, any geometrical modification has been through perturbation of the same design. No studies exist in the literature comparing several injection concepts at the same conditions in order to make a direct comparison.

There is also a lack of proper characterization of injector performance in the literature. In the general literature of fuel injection and mixing, many studies neglect to make any characterization of the losses incurred by the injector concept. The typical means of measuring the efficacy of a particular concept is to limit the analysis to positive metrics such as mixing efficiency, or to a more coarse extent, fuel penetration or injected plume area. By ignoring losses, it is not possible to truly gain an understanding of the relative performance of different injectors, as will be discussed in Chapter 2. Of the studies that do attempt an analysis of losses, many use the common metric of total pressure

loss. While this metric is appropriate for determining the losses incurred during a general compression process, it is not appropriate where the mixing of gases is occurring (this will also be discussed in Chapter 2). Finally, of the studies that do make a proper characterization of losses, there is little clarity as to how to properly compare positive metrics to loss metrics. This is because mixing itself is a loss-producing process.

**Autoignition Mitigation:** The tendency for fuel injected on a vehicle forebody to ignite when exposed to the hot boundary layer region has long been identified as a potential problem for such concepts, but few options for mitigation exist in the literature as pertains to hypervelocity propulsion. To the author’s knowledge, the only concept for autoignition mitigation for a hypervelocity forebody is the slot injection of nitrogen at the base of a cantilevered ramp injector [24]. While it demonstrates promising results, other mitigation strategies may provide similar or better performance for lower amounts of injected transpirant.

**Shock Instability:** Shock instability at the combustor entrance has two potential sources. The first is due to the interactions and dynamics between the shock wave and the resulting reacting front. This phenomenon has been studied to a degree using blunt-body problems, but there is no comprehensive parametric study on what the effect of composition, temperature, pressure, and velocity has on the resulting dynamics. This is due to the logistics of the problem, where most researchers create axisymmetric computational grids with convergence requirements much higher than that which is needed for a rapid parametric study. The second instability is due to an unstable solution to the oblique shock problem. This issue has been looked at to some degree by researchers, but the effect

of this instability of fuel composition and wedge bluntness is not well characterized (although Matsuo conducted a small study of PMSIC on a blunted wedge for two bluntness radii).

#### ***1.4 Objectives and Contributions***

It is the goal of this dissertation to address the knowledge gaps outlined in the previous section. The same categories of knowledge gaps will compose the major sections of this thesis. The first objective of this dissertation will be to compare injection methodologies at the same flow conditions to determine relative benefits of each. Note that the objective of this study is not to provide optimized solutions to the problem of forebody injection and mixing, but rather to conduct comparative studies to identify methods that outperform others. In addition, quantitative benefit and loss metrics will be compared directly in order to determine the value of one concept over another.

The second objective will be to address the issue of autoignition in the vicinity of the fuel injectors. In order to reduce the number of injectors considered, only the best performing injectors from the comparative study will be evaluated. Film and transpiration cooling will be evaluated for their ability to mitigate autoignition and a parametric study will be conducted to understand the effect of different coolant flow variables.

Finally, the issues of shock/reaction front stability will be investigated. The axisymmetric Navier-Stokes equations will be reformulated in a form that lends itself to rapid analysis with minimal loss of fidelity. The shock/reacting front dynamics will be characterized with respect to the important parameters affecting the flow. Furthermore, it will be determined if instabilities occur in a constant area duct representative of a notional combustor.

The specific, unique contributions of this research that advance the body of work

in this flight regime include:

1. Transverse, ramp, and strut injection concepts simulated at the same conditions to determine...
  - (a) ...mixing efficiency and thrust potential as a function of distance from injector leading edge.
  - (b) ...the relative performance of each concept using the ratio of mixing efficiency and thrust potential as a function of distance from the injector leading edge.
  - (c) ...where autoignition is present in the vicinity of best-performing injectors and the mechanisms by which autoignition occurs.
2. How best to mitigate autoignition in the vicinity of the wall using film cooling and wall transpiration, including...
  - (a) ...the best selection of transpiration locations relative to the injector.
  - (b) ...the proper selection and effect of cooling parameters such as wall porosity, mass flow rate, species, and coolant temperature.
3. Determination of the optimum notional combustor length for different points on a notional airbreathing trajectory as well as evaluating if there are instabilities present in the internal flow.
4. Improved predictions of the regimes of shock/reacting front stability by enabling a rapid simulation framework by the re-formulation of the Navier Stokes equations in a quasi-1D form.

These objectives will be accompanied by numerical studies to validate the specific physics controlling the behaviors of each type of flow (e.g. mixing, combustion, unsteady dynamics) as simulated by the CFD code chosen for the analysis.

## **1.5** *Dissertation Preview*

**Chapter 2** concerns the injection and mixing of fuel with air at conditions relevant to a hypervelocity vehicle on a 71,820 Pa (1500 psf) trajectory at the Mach 12 trajectory point. Injection is studied in nonreacting simulations among the major categories of injection: flush-wall, ramp, and strut injection.

**Chapter 3** concerns the mitigation of autoignition on a notional shcramjet vehicle forebody. For this study reacting simulations of film and transpiration cooling concepts are evaluated as a means to cool the boundary layer.

**Chapter 4** concerns the stability of the shock and reaction front located at the entrance of a notional shcramjet combustor entrance. Optimum combustor lengths will also be obtained as a function of point on the trajectory using stream thrust potential.

**Chapter 5** concerns the development of a tool to rapidly analyze the stability characteristics of a premixed, shock-induced combustion shock and reaction front ahead of a supersonic, blunted projectile.

**Chapter 6** provides a summary and conclusion to the research presented herein, as well as avenues for future research.

## CHAPTER II

### FOREBODY INJECTION AND MIXING

Much of the literature on fuel injection research for scramjet combustion has been at Mach numbers representative of mid-range hypersonic flight (Mach 5 - 8). Of these, most numerical and experimental studies have been conducted at conditions relevant to the combustor as typical fuel injection schemes begin at the transition from the isolator<sup>1</sup> to the combustor. Therefore, most studies have taken place around Mach 2 - 3 in duct flow. In this speed regime, a significant number of experiments have evaluated perpendicular wall injection, [25], near-parallel injection concepts (e.g. swept ramp injectors) [26, 27], transpiration/effusive injection cooling for transverse injection [28], and the effect of fuel injector nozzle geometry on mixing characteristics [29, 30, 31]. The use of cavities for injection and flameholding has also been a subject of past research [32]. The use of oblique shock waves to enhance mixing has been proposed, tested, and used in practice [33, 34].

Other studies have investigated the use of pre-injection on the vehicle forebody in order to allow more time for mixing with the goal of reducing combustor length. Rubins and Bauer [9] described an early analytic treatment of pre-injection with application to scramjet engines from Mach 9 to 22 flight conditions and concluded that premixing with hydrogen has the ability to improve inlet pressure recovery, reduce friction, and shorten the vehicle combustor. A numerical study of slot-injection into a Mach 6.3 flow was conducted by Gonzalez [22], investigating the parametric effect of fuel temperature and pressure on the potential for ignition in the boundary

---

<sup>1</sup>The isolator section of a scramjet is a component to protect the inlet of the vehicle from the pressure rise in the combustor for low supersonic Mach numbers. Without the isolator, engine unstart may occur at some conditions.

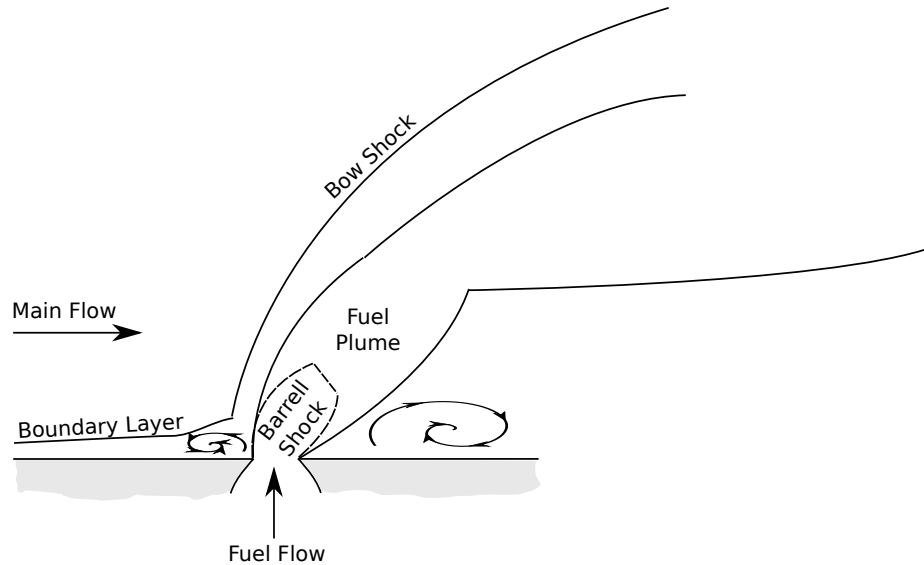


**Figure 11:** A schematic of the flow in the vicinity of an underexpanded transverse fuel injector in supersonic flow is shown.

layer. Recent advances in pre-injection for the scramjet forebody with hydrogen and hydrocarbon fuel considered the use of cantilevered injectors with slot cooling to prevent boundary layer autoignition [35, 24, 36, 23, 37, 38].

A schematic of the flowfield about a transverse, underexpanded fuel injector is shown in Figure 11. The penetration of a transverse fuel jet into a crossflow is largely governed by the dynamic pressure ratio,  $J$ , of the fuel jet to the crossflow (e.g. relative force of blowing) [25], the geometry of the jet itself (e.g. disturbance to the crossflow) [30, 39], and the angle of injection. The dynamic pressure ratio is bounded by maximum fuel system pressure and the desire to produce an underexpanded plume. An underexpanded plume is desirable because it prevents losses due to shock structures forming within the jet. The geometry of the jet is governed by the injector nozzle and its exit shape with more complex geometries representing a more difficult problem in fabrication and survivability. The angle of injection represents a design tradeoff between high-penetration/high-loss normal injection and low-penetration axial injection that imparts a beneficial thrust to the vehicle due to the fuel jet itself.

Identifying an injector that best penetrates and promotes mixing of fuel into the

main flow is insufficient when considering how the injected plume is to subsequently mix with its surroundings. Molecular mixing is governed by diffusion, and how quickly fuel and air diffuse through a unit area of interface is largely out of the designer's control. Therefore, increasing the mixing rate through the fuel-air interface is accomplished by stretching the interface using vorticity in the flow. Vortical stirring structures can be induced via geometry placed in the flowfield as is the case with the swept ramp concept [26] and by flow interaction phenomena such as that between a fuel jet passing through a shockwave [34]. Care should be taken in designing such an interacting flowfield, however, as stirring phenomena can work against the designer. For example, some character of shock waves can turn fuel back toward the wall [35].

Once a fuel injector is identified that has excellent penetration and mixing characteristics, the designer is once again presented with a challenge in the form of losses produced by the injector concept. For example, there may exist an injector concept that is able to achieve perfect mixing but at the cost of depleting the main flow of the momentum upon which the vehicle depends for producing thrust. There are a number of loss sources that must be taken into account when designing and implementing a forebody injector. For example, separation zones are likely to develop that may entrain the fuel from the injector and enhance local combustion. In particular this is observed in flush-wall injection [40]. This is a potential source of drag from combustion on the forebody as well as fuel loss. Combustion in the vicinity of the injector also has the potential for increasing local heating rates. Another source of drag is autoignition due to the fuel entering the hot boundary layer, igniting, and pressurizing the forebody. This is a significant source of drag, fuel loss, and intense heating at the wall. This issue can be mitigated with film or transpiration cooling; however, care should be taken in this approach due to the negative impact on the specific impulse with excess fueling. Other sources of drag include intrusive geometries and unpressurized, rearward facing steps. Finally, injection schemes that deviate

from axially directed injection suffer increasing momentum losses as the angle of injection approaches 90 degrees. Some of these factors may actually be a benefit in the context of internal injection (e.g. rapid autoignition) but are detrimental for forebody injection.

The purpose of this chapter is to report on the study of forebody fuel-air mixing on a notional forebody at conditions representative of hypervelocity flight. Hydrogen fuel injection was simulated on flat plate with the crossflow conditions representing conditions of a Mach 12 point on a 71,820 Pa (1500 psf) trajectory after being shocked through two forebody shocks. Flush wall, ramp, and strut injection were simulated numerically and compared using a novel methodology for reducing the mixing and loss metrics extracted from the flow.

## ***2.1 Numerical Framework and Approach***

While a great deal of effort could have been spent to develop a new CFD solver for the work contained in this dissertation, it was decided instead to leverage the capabilities of an existing numerical code. This is because the main objective of the mixing and autoignition studies is physical investigation, not tool development. Therefore, the numerical studies in Chapters 2 and 3 were carried out using the Viscous Upwind aLgorithm for Complex flow ANalysis (VULCAN) [41] CFD code, developed and maintained at NASA Langley Research Center. VULCAN uses a finite-volume, cell-centered scheme for solving calorically- or thermally-perfect flows on a structured grid. While some CFD codes permit the use of unstructured grids, beneficial when creating topologies for complicated geometries, the structured grid capabilities of VULCAN allow for generally higher accuracy for fewer grid points. This is especially true when evaluating viscous regions which are important in this dissertation.

VULCAN began development in 1992 under the name Langley Algorithm for Research in Chemical Kinetics (LARCK) as a replacement of the SPARK code [42], motivated by the desire to study complex geometries and incorporating upwind schemes into the simulation capability<sup>2</sup>. Instead of modifying SPARK to suit evolving needs for high speed propulsion applications, LARCK began development without a heritage codebase. Because turbulence-chemistry interaction problems were of interest at the time, LARCK also included models for such phenomena. Early in its development, LARCK was successfully validated against multidimensional flat plate and ramp flows as well as used in the simulation of integrated scramjet flowpaths [43]. In 1996, LARCK was upgraded with new space marching capabilities and turbulence wall functions under contract from the Air Force and it was at this time the code was renamed to VULCAN<sup>2</sup>. In the late 1990s, an effort was undertaken to parallelize the code. Some examples of validation studies undertaken with VULCAN include Mach 3 flow over a cavity flameholder [44], Mach 1.8 coaxial jet flow [45], Mach 2 vitiated flow in a facility nozzle [46], a Mach 4 sidewall compression inlet [47], and a Mach 6 streamline traced inlet [48].

The VULCAN code is designed for and excels at the computation of high speed, exothermic flows characteristic of scramjet engines. The algorithm is valid from roughly Mach 0.1 to any speed regime that would cause a thermochemical breakdown in the flow. For example, while at the time of this writing vibrational nonequilibrium is being integrated into the code, it is currently unsuitable for the simulation of very high speed endothermic flows such as those studied in entry, descent, and landing applications. Because of its development and specialization in the simulation of high speed, exothermic flows, VULCAN has entered wide use for both fundamental hypersonic research and in successful test programs such as Hyper-X (X-43A/B/C), X-51, and HIFiRE.

---

<sup>2</sup>Jeffrey A. White, personal communication

The flow for this study was assumed to be viscous and thermally perfect. Non-reacting simulations were carried out in the mixing studies of this chapter and reacting simulations and the effect of autoignition were addressed in Chapter 3. Selected capabilities of the VULCAN CFD code are summarized in Table 1. In this study the flow was integrated spatially using the LDFSS scheme [49] to improve simulation robustness and discontinuity resolution in the flow field. The MUSCL interpolation scheme was chosen to be third order upwind-biased to reduce truncation error and the use of a van Leer flux limiter assured that the solution is total variation diminishing (TVD). Unless otherwise noted, the flow was integrated temporally using the DAF scheme [50] with local time stepping and an increasing Courant-Friedrichs-Lewy (CFL) number schedule. The use of DAF allows for more stable behavior during solution although ILU increases the CFL number limit at the cost of significantly increased storage requirements.

Unless otherwise stated, the simulated flow was assumed to be fully turbulent. VULCAN is equipped for Reynolds-averaged simulation (RAS) using the one equation turbulence model of Spalart or two equation models of Menter (with and without shear stress extension) or Wilcox. Recent VULCAN developments include simulating turbulence using large eddy simulation (LES) and hybrid RAS/LES. While the LES and hybrid methods both provide improved accuracy and physical reproduction, for this dissertation it was decided to treat turbulence using RAS in order to take advantage of the significantly improved simulation time of the two-equation methods. Therefore, turbulence calculations in this study use the two-equation Menter  $k-\omega$  model [51] with a turbulent Prandtl number (governing turbulent energy diffusion) of 0.9, turbulent Schmidt number (governing turbulent mass diffusion) of 1.0, and a turbulence intensity of 0.1. The turbulence parameters were held constant for each simulation to ensure consistency of comparisons made between cases. For wall-bounded flows, VULCAN has options for either solving-to-the-wall or employing

---

---

**Table 1:** A capability summary of the VULCAN CFD code

---

---

**Spatial integration schemes**

Parabolic (space marching)  
Elliptic

**Inviscid flux reconstruction schemes**

None  
Roe flux differencing  
Local Lax Friedrichs  
van Leer flux vector splitting  
Harten, Lax, van Leer, and Contact flux splitting  
Edwards low dissipation flux splitting  
Edwards low Mach number preconditioned flux splitting

**Flux limiters**

None  
Minmod (TVD)  
van Leer (TVD)  
van Albada  
Smooth  
Koren  
Minmod (ENO)  
van Leer (ENO)

**Turbulence models**

Laminar  
One-equation incompressible Spalart  
Two-equation Menter blended Wilcox 1988  $k-\omega$ /Jones Launder  $k-\epsilon$   
Two-equation shear-stress transport Menter variant  
Two-equation 1998 Wilcox  $k-\omega$   
Two-equation 2006 Wilcox  $k-\omega$   
Explicit Algebraic Stress model of Rumsey and Gatski (2003)  
Constant coefficient Smagorinsky sub-grid scale model  
with van Driest wall damping

**Chemistry modeling**

Frozen  
Finite Rate (Arrhenius with or without Troe falloff parameters)  
Computer Automated Reduced Mechanism (CARM)  
CARM with In-Situ Automated Tabulation (ISAT)

**Point-implicit chemistry treatment**

Analytical Jacobian  
Numerical Jacobian

**Temporal integration schemes (local or global)**

Diagonal Approximate Factorialization (DAF)  
Implicit LU-Factorialization (ILU)

**Other options**

Multi-grid cycling  
2D, Axisymmetric, or 3D domains

---

---

wall matching functions (WMF). It was decided to use the wall matching function of Wilcox [52] in order to relax the grid spacing requirements at the wall. Without WMF, the first point in the topology typically needs to be located in the viscous sub-layer at a  $y^+$  value between 1.0 and 2.0 while the use of matching functions relaxes this requirement to somewhere between 20.0 and 200.0 [53] with lower values corresponding to better prediction. For  $y^+$  values under 10.0, VULCAN uses a blending scheme to transition from wall matching to a solve-to-the-wall method.

## 2.2 *Validation*

The process of validating a tool is an important step to ensure that a particular code or model is accurately reflecting the physics of the modeled regime. The Department of Defense [54] defines validation as

*“Validation: The process of determining the degree to which a model is an accurate representation of the real world from the perspective of the intended uses of the model.”*

In other words, a tool has been validated for use *in a particular regime* if simulations carried out with the model at the same conditions accurately match reality through the use of validation data (e.g. experimental data). Validation should not be confused with verification (i.e. establishing that the programmed model matches the conceptual/theoretical model) or qualification (i.e. establishing that the conceptual/theoretical model matches reality with a defined level of fidelity).

The computational fluid dynamics software of choice in this study was VULCAN, a NASA Langley Research Center code specializing in the simulation of supersonic, exothermic flows. More information on the code was given in Section 2.1. The ability of VULCAN to properly predict the physics of fuel injection into a quiescent or flowing reservoir was verified by comparing simulated results against theory and experiment at similar conditions. The validation questions are summarized as:

Can VULCAN...

- ...successfully predict the Mach disk height, Mach disk width, and wavelength of the jet plume when injected into quiescent air at various jet pressure ratios?
- ...successfully predict the Mach disk height of a jet plume injected into a supersonic crossflow?
- ...successfully predict the mixing plume characteristics for axial injection into a supersonic coflow?

These questions were chosen because the important controlling physics for the injection and mixing studies to follow include the displacement of injected fuel jets from the wall as well as the effect of vorticity on the mixing of fuel with air. If the answer to each of these validation questions is “yes,” it can be reasonably concluded that VULCAN can predict the physics of injection and mixing in the present study assuming similar flow features are present and/or the conditions are comparable.

### **2.2.1 Transverse Injection into a Quiescent Medium**

The ability of VULCAN to simulate the physics of sonic jet injection into a quiescent medium will now be summarized. This problem has been studied in the past by many researchers numerically, experimentally, and theoretically and is therefore a good validation problem to give confidence to VULCAN’s capability in predicting such physics. There is similarity between the current validation problem and the transverse injection and mixing study contained in this thesis in that a diatomic gas is being injected at sonic conditions, although the speed of the medium is different between the validation case. The primary purpose of this study was to evaluate VULCAN’s ability to predict the structure of the barrel shock of the injected jet.

A cutaway of the topological grid used in this study is shown in Figure 12 with every fourth grid point drawn. The grid had 2.5 million grid cells and was clustered

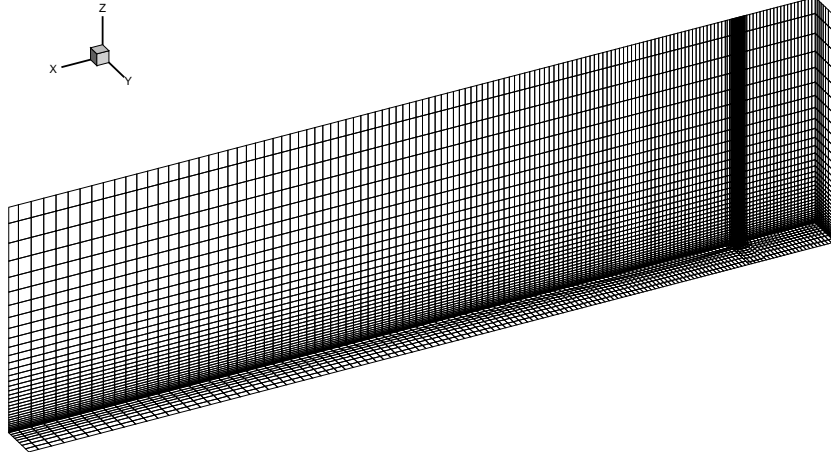


**Figure 12:** The grid used for injection validation is shown with every fourth grid point drawn. For cases with crossflow, the flow originates from the upper right.

near the injector, the wall, and the symmetry centerline. A detail view of the circular injector in Figure 13 shows the grid topology of the injector, which consisted of a C-grid wrapped around a H-grid. Studies involving jet injection into a quiescent medium typically use an axisymmetric grid that extends radially from the plane of the jet exit and axially downstream of the jet centerline. It was decided, however, to use the same grid for both cases of a sonic jet issuing into a quiescent and supersonic crossflow. This also reduced the presence of instabilities typically found in axisymmetric simulations of jets issuing in to quiescent mediums.

Experimental evaluations of sonic jets containing 95% N<sub>2</sub>/5% NO by volume into a quiescent chamber were done by Wilkes *et al.* [55] at NASA Langley Research Center. The Nitrogen jets were seeded with NO in order to provide visualization capability by planar laser-induced fluorescence of nitric oxide (NO-PLIF). The visualization method used was able to capture clear images of the structure of each underexpanded jet into a quiescent chamber. Multiple jet conditions were tested that provided data of jet primary wavelength as well as Mach disk width and standoff distances as a function of the pressure ratio between the jet and the chamber. Therefore, these experimental results are a good source of high-quality data against which to compare the present

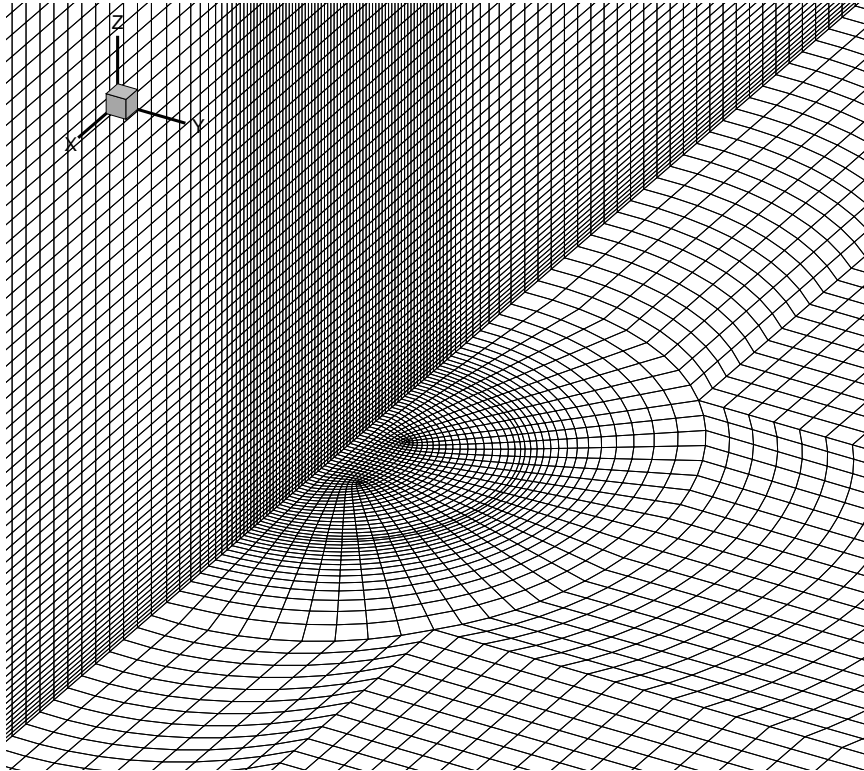


**Figure 13:** Injector detail for the validation grid with all grid points drawn. The injector topology consists of an H-grid near the center of the injector with a C-grid wrapped around it.

numerical results. Figure 14 shows an annotated bisection of a jet from a converged VULCAN simulation with a total pressure ratio of 20.

The empirical and theoretical results of Love, *et. al* [56] also provide another point of comparison for the present numerical results. For their study, they looked at the effect of injector Mach number, pressure ratio, and nozzle divergence angle on jet primary wavelength and the Mach disk width and standoff distance. Jets were tested at Mach numbers ranging from 1 to 3 and for each case of Mach number the pressure ratio was varied over a wide range. Not only did they consider the characteristics of jets issuing into a quiescent medium, but they also considered cases of jets issuing into a supersonic coflow. Only the quiescent results are considered here, however. The quality and detail of the results in these experiments provide another good comparison point for the present numerical results.

Converged results from VULCAN are compared to experimental results in Figures 15 to 17. Each case consisted of a sonic, 300 K, 100% hydrogen jet issuing into quiescent air at an ambient temperature of 300 K and at a pressure of 2000 Pa. Jet pressure ratios of 2, 3.8, 5, 10, 16.8, 20, and 27.6 were simulated. The non-integer pressure ratios correspond to experimental conditions. Hydrogen was chosen as the injectant due to the desire to use the same injectant gas as will be used in the later numerical simulations. This discrepancy in injectant gas between simulation and experiment is not anticipated to cause an issue, however, because the important parameters for this problem as identified by previous researchers are jet Mach number, pressure ratio, and ratio of specific heats [25, 57, 58]. For example, a semi-empirical relation by Billig *et al.* [25] expresses the Mach disk standoff distance in a quiescent crossflow as a function of jet Mach number and pressure ratio as

$$\frac{H_{mid}}{D_e} = \left[ M_j^{1/2} \left( \frac{p_i}{p_\infty} \right) \right]^{1/2} \quad (1)$$

In the same paper, Billig validates this relation against a wide range of experiments using different injectants.

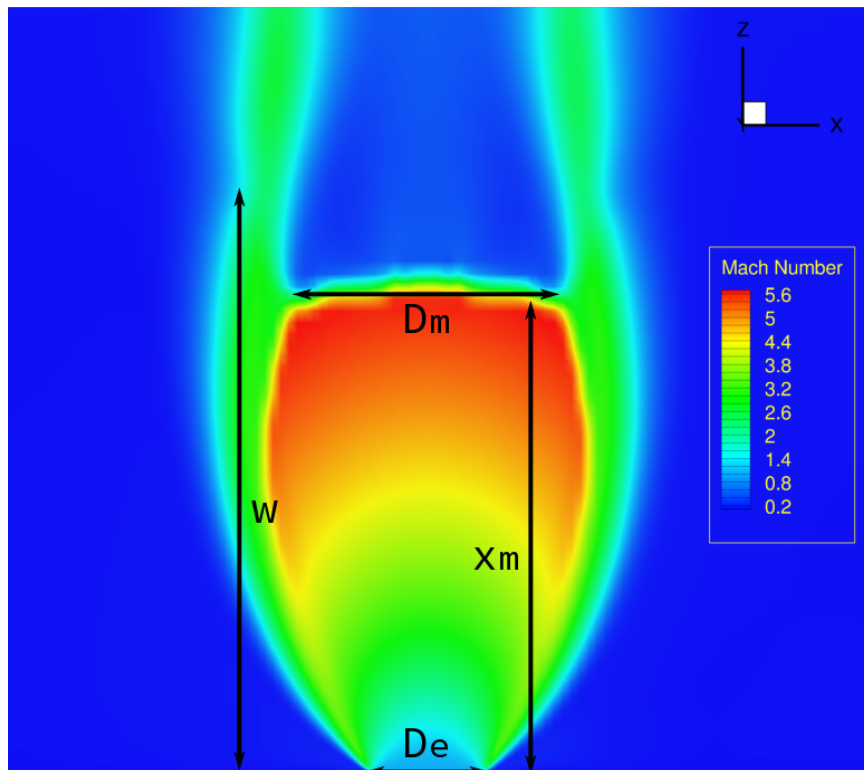


**Figure 14:** A plane bisecting the sonic jet is shown from the converged case of jet pressure ratio equal to 20. Parameters of the jet are shown, consisting of wavelength,  $w$ , Mach disk diameter,  $D_m$ , exit diameter,  $D_e$ , and Mach disk standoff distance  $x_m$ .

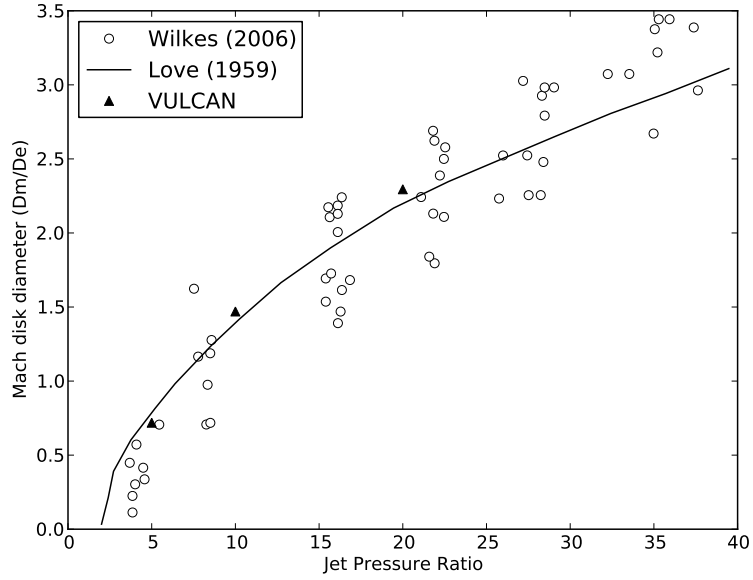


**Figure 15:** Normalized Mach disk diameter as a function of jet pressure ratio. Numerical results from Vulcan are compared against the results of Wilkes *et. al* [55] and Love *et. al* [56].

Figure 15 compares computations to experiments of normalized Mach disk diameter over pressures ranging from roughly 5 to 40. The scatter of the results of Wilkes *et. al* can be explained due to the variation in Reynolds number for different runs. Regardless, the semi-empirical results of Love *et. al* at the same Mach number pass through the center of the NO-PLIF data, indicating general agreement between the two experiments. The present numerical results are indicated by solid triangles and show that the present results from VULCAN lie in the experimental scatter.

Figure 16 shows the experimental and empirical jet Mach disk standoff location compared to the predictions by VULCAN for a sonic jet over the same range of pressure ratios. Here some divergence can be seen between the two experimental results as pressure ratio is increased. Love [56] does mention that the semi-empirical relation tends to overpredict the wavelength for high jet pressure ratios at low Mach numbers; however, the relation derived by Love is fit for the sonic case and matches their experimental data closely. Therefore, the cause of the discrepancy is not clear.

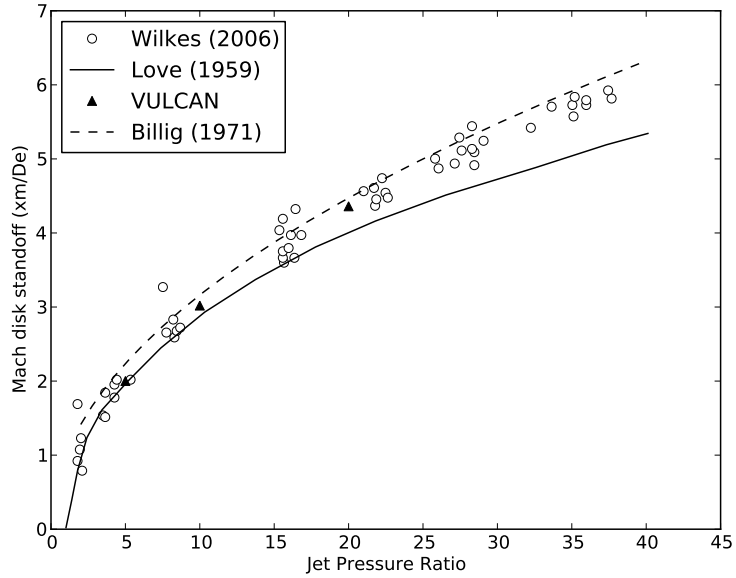


**Figure 16:** Normalized Mach disk standoff distance as a function of jet pressure ratio. Numerical results from Vulcan are compared against the results of Wilkes *et. al* [55] and Love *et. al* [56].

The semi-empirical relation of Billig from Equation 1 is also plotted and shows good agreement with the present results and the data taken by Wilkes. Billig [25] also noted that Love’s relation for Mach disk standoff location tended to not match a general data set of experimental results.

Figure 17 compares the experimental jet wavelength to that predicted by VULCAN at the same range of pressure ratios. As with the Mach disk standoff distance, there is a divergence between the two experimental results. As previously stated, the cause of this discrepancy is unclear. The present numerical results, however, agree well with both experimental results, lying between them. The results also lie within the experimental scatter.

It has been shown that VULCAN is able to successfully predict the physics of sonic jets issuing into a quiescent medium. Numerical results have been compared against experimental data and semi-empirical relations for the parameters of jet wavelength, Mach disk standoff distance, and Mach disk width. The present numerical results

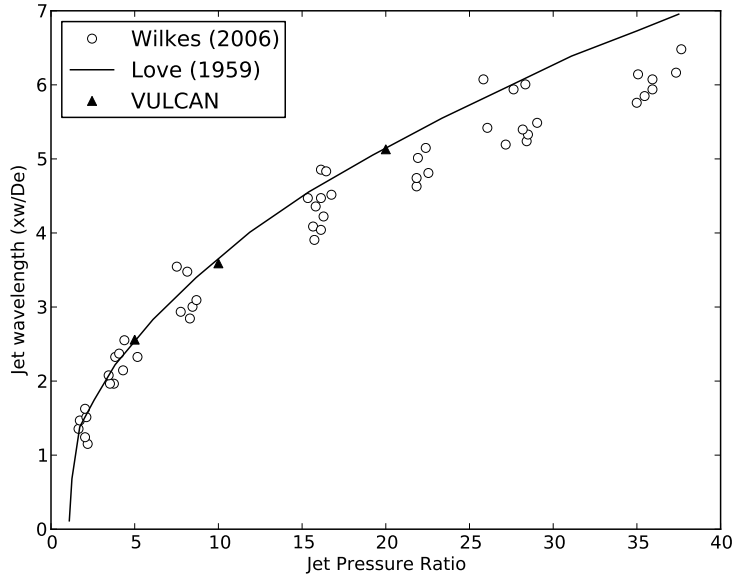


**Figure 17:** Normalized jet wavelength as a function of jet pressure ratio. Numerical results from Vulcan are compared against the results of Wilkes *et. al* [55] and Love *et. al* [56].

accurately predict the experimental results from the literature.

### 2.2.2 Transverse Injection into a Supersonic Crossflow

The ability of VULCAN to predict the physics of sonic injection into a supersonic crossflow will now be summarized. As with with injection into a quiescent medium, this case has been studied extensively by previous researchers at low Mach numbers. Therefore, this is another good case to study in order to validate VULCAN’s predictive capability in the flow regime of interest. As with the previous study, validation is occurring by injecting a sonic jet transverse to the flow. Although the cross flow Mach number of 2.1 is much lower than the cross flow Mach number in this dissertation, it is assumed that the results of this validation study can be extrapolated to higher Mach numbers due to the momentum-based nature of the jet trajectory [59] (i.e. no emergent effects due to increasing Mach number arises compared to an already supersonic cross flow).

As with the injection of a jet into quiescent flow, the location of the Mach disk for a supersonic crossflow has typically been a parameter of interest. Cohen *et al.* [58] proposed the relationship for Mach disk midpoint height as a function of jet and freestream parameters as

$$\frac{H_{mid}}{D_e} = \left[ \frac{2 \left( 1 + \frac{\gamma_j - 1}{2} M_j^2 \right)}{\gamma_j^2 M_j (\gamma_j + 1)} \right]^{0.25} \left[ \frac{1.25(1 + \gamma_\infty) \gamma_\infty M_\infty^2}{(1 - \gamma_\infty) + 2\gamma_\infty M_\infty^2} \right]^{0.5} J^{0.5} \quad (2)$$

which was validated against experiments at conditions ranging from  $0.55 < M_a < 2.92$  and  $1.0 < M_j < 2.2$ .

The trajectory of the jet as it travels downstream has also been of interest to researchers. The penetration of the fuel is defined to be either the maximum point away from the wall where fuel is detected or the centerline of the jet. Schetz and Billig [57], who chose the latter definition, used the curve fit

$$\frac{x}{D_j} = J^{-m} \left( \frac{y}{D_j} \right)^n \quad (3)$$

to describe the trajectory of the jet centerline at different dynamic pressure ratios. This relation has been compared successfully against experiment and has been validated more recently by Portz and Segal [60].

The grid topology used in this validation study was the same used in the study of a sonic jet issuing into a quiescent medium. While the pressure ratio was the main parameter of interest in the previous study, the current parameter of interest is the dynamic pressure ratio,  $J$ , of the fuel jet to the main stream. The dynamic pressure ratio was variable in this study while all other parameters were held constant. The Mach 2.1 cross stream is 300 K, 2000 Pa air for all cases. The sonic fuel jet is 300 K hydrogen with a variable density to match the desired dynamic pressure ratio.

The trajectory traveled by the fuel jet will now be examined. Figures 18 and 19 show the numerically solved hydrogen mass fraction on the flow centerline. Superimposed on the VULCAN solutions are the analytical relations of Equation 3 with

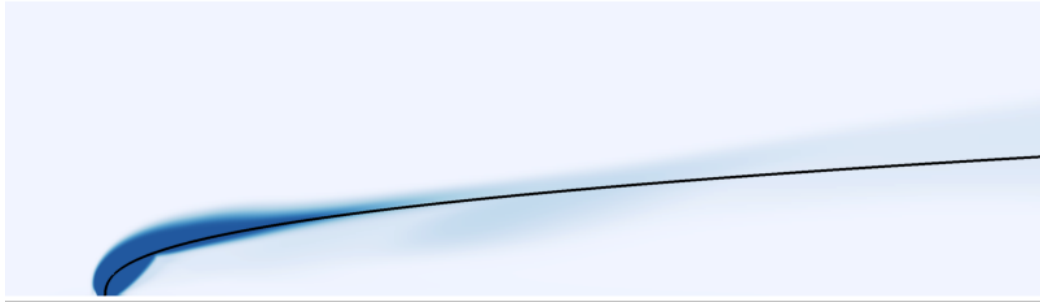


**Figure 18:** The centerline hydrogen mass fraction field of a converged VULCAN case where  $J = 4.75$  is shown compared to the analytical relation from Equation 3 with  $m = 1$ ,  $n = 2.55$ .

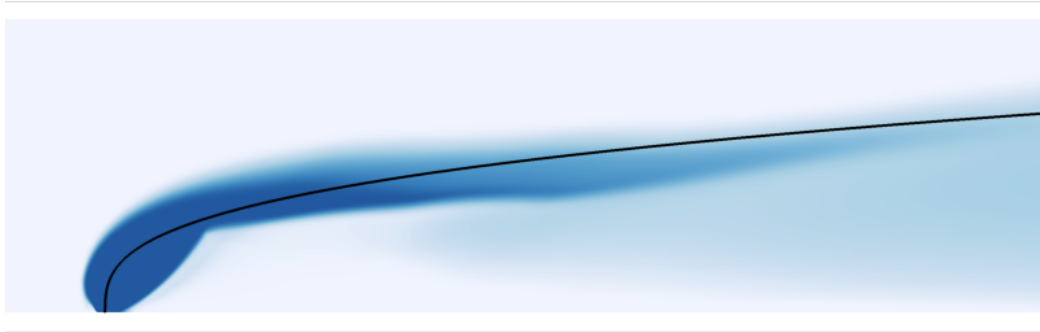


**Figure 19:** The centerline hydrogen mass fraction field of a converged VULCAN case where  $J = 16.35$  is shown compared to the analytical relation from Equation 3 with  $m = 1.3$ ,  $n = 3$ .

different values of  $m$  and  $n$ . It is observed that the jet plumes simulated using VULCAN tended to underpredict the Schetz jet penetration, but in general followed the empirically-derived trend.

The simulated location of the Mach disk will now be investigated and compared to Equation 2 using the same jet and crossflow parameters as those previously stated. Also included are experimental results by Schetz at similar freestream and jet Mach numbers. The VULCAN results are plotted and encompass a range of dynamic pressures from 4.75 to 50. It is observed that in general VULCAN overpredicted the location of the Mach disk midpoint, although the error is limited to between 10-20%.

It has been shown that VULCAN is able to successfully predict the penetration

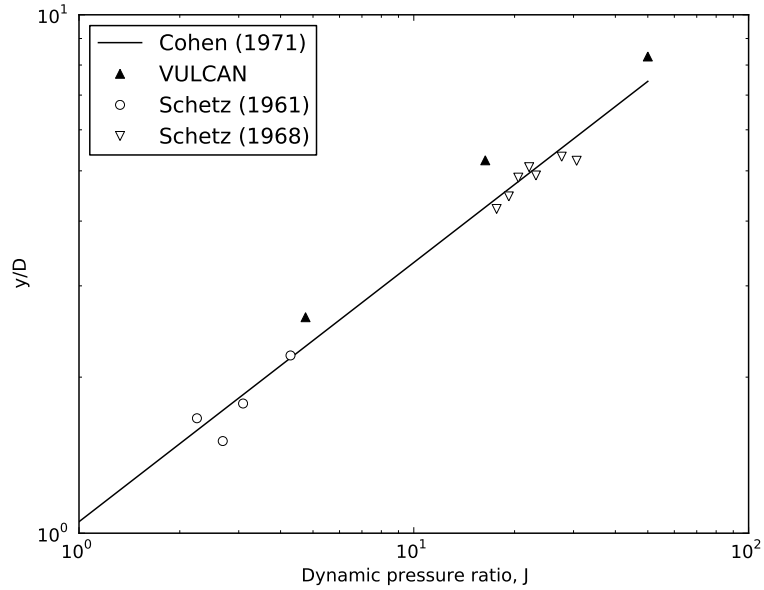


**Figure 20:** Vertical displacement of the Mach disk midpoint as a function of dynamic pressure.

characteristics of sonic jets issuing into a supersonic crossflow. Numerical results have been compared against both experimental results and empirically-validated relationships. Over- and under-prediction was evident in the comparisons, but the errors are deemed to be acceptable at the current level of validation fidelity; however, future attention should be given toward reducing these discrepancies.

### 2.2.3 Axial injection into a Supersonic Coflow

The ability of VULCAN to predict the physics of axial injection of fuel into a supersonic coflow will now be summarized. Numerical validation will be achieved by simulating a fuel jet issuing from the base of an expansion ramp situated in a supersonic airstream. Successful reproduction of experimental results for this case will show that VULCAN is capable of predicting the physics salient to such flows, including the penetration of the fuel jet, vorticity produced by the injector ramp, and the diffusion of the plume into the surrounding air. The injection and crossflow Mach numbers of this validation study are similar to those of ramp and strut injectors in

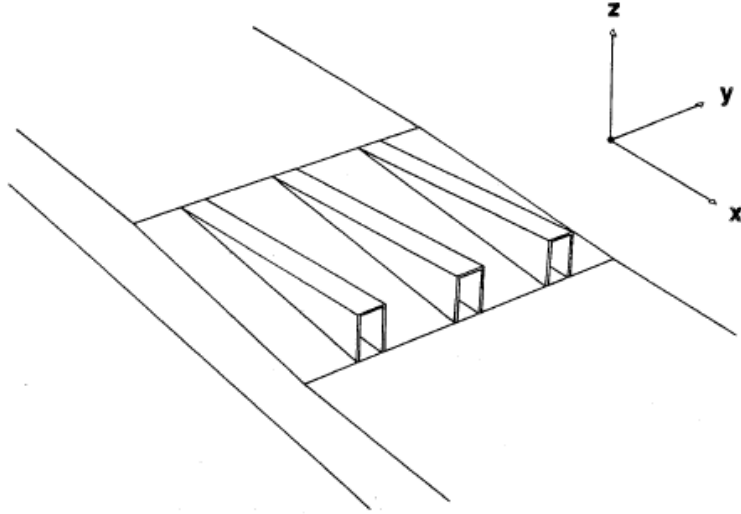


**Figure 21:** A schematic of the Waitz expansion ramp injector is shown (from [62]).

the primary study, and therefore is intended to be a more direct validation compared to the previous two validation studies.

The geometry used in this validation study was the same as evaluated by Waitz, *et al.* [61] in his study of Mach 1.7 helium injected into Mach 6 air from the base of an expansion ramp. The expansion ramp geometry is shown in Figure 23, the salient features being: a) the injector itself which is a wedge that turns the flow and injects fuel from its base, and b) a wall that turns away from the flow on either side of the ramp in order to create a shock wave at the ramp base to enhance mixing due to baroclinic torque between the fuel plume and the surrounding air. Vorticity is also created in the airstream as the fluid flows off either side of the ramp. The ramp studied here is unswept (i.e. parallel sides), although enhanced vorticity can be obtained by a swept ramp concept (i.e. sides converging toward the base).

For the validation study, the geometry was set up to match the Waitz geometry, the experimental apparatus of which is shown in Figures 21 and 22. The injector had a height at its base of 25.4 mm, a width of 6.35 mm, and a length of 152 mm. The top of the ramp injector had a slope of  $4.76^\circ$  and the expansion ramp was set to the

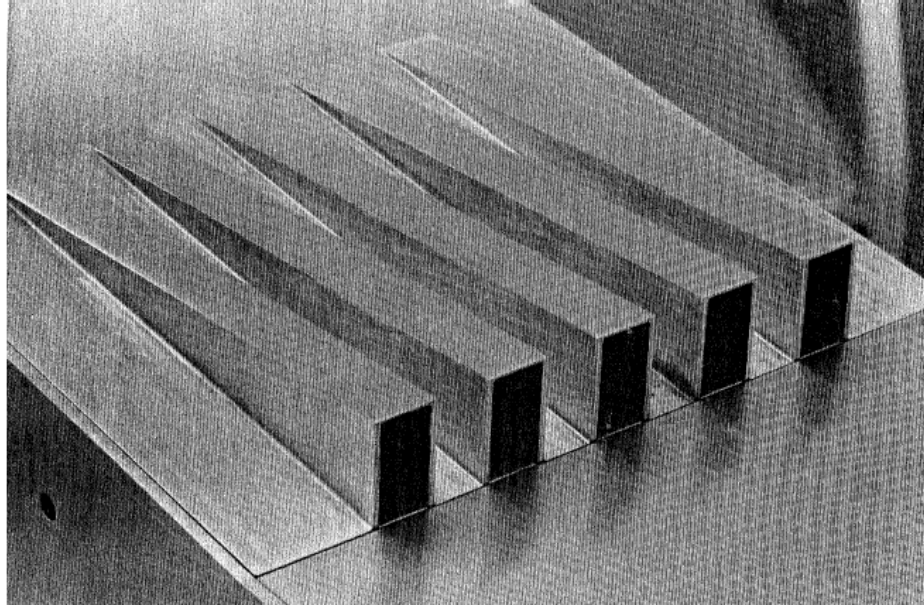


**Figure 22:** A photograph of the Waitz expansion ramp injector experimental apparatus is shown (from [62]).

same angle. The incoming Mach 6 air had a total pressure of 6.0 MPa and a total temperature of 520 K. The Mach 1.7 helium injectant had a total pressure of 23 kPa and a total temperature of 223 K. These conditions corresponded to the baseline case conditions given by Waitz.

A view of the computational geometry used in this study is shown in Figure 23. Symmetry planes were defined on the injector centerline and on the midpoint between neighboring injectors. All walls were defined to have a constant temperature of 300 K. During the course of his experiments, Waitz tripped the incoming boundary layer with gas so that it would have a controllable thickness. The baseline boundary layer thickness was 20% of the injector height. In order to provide the same thickness for the numerical study, a separate simulation was conducted on a 2D flat plate at the Mach 6 air conditions in order to allow a boundary layer to grow. At the plane where the boundary layer was 5.08 mm thick, the plane was saved in order to be extruded across the inflow of the primary simulation.

A view of the computational grid in the vicinity of the injector is shown in Figure

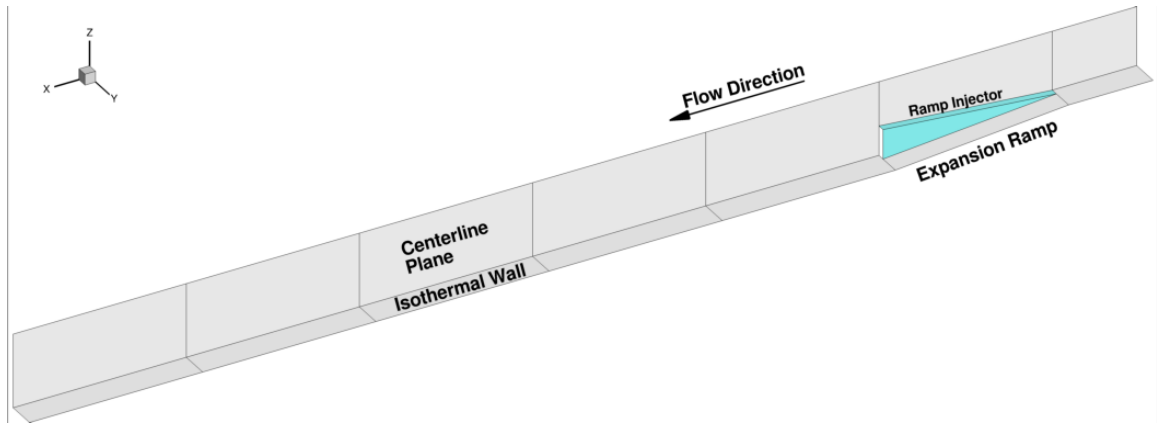


**Figure 23:** The expansion ramp geometry of Waitz for the validation study is shown.

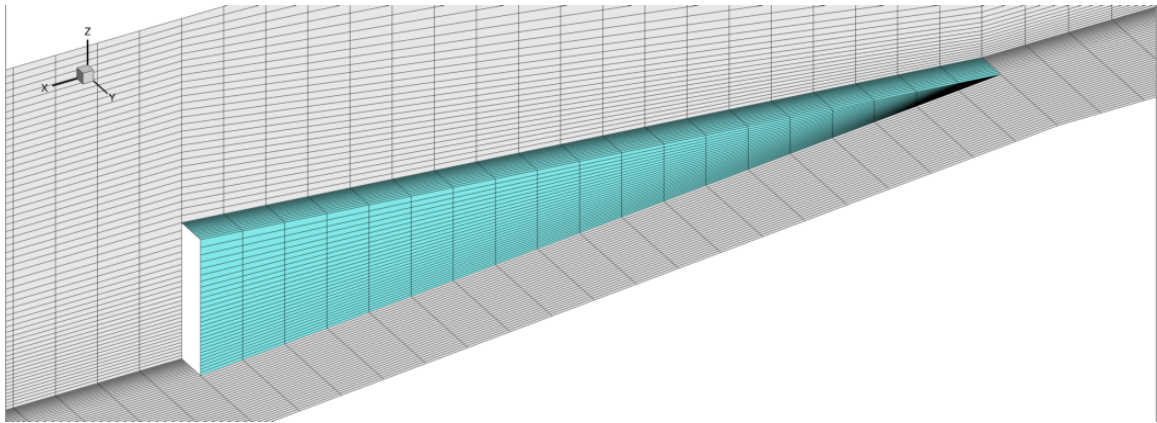


**Figure 24:** The computational grid for the validation study in the vicinity of the injector is shown.

24. While greater grid density can be achieved for reasonable simulation times, it was decided to emulate the general grid layout and point density chosen by Waitz. Waitz used point blanking<sup>3</sup> when building the injector geometry, something not employed in this study. Instead, the expansion ramp was designed to begin with a pole domain. This leads to a total of 334,000 grid points in the current topology instead of 266,000 in Waitz's grid.

The selection of turbulent Schmidt number has been shown to have a significant effect on the behavior of high speed mixing systems. The turbulent Schmidt number

---

<sup>3</sup>Point blanking is a method of constructing a grid topology where instead of building the grid around the geometrical features, the grid points that occupy the boundary of the geometry are simply removed.

is a ratio of the turbulent viscous diffusivity of the system to the turbulent mass diffusion, defined by,

$$Sc_t = \frac{\nu_t}{D_t} \quad (4)$$

Typically lower turbulent Schmidt numbers will enhance the turbulent mixing present in the system while higher numbers will produce a more conservative estimate of the mixing present in a system. Because this validation study endeavors to compare the simulated helium jet plume characteristics to experiment, it is evident that the Schmidt number is a key parameter. Therefore, a range of values were chosen between 0.1 and 1.0 and held constant through the entire domain. Recent studies have investigated the use of variable Schmidt numbers [63], but that is beyond the scope of this research.

A unique solution was computed for each value of turbulent Schmidt number with a standard Menter  $k-\omega$  turbulence model and compared against experiment to see what turbulence parameters produce the best results.. This process is known as calibration, which AIAA [64] defines as

*“**Calibration:** The process of adjusting numerical or physical modeling parameters in the computational model for the purpose of improving agreement with experimental data”*

Once each solution reached convergence, cross-section planes were interrogated for the maximum helium mass fraction at locations of 0, 1, 4, 8, and 13  $x/h_j$  ( $= \bar{x}$ ) distances downstream of the injector exit, where  $h_j$  is the height of the injector base. These values were chosen because the experiment of Waitz readily had data available at these locations. The comparison of Waitz’s experiment to each solution is shown in Figure 25. It is observed that simulations with lower turbulent Schmidt number had increased jet plume diffusivity and the scatter of the results indicates that the results of the simulation were highly sensitive to the chosen value of turbulent Schmidt

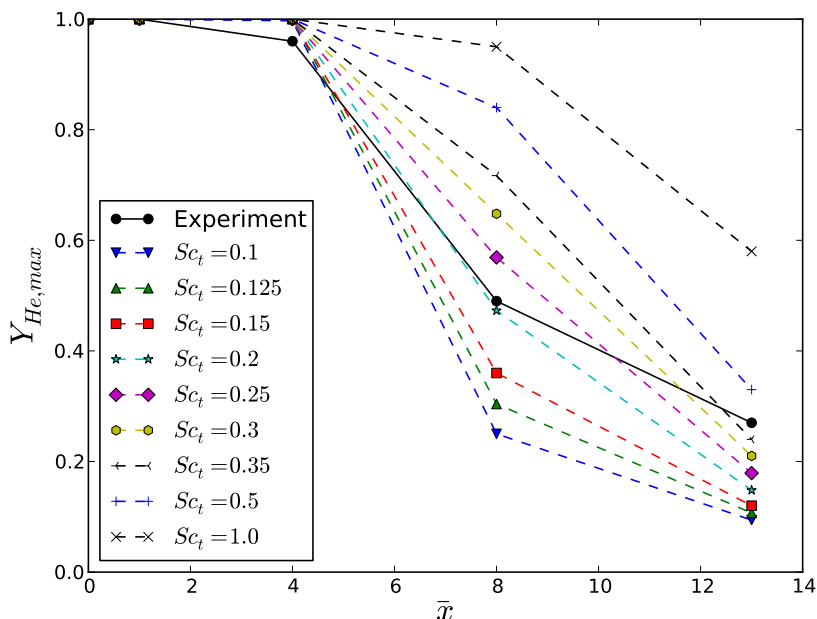


**Figure 25:** Comparisons of maximum helium mass fraction as a function of normalized distance from the injector exit between experiment and numerical simulations at various turbulent Schmidt numbers. Lines are for visual aid only and do not imply a curve shape.

number. Of all the values simulated,  $Sc_t = 0.25$  appears to have the best agreement with experiment, overpredicting maximum helium mass fraction at  $\bar{x} = 8$  by 16% and underpredicting by 33% at  $\bar{x} = 13$ .

Results from the work of Waitz in Figure 26 show experimental and numerical helium mass fractions at  $\bar{x} = 4, 8$  and 13. It should be noted that the numerical simulations conducted by Waitz did not use any turbulence modeling. Nonetheless, the general shape of the plume at each location shows agreement between experiment and numerical simulation. The present numerical results carried out in VULCAN are shown in Figure 27 for  $\bar{x} = 4, 8,$  and 13 and  $Sc_t = 0.25, 0.5,$  and 1.0. The helium contours plotted are the same values as plotted in the experimental results of Waitz in Figure 26. Again, it is observed that good morphological agreement between the numerical and experimental cross sections were achieved. It is also evident that for

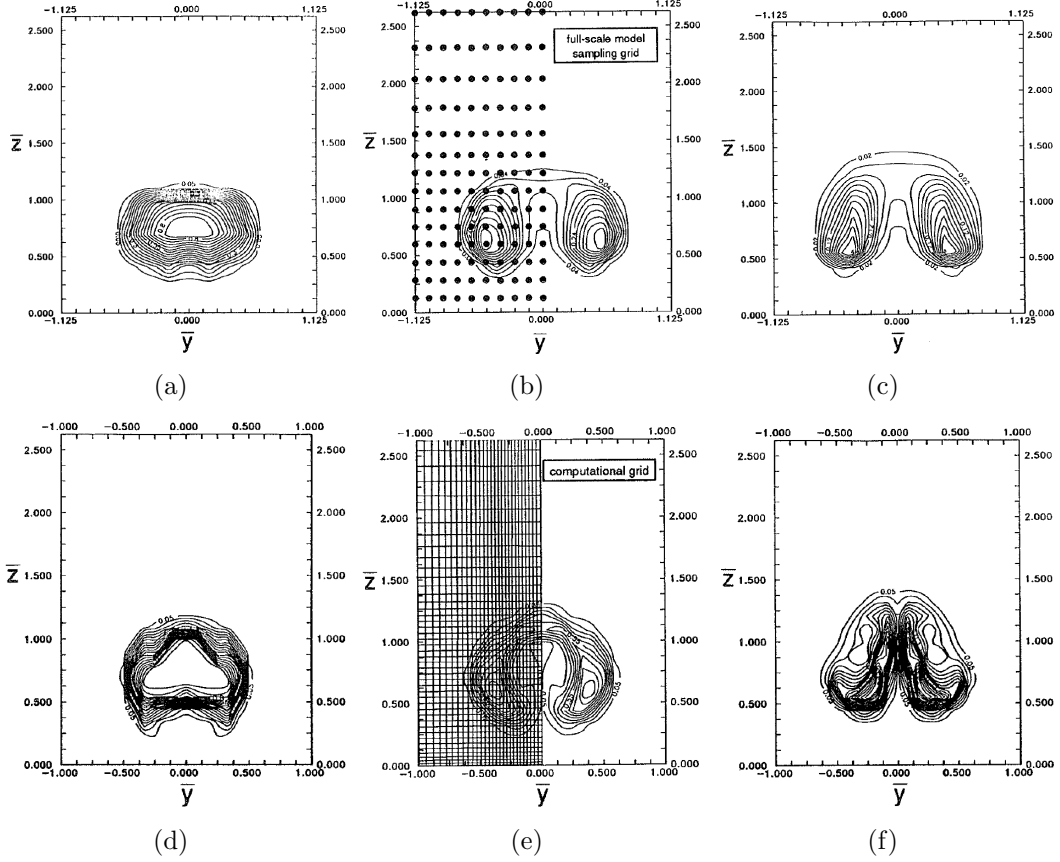


**Figure 26:** Experimental contours of helium mass fraction at normalized x coordinates of (a) 4, (b) 8, and (c) 13 from the injector exit are shown compared to numerical contours at normalized x coordinates of (d) 4, (e) 8, and (f) 13.

each cross-sectional plane, the chosen value of  $Sc_t$  had a weak effect on the shape of the plume; rather, the effect is most evident in the distribution of helium in the plume. Lower values of  $Sc_t$  produced shallower gradients of helium mass fraction due to the greater turbulent molecular diffusivity of those cases. Conversely, high values of  $Sc_t$  caused higher gradients of helium mass fraction due to inhibited diffusivity. It should also be noted that  $Sc_t = 0.25$  produced helium mass fraction contours that are similar to the experiment by Waitz, thus giving credibility for the choice of  $Sc_t$  for this set of experimental conditions.

It has been shown that VULCAN is able to successfully predict the physics of supersonic axial injection into a supersonic coflow. Many different mechanisms are

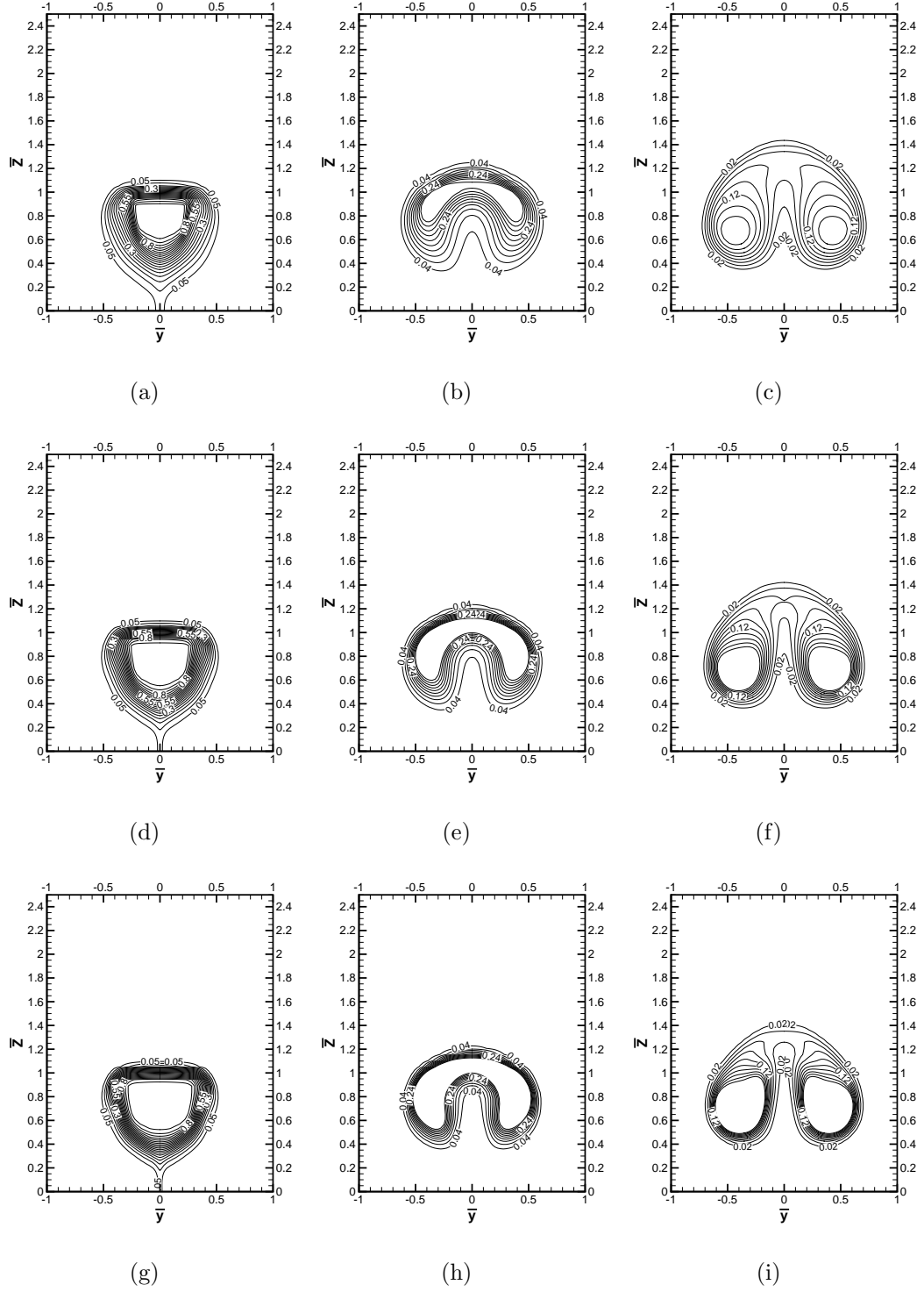


**Figure 27:** Numerically solved contours for helium mass fraction are shown for (a) - (c)  $Sc_t = 0.25$ , (d) - (f)  $Sc_t = 0.5$ , and (g) - (i)  $Sc_t = 1.0$ . The columns sequentially show normalized x coordinates of 4, 8, and 13 from the injector exit.

present in such a flow, for example vorticity generated due to the ramp injector, baroclinic torque due to the passage of a shock wave through a helium jet surrounded by air, and diffusion and mixing of helium into air. The present numerical results were compared against past experiment results and showed reasonable agreement between the two. Furthermore, the significant effect of turbulent Schmidt number was observed for this study, although the best value of  $Sc_t$  for these conditions does not necessarily hold true for disparate conditions.

## 2.3 Modeling and Simulation

### 2.3.1 Performance

#### 2.3.1.1 Mixing Efficiency

Mixing efficiency was used in this study as a measure of the effectiveness of a particular fuel injection concept to provide uniform mixing. Ideal conditions for combustion consist of uniformly distributed fuel-air at a local equivalence ratio of one at each point. Here mixing efficiency is an integrated value over a given flow plane and is defined by the ratio of mixed oxidizer mass flow rate divided by the total fuel plus oxidizer flow rate. The definition given by Mao [65] is

$$\eta_m = \frac{\dot{m}_{O_2, mix}}{\dot{m}_{O_2, total}} = \frac{\int_{A, Y=0} Y_R \rho u dA}{\int_{A, Y=0} Y \rho u dA} \quad (5)$$

where

$$Y_R = \begin{cases} Y & \text{for } Y \leq Y_S \\ \frac{1-Y}{1-Y_S} Y_S & \text{for } Y > Y_S \end{cases} \quad (6)$$

where  $Y_S$  is the mass fraction of oxygen at stoichiometric proportions with hydrogen and air. Because the forebody mixture was globally fuel rich due to spillage of predominantly oxygen-containing flow from the open geometry, the mass fractions in these equations are that of oxygen; otherwise fuel mass fractions would be used. Mixing efficiency represents an upper bound on the combustion efficiency, which is a measure of fuel consumption rather than mixing.

### 2.3.1.2 Stream Thrust Potential

The typical loss figure of merit used to evaluate forebody flows is total pressure recovery. This is due to the ease with which it can be calculated or one-dimensionalized from a multidimensional flow. The use of such a parameter as a true indicator of irreversibility generation in the forebody flow implicitly assumes a nearly constant total temperature. For forebody mixing problems, however, such an assumption breaks down due to the mixing of two streams of distinct total temperature and because flow spillage may be present. This issue was remedied by using the stream thrust potential parameter.

Past studies have used thrust-based methods to identify, account for, and optimize on different loss mechanisms occurring in a flowpath [40, 66, 67, 68]. Its usefulness has been demonstrated in the design of complete engine flowpaths [69]. Although the current study only considers a single component of a full flowpath (i.e. a forebody injector), stream thrust potential still provides a good metric for comparing different injection concepts. The stream thrust potential is given by the equation

$$F = \dot{m}u_{exp} + p_{exp}A_{exp} \quad (7)$$

where  $u_{exp}$  and  $p_{exp}$  are the velocity and static pressure when isentropically expanded from the simulated cross-sectional area to the expanded cross-sectional area  $A_{exp}$ . The stream thrust potential is obtained by one-dimensionalizing the flow at a given plane according to a method that conserves mass, energy, and entropy [70]. Once the one-dimensionalized parameters are obtained, the flow at a given flow station is expanded isentropically to a reference nozzle area, shown schematically in Figure 28 for channel flow. For this study the reference nozzle area was set equal to the capture area of the notional flight vehicle. Mixing, heat loss, friction, and shock waves in general reduce stream thrust potential while heat addition and axial fuel injection increase stream thrust potential. Hence, as with mixing efficiency, using

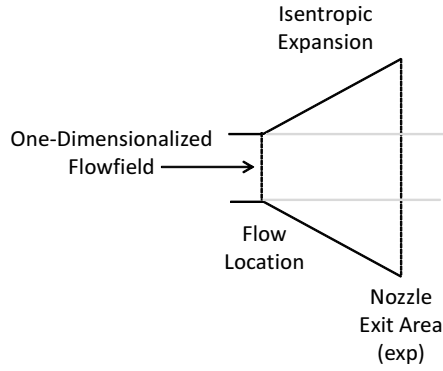


**Figure 28:** A schematic of the stream thrust potential methodology.

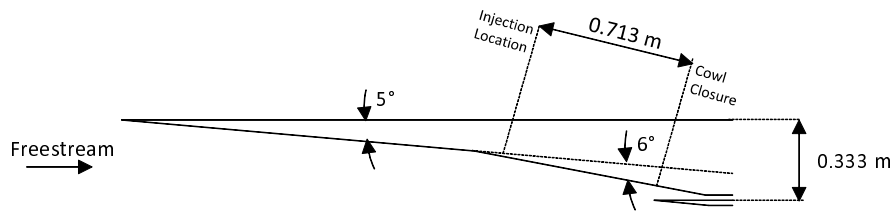


**Figure 29:** The baseline forebody geometry used in this study is shown.

stream thrust potential by itself as a metric for comparison is insufficient because enhanced mixing will negatively impact stream thrust potential.

### 2.3.2 Flow Conditions

The simulated flow was on a flat plate at conditions representative of the forebody of an airbreathing vehicle on a typical constant dynamic pressure (71,820 Pa) trajectory at Mach 12. Using the 1976 US standard atmosphere, such a point on the flight trajectory occurs at an altitude of 33.33 km. Representative flat plate conditions were obtained by processing the freestream flow through a five degree turn followed by a six degree turn. The notional forebody geometry used in this study to obtain the flat plate conditions is shown in Figure 29. Freestream and flat plate conditions are summarized in Table 2.

Each injector was sized assuming the engine flowpath captures 4.5 kg/s of air (corresponding to a small-scale engine) at the conditions in Table 2 and that the injector

**Table 2:** Freestream and flat plate conditions. Flat plate conditions are obtained by shocking the freestream flow through a 5 degree turning followed by a 6 degree turning. All cases use an air molar composition of 79% N<sub>2</sub> and 21% O<sub>2</sub>

	Freestream	Flat Plate
Static pressure	713 Pa	9111 Pa
Static temperature	232 K	541 K
Mach number	12.0	7.67

**Table 3:** Fuel injector exit conditions. All cases use 100% H<sub>2</sub> at a static temperature of 390 K.

	Transverse	Ramp (Matched)	Ramp (Sonic)	Strut (Matched)
Injector Mach number	1.0	3.92	1.0	3.92
Dynamic pressure ratio	1.0	0.26	0.07	0.26
Static pressure	535,000 Pa	9111 Pa	35,715 Pa	9111 Pa
Injector exit area	52.6 mm <sup>2</sup>	790 mm <sup>2</sup>	790 mm <sup>2</sup>	790 mm <sup>2</sup>

was one of five on the forebody combining to provide a globally stoichiometric fuel flow rate. For the case of transverse fuel injection, sonic injection with a dynamic pressure ratio of 1.0 was ensured. For transverse injection, the fuel jet was underexpanded in order to prevent oblique shock structures from forming within the jet [71]. For ramp and strut injection, pressure matching between the injector exit and the inflow was assumed in an attempt to preserve vortical flow structure. An additional ramp injection case with sonic injection was simulated to evaluate the effect of higher pressure on injection and mixing. In all cases it was assumed that the fuel system is able to supply the pressures required for the injection system. The assumed and derived injector conditions are summarized in Table 3.

The inflow boundary layer thickness was set to be 10 mm in this study. To accomplish this, a separate flat plate simulation was conducted at the conditions in Table 2. At the location where the boundary layer thickness grew to 10 mm, the flow profile was output at that point and extruded across the inflow plane of the injector simulations.

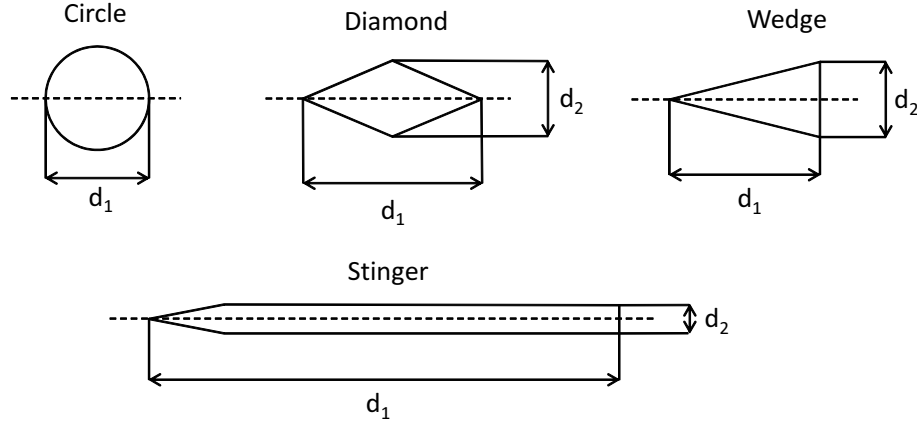


**Figure 30:** Notional geometry for flush wall injectors.

**Table 4:** Injector geometry for flush-wall injection. All injectors have the same exit area.

Geometry	$d_1$ (mm)	$d_2$ (mm)
Circular	8.19	-
Diamond	24.44	4.31
Wedge	17.28	6.09
Stinger	36.83	1.64

### 2.3.3 Injector Geometries

#### 2.3.3.1 Flush-Wall Injection

In this study transverse injection was simulated through flush-wall nozzles of varying exit geometry. While flush wall injectors could be angled to achieve an axial component of the fuel flow, only transverse injection was considered herein in order to understand the limits of mixing obtainable by a flush wall injector. Injector concepts to be considered included a circular wall injector as well as injectors with leading edge geometrical modifications that make them more suitable for a forebody injection environment.

The flush wall nozzle geometries studied herein are depicted in Figure 30 with parameters given in Table 4. Of the four geometries considered, three are primitive shapes designed to give a basic understanding of the effect of leading- and trailing-edge bluntness and sharpness on the evolution of mixing and losses downstream of

the injection location. Sharp leading edge modifications to flush-wall injectors were proposed to reduce upstream recirculation of fuel. The fourth geometry was proposed by Hirano [30] and was demonstrated to produce enhanced plume area and penetration in a low Mach number cross flow. However, it was not characterized in terms of mixing efficiency or losses. This geometry, referred to as a stinger, was evaluated to study its effect in high Mach number cross flow.

#### 2.3.3.2 Ramp Injection

The ramp geometry has been studied and used in internal supersonic flows for the axial injection of fuel as well as inducing vortical flow structures to enhance mixing. Marble [34] proposed an expansion ramp concept in order to enhance mixing through the interaction of the fuel plume with the shock wave emanating from the base of the ramp. This interaction induces baroclinic torque due to the unaligned density and pressure gradients at the fuel-air boundary and causes a roll-up of the fuel in the direction the shock sweeps through the fuel plume. Ramp injectors that are swept induce additional vorticity as flow rolls off of the edges of the ramp [26].

In this study the expansion ramp injector of Waitz [72] was modified for the specific requirements of forebody fuel injection. The face of the injector base below the injection location was cut back upstream in order to eliminate the fueled recirculation region that would otherwise be observed at the base. Such a recirculation region increases the possibility of autoignition on the forebody due to the hot stagnation region behind the ramp. The geometry modification was done in two ways. The first was by simply cutting a cavity out of the base of the injector below the duct that is supplying fuel. This type of geometry has been studied by Parent *et al.* [35, 24, 36, 23, 37, 38] at similar conditions and is referred to as a cantilevered ramp injector. The second modification cut back the injector base in an expansion wedge, as shown in Figure 31. This geometry was used in an attempt to increase pressurization

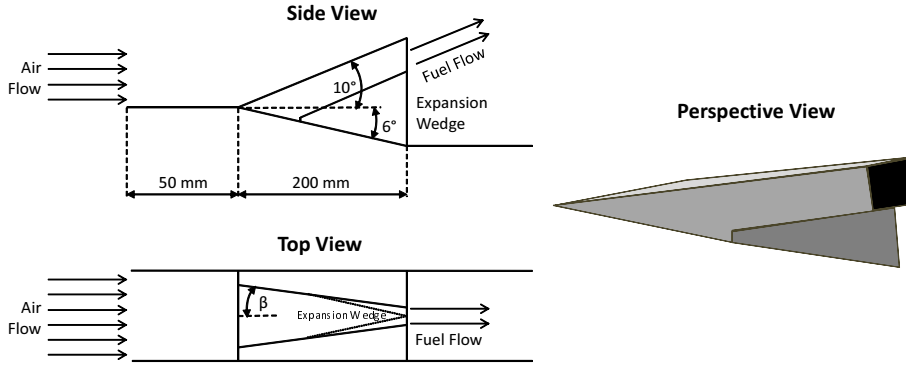


**Figure 31:** Side-, top-, and perspective-view geometry for modified ramp injectors.

**Table 5:** Modified ramp cases.

Case	$\beta$ (deg)	Base Wedge?
Swept ramp (no wedge)	3.0	No
Swept ramp (with wedge)	3.0	Yes
Unswept ramp (no wedge)	0.0	No
Unswept ramp (with wedge)	0.0	Yes

on the base of the injector while discouraging recirculation. A summary of the cases tested are given in Table 5.

### 2.3.3.3 Strut Injection

Like the ramp injector, the strut has also been used in internal flows for supersonic fueling and mixing. The typical strut extends through the entire flowpath height and is characterized as a fuel placement device rather than a fuel mixing device. The strut injector may potentially be the ideal fuel injector for large-scale (e.g. orbital access) flowpaths where the ability for ramps or flush-wall injectors to access the core flow is diminished. Geometries that have heights deep into the fuel core but do not access the entire flowpath height have been called either struts or pylons in the literature—for the purposes of this study they will also be called struts. Up to this point studies of forebody injection via struts have not been deeply investigated in the literature.

This study considered a single strut injector geometry that was swept back 45 degrees and injected fuel away from the injector centerline at a 10 degree angle. A

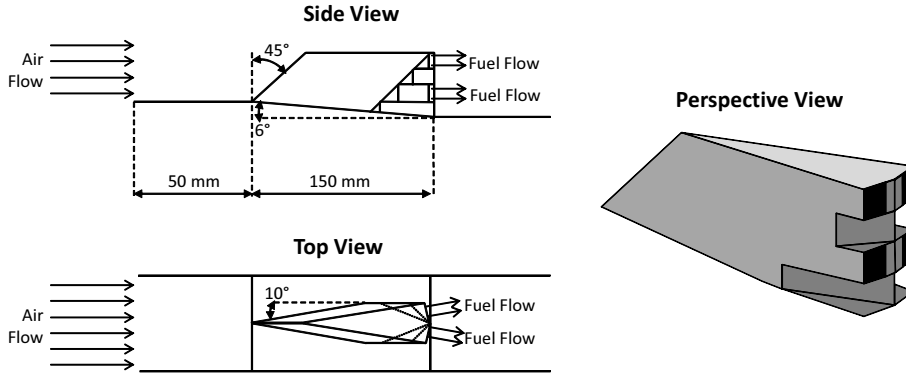


**Figure 32:** Side- and top-view geometry for strut injector.

schematic of the injector is shown in Figure 32. As with the ramp injector, the strut injector was placed on an expansion ramp in order to take advantage of shock-induced baroclinic torque between the fuel plume and the surrounding air. Rectangular ports supplied fuel injection with expansion wedges cut between injectors in order to reduce base recirculation and increase pressurization. The strut design proposed here is a non-optimized point design meant to be a pathfinding investigation into forebody strut injection.

### 2.3.4 Computational Domain

The computational grids had approximately 5.8 - 7.8 million grid points with clustering near the injector location. The computational domains were representative of one-half of the physical domain by using a symmetry boundary condition along the flow centerline bisecting the injector. All walls were set to be isothermal surfaces at a temperature of 500 K. The inflow boundary was fixed at the conditions given in Table 2, representative of conditions on the second ramp of the notional Mach 12 vehicle forebody. Shocks that would otherwise appear due to forebody flow turning were ignored for this study. A 10 mm portion of each fuel injection tube was simulated with slip walls; thus, the effects of boundary layer buildup and vorticity production within the injector nozzle were neglected. A schematic of a general computational domain

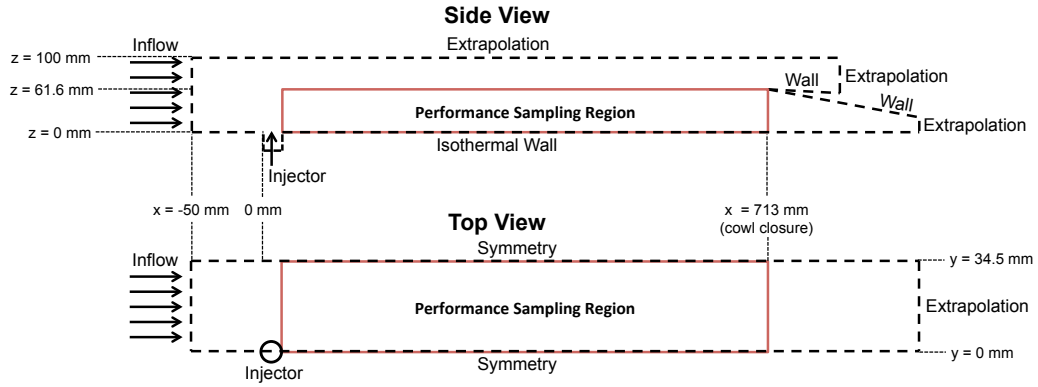


**Figure 33:** A side- and top-view schematic of the computational domain is shown.

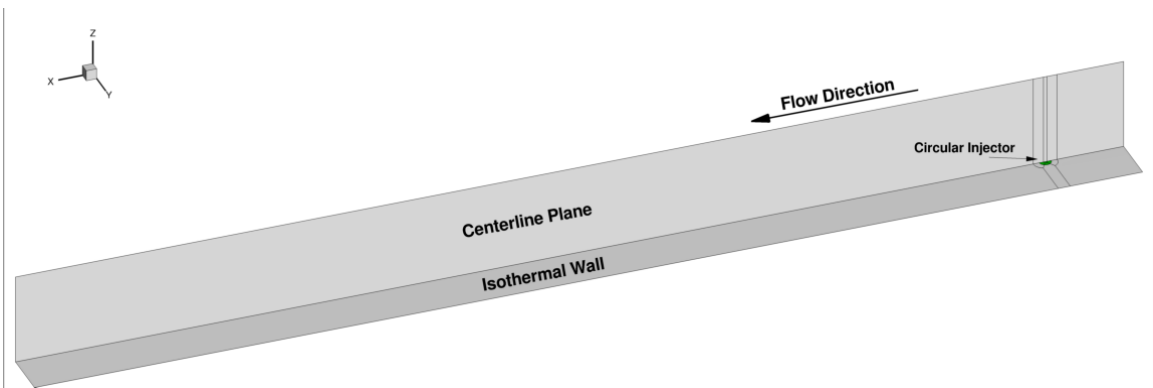


**Figure 34:** The circular injector (green) is shown positioned in the portion of the computational domain where performance sampling occurs.

with a flush wall injector is shown in Figure 33. The dimensions of the domain are representative of the second ramp of the Mach 12 reference vehicle. In each case there was a 50 mm ramp leading up to each injector, which occupies a 713 mm long region until the notional cowl closure location. The distance between the injector centerline and the halfway point between neighboring injectors was 34.5 mm.

Structured grids were used throughout each topology due to VULCAN only accepting such grids at the time of this study. The topologies upstream and downstream of the injectors were simple H-grids with spacing at the wall in each case designed to be 0.127 mm. Grid spacing normal to the wall was designed to gradually grow from 0.07% at the wall to 2.75% away from the wall according to the hyperbolic tangent stretching function. These characteristics were chosen to target a  $y^+$  near 10

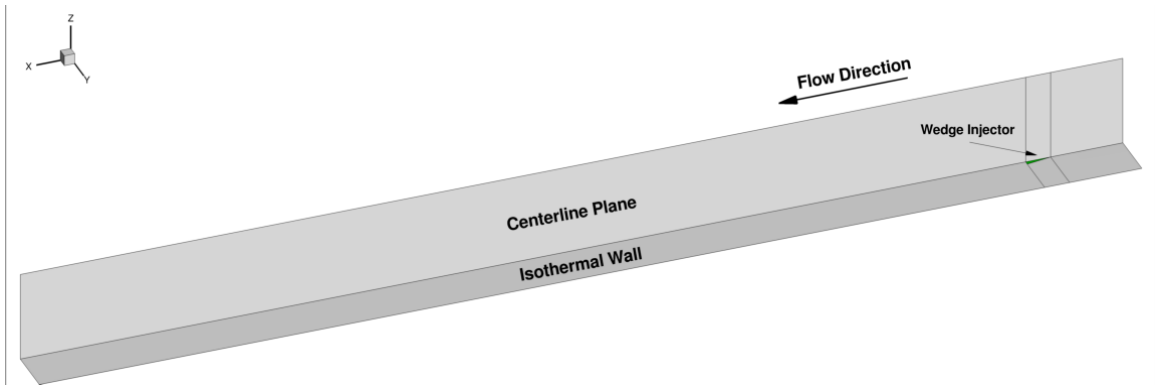


**Figure 35:** The wedge injector (green) is shown positioned in the portion of the computational domain where performance sampling occurs.

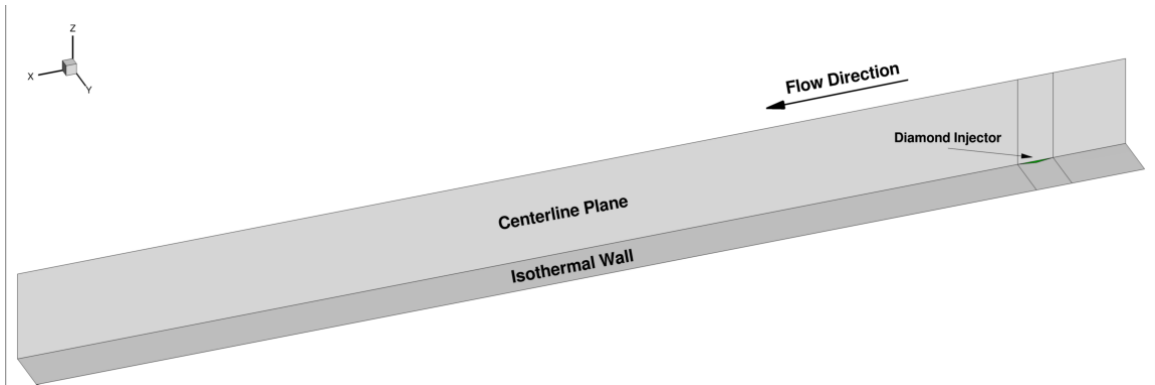


**Figure 36:** The diamond injector (green) is shown positioned in the portion of the computational domain where performance sampling occurs.

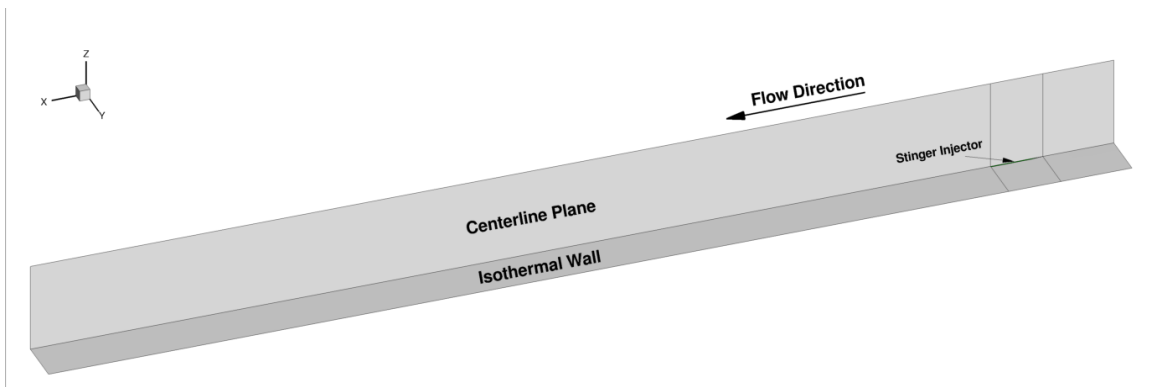


**Figure 37:** The stinger injector (green) is shown positioned in the portion of the computational domain where performance sampling occurs.

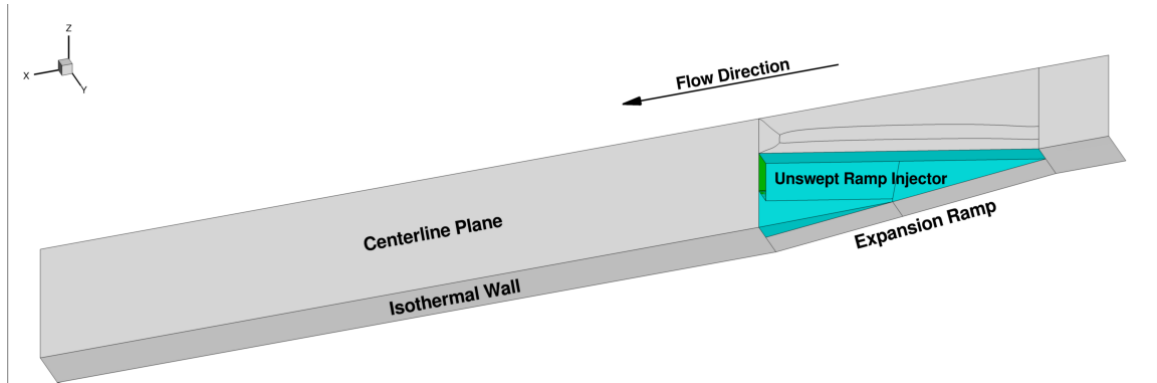


**Figure 38:** The unswept ramp (blue) injector is shown positioned in the portion of the computational domain where performance sampling occurs.

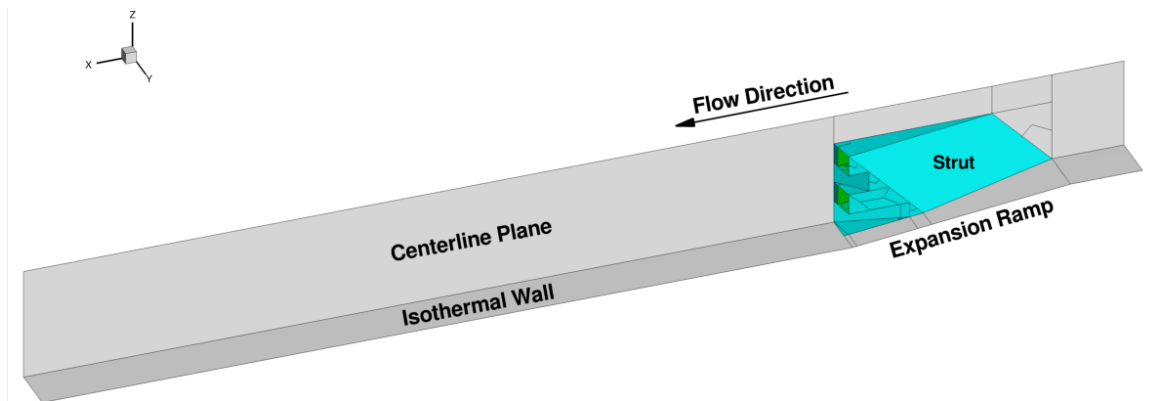


**Figure 39:** The strut injector (blue) is shown positioned in the portion of the computational domain where performance sampling occurs.

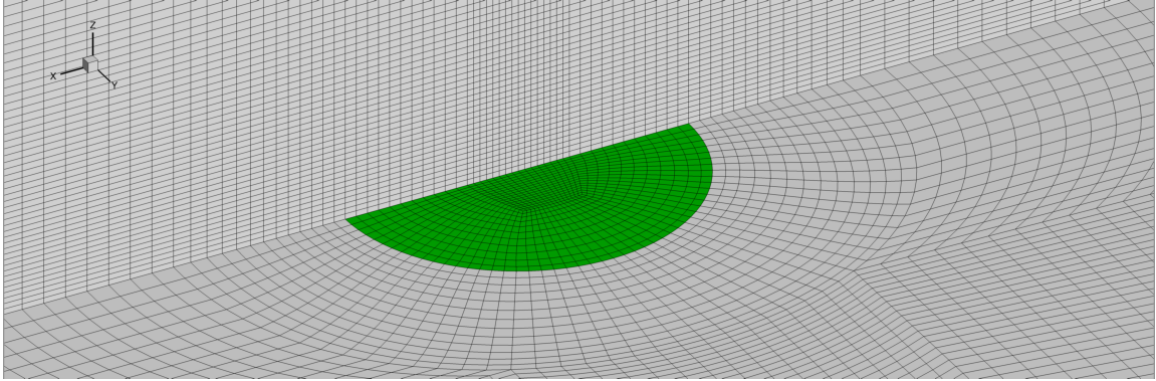


**Figure 40:** The computational grid in the vicinity of the circular injector (green) is shown.

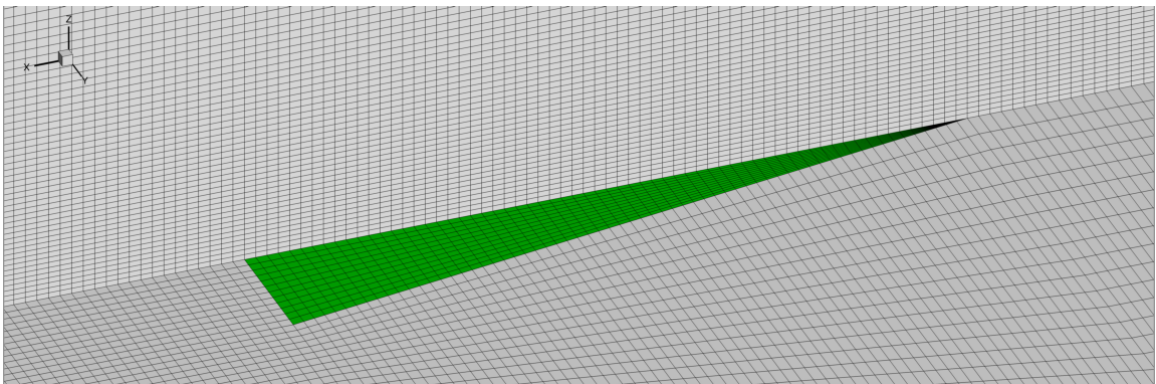


**Figure 41:** The computational grid in the vicinity of the wedge injector (green) is shown.

upstream of each injector. This value of  $y^+$  was deemed appropriate due to the use of wall functions in VULCAN.

The grid topologies in the vicinity of the flush-wall injectors are shown in Figures 40 to 43. The circular injector consisted of a central H-grid wrapped with a C-grid that was then connected to the rest of the wall topology consisting of H-grids. Thirty grid points were placed along the diameter of the circular injector with the resulting injector grid spacing used to place grid points in the diamond, wedge, and stinger geometries. For the injectors with sharp leading or trailing edges, H-grids with pole domains were used to collapse the grid into single point(s) due to the shallow angles involved.

The grid topology near the unswept ramp with an expansion wedge feature is

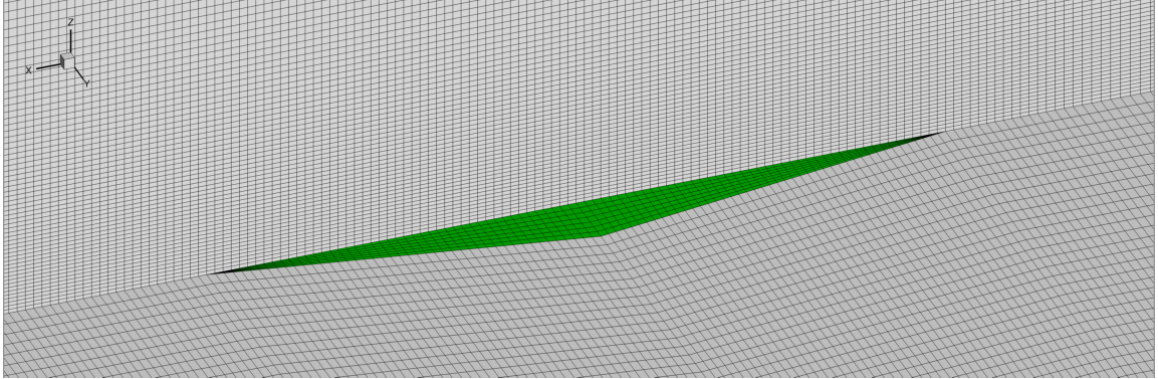


**Figure 42:** The computational grid in the vicinity of the diamond injector (green) is shown.

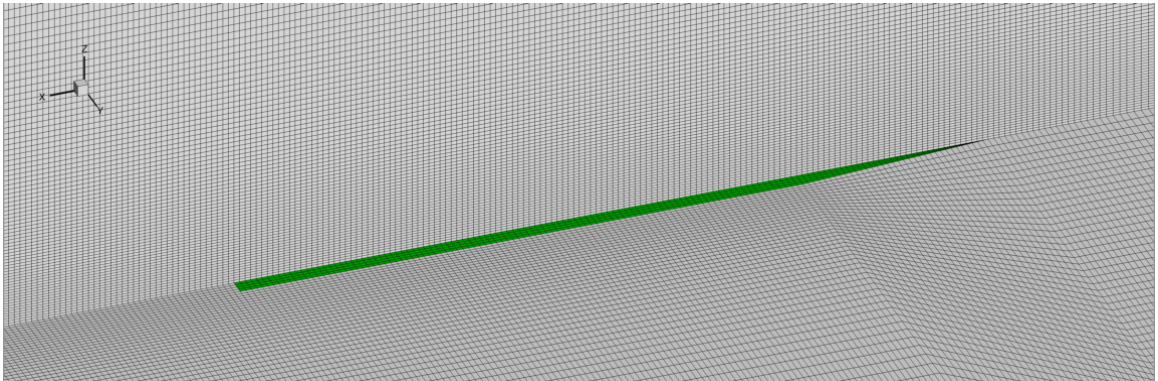


**Figure 43:** The computational grid in the vicinity of the stinger injector (green) is shown.

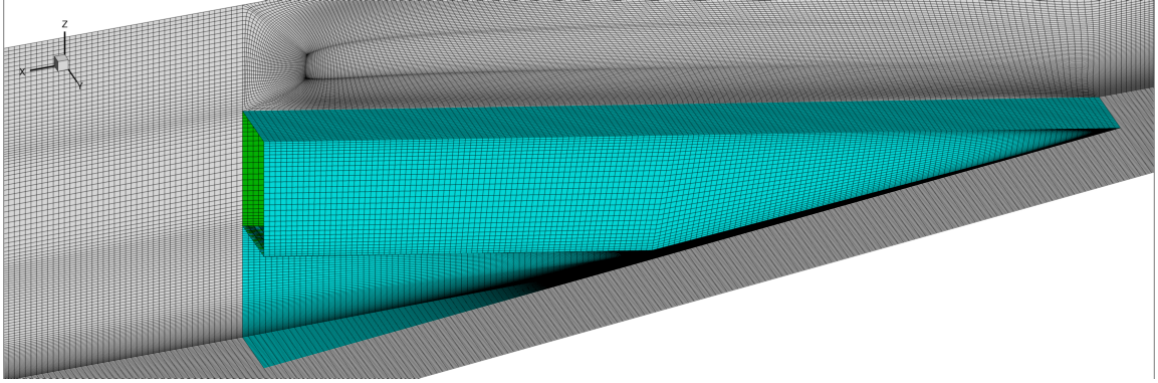


**Figure 44:** The computational grid in the vicinity of the unswept ramp wedge injector (blue) is shown.

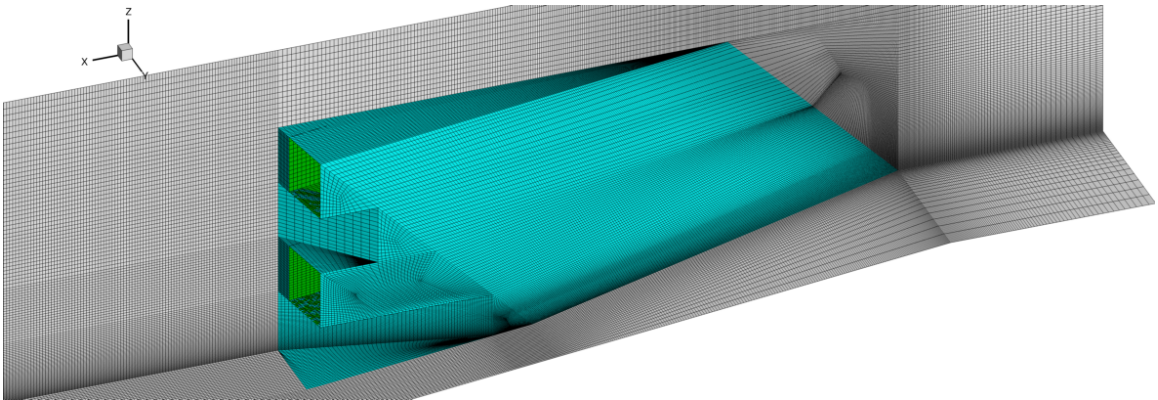


**Figure 45:** The computational grid in the vicinity of the strut injector (blue) is shown.

shown in Figure 44 and is representative of the topology of the four ramp geometries considered. Pole domains were used to run the H-grids on the side of the injector toward the single point on the leading edge of the injector. For cases with the expansion wedge present, an H-grid with pole domain was similarly used on both the wall and underside of the injector. The injector exit of the ramp was designed to have 30 grid points across both the width and the height of the exit.

The grid topology near the strut injector is shown in Figure 45. The topology of the strut injector used H-grids with pole domains being located at the leading edge of the strut as well as on the expansion wedge between the two injection ports.

A summary of the total number of grid points in each computational domain and

**Table 6:** Number of grid points full computational domain for each injector concept.

	<b>Total Cells</b>
Circular	6.6M
Diamond	6.2M
Stinger	6.4M
Wedge	5.8M
Ramp	7.8M
Strut	5.9M

**Table 7:** Number of grid points in the performance sampling region in each direction as well as total cells.

	<b>I</b>	<b>J</b>	<b>K</b>	<b>Total Cells</b>
Circular	541	69	121	4.4M
Diamond	531	60	121	3.8M
Stinger	522	60	121	3.7M
Wedge	537	60	121	3.8M
Ramp	396	73	124	3.5M
Strut	434	57	121	2.9M

in the performance sampling region shown in Figure 33 are given in Tables 6 and 7, respectively. Downstream of each injector the I, J, and K directions were aligned with the X, Y, and Z coordinates, respectively. In the performance sampling region each topology was sized to give roughly the same number of grid points in the wall-normal and lateral directions while the longitudinal spacing was varied depending on the downstream distance occupied by the injector itself.

## ***2.4 Mixing Results***

### **2.4.1 Flush Wall Injection**

This subsection investigates the relative performance between different transverse wall injectors at the same fuel injection mass flow rate and injector area. Figure 50 shows fence plots of hydrogen mass fraction contours for the flush wall injectors. In general, the fuel plumes from the flush wall injectors remained close to the wall. This is undesirable when trying to prevent autoignition of the fuel in the boundary layer. Even the stinger, which exhibited the best penetration of fuel into the main flow

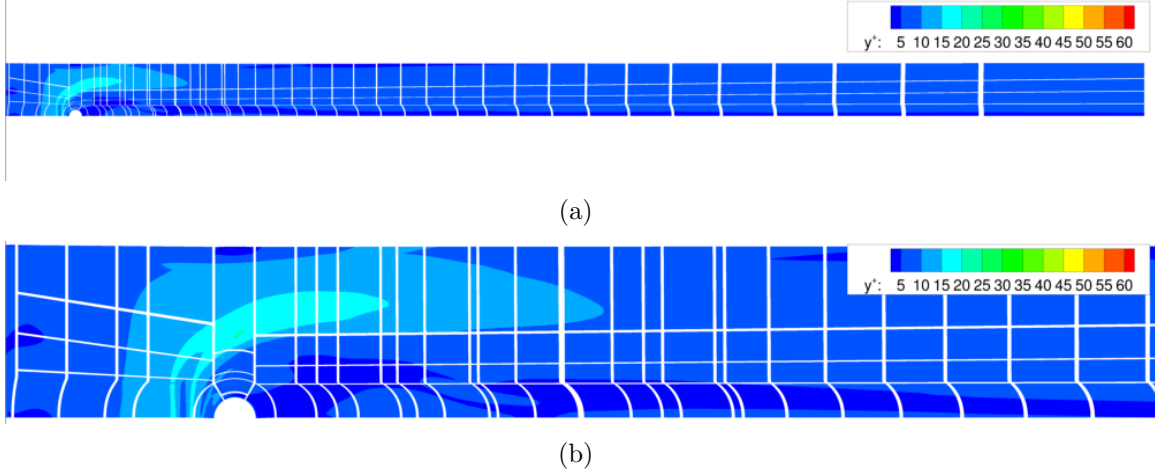


**Figure 46:** Contour plots of wall  $y^+$  for the (a) full flowpath and (b) in the vicinity of the fuel injector. Flow is from the left to the right and hydrogen issues from the injector out of the page.

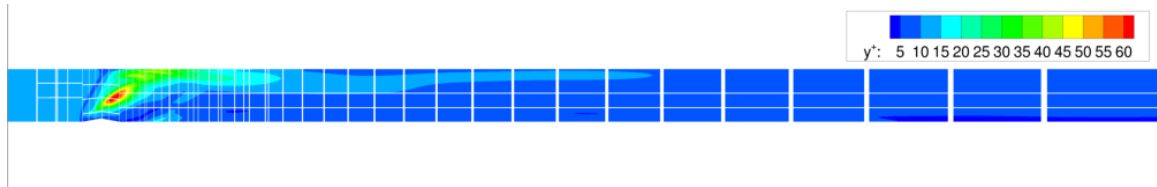
**Table 8:** Maximum  $y^+$  values along the wall for each flush-wall fuel injection concept.

	Circular	Diamond	Stinger	Wedge
$y_{max}^+$	20.13	63.93	54.50	55.19

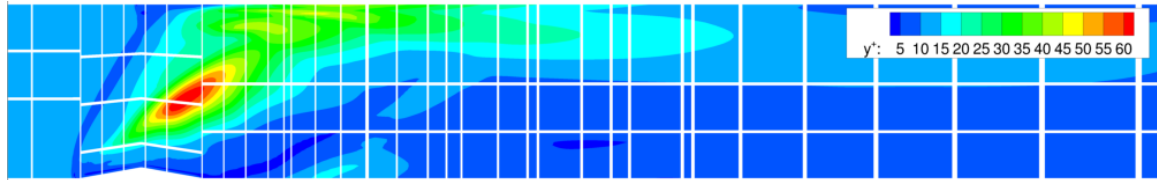
of the four cases, maintained a fuel rich region near the wall. The circular injector had a large recirculation region upstream of the jet which increases the possibility of autoignition due to the increased residence time of entrained fuel combined with high temperatures in this region. Switching to a geometry with a sharp leading edge largely eliminated this upstream recirculation region, which is beneficial for mitigating autoignition.

Contours of wall  $y^+$  values for each flush wall injection geometry are shown in Figures 46 to 49 using the same color scale with the maximum values for each case given in Table 8. Upstream of each injector a  $y^+$  of 11 was achieved, while downstream in the mixing region values dropped below 10. The maximum values for each case occurred in the vicinity of the injectors near the bow shock created by the fuel plume. Although these maxima occur in small regions relative to the full flowpath, they are still within the valid range of using wall matching functions.

Figure 51 shows the performance of each injector as a function of downstream



(a)

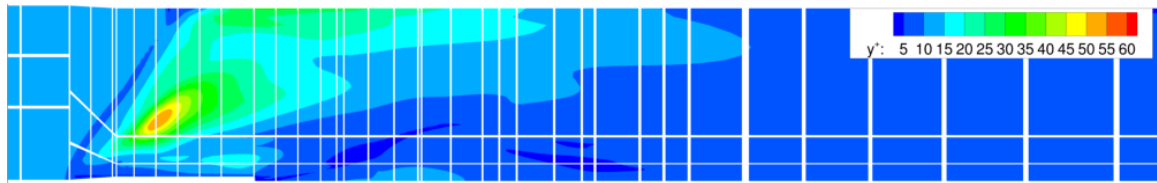


(b)

**Figure 47:** Contour plots of wall  $y^+$  for the (a) full flowpath and (b) in the vicinity of the diamond fuel injector. Flow is from the left to the right and hydrogen issues from the injector out of the page.



(a)



(b)

**Figure 48:** Contour plots of wall  $y^+$  for the (a) full flowpath and (b) in the vicinity of the diamond fuel injector. Flow is from the left to the right and hydrogen issues from the injector out of the page.

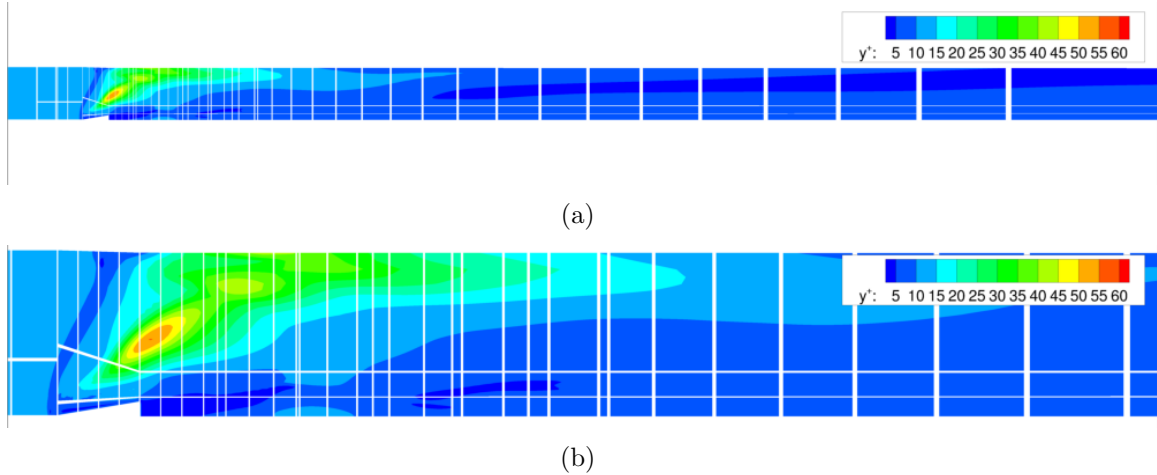


**Figure 49:** Contour plots of wall  $y^+$  for the (a) full flowpath and (b) in the vicinity of the diamond fuel injector. Flow is from the left to the right and hydrogen issues from the injector out of the page.

distance for the metrics of mixing efficiency and stream thrust potential. Note that the spatial coordinate has its origin at the leading edge of each injector. The mixing efficiency curve for each injector followed a monotonically increasing trend as shown in Figure 51(a). In terms of mixing efficiency, the stinger injector was the best performer by a significant margin while the classic circular injector and the diamond injector were the worst performers at cowl closure. It is also notable that the stinger injector has the greatest fineness ratio versus the circular injector. Because each injector type had only one example of fineness ratio (i.e. injectors with the same shape but different aspect ratios were not studied), the ability to identify this as the dominant driver of mixing efficiency was limited.

Stream thrust potential as a function of distance from the injector leading edge is shown in Figure 51(b). Each of the injectors with sharp leading edges had roughly the same stream thrust potential loss with the stinger injector being the worst of the three as the cowl closure location was approached. For most of the mixing region the circular injector had a worse stream thrust potential compared to the sharp leading edged injectors and better performance as the cowl closure location was approached.

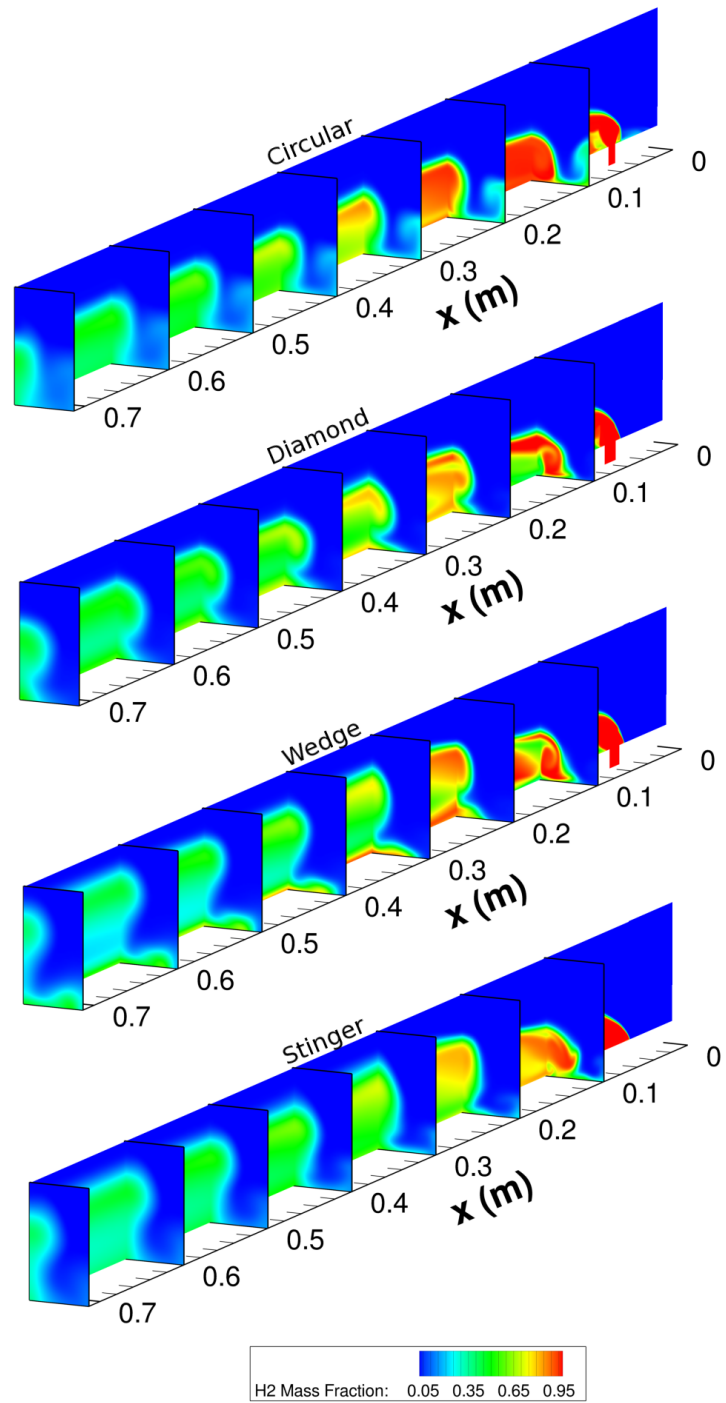
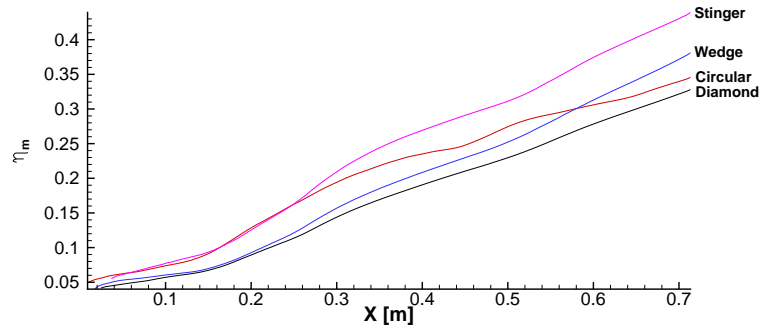
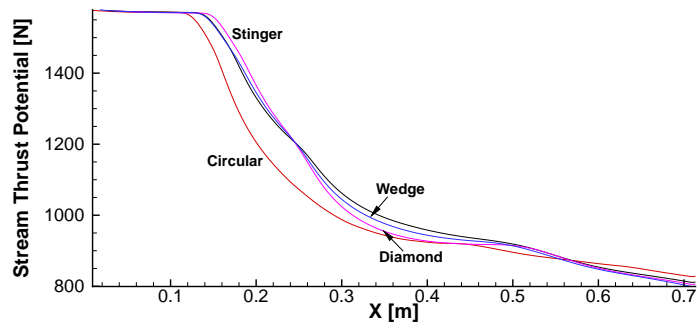


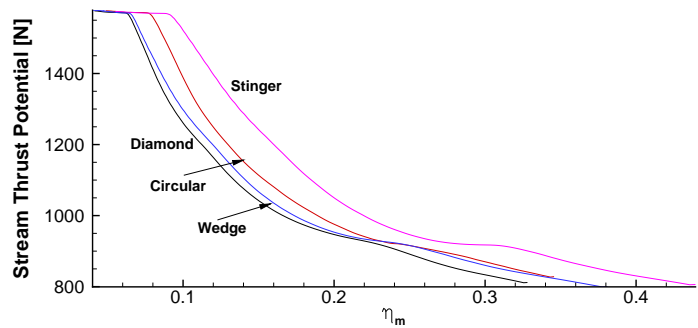
**Figure 50:** Fence plots of hydrogen mass fraction for the flush-wall injection cases.



(a)



(b)



(c)

**Figure 51:** Performance of transverse injection concepts: (a) mixing efficiency versus  $x$ , (b) stream thrust potential versus  $x$ , and (c) stream thrust potential versus mixing efficiency.

In general, the stream thrust potential experienced a slight decline initially due to friction and mixing. At around  $x = 0.2$  m the stream thrust potential experienced a sharp decline due to flow spillage from the top of the investigated domain. Because the mass flow rate is a dominant parameter in the stream thrust potential equation this caused a corresponding drop in stream thrust potential (even if the studied area and total pressure remained otherwise unaffected). Therefore flow spillage was accounted for in the stream thrust potential calculation (as opposed to total pressure loss, which may be unaffected by spillage).

It is difficult to analyze mixing efficiency and stream thrust potential separately to get an idea of which injector performs the best. For example, just considering mixing efficiency, the stinger injector performed the best while stream thrust potential indicates that the circular injector was the best performer. Additional insight can be gained by considering stream thrust potential as a function of mixing efficiency, plotted in Figure 51(c). This plot shows how much stream thrust potential was recovered for a given level of mixing for each concept. This curve gives the analyst an idea of the value of each injector. Among the flush wall injectors considered, the stinger injector was the best value because for any given level of mixing it had the greatest stream thrust potential. Because it was able to achieve higher levels of mixing overall, it would be able to mix out faster than any other concept (thereby reducing the required forebody length).

Plots of fuel equivalence ratio just downstream of the injector and at the cowl closure location are shown in Figure 52. Just downstream of the injection location for each injector a vortex core formed in the fuel plume. The vortices at the cowl closure for each injector case were relatively weak. The vorticity observed in the stinger case combined with the rising fuel bubble visible near the centerline led to enhanced diffusivity of the fuel plume that yielded its advantageous mixing performance. Because of the importance of characterizing fuel spillage, the spillage values at cowl closure are

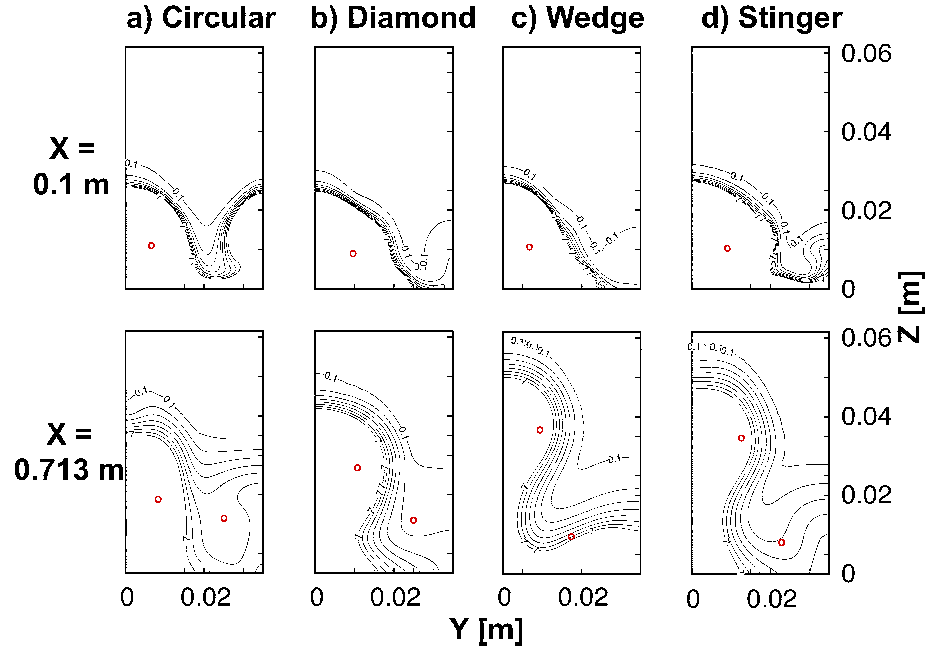


**Figure 52:** Fuel equivalence ratio contours for the (a) circular, (b) diamond, (c) wedge, and (d) stinger injection case at  $x = 0.1$  m and  $0.713$  m. Lines are plotted as  $\phi = 0.1, 1, 2 \dots 7$ . Circular marker indicates vortex center.

**Table 9:** Flush-wall injected fuel spilled at cowl closure as a percentage of the nominal fuel injection mass flow rate of  $0.02639$  kg/s.

	Circular	Diamond	Stinger	Wedge
% Fuel Spilled	2.9%	1.4%	3.0 %	1.8 %

given in Table 9. Low values of fuel spillage were observed for each injection concept. Because the displacement of the fuel plume is a function of dynamic pressure ratio, these low values of spillage may not hold for higher dynamic pressure ratios. However, it is shown that for a dynamic pressure ratio of unity the fuel is able to access much of the captured flow area while spilling only a small percentage.

#### 2.4.2 Ramp Injection

This subsection assesses the performance of forebody ramp injection for the cases listed in Table 5. The objective was to assess the relative performance of ramp injectors as a consequence of varying ramp geometry and injector pressure. For each case the equivalence ratio was held constant and consideration was made toward the

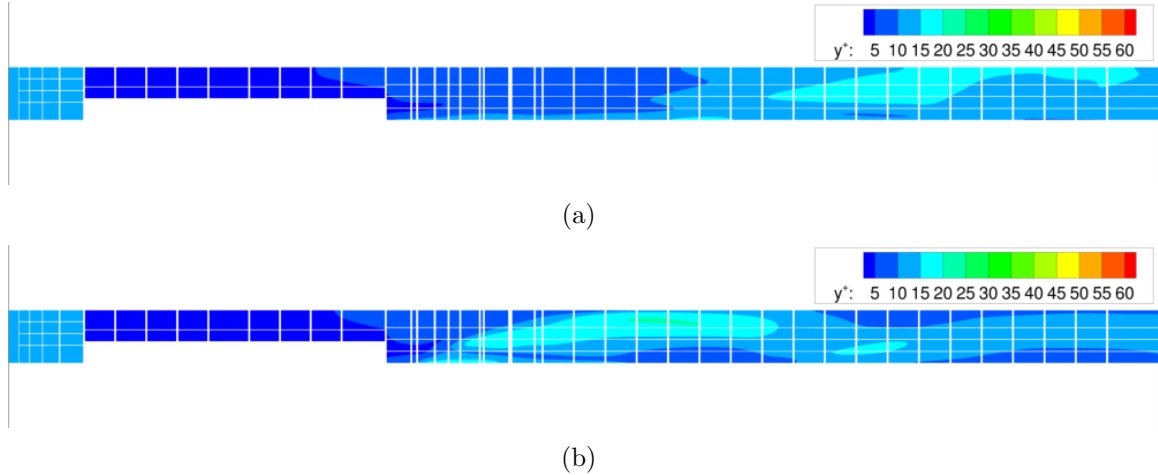


**Figure 53:** Contour plots of wall  $y^+$  for the full flowpath of the unswept ramp fuel injector with cavity at both a (a) pressure matched and (b) sonic pressure condition. Flow is from the left to the right and the ramp itself is blanked out.

**Table 10:** Ramp injected maximum wall  $y^+$  values. Legend: C(antilivered), W(edge), M(atched pressure), S(onic pressure)

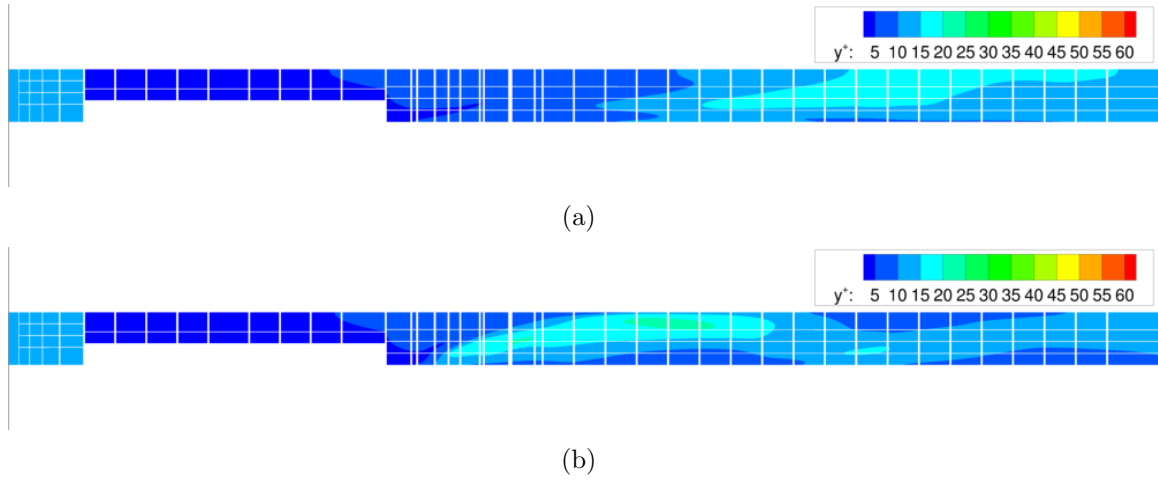
Base	Unswept Ramp				Swept Ramp			
	C		W		C		W	
Pressure	M	S	M	S	M	S	M	S
$y_{max}^+$	16.77	20.37	17.37	20.99	20.56	15.05	20.47	14.88

spillage of air from the capture streamtube.

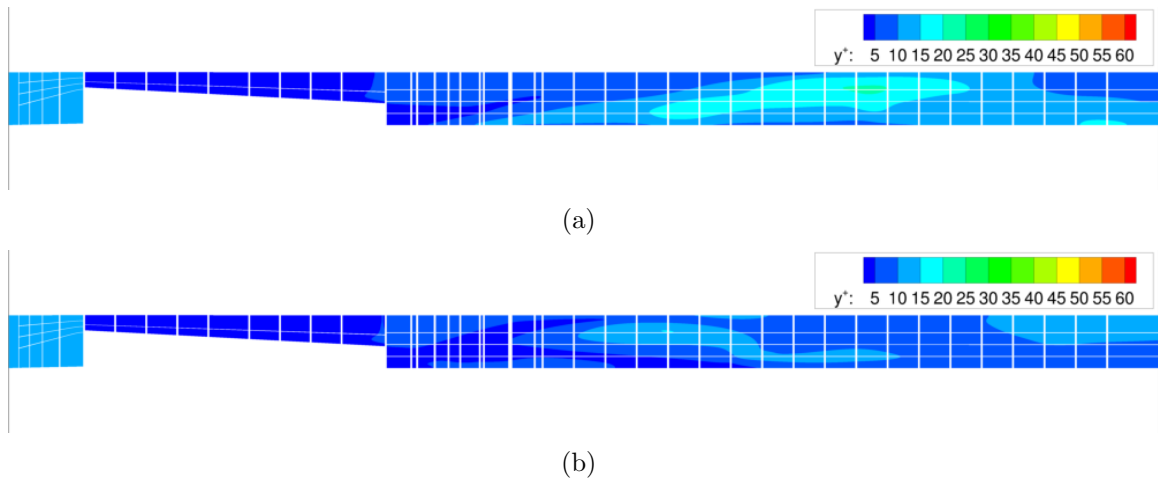
Contours of wall  $y^+$  values for each simulated case are shown in Figures 53 through 56. The inflow  $y^+$  value for each case was 11 with maximum values given in Table 10, each occurring downstream of the ramp in the mixing region and within the range of validity for using wall matching functions.

Figure 57 shows fence plots of hydrogen mass fraction contours for the ramp injector without the base expansion wedge. The pressure matched ramps, both swept and unswept, were able to inject fuel such that it mixed away from the wall. Increasing the injection pressure to a sonic condition caused the fuel to expand toward the wall and, in the case of the swept ramp, created a recirculation region under the ramp that consequently mixed fuel near the wall.

An initial evaluation of the performance of each injector was made using stream



**Figure 54:** Contour plots of wall  $y^+$  for the full flowpath of the unswept ramp fuel injector with expansion wedge at both a (a) pressure matched and (b) sonic pressure condition. Flow is from the left to the right and the ramp itself is blanked out.



**Figure 55:** Contour plots of wall  $y^+$  for the full flowpath of the swept ramp fuel injector with cavity at both a (a) pressure matched and (b) sonic pressure condition. Flow is from the left to the right and the ramp itself is blanked out.

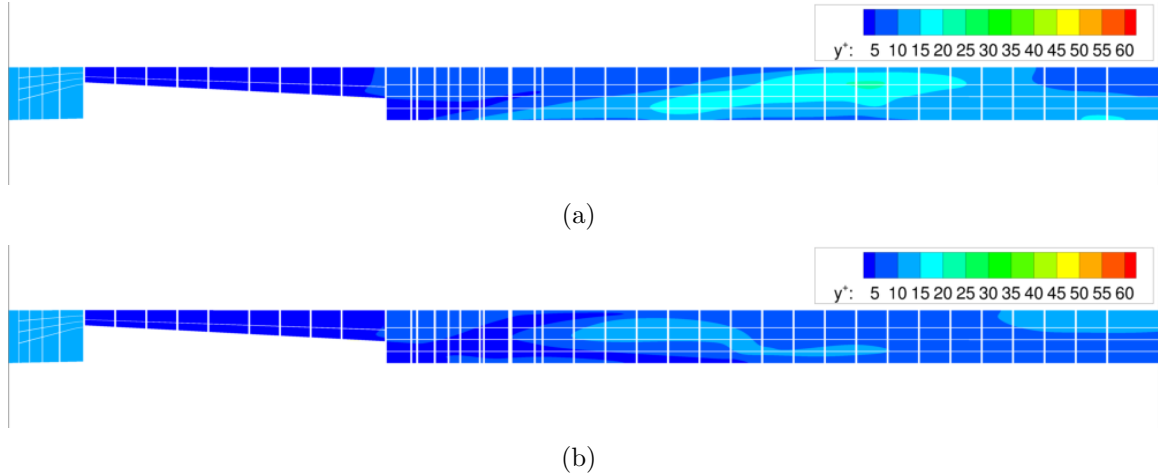


**Figure 56:** Contour plots of wall  $y^+$  for the full flowpath of the swept ramp fuel injector with expansion wedge at both a (a) pressure matched and (b) sonic pressure condition. Flow is from the left to the right and the ramp itself is blanked out.

thrust potential and mixing efficiency. Figure 58 shows the effect of geometry on the mixing efficiency and stream thrust potential for a fuel plume pressure matched to the air inflow. Geometry considerations included the sweep of the ramp and the presence of a wedge on the underside of the fuel duct. Figure 58(a) shows the mixing efficiency as a function of x-location and begins at the injector exit. This figure demonstrates an advantage in mixing by the addition of the wedge feature and an advantage in mixing by ramp sweep. The latter result is expected due to the enhanced vorticity of the swept ramp case.

A larger difference in performance is observed by considering Figure 58(b), which plots stream thrust potential as a function of distance for each ramp case. Here the unswept ramp had a consistent performance benefit over the swept ramp. This was due to the fact that the wider leading edge of the swept ramp caused overall increased mass flow spillage and flow expansion due to the shock wave originating from the ramp leading edge. Eventually the flow expansion turned the downstream velocity vectors near the cowl-closure y-location back toward the body and increased the mass flow rate in the studied region. This is demonstrated by plotting centerline streamtraces

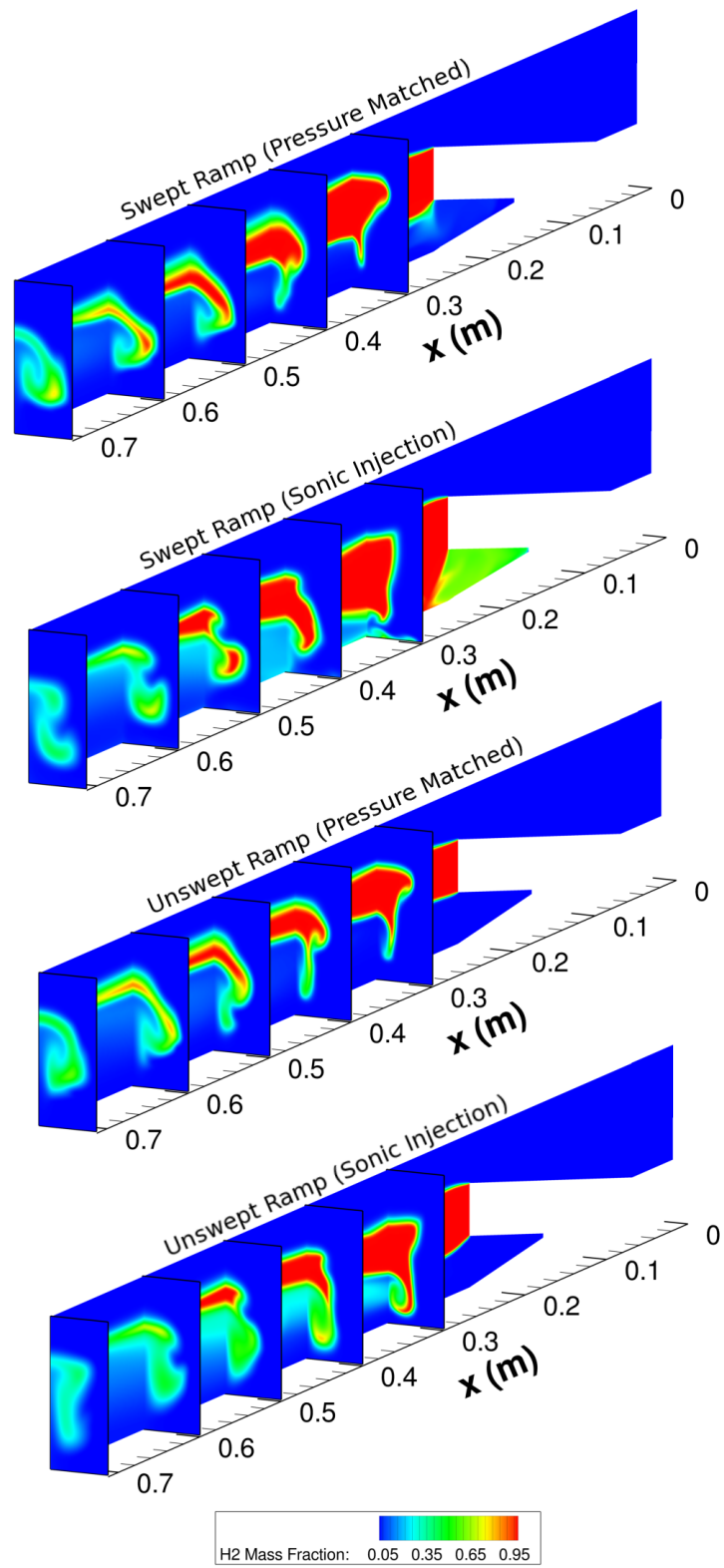
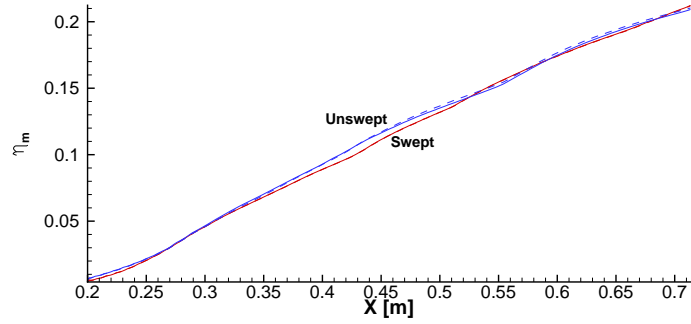
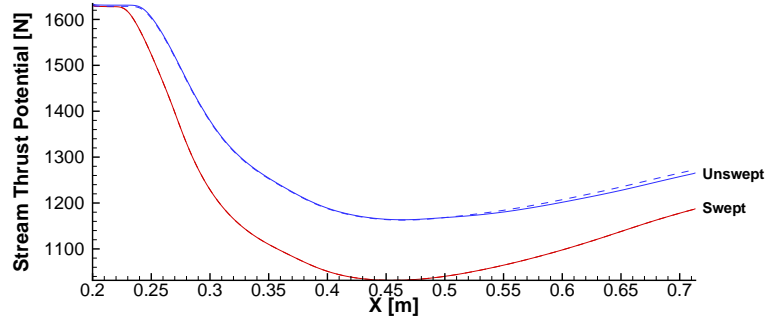


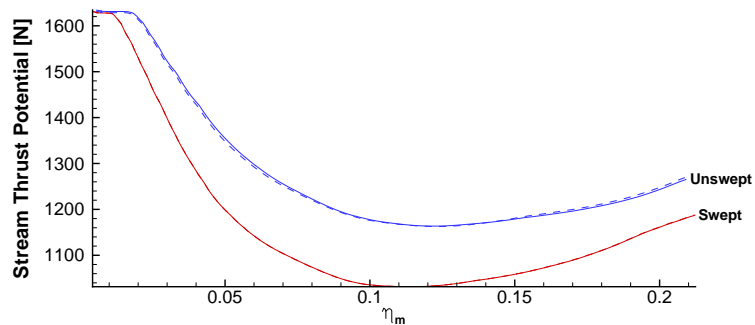
**Figure 57:** Fence plots of hydrogen mass fraction for the ramp injection cases without the base expansion wedge.



(a)



(b)



(c)

**Figure 58:** Performance of ramp injection concepts for matched pressure: (a) mixing efficiency versus  $x$ , (b) stream thrust potential versus  $x$ , and (c) stream thrust potential versus mixing efficiency. Dashed lines indicate cases with the expansion wedge feature.

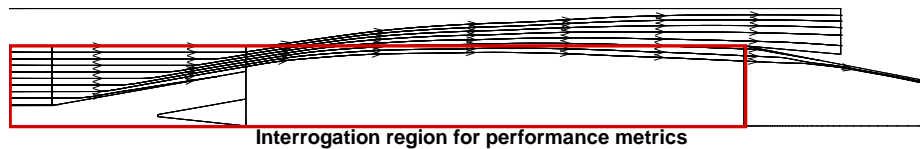


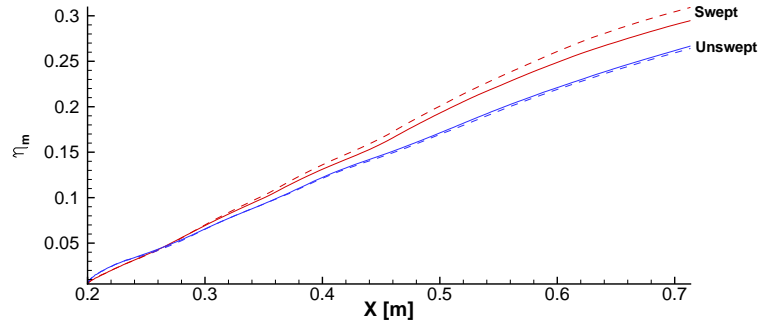
**Figure 59:** Stream traces that indicate flow arcing.

in Figure 59. This caused a corresponding increase in stream thrust potential that affected each case similarly (and therefore does not substantially affect the relative performance of each concept).

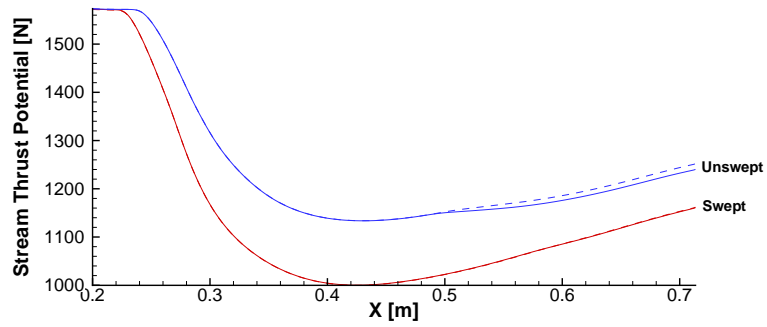
Figure 58(c) plots the value of each injector concept by plotting the stream thrust potential as a function of mixing efficiency. Here it is observed that adding the expansion wedge provided a slight advantage over the cases without the feature. Furthermore, using an unswept ramp provided the best stream thrust potential for the amount of mixing obtained.

Figure 60 plots performance metrics of the ramp cases when the injector pressure is raised by a factor of 3.92 (resulting in sonic injection). Figure 60(a) shows enhanced mixing on a case-by-case basis with increased fuel pressure. This is due to the under-expanded fuel plume reaching more of the main flow and inducing additional vorticity (discussed later). At cowl closure the high pressure, swept ramp case had 22% better mixing relative to the pressure matched case for the same geometry. However, the high pressure case had lower stream thrust potential relative to the pressure matched case, as seen in Figure 60(b). Because of this, the stream thrust potential versus mixing efficiency curve in Figure 60(c) is lower than that for the pressure matched case. Therefore, among the cases considered, pressure matching is preferred—although this conclusion does not necessarily imply superiority over all other injector pressures.

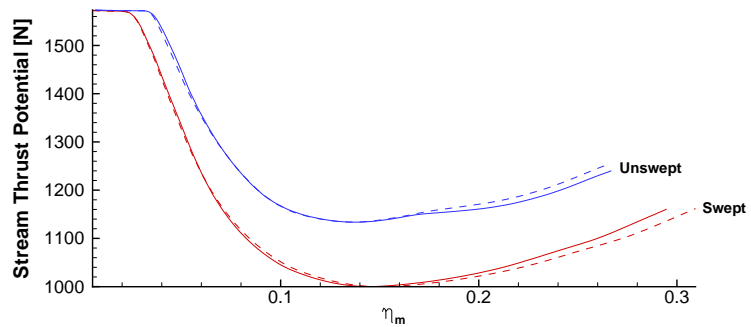
A comparison of cross sectional slices of the flow for the pressure matched and sonic ramps are shown in Figure 61. The cross sectional slices for the cases with an expansion wedge on the injector base are substantially the same as those without,



(a)



(b)



(c)

**Figure 60:** Performance of ramp injection concepts for sonic pressure: (a) mixing efficiency versus  $x$ , (b) stream thrust potential versus  $x$ , and (c) stream thrust potential versus mixing efficiency. Dashed lines indicate cases with the expansion wedge feature.

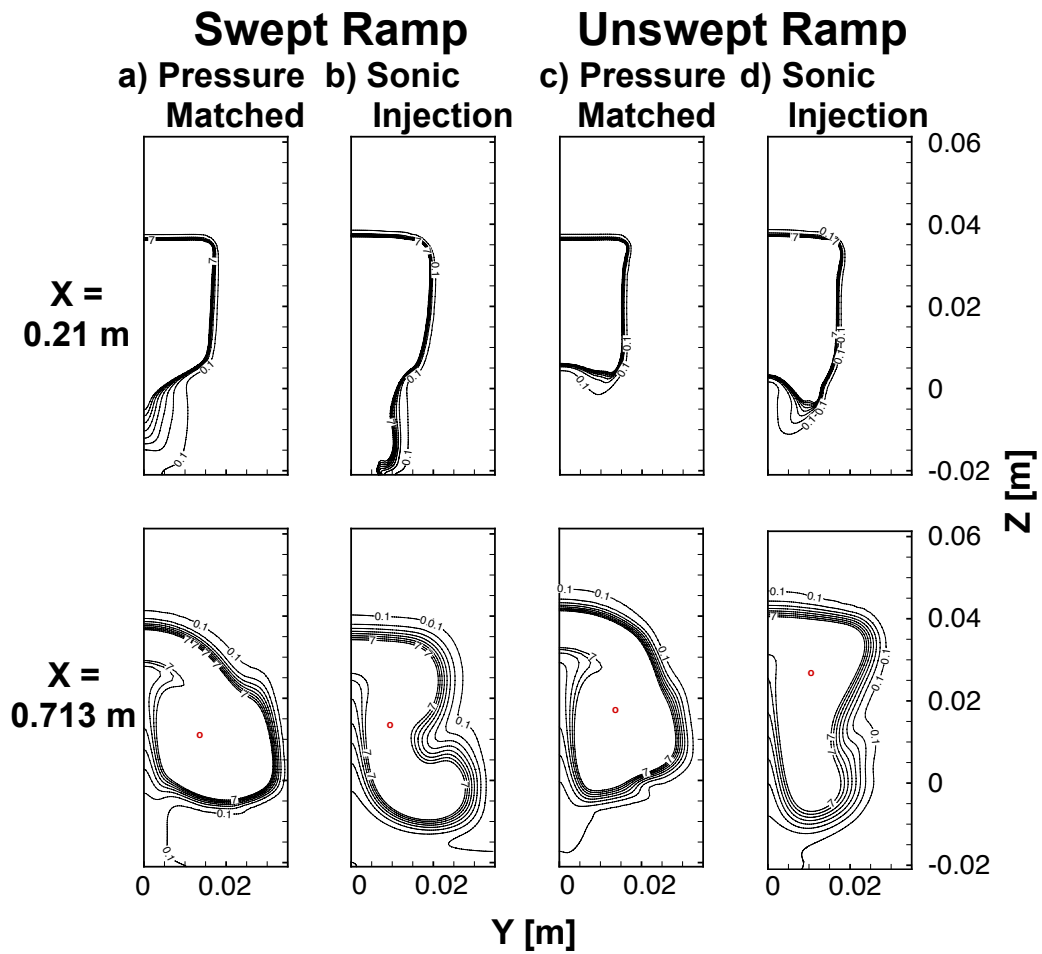


**Figure 61:** Fuel equivalence ratio contours for the swept and unswept ramp cases at  $x = 0.21$  m and  $0.713$  m. Lines are plotted as  $\phi = 0.1, 1, 2, \dots, 7$ . Circular marker indicates vortex center.

**Table 11:** Ramp injected fuel spilled at cowl closure as a percentage of the nominal fuel injection mass flow rate of 0.02639 kg/s. Legend: C(antiverged), W(edge), M(matched pressure), S(sonic pressure)

Base	Unswept Ramp				Swept Ramp			
	C		W		C		W	
Pressure	M	S	M	S	M	S	M	S
% Fuel Spilled	1.4%	0.9%	1.1%	1.1%	0.7%	1.0%	0.6%	0.8%

so the wedge cases are omitted here. The pressure matched cases both had the classic “kidney bean” shape at the cowl closure location that is indicative of enhanced mixing due to vorticity. The sonic injector had an additional lobe on the periphery of the fuel plume due to a secondary vortex that further enhanced mixing over the pressure matched case. The pressure matched case began to form the second vortex at an intermediate location but it was quickly absorbed by the primary vortex. The sonic injection case also had enhanced mixing near the wall which may have consequences for the possibility of boundary layer autoignition. This infiltration near the wall is due to the fact that fuel was entrained upstream of the ramp injector exit for the higher pressure case and was mixed closer to the wall due to the vorticity initiated by the ramp itself. Fuel spillage was characterized for each ramp case and is summarized in Table 11. For each case the injected fuel only had small levels of spillage, thereby giving credibility to the ramp design in terms of being able to capture the injected fuel.

### 2.4.3 Strut Injection

Note that the discussion contained in this subsection for strut injection is only for a point strut design and does not necessarily represent an optimum configuration. In this dissertation, parametric studies of strut sweep angle, fuel injection angle, and fuel pressure were not conducted for the given configuration. The purpose of this discussion is to get an idea of some of the general performance characteristics of a strut in forebody flow conditions as a starting point for future analysis.

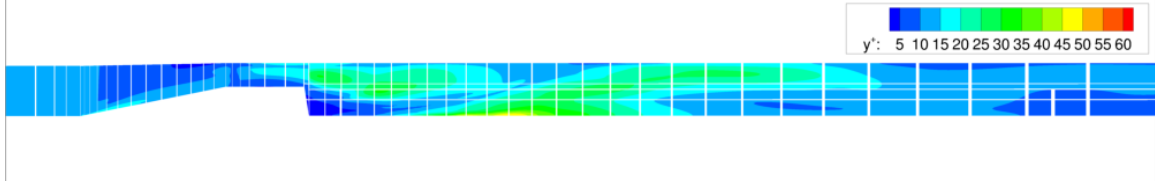


**Figure 62:** Contour plots of wall  $y^+$  for the full flowpath of the strut injector. Flow is from the left to the right and the strut itself is blanked out.

Contours of wall  $y^+$  values are shown in Figure 62 for the strut injector. The inflow  $y^+$  value was 11 with a maximum value of 50.11 occurring downstream of the strut on the centerline of the mixing region, within the range of validity for using wall matching functions.

Figure 63 shows a fence plot of hydrogen mass fraction contours for the strut injector. Overall the fuel plume had excellent mixing into the surrounding air, although there was some undesirable mixing near the wall. This could be mitigated in future strut designs by placing fueling ports farther from the wall. The effect of shock waves turning fuel toward and away from the centerline can also be observed in this figure.

Figure 64 summarizes the performance characteristics of the strut injector concept. Because the strut is a fuel placement apparatus, the flow was able to be seeded in multiple locations (four for this injector). The benefit to mixing efficiency is visible in Figure 64(a). The strut injector had significantly higher mixing efficiency at cowl closure than the ramp injector. One reason for this is due to the multiple-port characteristic of the apparatus. By having multiple ports, the contact surface between the fuel and the air was lengthened, allowing for improved mixing of fuel into air.

The stream thrust potential of the strut in Figure 64(b) follows a monotonically decreasing trend. Near the cowl closure point there was a shock wave that spilled an additional amount of fuel. When considering the value of the mixing efficiency in Figure 64(c) it is evident that the strut was able to maintain a relatively high level of stream thrust potential for the mixing efficiency it achieves. The relative performance of this concept with respect to the other concepts is discussed in the next section.

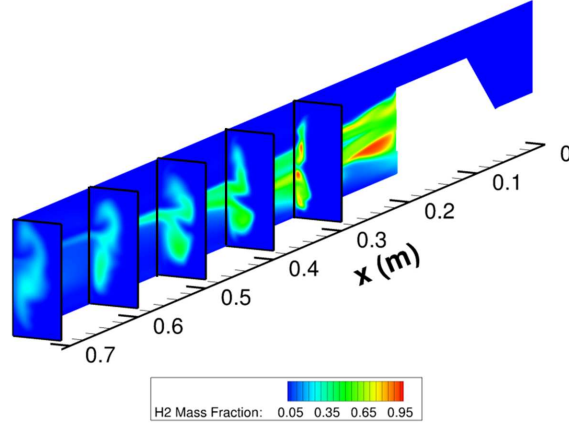


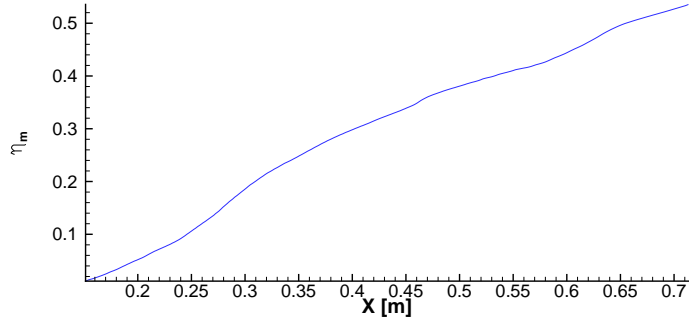
**Figure 63:** Fence plot of hydrogen mass fraction for the strut injection case.

Cross sections of fuel equivalence ratio for the strut injector just downstream of the trailing edge and at cowl closure are shown in Figure 65. In general, the flow for the strut case was shock-dominated, with the fuel jet turned toward and away from the centerline as shock waves reflect off of the two symmetry boundary conditions. The fuel plume mixed well overall with a smaller core than found with previous injector concepts. There is also vorticity present near the bottom of the fuel plume that further enhanced mixing and is sustained through cowl closure. Fuel spillage for the strut injector at cowl closure was 3.0% relative to the nominal injected fuel mass flow rate of 0.02639 kg/s. This value of spillage, although low, may be reduced if the strut height is similarly reduced.

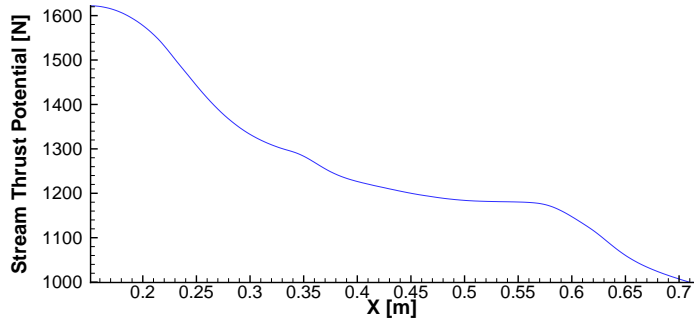
#### 2.4.4 Injector Comparisons

Comparison between injection strategies was conducted by selecting the best value performers from each injector category (transverse, ramp, and strut) and evaluating their relative performance. The best performers from the first two categories were the stinger and unswept ramp with expansion wedge. The strut is included for completeness. Figure 66 summarizes the performance of each top-performer.

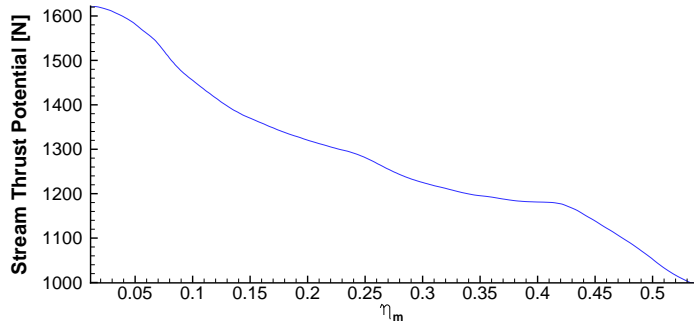
Figure 66(a) shows the mixing efficiency as a function of location for each injector concept. While the strut injector began to inject fuel farther downstream, it rapidly



(a)



(b)



(c)

**Figure 64:** Performance of the strut injection concept: (a) mixing efficiency versus  $x$ , (b) stream thrust potential versus  $x$ , and (c) stream thrust potential versus mixing efficiency.

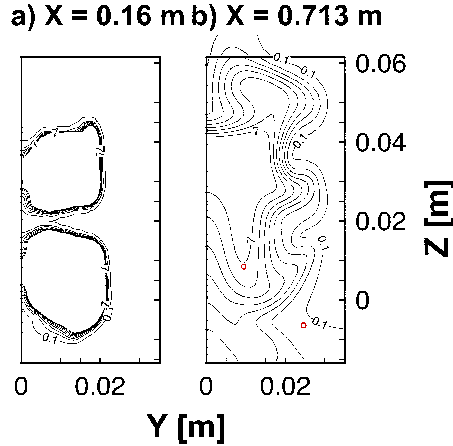
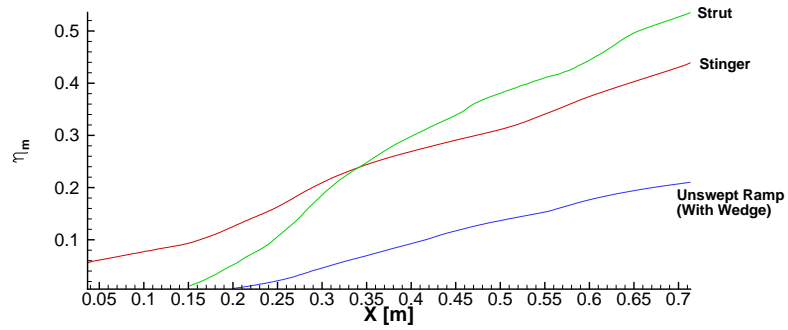


**Figure 65:** Fuel equivalence ratio contours for the strut injector case at  $x = 0.16$  and  $0.713$  m. Lines are plotted as  $\phi = 0.1, 1, 2, \dots, 7$ . Circular marker indicates vortex center.

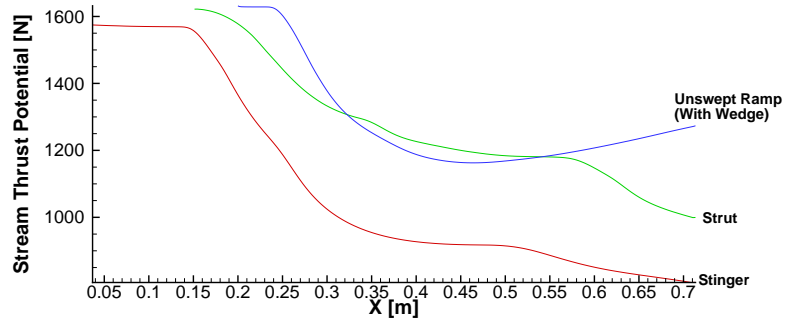
approached and exceeded the mixing efficiency achieved by the transverse stinger injector. The ramp injector had significantly lower mixing efficiency compared to the other two concepts, even considering its delayed injection location.

Figure 66(b) compares the stream thrust potential of each injector concept. The best comparison is made at the cowl closure location which represents the true captured stream tube for each concept. At this point, the ramp wedge maintained the most stream thrust potential with the transverse injector having performed the poorest. This is an expected result due to the axial direction of the ramp injection and the high loss nature of transverse injection. The strut injector performed worse than the ramp injector, which may be in part due to the enhanced mixing of the strut as they both had relatively similar thrust potential at their injection locations.

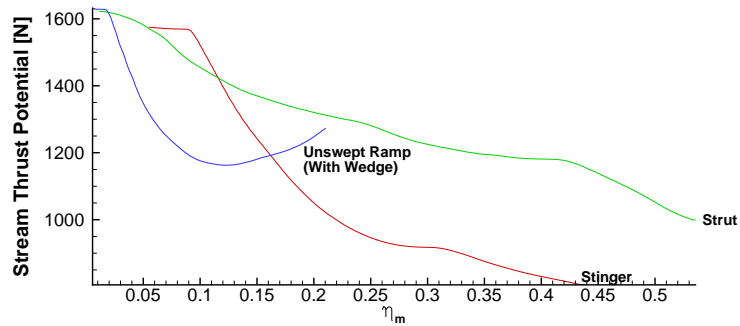
Figure 66(c) plots the stream thrust potential as a function of mixing efficiency. The location of greatest mixing efficiency for each concept was at cowl closure. The ramp injector was found to perform between the strut and transverse injectors, with the strut having had the best stream thrust potential for the amount of mixing it achieved. The strut also implies a much shorter mixing length (similar to the transverse injector, only with much less stream thrust potential loss) over the ramp injector.



(a)



(b)



(c)

**Figure 66:** Performance of the best injection concepts: (a) mixing efficiency versus  $x$ , (b) stream thrust potential versus  $x$ , and (c) stream thrust potential versus mixing efficiency.

This indicates the competitiveness of the strut injection concept and that it should be included in future forebody injection studies.

#### **2.4.5 Effect of Turbulent Schmidt Number**

The effect of turbulent Schmidt number on the performance metrics of the stinger, unswept ramp with wedge, and strut will now be discussed. It was observed in the validation study with the Waitz geometry that the selected value of  $Sc_t$  had a strong effect on the diffusion between the injectant and the surrounding air stream. This will have an effect on the calculated mixing efficiency for each injector concept. The value  $Sc_t = 1.0$  was chosen with the underlying assumption that while the true value of the performance metrics will not be necessarily calculated, this was allowable because the primary interest was comparison between injector concepts.

Three values of  $Sc_t$  were compared—1.0, 0.5, and 0.25—with  $Sc_t = 1.0$  being the baseline case that has already been the basis of the comparisons described to this point. All other simulation parameters were held constant. Figure 67 shows the thrust potential plotted as a function of mixing efficiency for the stinger, strut, and unswept ramp with wedge for each value of turbulent Schmidt number. It is observed that the selected value of Schmidt number does impact the level of mixing achieved for each concept, although this effect is varied depending on the injector studied. For example, the stinger injector maximum mixing levels varied between 0.42 and 0.46, compared to the strut that varying between 0.49 and 0.58. This may be due to the enhanced interfacial area between the strut fuel plume and the surrounding air. Also of note is that the thrust potential levels were not substantially affected, as might have been expected due to the losses normally incurred due to mixing. For each case of turbulent Schmidt number, the trend and range of thrust potentials was roughly the same. This is due to the fact that the dominant contributor to loss was the spillage of flow from the domain.

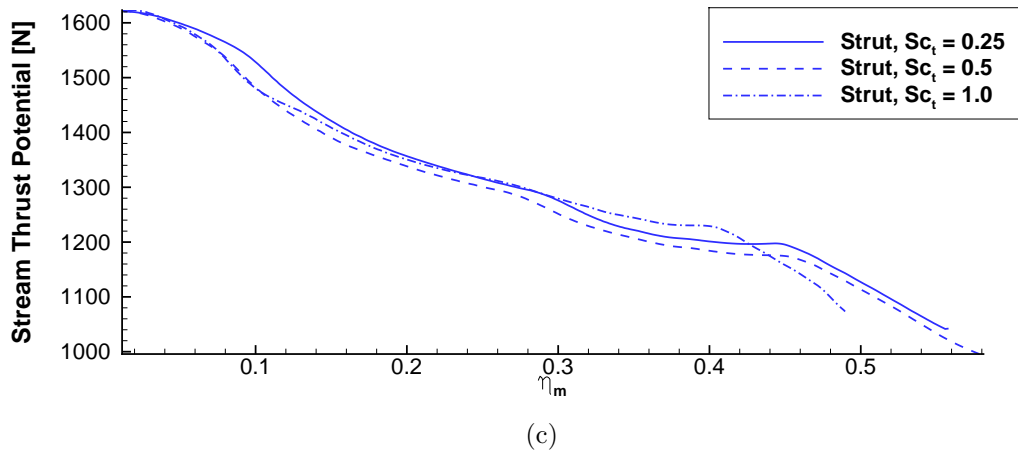
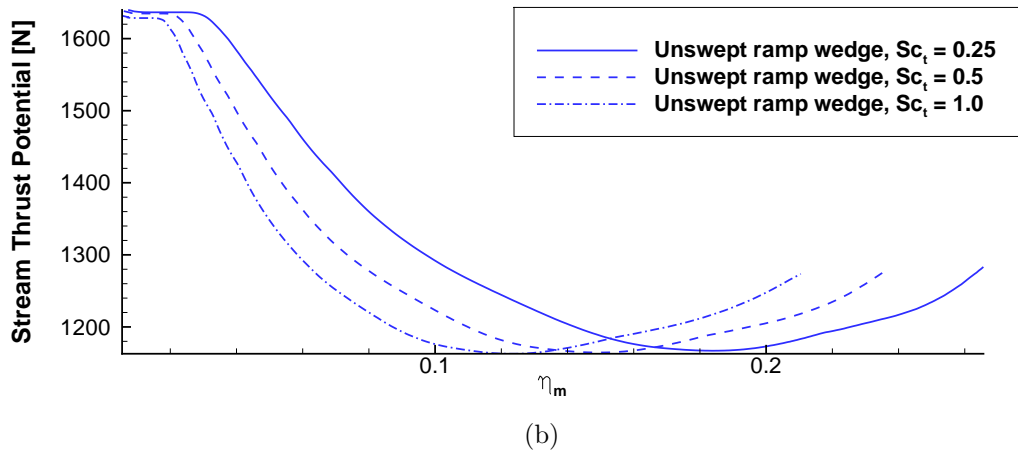
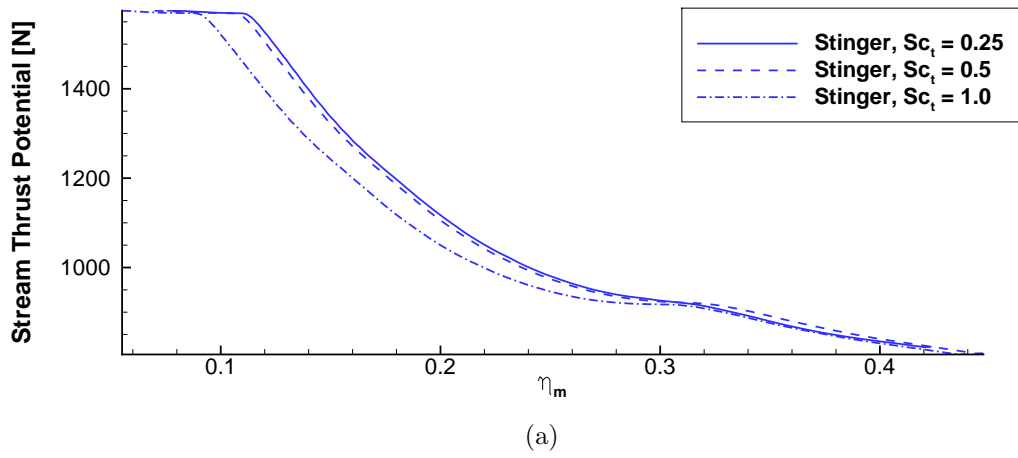


**Figure 67:** Comparisons of stream thrust potential versus mixing efficiency between the (a) stinger, (b) unswept ramp with wedge, and (c) strut injectors for  $Sc_t = 0.25 - 1.0$ .

An important conclusion to draw from looking at the effect of turbulent Schmidt number is that when comparing different injector concepts, the same conclusions can be drawn as was drawn before. For example, the stinger performed the best when valued against mixing efficiency. It also achieved the greatest level of mixing and therefore will have the shortest mixing length of the considered concepts. Therefore, while the solution was sensitive to the selection of turbulent Schmidt number, the present comparative study was not substantially dependant on the selection of the parameter.

It should be noted that this study cannot give any recommendation on which value of turbulent Schmidt number should be chosen for the present regime of flight based on the current results. This underscores the importance of producing experimental validation data in a regime relevant to the forebody of a hypervelocity vehicle. Such experimental databases will provide important information for calibrating future RANS simulations to produce results that can accurately predict losses and mixing achieved for forebody fueling concepts.

## ***2.5 Chapter Summary***

The current study of injection and mixing on a vehicle forebody at hypervelocity conditions concerns the efficiency of three major categories of injection: flush-wall, ramp, and strut injection. Each injector was sized and designed to provide stoichiometric fuel to air mass flow given a notional forebody design and vehicle capture. In evaluating the value each injector provided to the system, two metrics were used: mixing efficiency and thrust potential. Mixing efficiency was used to gauge how well each concept mixed (and is a metric that is typically maximized) while thrust potential was used to gauge what losses were incurred through the injection and mixing process. It was proposed that comparing the two metrics directly gave a valuable means to compare different injection concepts.

Flush-wall injection was shown to overall achieve high levels of mixing, but at the cost of very high losses. This was mostly due to the fact that a perpendicularly-directed fuel jet produced a bow shock ahead of the fuel plume that provided a large amount of disturbance to the main flow. Furthermore, because the fuel was issued normally to the upstream velocity vector, the system was unable to take advantage of the thrust produced by the jet. Worse still, energy must be expended to turn the fuel plume in the axial direction. While flush-wall, angled injection would be able to alleviate some of the losses incurred, it would be at the expense of mixing efficiency. In addition to the quantitative performance of the flush-wall injectors, other qualities of the flow proved undesirable. For example, a recirculation region tended to form upstream of the injector that entrained fuel and provided a long fuel residence time. This increased the risk of autoignition occurring in such regions, something that is needed to be avoided for forebody injection concepts.

## CHAPTER III

### AUTOIGNITION MITIGATION

The premixed or mixing flow on a forebody shares a cooling requirement with an internal flow in that surface temperatures and heat loads below the wall material limit are needed for basic structure survivability. However, such forebody flows have an additional requirement: to minimize (and hopefully eliminate) the presence of ignition until the entrance of the combustor is reached. Premature burning not only consumes fuel before the fuel/air mixture can reach the combustor, but it also introduces pressure drag on the vehicle overall due to elevated pressures on the forebody. Like conventional scramjets, shcramjets are likely to operate on a thin margin of thrust—the introduction of both pressure drag and thrust losses (both through premature fuel consumption) may create design and mission infeasibility.

Both the film cooling and transpiration concepts have been studied a great deal in the literature and are used in many different aerospace systems encountering high heat load conditions. They have been considered and used for the protection of rocket nozzles [73], supersonic inlets [74], gas turbine blades [75, 76, 77], nose cones [78], reentry vehicles [79], and rocket combustors. They are generally distinguished in that film cooling works by injecting a cooled gas near the body through a tangential slot and transpiration cooling injects gas through perforations in the wall. Both concepts alter the thermal structure of the wall boundary layer as well as convect heat away from areas of high heat load. This introduction aims mainly to describe how each method behaves, with system-level impacts discussed in a later section.

Shown notionally in Figure 68, surface cooling by means of cooled gas through a porous wall is known by different terms in the literature. Distributed film cooling is

where a normally solid wall is drilled with an array of holes, inline or staggered, using mechanical, laser, or water drilling. Transpiration (and more uncommonly, effusive) cooling is where the wall is composed of a material that is manufactured to be porous. Examples of such materials include carbon/carbon composites (C/C) [80, 81], ceramic matrix composites (CMC) [82], and porous stainless steel manufactured by layering and sintering stainless steel mesh [77]. For the purposes of this study, no practical distinction is made between distributed film cooling and transpiration—both will be referred to under the umbrella term “transpiration.” A transpiration cooling concept cools the surface in two ways. The first process occurs as the cool gas travels from a subsurface plenum to the surface through pores in the wall. As the gas travels through the wall, the material is cooled convectively as heat travels from the wall to the fluid. The second process occurs once the fluid emerges from the surface. If the mass flux ratio between the injectant and the main flow is high enough, a protective, cool layer of gas will form on the wall and reduce the heat load traveling from the previously hot shear layer to the wall. This process is nominally called “film cooling”, not to be confused with the film cooling method of introducing coolant to the flow.

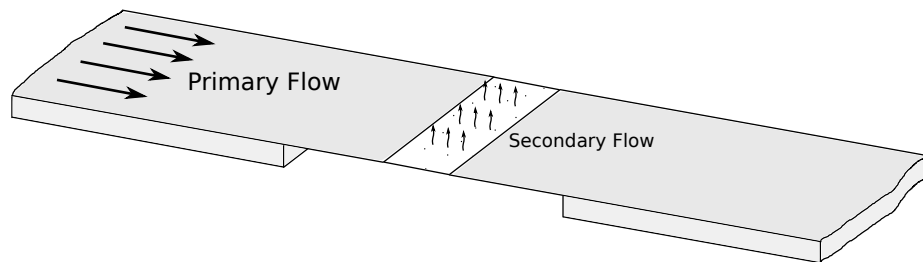


**Figure 68:** Notional diagram of wall transpiration.

Film cooling as a primary cooling method is typically achieved by injecting cool fluid tangentially or at an angle to the wall. Both of these methods are shown notionally in Figure 69. This flow may be introduced via a slot or ports on a backward-facing step, although transverse injection is another possible, albeit less conventional, method of injection. The effectiveness of film cooling is rooted in the “film cooling”

process mentioned previously: a layer of gas provides wall protection from a high heat load that would otherwise be introduced by a hot, upstream shear layer. This protection is introduced not only by having a cool layer in the vicinity of the wall, but also by altering the structure and thickening the thermal boundary layer as the cool gas mixes with the upstream shear layer, thereby reducing heat loads and temperatures present in the boundary layer.

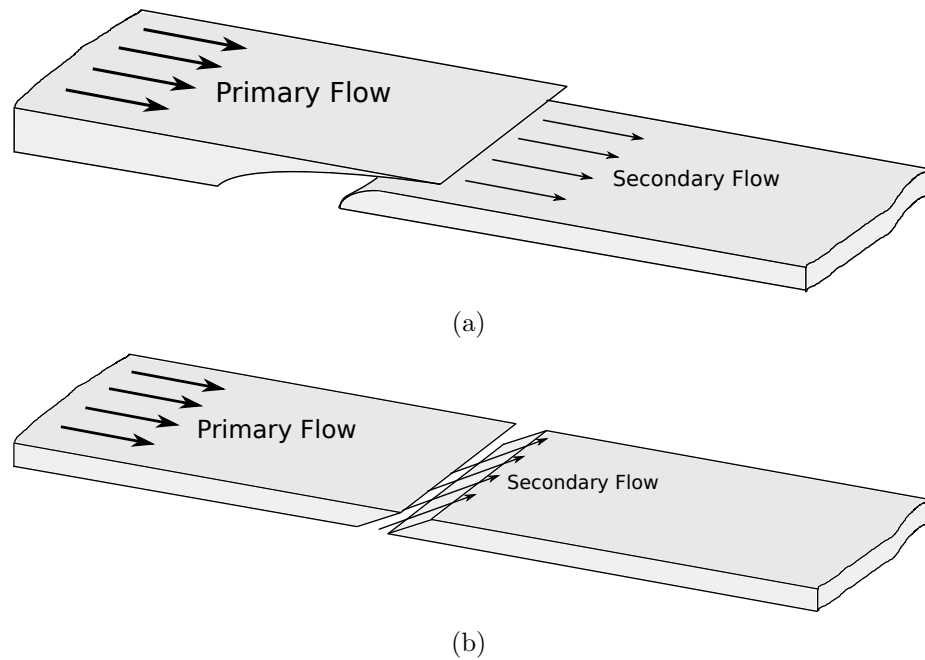


**Figure 69:** Notional diagram of film cooling via a slot for both (a) tangential and (b) angled injection.

Most of the literature, reflected in the general description of the cooling methods to this point, has a single-objective focus on the desire to lower heat loads at and traveling through the wall. In essence, temperatures experienced away from the wall (as long as they do not affect the wall heating) are of little consequence. For example, a film or transpiration cooler that uses a combustible gas such as hydrogen as its coolant performs well if the hydrogen is successfully able to keep the surface cool even if the edge of the cooling layer begins to combust due to the high temperatures in that region [83]. Similarly, if the primary flow is composed with a fuel, burning

on the coolant edge is also acceptable as long as heat loads remain low at the wall. This is because for a cooling concept occurring internally in a combustion chamber additional burning occurring away from the wall is not necessarily a detriment (and possibly is a benefit)—a combustor is not a region where ignition mitigation is desired. For a forebody flow, however, this is a disastrous outcome because of the increased wall pressure and associated forebody drag.

This chapter focuses on the study of autoignition mitigation in the locality of the forebody fuel injectors studied in Chapter 2. Reacting simulations of the mixing regions of the stinger, ramp, and strut injectors were evaluated in order to determine the autoignition characteristics of each injector. After identifying injectors that showed promise for autoignition mitigation, surface cooling was added to the simulations in order to determine the parametric effect of coolant species and secondary injection parameters on the presence of autoignition in the wall region.

### ***3.1 Model Selection and Validation***

#### **3.1.1 Chemical Model Selection via Ignition Delay**

The prediction of chemical induction and subsequent ignition is highly sensitive to the chemical model used in the numerical analysis. Because the ignition delay time has significant consequence concerning forebody autoignition, it is critical that the correct chemical model be used for the regime of interest.

The chemistry solver and model used in this study were chosen using the following methodology:

1. Compare the ignition time predicted between solvers. Choose the best solver depending on its solution time and its performance against validation data.
2. Using a selected solver, compare the ignition time predicted between various models. Pick the model that best matches validation data.

3. Using a selected solver and full chemical model, compare the ignition time predicted using reduced models.

There are three solvers whose performance and predictive capability were be compared: Cantera, CVODE, and  $\alpha - QSS$ . The selection of the chemical solver has importance for the construction of the QUIVR code used in Chapter 5 as VULCAN has its own chemistry solver, validated in Section 3.1.2. The evaluated solvers were:

- **Cantera**<sup>1</sup>, an open source, Python-based chemical kinetics package led in development by Dr. D. Goodwin of Caltech. The package is designed to interface with C++, Fortran, Python, or MATLAB.
- The **CVODE** package of SUNDIALS<sup>2</sup>, an open source nonlinear and differential equation solver suite developed by Lawrence Livermore National Laboratories. The package is able to interface with C++, Fortran, or MATLAB.
- The  $\alpha - QSS$  algorithm, developed by Mott *et al.* [84], which is specifically tuned for the solution of stiff chemical equations.

The Cantera solver was called from a lightweight Python script coded by the author. The CVODE and  $\alpha - QSS$  routines were called from a Fortran 95 zero-D reactor program also coded by the author which can accept any general set species and reactions without pressure dependent terms. When comparing chemical models against each other and experimental data, the combustion problem was modeled as occurring in a constant pressure reactor.

The literature indicates at least four ways to determine when combustion occurs, and therefore ignition delay time. The first is by locating the time of maximum rate of temperature change. The second is by finding the maximum rate of OH

---

<sup>1</sup>Code and documentation are obtainable from <http://code.google.com/p/cantera/>

<sup>2</sup>Code and documentation are obtainable from <https://computation.llnl.gov/casc/sundials/main.html>

production [85]. The third is by defining a threshold of OH concentration, for example  $0.005 \text{ mol}/m^3$  [86]. A fourth method defines a threshold ignition temperature [86]. The third definition was used in this study because it is also a convenient means to determine ignition location in a multidimensional flow simulation.

For the purposes of comparing solvers, the full Jachimowski chemical model was chosen as the baseline chemical model. The Jachimowski model has been used extensively in past numerical studies and has been validated over a wide range of conditions [87]. Ignition delay times using the model were simulated using a constant-volume combustion code by McLain and Rao [88] and compared against the experimental results of Slack and Grillo [85] with most simulated delay times being within 20% of experiment. Burning velocities were compared against data compiled by Warnatz [89] and Milton and Keck [90] using a premixed, 1D flame code written by Kendall and Kelly [91]. Generally good agreement between simulation and experiment were found both in terms of maximum burning velocity as well as burning velocities with varying equivalence ratio. Finally, scramjet combustor simulations were conducted at flight enthalpies ranging from Mach 8 to 25 which demonstrated the importance of including  $\text{HO}_2$  chemistry in the chemical model due to the high sensitivity of the results to that chemical species. It was also observed that at flight enthalpies above Mach 12, nitrogen chemistry became important.

The performance of each solver over a fixed temperature range at a pressure of 2.0 atm is shown in Figure 70. The shock-tube experiments of Slack and Grillo [85] at the same ambient conditions were plotted in order to provide a means of comparison. At high pressures these experiments provide high quality results, although the quality diminishes at lower pressures due to the influence of the boundary layer in the shock tube. The general trend is observed to have long ignition delay times at low temperatures with the delay time rapidly shortening as temperature was increased. As temperatures increased past the knee in the curve, the decrease in ignition delay time

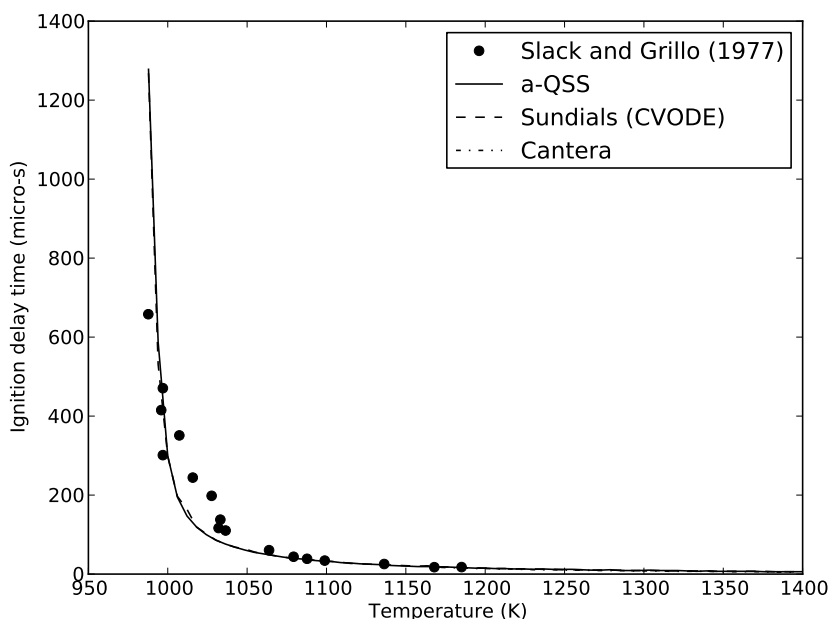


**Figure 70:** Comparing ignition delay time as a function of initial reactor temperature for a constant pressure of 2.0 atm using different solvers.

becomes more gradual. It is evident that regardless of the solver used, the ignition time predictive capability was the same. Because there is computational overhead required in using the Sundials and Cantera packages, versus  $\alpha - QSS$  which can be simply coded,  $\alpha - QSS$  was chosen to be the best algorithm for this study for the QUIVR code.

With the solver comparison complete, the effect of using different models was ascertained. A number of models were chosen, including the Jachimowski, O Conaire [92], Rogers and Schexnayder [86], and San Diego [93] models. Appendix D gives a summary of each mechanism. Figure 71 shows each model's predicted ignition times compared to the experiment of Slack and Grillo at a pressure of 2 atm. It is observed that each model gave a reasonable representation of experimentally determined ignition delay times. The largest differences occurred at low initial temperatures. Figure 72 compares the same models against an experiment conducted by Bhaskaran [94] at a pressure of 2.5 atm. Generally good agreement is again achieved, although the San

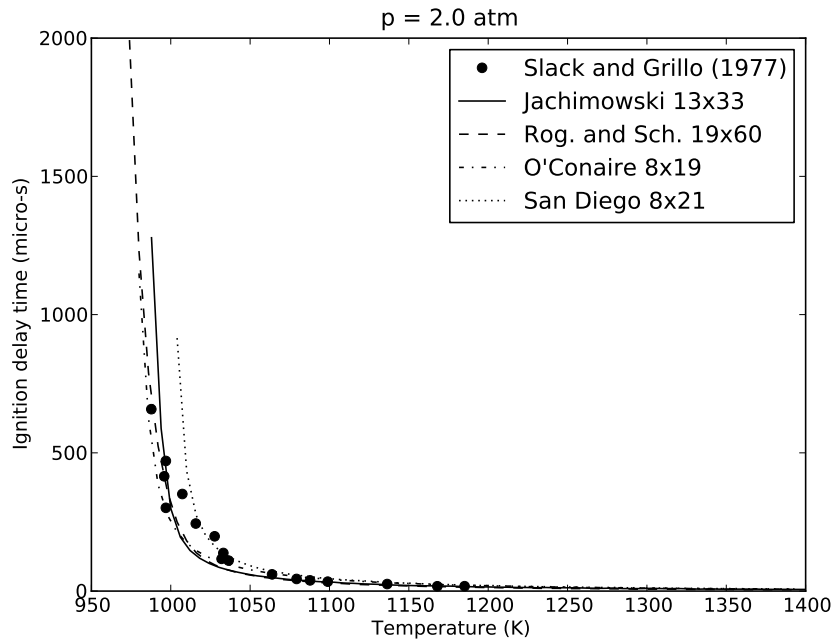


**Figure 71:** Comparing ignition delay time as a function of initial reactor temperature for a constant pressure of 2.0 atm using different chemical models.

Diego model agreed closest with experimental data at low temperatures.

Because of the simplicity of the model, its established use in flows with scramjet-like conditions, and generally good agreement with experiment, the Jachimowski model was chosen to be the model used in the present chemically reacting flow studies. Because running the full chemistry model had a significant adverse impact on the computational resources required to converge a numerical simulation, a study of the effect of reducing the model is undertaken here. This was accomplished by removing selected species from the mechanism and related reactions and evaluating the effect on ignition delay time. The result of this is shown in Figure 73, which shows the ignition delay time predicted by reduced Jachimowski models compared to the 2 atm shock tube experiment of Slack and Grillo. Here it is observed that removing all of the nitrogen chemistry as well as hydrogen peroxide ( $H_2O_2$ ) chemistry had a negligible effect on the prediction of ignition delay time at these conditions. The relative unimportance of hydrogen peroxide for high temperature combustion has been

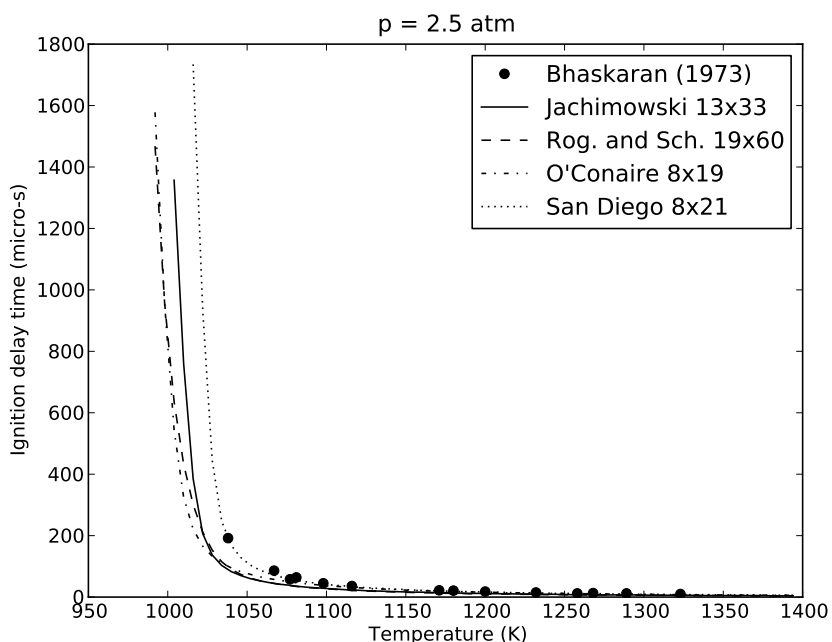


**Figure 72:** Comparing ignition delay time as a function of initial reactor temperature for a constant pressure of 2.5 atm using different chemical models.

established in the literature [95]. Therefore, the 8-species, 13-reaction reduced Jachimowski chemical mechanism was chosen to be the preferred chemical kinetic model moving forward.

### 3.1.2 Blunt-Body, Premixed, Shock-Induced Combustion

The VULCAN CFD code in a chemically reacting mode of operation can be validated against blunt-body, premixed, shock-induced combustion experiments conducted by Ruegg and Dorsey, and H.F. Lehr. In both cases, a spherically-blunted projectile was fired into quiescent hydrogen-air at various combinations of Mach number and ambient pressure. Computational validation is assumed to be achieved if simulations are able to produce the physical mechanisms observed in experiment as well as quantitative matching of different experimental quantities such as standoff distances and reaction front frequency (for the unstable cases). Therefore the validation questions here are summarized as:

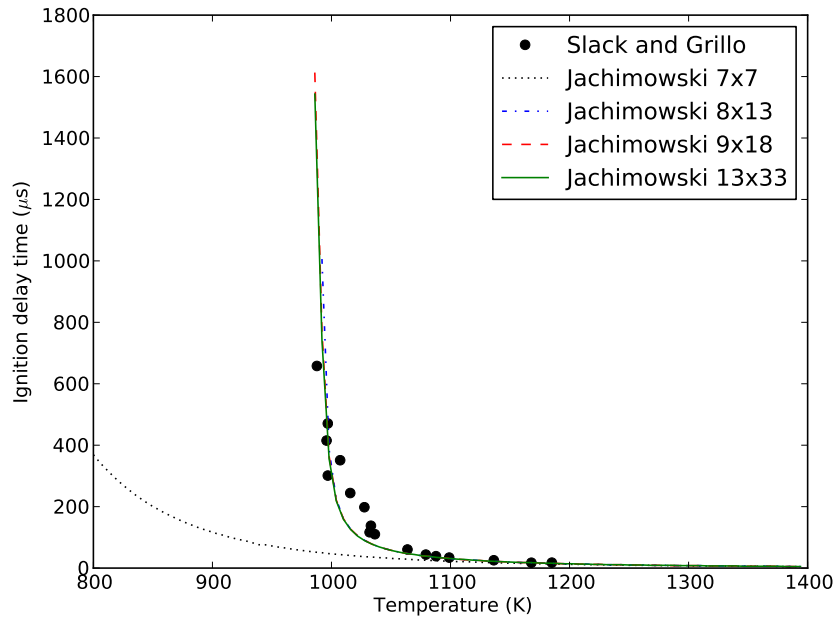


**Figure 73:** Comparing ignition delay time as a function of initial reactor temperature for a constant pressure of 2.0 atm using different reduced models from the Jachimowski mechanism.

Can VULCAN...

- ...successfully reproduce the stability conditions observed in experiment at the same conditions?
- ...accurately predict the reaction and shock front standoff distances observed in experiments at the same conditions?
- ...accurately reproduce the same reaction front frequencies as observed in experiments at the same conditions?

These validation questions were chosen due to the importance of ignition delay time and chemical model on the behavior of autoignition.

The computational grid used to model the spherically-blunted experimental projectiles is shown in Figure 74. Although the important physical mechanisms responsible for the unsteady behavior observed in experiment was hypothesized to occur

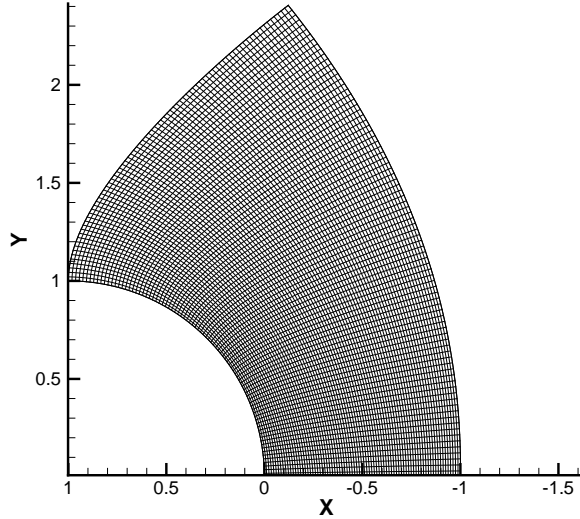


**Figure 74:** The grid used in the validation study is shown with every tenth grid point normal to the surface and every third grid point tangential to surface.

in the stagnation region, the flow is simulated up until the shoulder region of the projectile. The grid was non-dimensionalized to the sphere radius in order to allow the grid to be sized easily to different projectile radii. This also produced the final results with dimensions normalized to sphere radius, a typical normalization used in such flows. For each case the grid had 800 points normal to and 256 points along the projectile surface. The fineness of the grid normal to the surface allowed the resolution of the mechanisms responsible for unstable behavior in the reaction zone. All cases were simulated with the Jachimowski 8-species, 13-reaction model [87] as this model was concluded to be sufficient for the accurate prediction of ignition delay times. During the chemically reacting integration the global CFL number was set to be 5.0, which corresponded roughly with a time step of 7 ns.

In their ballistic experiments, Ruegg and Dorsey [96] shot 20 mm diameter, spherical projectiles into quiescent hydrogen-air and measured, among other things, the shock- and reaction-front standoff distances at different Mach numbers and ambient pressures. They also published Schlieren images that clearly showed different stability

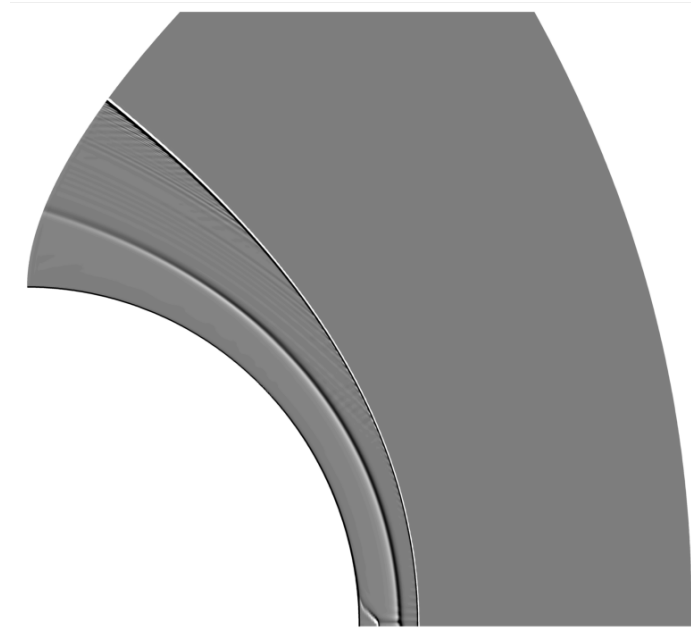
**Table 12:** Cases simulated for the Ruegg and Dorsey experiments are listed. All conditions are at 300 K with a spherical diameter of 20 mm

Case ID	Mach	p (atm)	Stability Regime
RD-1	5.0	0.1	Steady
RD-2	4.9	0.25	Regular, Unsteady
RD-3	4.8	0.5	Large Disturbance, Unsteady

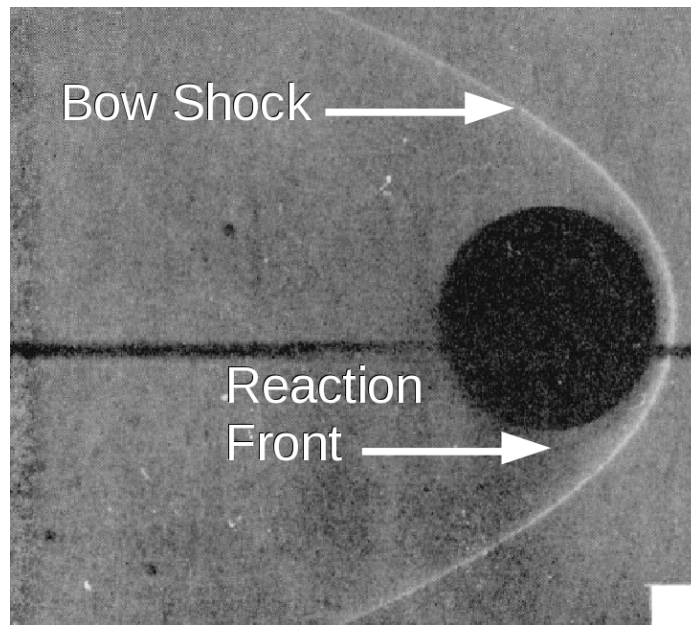
regimes for various combinations of Mach number and ambient pressure. They linked the relative standoff distance between the shock and reaction front to ignition delay time and made estimates of that time quantity for each experimental case. Both qualitative and quantitative comparisons can be made between VULCAN and experiment. First, qualitative comparison between the simulated reacting flowfield and experimental shadowgraphs can be made to ensure the same stability regime is being reproduced at the same conditions. Second, quantitative comparison can be made between the computed reaction front and shock standoff distances and those determined from experimental Schlieren imagery.

Qualitative comparisons of VULCAN results were made against experimental imagery. Conditions were chosen from Table 12 in order to reproduce the three major regimes of stability observed in experiment. Figure 75 shows the VULCAN density solution of case RD-1 compared to the Schlieren image captured at the same experimental conditions. This case demonstrates steady behavior of both the reaction front and the bow shock. Such a case is characterized by smooth reaction and shock fronts with no direct interaction between either except for the temperature being raised behind the shock such that chemical induction may occur. Qualitatively the numerical results matched the experimental results as the Schlieren image also indicated stable reaction and shock fronts.

The regular, unsteady behavior characteristic of case RD-2 is observed in Figure 76. Here the shock and reaction fronts exhibited periodic motion normal to the



(a)



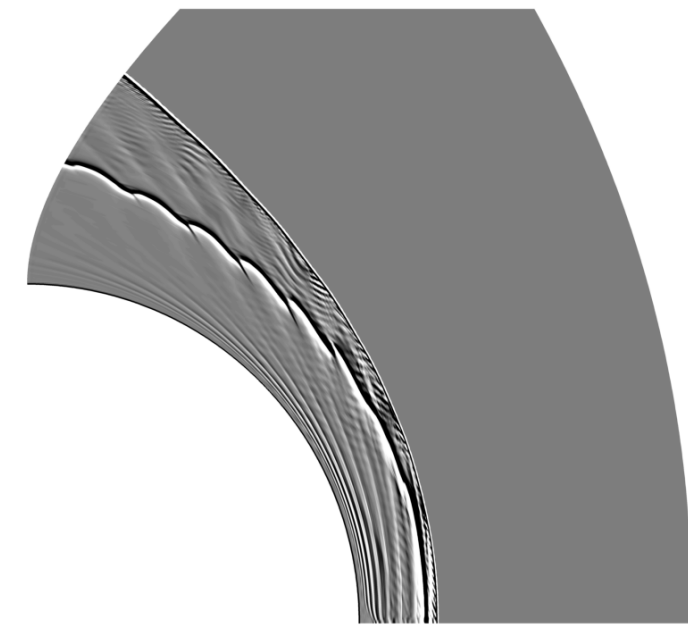
(b)

**Figure 75:** (a) Numerical shadowgraph of a Mach 5, 20 mm spherically blunted projectile fired into 0.1 atm quiescent H<sub>2</sub>-Air is shown and compared to the (b) experimental shadowgraph [96].

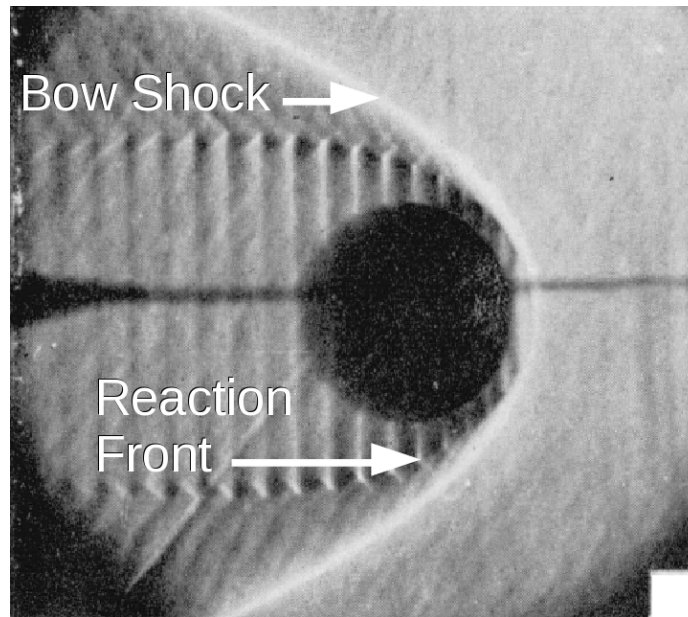
surface of the nose of the projectile with the distortions then being convected downstream. The greatest disturbance was observed in the reaction front. The density flowfield shows all of the salient features which encompass the mechanism of stability including contact discontinuities connecting each corrugation to the bow shock. This mechanism is discussed in more detail in Chapter 5.

The final regime of stability, the large disturbance regime, is reproduced in case RD-3 as shown in Figure 77. The experimental results at the same conditions show that a large amplitude disturbance was present on the reaction front. Numerical results also show this behavior, which was due to a deflagration-to-detonation transition (DDT) that caused the reaction front to advance upstream in a superdetonation and interact directly with the shock front. It is difficult to discern other details from the Schlieren image, but qualitatively both flowfields have the same large amplitude behavior with respect to the reaction front. Therefore there is qualitative agreement between the numerical simulation and experiment, lending confidence that VULCAN is able to simulate the salient physics of this regime, in this case the presence of DDT.

Attention is now given to a quantitative comparison of VULCAN's predictive capability with results from the experiments. For each combination of projectile Mach number and ambient pressure, Ruegg and Dorsey noted the shock and reacting front standoff distances. The data are shown in Figures 78 through 80 and present the experimental and simulated standoff distances (normalized with respect to projectile radius) for the three cases presented up to this point. Experimental trendlines are also indicated. Some experimental values lying far from the trendline are actually from a separate experiment from the Ruegg and Dorsey experiments that used a different method of visualization. Therefore, the trendlines ignore the effect of these outlier cases. The extracted standoff distances from the simulated cases lie comfortably within the experimental scatter and near the fitted trendline. This shows that VULCAN is accurately predicting the quantitative shock and reaction front standoff

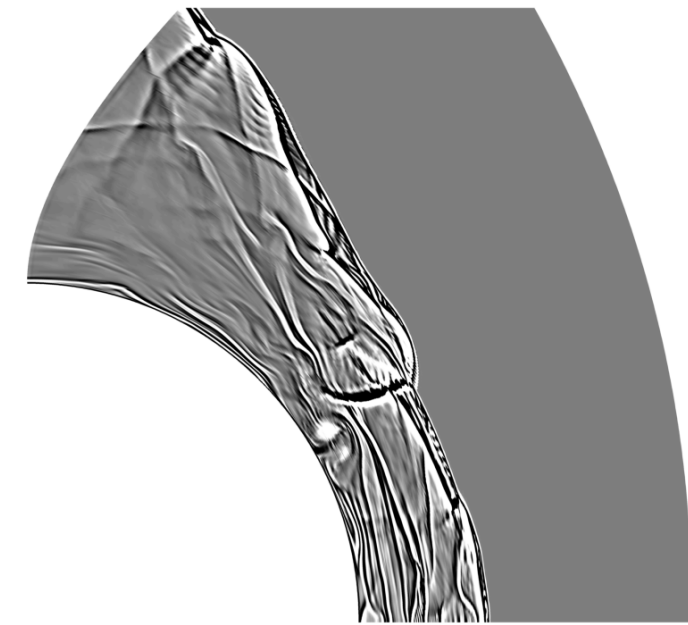


(a)

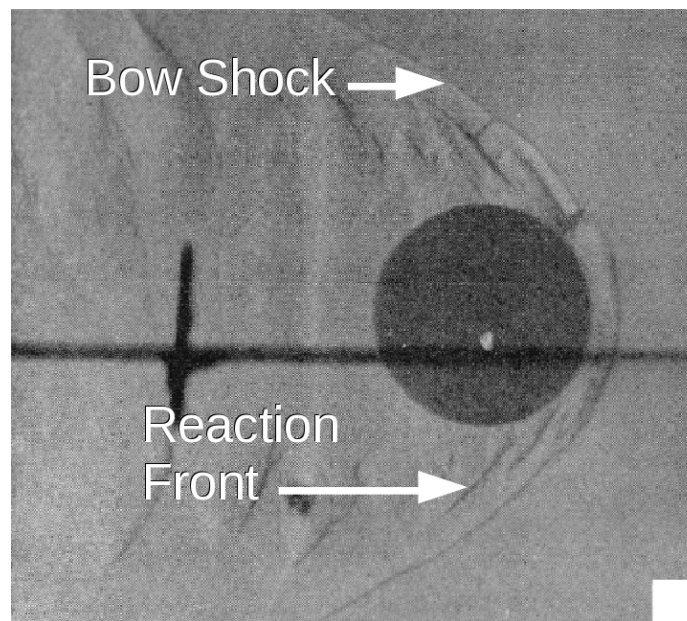


(b)

**Figure 76:** (a) Numerical shadowgraph of a Mach 4.9, 20 mm spherically blunted projectile fired into 0.25 atm quiescent H<sub>2</sub>-Air is shown and compared to the (a) experimental shadowgraph [96].



(a)



(b)

**Figure 77:** (a) Numerical shadowgraph solution of a Mach 4.8, 20 mm spherically blunted projectile fired into 0.5 atm quiescent H<sub>2</sub>-Air is shown and compared to the (b) experimental shadowgraph [96].

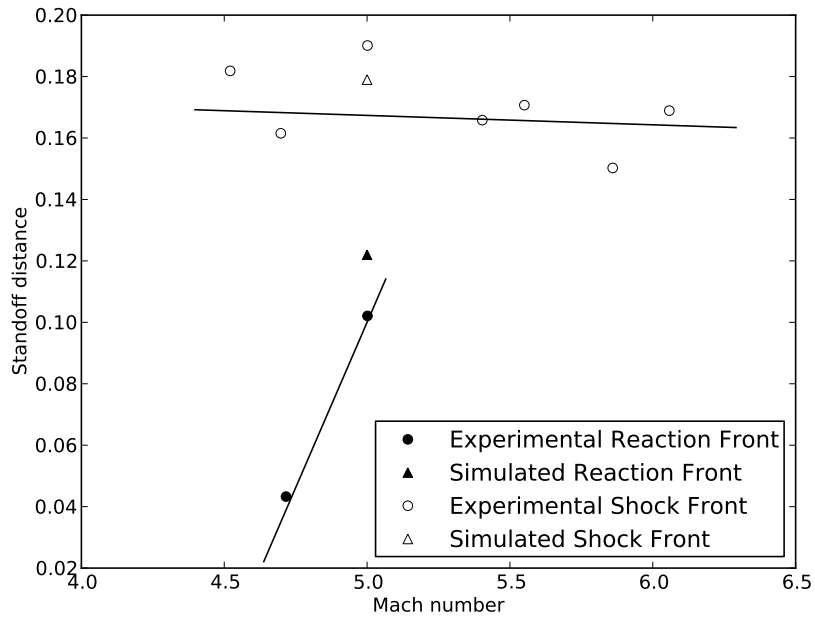


**Figure 78:** A comparison is shown between shock and reaction front standoff distances for experiment and the present simulation at 0.1 atm.

distances.

The final validation question relates to the ability of VULCAN to predict the reaction front frequency for a regular, unsteady regime case. If the reaction front is positioned far enough away from the projectile nose, the periodic reaction front behavior can be considered to be inviscid in nature, with the induction time between the shock and reaction front being the dominant parameter of interest. Hartmuth F. Lehr conducted early experiments [10] of reaction front frequency ahead of 15 mm diameter projectiles fired into 0.421 atm, 292 K, quiescent hydrogen-air.

The frequency results presented herein used the same computational grid and models used in the Ruegg and Dorsey simulations. The only differences are the ambient conditions and projectile diameter. The solution was considered to be converged whenever the transients passed from the system, leaving only the physical, periodic behaviors. The converged Mach 4.47 flowfield in Figure 81 shows a numerical shadowgraph with both the reaction and shock fronts clearly visible. The reaction front

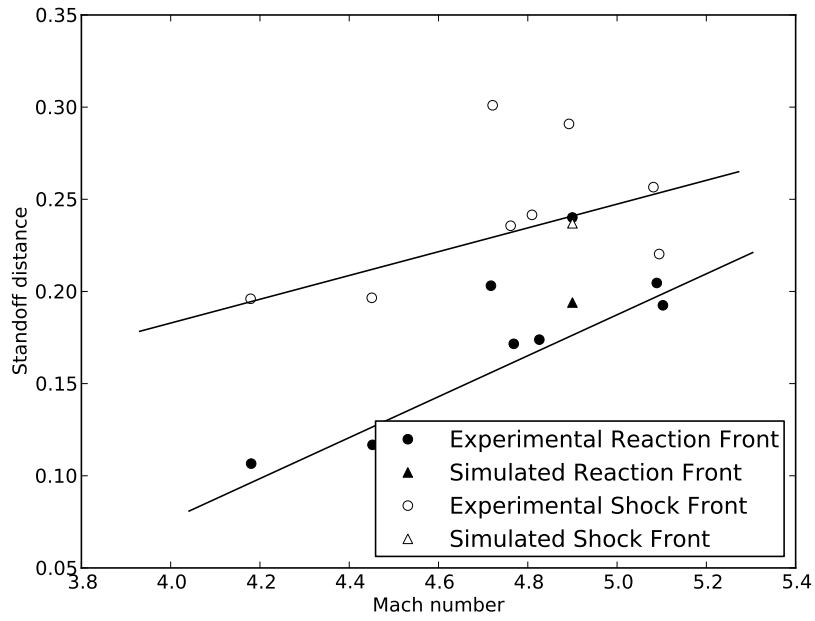


**Figure 79:** A comparison is shown between shock and reaction front standoff distances for experiment and the present simulation at 0.25 atm.

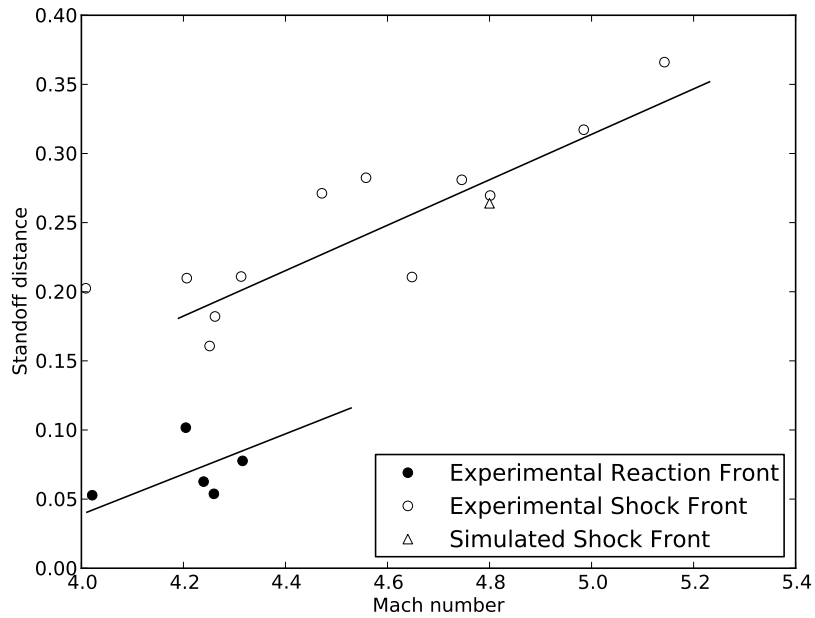


**Figure 80:** A comparison is shown between shock and reaction front standoff distances for experiment and the present simulation at 0.5 atm.

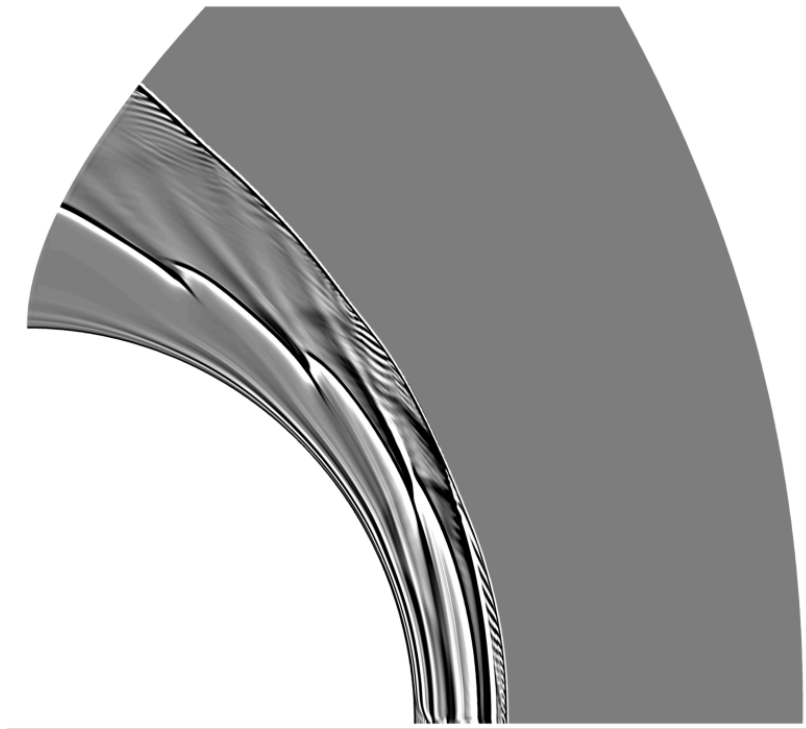


**Figure 81:** Numerical shadowgraph for the Mach 4.47 projectile case with stoichiometric H<sub>2</sub>-air at 0.421 atm and 292 K ambient conditions.

shows a corrugated shape indicative of the regular, unsteady regime.

Further interrogation of the flowfield was required in order to obtain the reaction front frequency. Lehr calculated his reaction front frequencies by simply measuring the spaces between corrugations in the wake of the projectile and combining that with an estimate of post-shock velocity. The current methodology simply interrogated the stagnation streamline at defined time intervals, a density plot of which is shown in Figure 82. It is observed that the regular regime behavior closely matches the model shown in Figure 122.

Once the stagnation streamline distance versus time plots were obtained, it was a relatively straightforward process to obtain reaction front frequencies. The process was to take a time-varying slice at a chosen value of  $n$  and then compute a discrete Fourier transform to obtain the frequencies present at this slice. Any arbitrary location can be chosen behind the reaction front, and in this case it was chosen to take

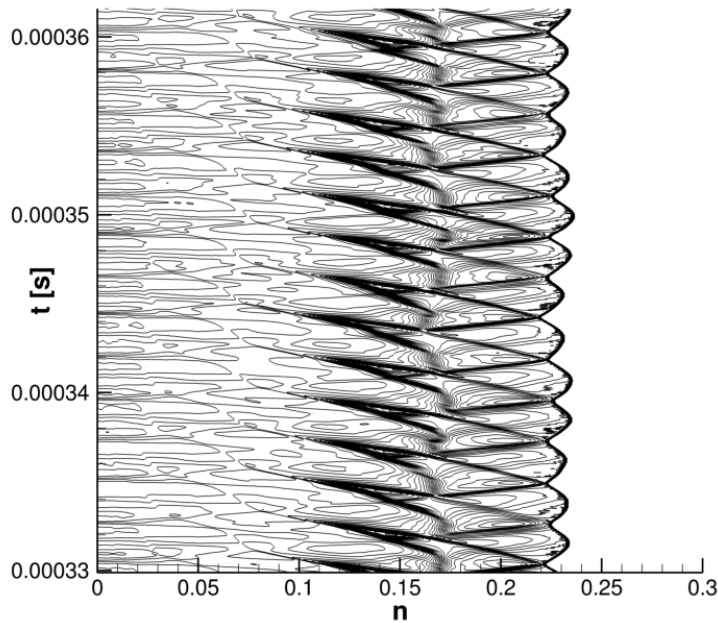


**Figure 82:** Density contours on the stagnation streamline for the Mach 4.47 case are presented as a function of distance from the projectile nose and time.

the slice at the wall. The time-varying water mass fraction at the wall for the Mach 4.47 case is shown in Figure 83. Note that in addition to the high frequency, high amplitude behavior there was also a low frequency, low amplitude behavior superimposed on the trend. This was a physical behavior as this case resides in what is referred to as the Envelope Regime [97], where two frequencies are present in the flow. The low frequency behavior is a gradual advance and retreat of the reaction front as a function of time and would not be visible on a Schlieren image as it does not manifest itself by a density change as with the high frequency behavior.

A discrete Fourier transform of the Mach 4.47 data shown in Figure 83 with a rectangular windowing function is plotted in Figure 84. There is a low-frequency peak at 87 kHz and a high frequency peak at 434 kHz. Note that there is some variance to these peaks because of uncertainty due to spectral leakage. At the same condition, Lehr computed a reaction front frequency of 425 kHz, resulting in a 2.1% relative

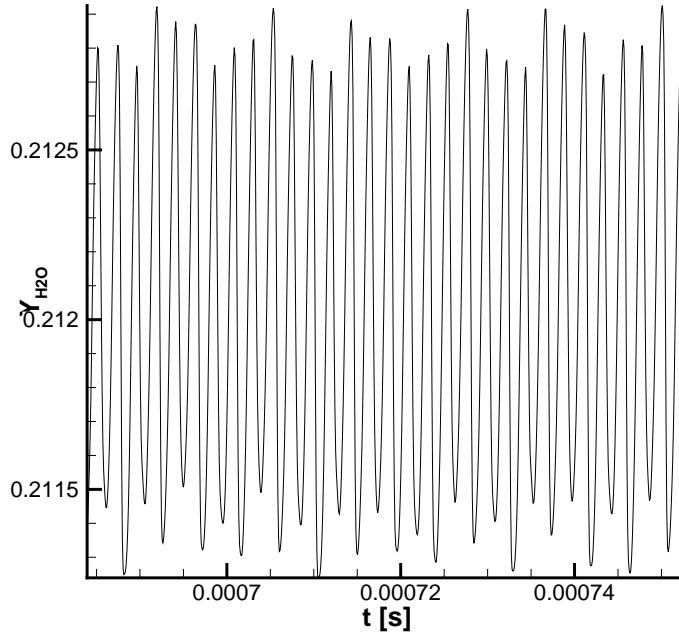


**Figure 83:** Water mass fraction as a function of time at the projectile wall for the Mach 4.47 case.

error between the numerical simulation and experiment. A lower frequency is not reported by Lehr, but numerical work by Myles Sussman [98] reports a value of 74 kHz, resulting in an 8% relative error with respect to the mean.

It has been shown that VULCAN is able to accurately predict the characteristics of time varying, chemically reacting flow fields. The selection of premixed, shock-induced combustion as a method of validation was a good one because the problem contains many different mechanisms against which to evaluate a code. First, depending on the regime studied, the reaction front varies with time with a prescribed frequency. The ability of the code to capture this behavior gives credibility in its ability to properly simulate the physical dynamics occurring in the flow field. Second, the reaction front location and frequency are strongly dependent on the ignition time of the fuel-air mixture behind the shock wave. Neither can be accurately determined without a proper handling of the chemistry and careful selection of the chemical

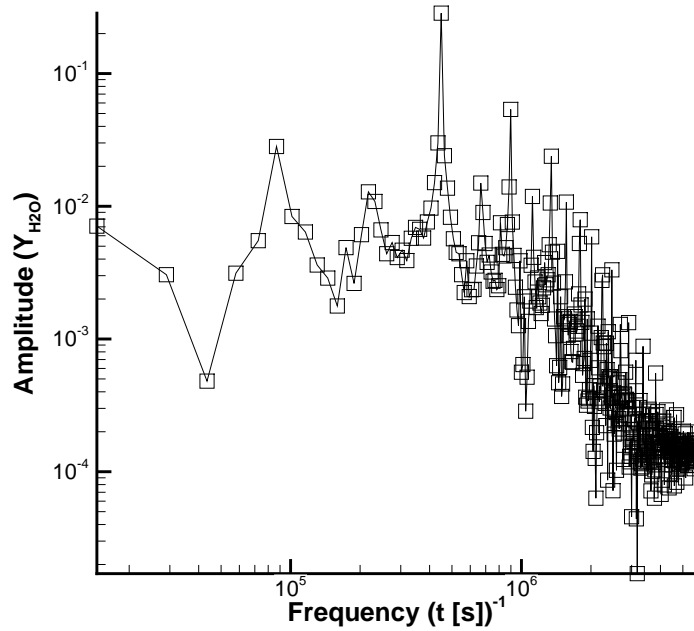


**Figure 84:** The discrete Fourier transform taken of the wall water mass fraction for the Mach 4.47 case.

model. Because the VULCAN code was able to predict the regimes of stability, the shock and reaction front standoff distances, and the reaction front frequencies as compared to experiment, it is concluded that VULCAN and the Jachimowski reduced chemical model are valid for the regimes of interest studied in this dissertation with the assumption that the methods are valid and extrapolate to higher Mach numbers.

## ***3.2 Flow Simulation and Metrics of Performance***

### **3.2.1 Flow Conditions and Computational Domain**

Unless otherwise indicated, the flow conditions were the same as those used in the mixing study of Chapter 2. For the initial autoignition studies, the same grid topology was used as those used in the mixing study. Transpiration cooling cases used the same grid topology as the uncooled geometry with the change being that transpiration was applied as a boundary condition. This also holds true for angled film cooling. For

axial film cooling, a backward-facing step was placed at the wall at the cooling location with the wall-normal grid spacing held constant and equal to the grid spacing at the wall without the backward facing step.

### 3.2.2 Measurement of Oxygen Burning

In this study combustion efficiency and the change of oxygen burned in the sampling region were the means of quantitatively gauging the effectiveness of any given autoignition mitigation strategy. Combustion efficiency is a numerical value between zero (no combustion) and one (complete combustion where all reactants not in excess are consumed) that is typically employed in a fashion where higher values occurring sooner are better. Because the current study was situated on the vehicle forebody, however, it was desired to delay combustion as long as possible, thereby making combustion efficiency a metric to be minimized. There are many ways to define combustion efficiency depending on the particular application. Typical measures of combustion efficiency include measures of

1. Water produced in the domain of interest compared to the reactant not in excess.
2. Consumed reactant mass not in excess compared to the initial reactant mass.
3. Current temperature compared to the adiabatic flame temperature.

In high speed, airbreathing propulsion systems combustion typically occurs in an enclosed space (e.g. combustion chamber and/or nozzle). Because of this, combustion efficiency metrics generally do not account for spillage of reactants such as that shown notionally in Figure 85. Therefore, a new combustion efficiency metric that takes reactant spillage into account will now be proposed.

For the performance sampling region notionally shown in Figure 85, reactants entering the system are spilled in some proportion relative to the inflow. Because

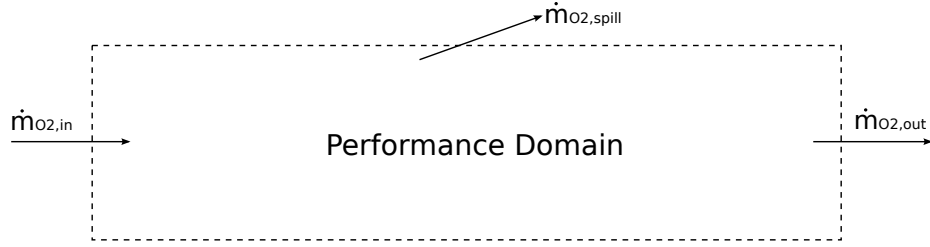


**Figure 85:** Top-level schematic of performance sampling region that spills oxygen (for a system where fuel is in excess).

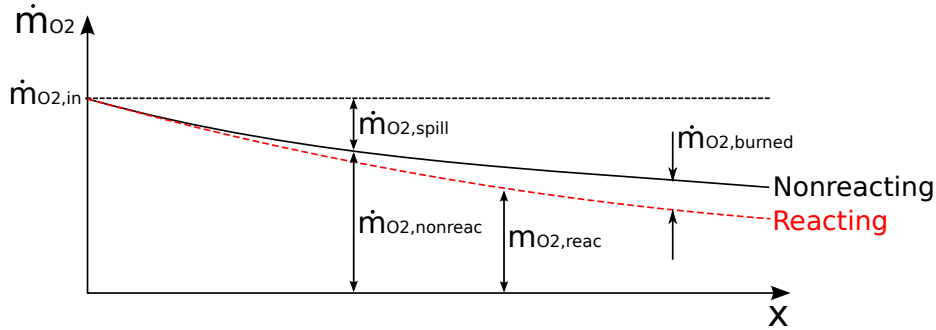


**Figure 86:** Notional oxygen mass flow rates as a function of distance along sampling region with spilled and burned quantities indicated.

hydrogen is typically in excess for the flows studied here, oxygen was the tracked reactant. Figure 86 shows a notional plot of oxygen mass flow as a function of distance along the body for both a reacting and nonreacting simulation. The two main quantities of interest for computing combustion efficiency, nonreacting and burned mass flow rates, are indicated in the figure. Note that in order to obtain the burned oxygen mass flow rate, both a nonreacting and reacting simulation of the same flow are required.

Once the nonreacting and reacting mass flow rates are obtained for a particular case, it is relatively straightforward to define a combustion efficiency parameter that satisfies the requirements that it be equal to zero when no burning has occurred at a particular location and equal to unity when all available oxygen at a particular flow station has been consumed. The combustion efficiency metric that takes into account

reactant spillage is defined as

$$\eta_c = \frac{\dot{m}_{O_2,burned}}{\dot{m}_{O_2,nonreact}} = 1 - \frac{\dot{m}_{O_2,react}}{\dot{m}_{O_2,nonreact}} \quad (8)$$

To obtain the combustion efficiency at a particular station, the reactant mass flow rate for the nonreacting and reacting simulation must be obtained. For codes that do not output these quantities automatically, this process is the summation of cellular mass flow rates multiplied by the mass fraction of the reactant of interest in that cell.

For comparing different geometries, a more general metric was used, the change in oxygen burned in the sampling region. Different cooling methods and secondary injection conditions will change the spillage properties of a particular geometry being analyzed. Therefore, spillage must be taken into effect directly in the metric measuring oxygen burned. This equation, using Figure 85 as a reference, is

$$\dot{m}_{O_2,burned} = \dot{m}_{O_2,in} - (\dot{m}_{O_2,spill} + \dot{m}_{O_2,out}) \quad (9)$$

The change in oxygen burned can then be computed by evaluating this expression separately for the baseline reacting geometry and for the cooled geometry being investigated, subtracting the former from the latter.

### ***3.3 Baseline Simulations of Autoignition***

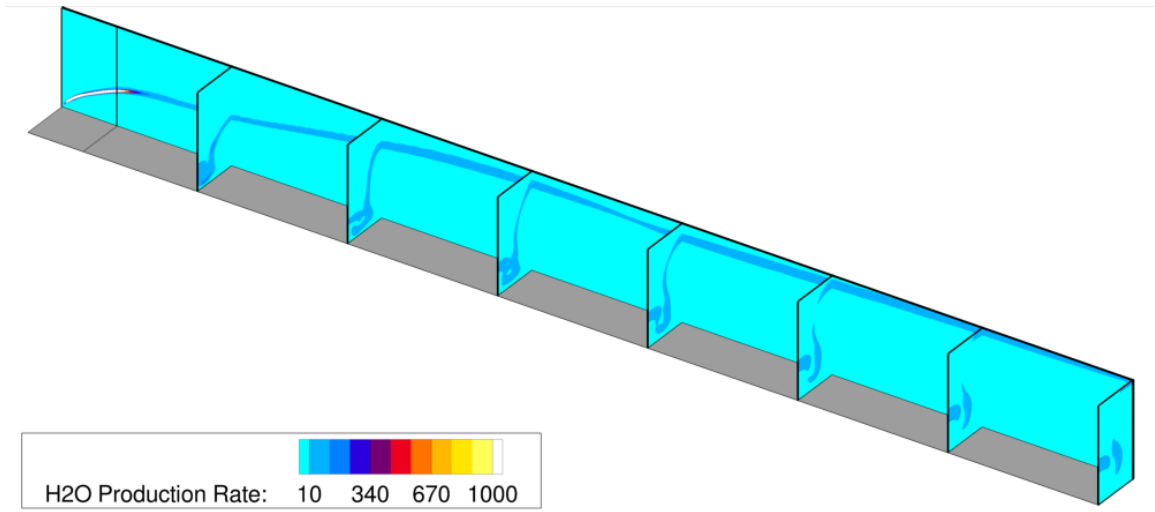
For the present results, the geometries shown in Figures 37, 38, and 39 were simulated at the conditions in Table 3. The simulations were allowed to first converge without chemistry, at which point chemistry was activated and the simulation was allowed to reach convergence again. Upon convergence, chemical ignition is tracked by the water production rate in units of kg/m<sup>3</sup>/s. Because the fuel is pure hydrogen, the production of water was also tracked in the flow.

The converged solution of the stinger flush-wall injector showed the greatest amount of chemical reaction of the three injector concepts tested. Figure 87 shows

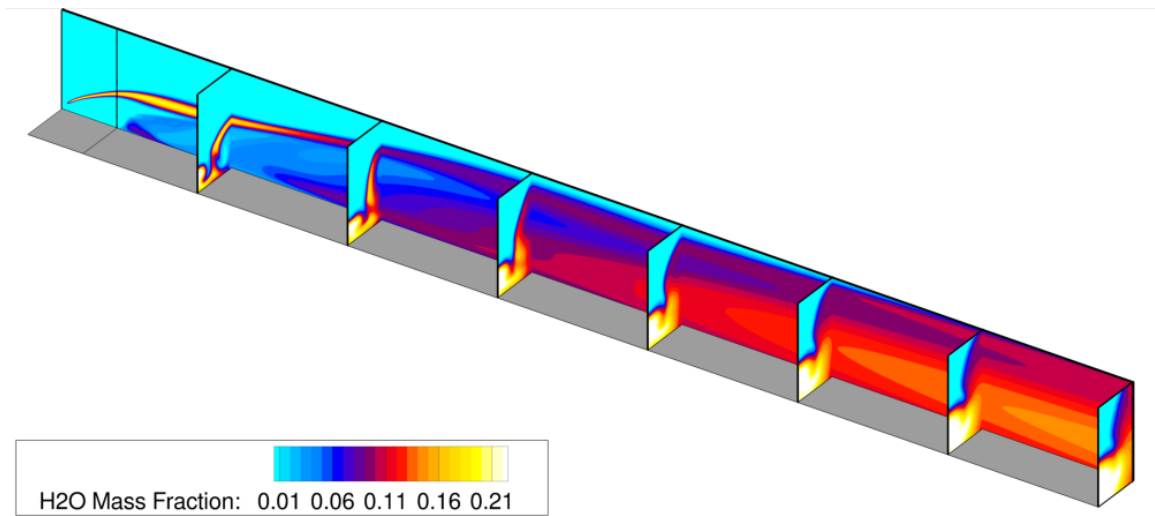
centerline and cross-stream slices of water production and water mass fraction. The water production are good indications of where ignition begins. Two primary ignition points are evident: behind the bow shock of the injector plume and laterally on the centerline between neighboring injectors. The ignition region behind the bow shock appears to contribute the most to the combustion occurring in the flow by wrapping the entire fuel plume in shock-heated air and easily causing ignition as hydrogen diffuses out of the fuel rich plume. This shock-layer burning has been observed in OH-PLIF experimentation by Ben-Yakar, *et al.* [99] for circular jet injection into a hypervelocity, Mach 13 flight enthalpy flow. The stinger injector geometry, however, lacks the upstream recirculation burning observed with circular injection due to the sharp leading edge of the injector eliminating such a recirculation zone. It is unclear how a shock layer ignition zone can be mitigated using a wall cooling strategy because this ignition zone is caused by high temperatures behind the bow shock, not high temperatures in the boundary layer.

The secondary region of ignition on the symmetry plane between neighboring injectors was due to high vorticity that entrained fuel and mixed it with the hot boundary layer near the symmetry plane. This created a large, high-temperature region in region of the flow that also was a secondary location for autoignition. Such an autoignition region may be mitigated by wall transpiration in the locality of the symmetry plane.

A plot of combustion efficiency as a function of distance behind the stinger injector is shown in Figure 88. In this plot the amount of combustion throughout the flowfield was quantified and accounts for spillage in the computation. It is observed that by the time the outflow plane was reached, the combustion efficiency achieved a value of 45%, indicating extensive combustion and fuel depletion. While this may be a good trend for internal combustion, it is bad for forebody injection. Because shock-heating of the air plays an important part in the trend, film cooling may be an



(a)



(b)

**Figure 87:** Stinger injector contours of (a) water production and (b) water mass fraction in the flow domain of interest. Flow is from the upper left to the lower right.

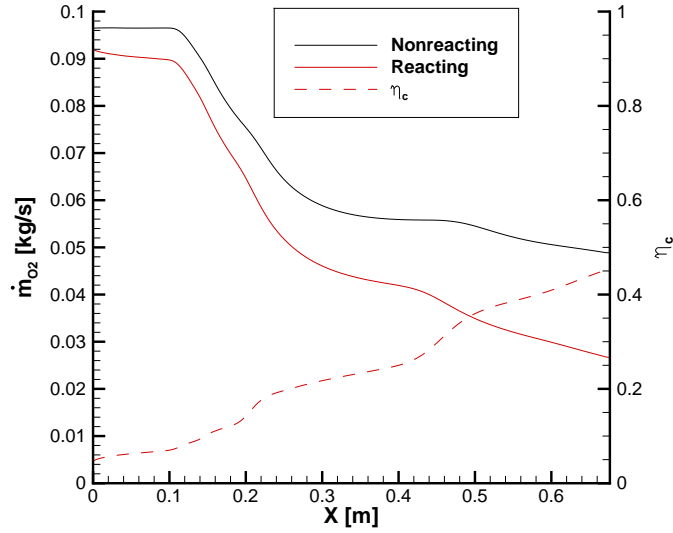


**Figure 88:** Mass flow rates of oxygen and combustion efficiency downstream of stinger without autoignition mitigation.

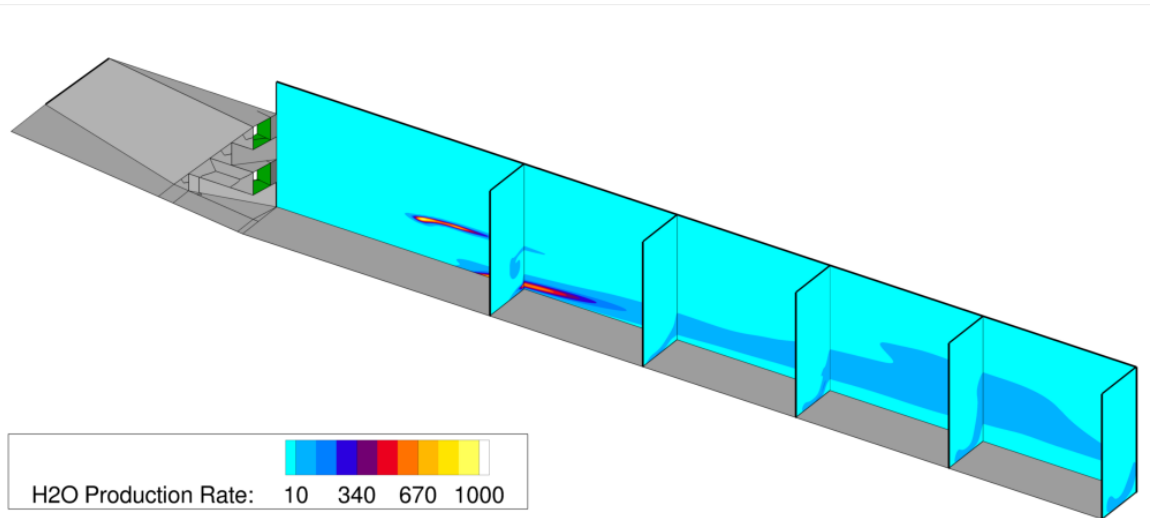
infeasible approach for autoignition mitigation. The high losses experienced by the transverse injector in a previous study [100] combined with the present autoignition characteristics disqualifies the transverse injector as a feasible method for forebody injection.

The strut injector experienced a moderate amount of autoignition in the wake of the concept. Two distinct zones of ignition are observed, one away from the wall in the fuel plume vortex and another at the wall, both shown in Figure 89. Shock interactions behind the strut cause subsequent ignition which is extinguished relatively rapidly as the products are folded into the cooler fuel plume. Downstream of the first ignition point, a second ignition occurred at the wall as the fuel plume entered into the hot boundary layer region. Downstream of the second ignition point combustion is sustained near the wall, evident by the continuous production of OH at the wall. While the ignition region at the wall may be addressed by wall cooling, the small ignition region in the fuel plume may require modification to the injector geometry in order for complete autoignition mitigation to occur. The extent of the

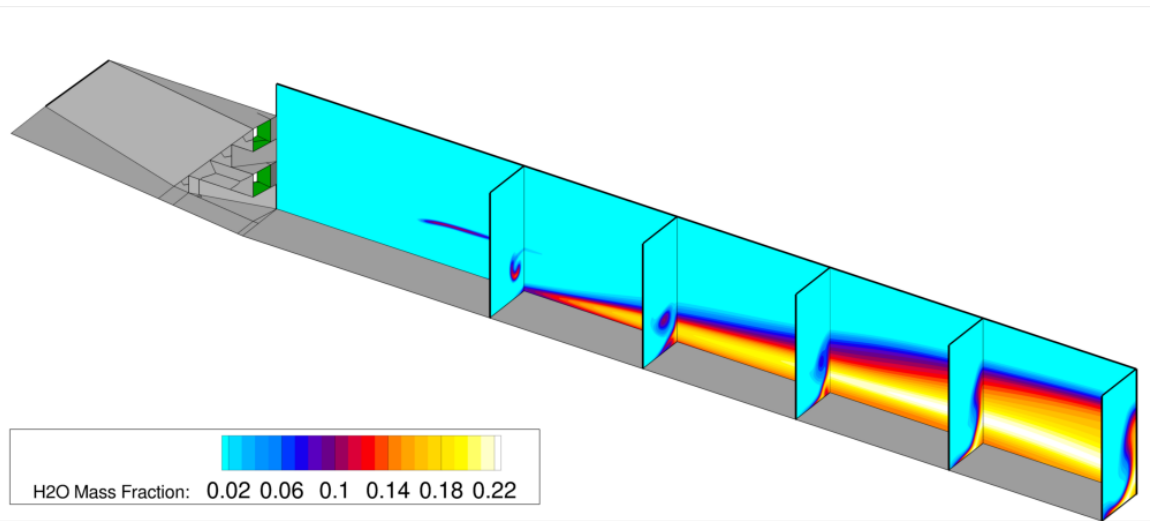
combustion occurring for the strut concept is shown quantitatively in Figure 90. Much lower levels of combustion are evident versus the stinger concept with combustion efficiency approaching only around 12%.

The unswept ramp injector with wedge feature experiences a single region of autoignition downstream of the injector at the wall and near the outflow plane. Contours of water production rate and water mass fraction are shown in Figure 91. Here it is again seen that ignition occurred near a region where the fuel entered the hot boundary layer near the flow domain exit. Because this is the only zone of autoignition in the flow and it is near the wall, wall cooling is a strong candidate for mitigating ignition in this area. Figure 92 quantitatively confirms that no substantial combustion is occurring in the flow, with the combustion efficiency trend mostly reflecting numerical errors.

Through investigation of autoignition for the stinger, strut, and unswept ramp injector with base wedge, the strut injector distinguishes itself as an attractive candidate for further study in autoignition mitigation. The stinger injector is not an attractive candidate for further study simply due to the large extent of combustion present, its difficulty for mitigation, and other losses incurred even without reaction present. Similarly, the ramp injector is not an attractive candidate to study due to its general redundancy with the strut case. It, like the strut, has autoignition occur once the fuel plume enters into the hot boundary layer. Its main distinction is that this effect occurs farther downstream than the strut injector. It can be assumed that strategies that are successful for the strut injector will also be successful for the ramp injector. Therefore, the study of autoignition mitigation strategies will concentrate on the strut injector from this point onward.



(a)



(b)

**Figure 89:** Strut injector contours of (a) water production and (b) water mass fraction in the flow domain of interest. Flow is from the upper left to the lower right.

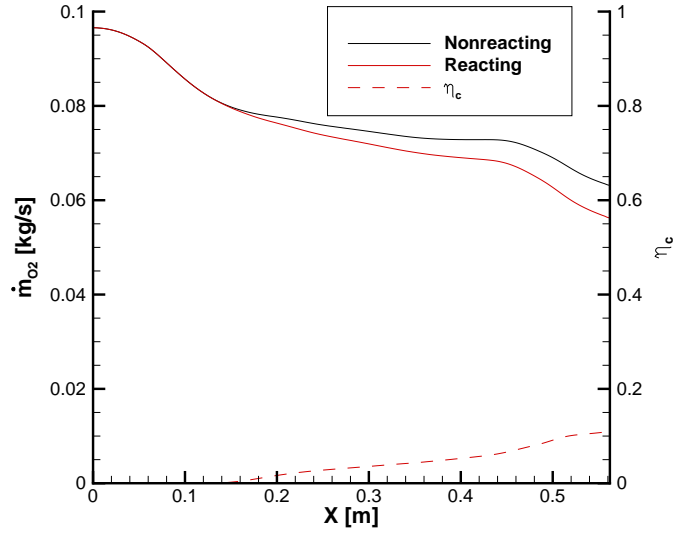


**Figure 90:** Mass flow rates of oxygen and combustion efficiency downstream of strut without autoignition mitigation.

### 3.4 Autoignition Mitigation Strategies for Forebody Flows

#### 3.4.1 Overview of Wall Cooling Strategies

Wall cooling using both wall transpiration and film cooling were evaluated in this study to ascertain their performance in mitigating forebody autoignition. In both cases a secondary injectant was introduced into the main flow at the wall in order to lower the temperatures encountered in the boundary layer below those that would cause autoignition to occur. The physical modeling in this study makes no distinction between the transpiration and distributed film cooling strategies, with the main distinctions arising due to material, structure, and subsystem design. Both strategies will henceforth be referred collectively as “transpiration cooling.” Transpiration is shown notionally in Figure 68 and film cooling is shown notionally in Figure 69.

Both transpiration and film cooling have benefits and detriments beyond the system-level metrics shown in the table. For example, transpiration is typically a good strategy for providing localized cooling at the wall throughout the region transpiring coolant. Beyond the transpiration patch, however, cooling capacity drops

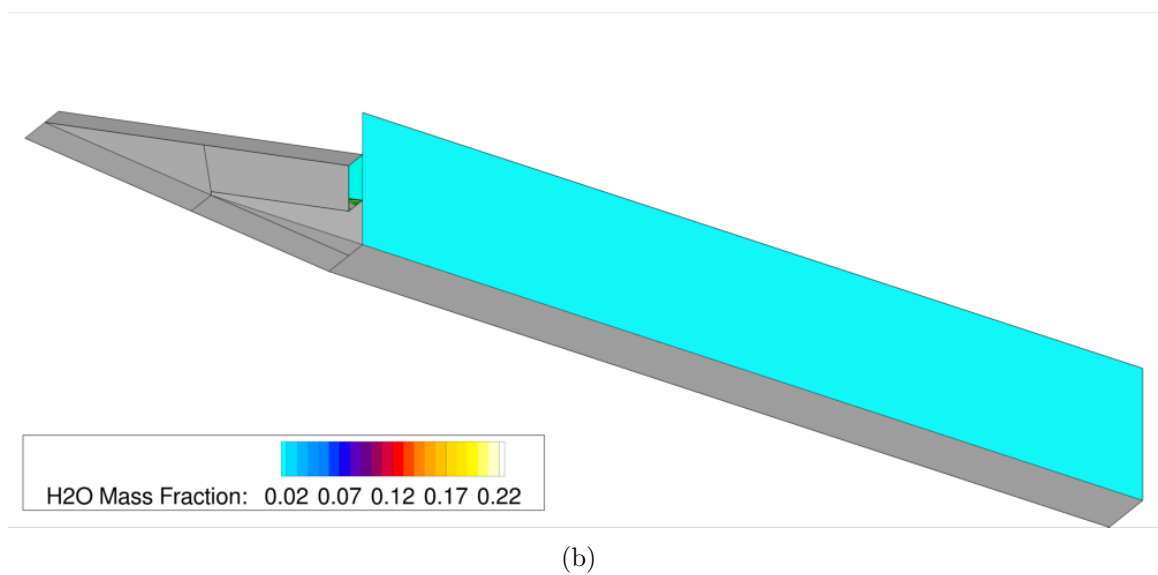
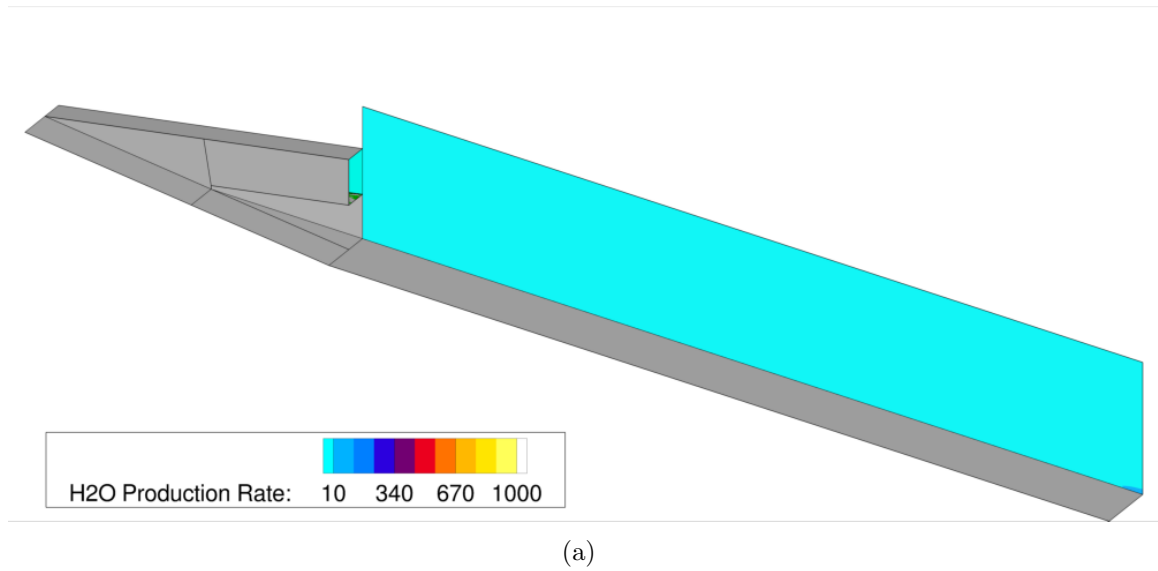


**Figure 91:** Unswept ramp injector contours of (a) water production and (b) water mass fraction in the flow domain of interest. Flow is from the upper left to the lower right.

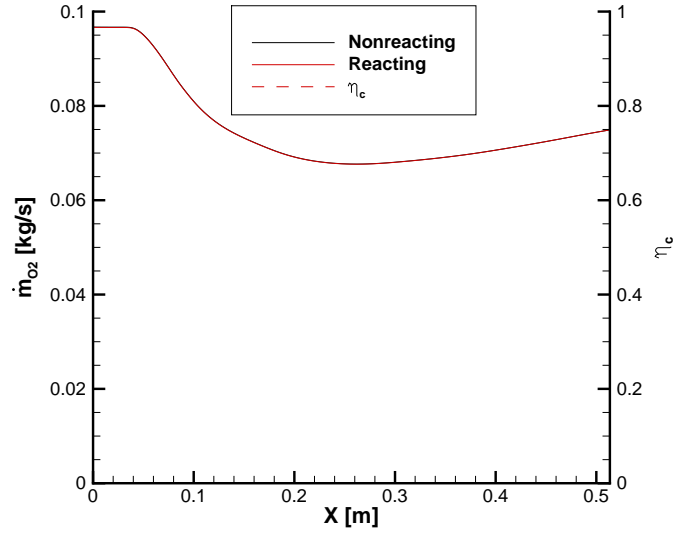


**Figure 92:** Mass flow rates of oxygen and combustion efficiency downstream of strut without autoignition mitigation.

off quickly. Wall transpiration also typically provides good cooling effectiveness while also minimizing disturbance to the main flow [28, 78]. Film cooling, which injects fuel at a single location in order to cool the wall downstream, typically requires more mass flow from the injector to achieve the same amount of wall cooling due to decreased cooling capacity as the injectant flows downstream.

A blowing parameter is defined in order to control the amount of secondary gas flowing into the wall boundary layer. This parameter is a function of the mass flow rate both through the primary injector and through the secondary injector and is defined as

$$B = \frac{\dot{m}_{cool}}{\dot{m}_{cool} + \dot{m}_{inj}} \quad (10)$$

where  $\dot{m}_{cool}$  is the mass flow rate issuing from the film or transpiration cooler and  $\dot{m}_{inj}$  is the mass flow rate issuing from the injector.

The secondary gases in this study were chosen to be hydrogen, helium, and nitrogen. Hydrogen was considered because it is the same gas as the fuel and, therefore, would only require the system to provide a single fuel storage solution. It also has

a high heat capacity by mass, which will possibly provide for lower temperatures as the transpired gas mixes with the main flow. A detriment to using hydrogen is its chemical activity as it readily and rapidly burns.

Helium and nitrogen provide respectively low and high molecular weight alternatives to hydrogen as secondary gases. Their primary benefit compared to the use of hydrogen is that they are both inert at the temperatures of interest in the current study. Both have detriments compared to hydrogen in that they would require separate storage and cryogenic cooling requirements from the fueling system. In addition, nitrogen has poor heat capacity by mass compared to hydrogen, although it is an inexpensive and prevalent. Helium can provide a comparable heat capacity by mass to hydrogen, although it is more expensive and less available than nitrogen.

Other examples of coolant candidates include water, ammonia ( $\text{NH}_3$ ), and methane ( $\text{CH}_4$ ). Water was initially excluded due to risk of oxidation of cooling passages, ammonia due to the increased cooling mass required, and methane due to the possible presence of graphite coking in the potentially hot cooling passages [101].

The selection of the blowing parameter value has a direct impact on the global equivalence ratio of the system, with higher blowing parameters necessarily increasing the global equivalence ratio and mass flow rate of hydrogen demanded on the system. Because secondary gas is intended to inhibit autoignition, regardless of whether the selected gas may burn or not, any increase in fuel mass flow rate can be construed to be parasitic on the overall system performance. Figure 93 shows the effect on the global equivalence ratio by increasing the blowing parameter as given by the equation

$$\phi_G = \frac{\dot{m}_{inj}}{\dot{m}_{air}} \frac{OF}{(1-B)Y_{OX}} \quad (11)$$

where OF is the oxidizer-to-fuel mass ratio and  $Y_{OX}$  is the stoichiometric mass fraction of the oxidizer. This shows that, for a general fuel-air system, as blowing parameter is increased, the total global equivalence ratio supplied by the injection and cooling systems increases.

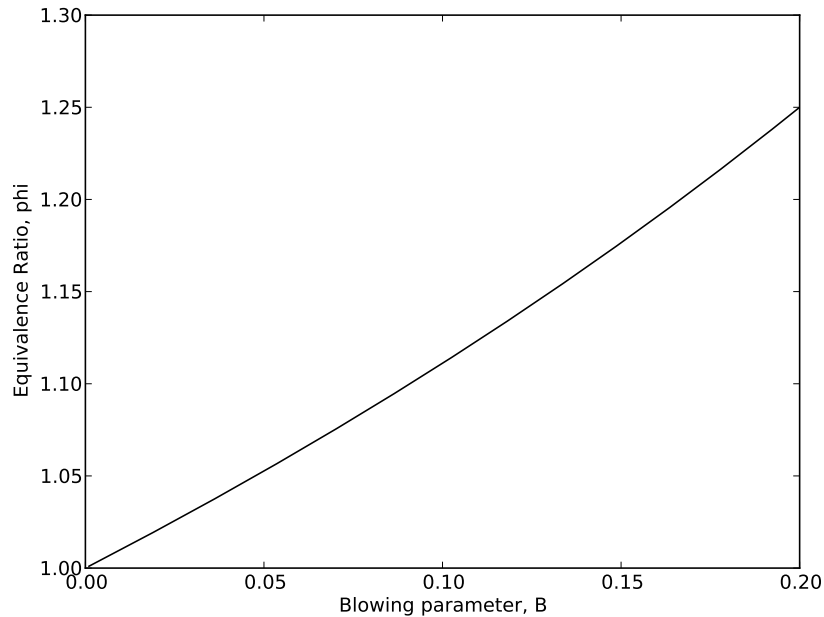


**Figure 93:** Global equivalence ratio as a function of blowing parameter

Because the mass flow rate of fuel—coolant gas also being counted as fuel regardless of flammability—factors directly into the calculation of specific impulse, a system-level efficiency metric, the effect of blowing parameter on the change in this parameter can be assessed. Figure 94 shows the relative change in specific impulse on the choice of blowing parameter, assuming the thrust produced is unaffected. Here it is observed that low blowing parameters can have a rather drastic effect on the performance of a system using wall cooling. Therefore, the importance of using only the minimum amount of secondary gas is emphasized.

### 3.4.2 Wall Transpiration

Wall transpiration (i.e. blowing) of cold gas into the hydrogen/air main stream was chosen as one method for autoignition mitigation in this study. Transpiration has been used in the past for wall cooling in Mach 2-3 flows with flush-wall injection. While it is not the only way to provide cooling near the wall, transpiration has good wall cooling effectiveness while also minimizing the disturbance to the main flow.

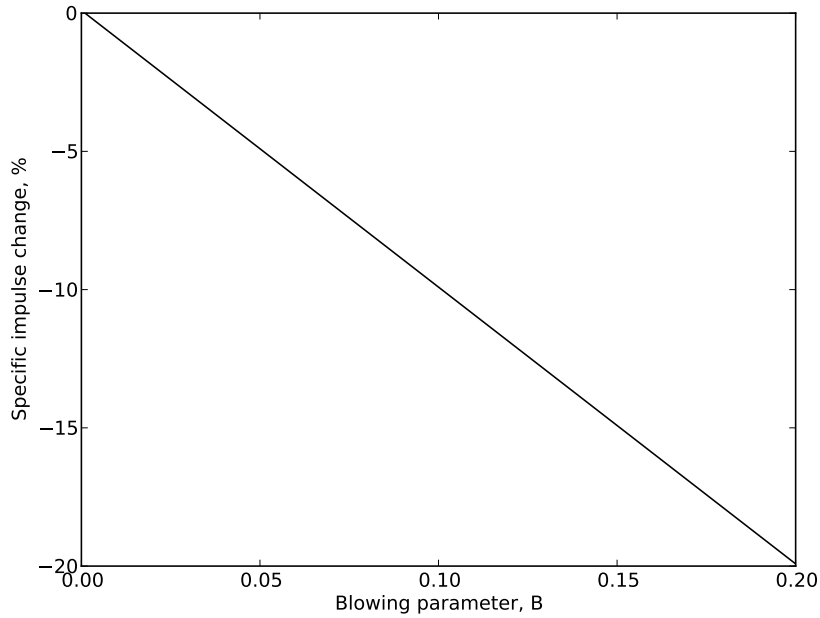


**Figure 94:** Relative change in specific impulse as a function of blowing parameter

For the sake of computational simplicity, fluid flow through transpiration injection ports was modeled using a representative bleed model rather than gridding and simulating distinct wall holes and a plenum. This allowed rapid evaluation of the effect of different porosities and mass flows without altering the grid topology. Note that the use of such a model is particularly attractive for blowing studies because of the insensitivity of the solution to the shear stress at the wall for this case [102]. The ability of VULCAN to accurately model this phenomenon has been studied by Baurle and Norris [103].

The transpiration conditions used in the study are given in Table 13 for the transpiration schematic shown in Figure 95. The transpiration model parameters in VULCAN are the mass flow through the surface, the total temperature of the fluid in the plenum, and the porosity of the wall. The porosity is defined as the ratio of the combined area of the transpiration holes in the wall to the total area of the transpiration wall. The porosity was estimated from past experiments by Byington *et al.* [28].

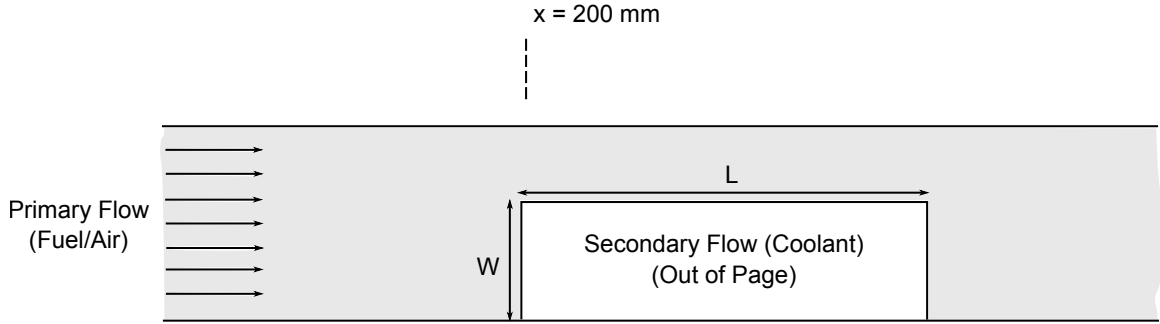


**Figure 95:** Schematic diagram of wall transpiration.

Therefore, the porosity for this study was set to be 2% in order to create the greatest possible plenum pressure. It is also the lower limit of validation for the transpiration model. The total temperature of the transpirant was set to be near the wall temperature. Besides the species and blowing parameter, the size of the transpiration patch was another variable for the current study.

**Table 13:** Transpiration array conditions

Blowing parameter ( $B$ )	5.0 - 20.0%
Wall porosity ( $P$ )	2.0%
Transpirant total temperature	500 K
Wall temperature	500 K
Species	H <sub>2</sub> , He, and N <sub>2</sub>

### 3.4.3 Film Cooling

In addition to transpiration, film cooling was another candidate method for autoignition mitigation. Film cooling is distinct from transpiration in that the injectant is supplied via a channel or row of injectors instead of through an array of perforations in the wall. Furthermore, if the flow is to be supersonic, a contoured nozzle would be present in the film cooling channels. While injection through a channel transverse to the main flow is possible, axial injection is preferable due to the desire to keep the fluid near the wall. The use of tangential injection also reaps minor thrust benefits to the vehicle. Furthermore, when a low molecular weight gas like hydrogen is injected at the wall, reductions in skin friction may be achieved [104].

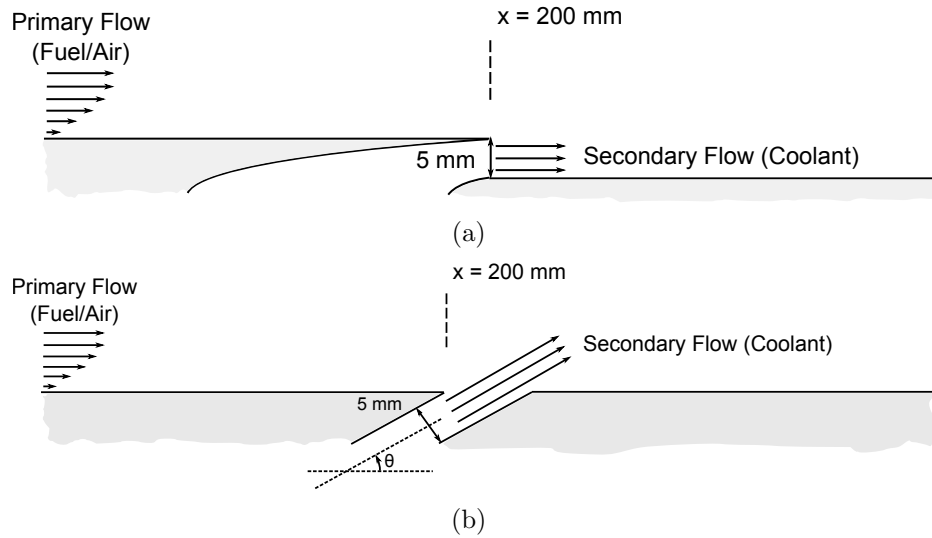


**Figure 96:** Schematic diagrams of film cooling via a slot for both (a) tangential and (b) angled injection.

The mass flow rate supplied to the film cooler, like the transpiration case, was parametrized in terms of the blowing parameter defined in Equation 10. Other parameters to be studied include the species injected and the exit temperature of the film cooling channel, summarized in Table 14 for the schematics shown in Figure 96.

**Table 14:** Film cooling conditions

Blowing parameter ( $B$ )	5.0 - 20.0%
Channel height	5 mm
Injection angle	$0^\circ$ , $10^\circ$ , and $45^\circ$
Exit temperature	100, 740 K
Species	$H_2$ , He, and $N_2$

While some film cooling concepts inject gas transverse to the flow, the current study was limited to concepts that contain a substantial tangentially-directed component. Three configurations will be tested: parallel injection,  $10^\circ$  injection, and  $45^\circ$  injection. Parallel injection is chosen to provide the least disturbance possible to the primary flow, while the  $10^\circ$  and  $45^\circ$  injection cases will both necessarily create a shock wave and some flow deflection. The reason for testing these angled film cooling concepts was to deflect the hot shear layer away from the wall and to see if such

**Table 15:** Coolant mass flow rates for each value of blowing parameter.

$B$ [%]	$\dot{m}_{fc}$ [kg/s]
20	0.003275
15	0.002312
10	0.001456
5	0.00069

benefits offset the creation of a shock wave and higher temperatures between the film cooling shock and the secondary flow.

### ***3.5 Simulation of Transpiration and Film Cooling***

#### **3.5.1 Simulation Matrix**

The performance evaluation of film cooling and transpiration was conducted in a systematic fashion to allow the best use of computational and research time. The strategies were parametrized in terms of species, blowing parameter, and nozzle exit temperature for film cooling and species, blowing parameter, and patch width for transpiration cooling. For the fuel mass flow rate utilized in the previous chapter, Table 15 shows the required film cooling or transpiration mass flow rate for values of blowing parameter ranging between 5 and 20%.

For evaluating film cooling cases, the systematic methodology for evaluating each concept consisted of first computing a pathfinding simulation at a particular combination of species and nozzle exit temperature with  $B = 20\%$ . This was a test case that showed if the particular combination of species and exit temperature were feasible (i.e. substantially reduces the presence of autoignition on the forebody). If a particular combination of species and exit temperature reduced autoignition substantially, the blowing parameter was gradually lowered to evaluate the effect of that parameter. Note that the mitigation of autoignition is not “all or none”—one can not hope to employ a strategy that will eliminate autoignition at all points downstream of the exit of the film cooler. This is because there will always be a distance downstream

**Table 16:** Simulation matrix for parallel film cooling cases with sonic injection. Checkmarks indicate cases that were run and x-marks indicate cases not run.

Species		H <sub>2</sub>				He				N <sub>2</sub>			
T <sub>e</sub> [K]	B [%]	20	15	10	5	20	15	10	5	20	15	10	5
100		✓	✓	✓	✓	✓	✓	✓	✓	✓	✓	✓	✓
740		✓	✓	✓	✓	✓	✓	✓	✓	✓	✓	✓	✓

**Table 17:** Simulation matrix for 10o film cooling cases with sonic injection. Checkmarks indicate cases that were run and x-marks indicate cases not run.

Species		H <sub>2</sub>				He				N <sub>2</sub>			
T <sub>e</sub> [K]	B [%]	20	15	10	5	20	15	10	5	20	15	10	5
100		✓	✓	✓	✓	✓	✓	✓	✓	✓	✓	✓	✓
740		✓	✓	✓	✓	✓	✓	✓	✓	✓	✓	✓	✓

where the primary and coolant streams have equilibrated and the boundary layer once again begins to increase in temperature. The best outcome is to delay the presence of ignition until the point where it is desired (i.e. the combustor entrance).

The film cooling cases tested for this study are shown in Tables 16 through 18, which cover the parallel, 10o, and 45o film cooling strategies. For each case the film cooling channel began at the  $x = 200$  mm station. The checkmarks on the tables show both the pathfinding cases (at  $B = 20\%$ ) and those additionally run cases to evaluate the effect of decreasing blowing parameter.

The transpiration cases tested for this study are shown in Table 19. Widths are percentages of the full width of the flowpath centered on the centerline and lengths are percentages of the length from the beginning of the transpiration patch at  $x = 200$  mm to the notional cowl closure location at  $x = 713$  mm. Similar to the film cooling cases, transpiration cases at high blowing levels were tested first in order to establish

**Table 18:** Simulation matrix for 45o film cooling cases with sonic injection. Checkmarks indicate cases that were run and x-marks indicate cases not run.

Species		H <sub>2</sub>				He				N <sub>2</sub>			
T <sub>e</sub> [K]	B [%]	20	15	10	5	20	15	10	5	20	15	10	5
100		✓	✗	✗	✗	✓	✓	✓	✓	✓	✗	✗	✗
740		✓	✗	✗	✗	✓	✓	✓	✓	✓	✗	✗	✗

**Table 19:** Simulation matrix for transpiration cooling cases with a porosity of 2%. Checkmarks indicate cases that were run and x-marks indicate cases not run.

Species		H <sub>2</sub>				He				N <sub>2</sub>			
W [%]	B [%]	20	15	10	5	20	15	10	5	20	15	10	5
	100	✓	✗	✗	✗	✓	✗	✗	✗	✓	✗	✗	✗
	50	✓	✗	✗	✗	✓	✗	✗	✗	✓	✗	✗	✗
	25	✓	✗	✗	✗	✓	✓	✓	✓	✓	✗	✗	✗
L [%]	B [%]	20	15	10	5	20	15	10	5	20	15	10	5
	50	✓	✗	✗	✗	✓	✓	✓	✓	✓	✗	✗	✗
	25	✓	✗	✗	✗	✓	✗	✗	✗	✓	✗	✗	✗
	12.5	✓	✗	✗	✗	✓	✗	✗	✗	✓	✗	✗	✗

the effectiveness of the strategy at those conditions. If negative net oxygen relative to the baseline was consumed at those levels, the blowing parameter was reduced to test the limits of the combination of species and patch size.

### 3.5.2 Results of Film Cooling

For each strut case run in Tables 16 through 18, the change in burned oxygen mass flow rate with respect to the baseline case was computed. Figure 97 shows a centerline numerical shadowgraph superimposed with water mass fractions for the baseline case without any film cooling.

The results are shown in Figure 98 for the case of slot injection of hydrogen. Negative values of change in oxygen burned indicate cases where less oxygen was burned in the control volume relative to the baseline case without any cooling. It was shown to be possible to inject hydrogen at the wall and have it mitigate autoignition that would otherwise occur without the secondary stream itself autoigniting. This was an important result at the system level because it supports the feasibility of a single fuel storage and cooling system for the purposes of primary and secondary (coolant) injection. While relatively large values of the blowing parameter were required for elimination of wall ignition, this could be addressed in a flight design by splitting the fueling between the primary injector and the wall slot so that they combine to the desired global equivalence ratio.

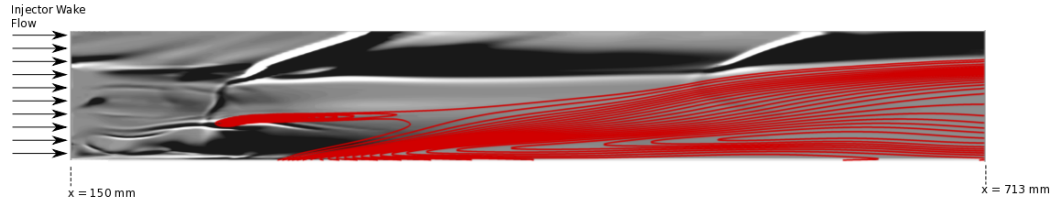
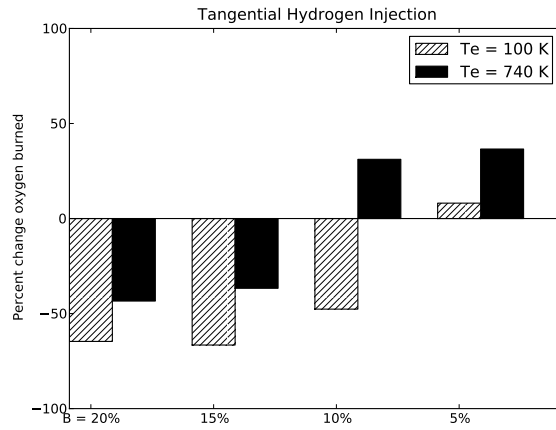


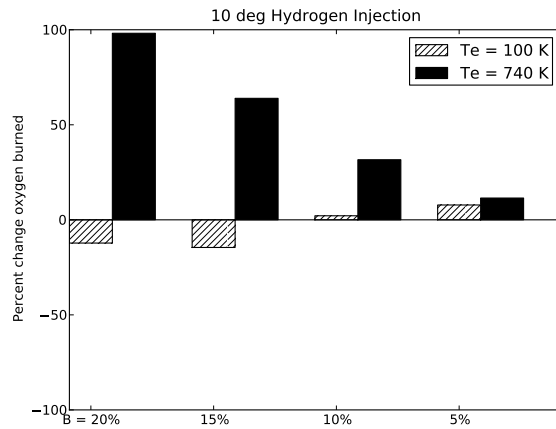
**Figure 97:** Baseline, reacting flow without autoignition mitigation is shown as numerical shadowgraph overlaid with oxygen water mass fractions.

In Figure 98(a) it is shown that in general, for tangential hydrogen coolant injection, lower coolant exit temperatures were more advantageous to reducing the amount of oxygen burned in the sampling region. This may be related to the increased heat sink capacity of the lower temperature coolant. In addition, the percent reduction in oxygen mass burning saturates around a 70% reduction when high coolant flow rates are used. Such cases succeed in eliminating autoignition at the wall but do not greatly affect the mid-stream autoignition zone, as seen in Figure 99. At higher coolant temperatures and blowing rates, the secondary hydrogen coolant in Figure 100 exhibited some initial burning while still mitigating a large percentage of the wall burning that would otherwise occur. Below 15% blowing, the high temperature injectant experienced a rapid drop in performance while the drop in performance for the low temperature injectant occurred below 10% blowing. These drops in performance reflect the presence of wall burning of hydrogen moving upstream as the blowing parameter was reduced. At 5% blowing, slightly more oxygen was burned relative to the baseline case for the high temperature injectant while for the low temperature injectant the amount of oxygen burned nearly broke even.

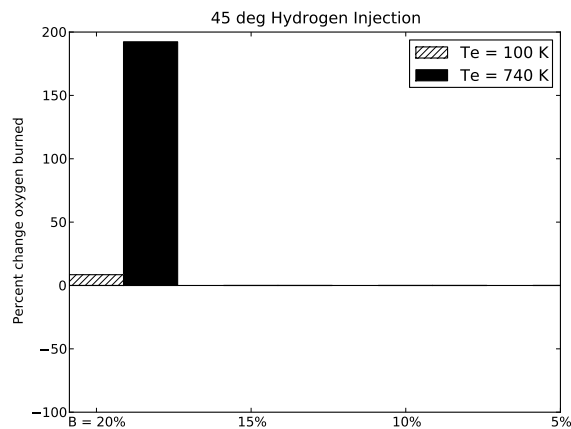
Ten degree slot injection performance for the low temperature hydrogen is shown in Figure 98(b) and indicates significantly reduced effectiveness of hydrogen coolant. For the high temperature coolant at a 20% blowing rate, a 100% increase in oxygen burning was realized as combustion occurred almost immediately at the location of injection as shown in Figure 101(b). This was due to the creation of a shock wave at the



(a)



(b)



(c)

**Figure 98:** Changes in mass flow of oxygen burned for secondary hydrogen injection is shown.

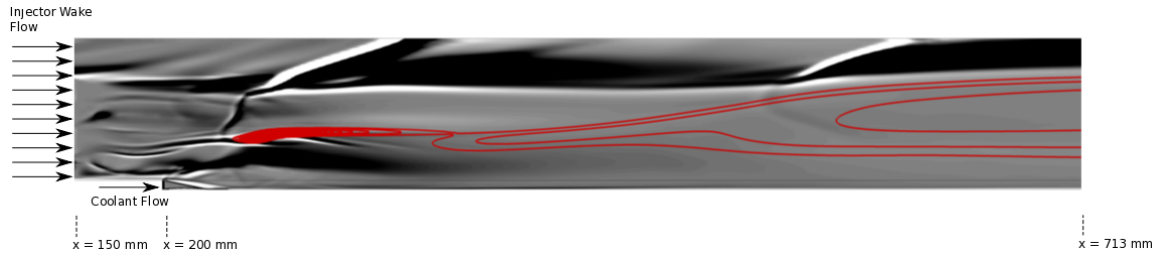


**Figure 99:** Numerical shadowgraphs overlaid with water contours  $Y_{H_2O} = 0.01, 0.02, \dots, 0.22$  for tangential film cooling with hydrogen. Coolant temperature of 100 K and  $B = 20\%$ .

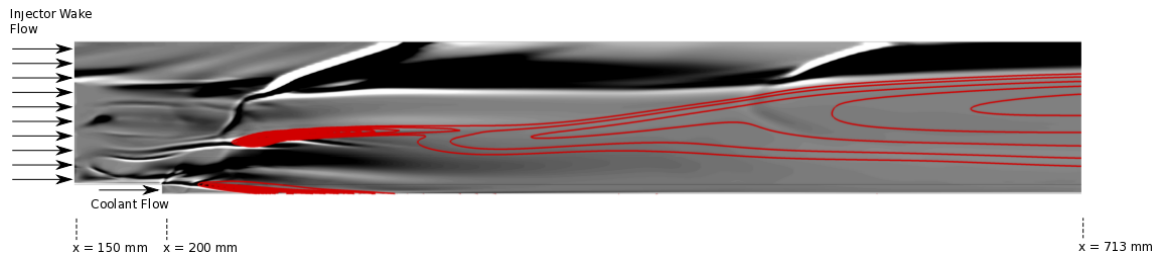
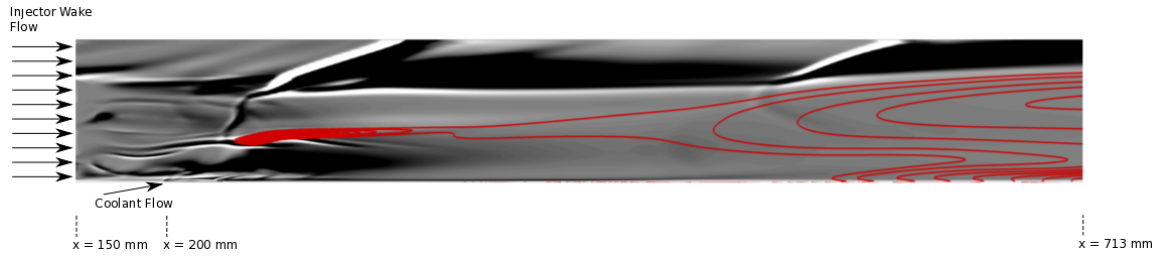


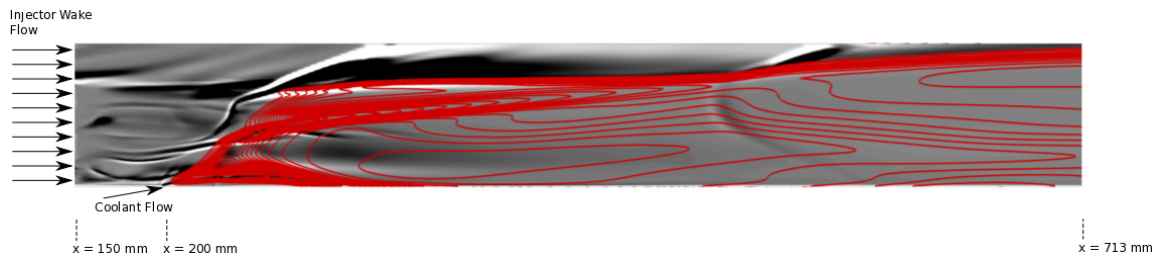
**Figure 100:** Numerical shadowgraphs overlaid with water contours  $Y_{H_2O} = 0.01, 0.02, \dots, 0.22$  for tangential film cooling with hydrogen. The coolant temperature is 740 K and  $B = 20\%$ .

leading edge of the film cooling slot that caused extensive amounts of coolant burning. Burning was reduced for the high temperature coolant by reducing the hydrogen mass flow rate to the slot. This may be due to two effects: reduction in strength of the leading-edge shockwave and less combustible fuel having been supplied to the wall region. This combustion zone was delayed relative to the baseline by lowering the injectant temperature as shown in Figure 101(a), although the lowered oxygen burning rates were marginal. These marginal gains by low temperature ignition were decreased by lowering the blowing parameter, roughly breaking even at 10% blowing, with the amount of burning increasing past 5% blowing.

Increasing the angle of secondary injection to  $45^\circ$  caused a 180% increase in oxygen burned in the injector wake for a high temperature coolant. This can be observed in the bar chart in Figure 98(c) and the numerical shadowgraph in Figure 102. This was primarily due to the presence of a stronger shock wave produced by greater obstruction of the primary flow by the secondary one. Lowering the injection temperature



(a)



(b)

**Figure 101:** Numerical shadowgraphs overlaid with water contours  $Y_{H_2O} = 0.01, 0.02, \dots, 0.22$  for 10 degree film cooling with hydrogen.  $B = 20\%$  and ambient temperatures of (a) 100 K and (b) 740 K are shown.

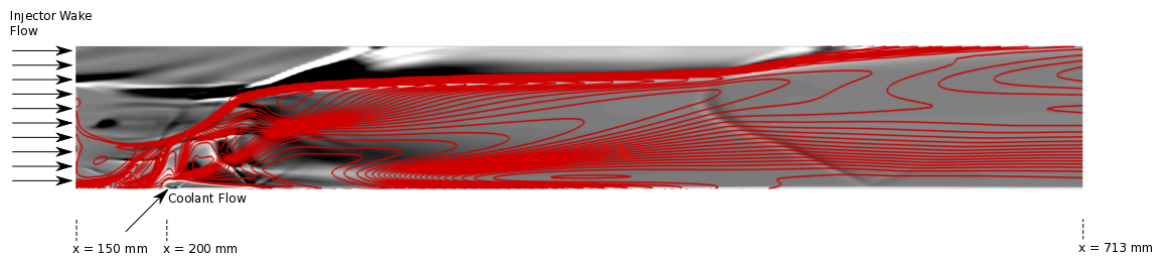


**Figure 102:** Numerical shadowgraphs overlaid with water contours  $Y_{H_2O} = 0.01, 0.02, \dots, 0.22$  for 45 degree film cooling with hydrogen. The coolant temperature is 740 K and  $B = 20\%$ .

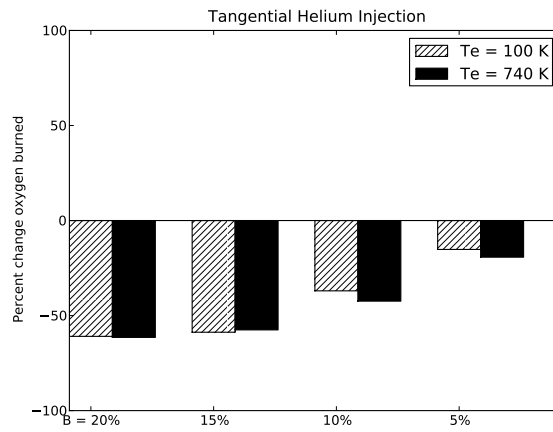
nearly broke even the amount of burning occurring. Overall, it appears that the slot injection of hydrogen at large angles to the primary flow is inadvisable relative to tangential or even low-angle injection.

The performance of helium slot injection for tangential,  $10^\circ$ , and  $45^\circ$  injection angles is shown in Figure 103. For the cases tested, the use of helium as a coolant was always able to provide mitigation of ignition relative to the baseline. For both tangential and angled injection, helium was able to meet or outperform hydrogen when compared on the bases of blowing rate and injectant temperature. This can be

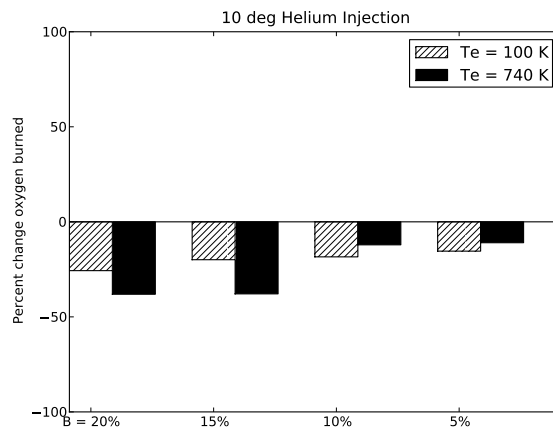
attributed to helium being an inert species.

At high tangential blowing rates of helium, Figure 103(a) shows that helium was able to achieve similar performance to hydrogen at both coolant temperatures. Unlike hydrogen, helium was not subject to the coolant burning observed in the hydrogen case. This allowed the helium coolant to experience a more gradual dropoff in performance compared to hydrogen as blowing was decreased. As the blowing parameter was decreased below 15%, low temperature helium experienced a slightly greater decrease in performance compared to high temperature helium. This was because the low temperature helium was traveling at a lower velocity versus the high temperature case. Therefore, more oxygen burning was occurring in the performance sampling region due to the shortened induction distances. It should also be noted that at low, 5% blowing levels, helium injection was still able to mitigate a small amount of autoignition, whereas hydrogen had excess burning at the same level of blowing.

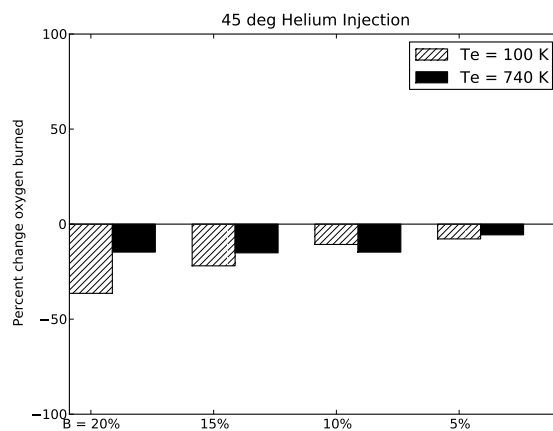
Over the range of blowing parameter values tested,  $10^\circ$  injection of helium shown in Figure 103(b) had worse performance relative to tangential helium injection. Compared to hydrogen, however, performance was better overall as there was no excess burning relative to the baseline case. Performance degradation as blowing was reduced was more gradual for low temperature helium versus the high temperature cases, which experienced a sharp drop in performance below  $B = 15\%$ , with the general trend resembling a step function over the blowing parameter range tested. This was because at  $B = 15\%$ , high temperature helium had a higher pressure of 12,700 Pa and achieved the “cushioning” effect initially desired for angled film cooling and mitigates ignition at the wall, shown in Figure 104(b). Lowering the blowing parameter below 15% eliminated this cushioning effect. Low temperature helium at  $B = 15\%$ , with a lower pressure of 4600 Pa, did not have the same cushioning effect as shown in Figure 104(a).



(a)



(b)



(c)

**Figure 103:** Changes in mass flow of oxygen burned for secondary helium injection is shown.

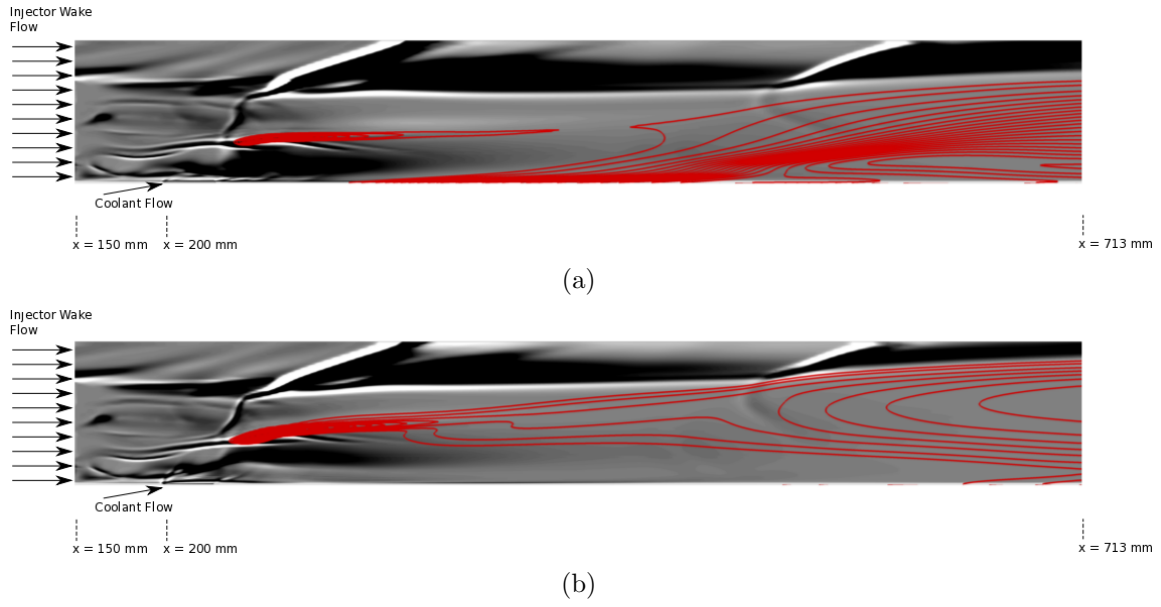


**Figure 104:** Numerical shadowgraphs overlaid with water contours  $Y_{H_2O} = 0.01, 0.02, \dots, 0.22$  for 10 degree film cooling with helium.  $B = 15\%$  and ambient coolant temperatures of (a) 100 K and (b) 740 K are shown.

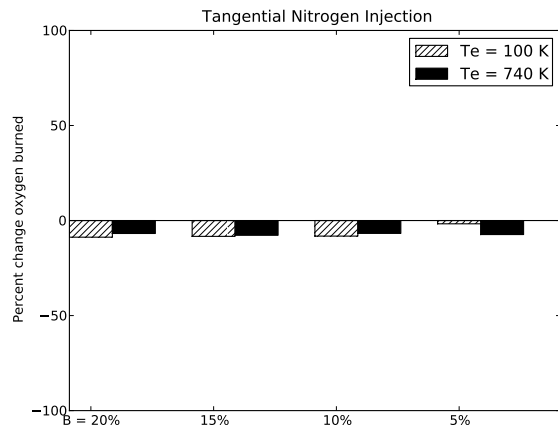
Injecting helium at a  $45^\circ$  angle to the main flow produced overall lowered performance relative to the  $10^\circ$  case, although there are some interesting features that can be observed in Figure 103(c). First, for low temperature helium, the performance at high levels of blowing was similar to the same case for low angle injection. For high temperature helium, a well-defined local minimum in burning reduction was observed at lower blowing rates. This was due to the tradeoff between high amounts of shock-induced burning at higher blowing levels with lower levels of heat sink capability at low levels of blowing. Therefore, the decrease in oxygen burned between 20% and 10% blowing can be attributed to the decrease in flow obstruction (and subsequent high temperature, shocked regions) and the increase in oxygen burned between 10% and 5% can be attributed to decreased cooling capacity. For the low temperature case, monotonically decreasing cooling capacity was witnessed over the entire range of blowing parameters because the coolant pressure at  $B = 20\%$ , low temperature blowing (6620 Pa) was less than that for  $B = 10\%$  high temperature blowing (8000 Pa). Thus, no local minimum was observed in the low temperature case.

The performance of nitrogen is shown in Figure 105. Overall it was evident that nitrogen was a relatively poor performer in mitigating autoignition when compared to hydrogen and helium. Two drawbacks nitrogen had over hydrogen and helium at the same temperatures and blowing levels were its relatively low specific heat with respect to mass and the low velocities with which it issued from the sonic slot. The first detriment impacted the ability of the secondary fluid to act as a heat sink to the shear layer near the wall. The second detriment impacted the ability of the coolant to convect the hot flow downstream and delay the occurrence of ignition once the cooling ability of the injectant was saturated.

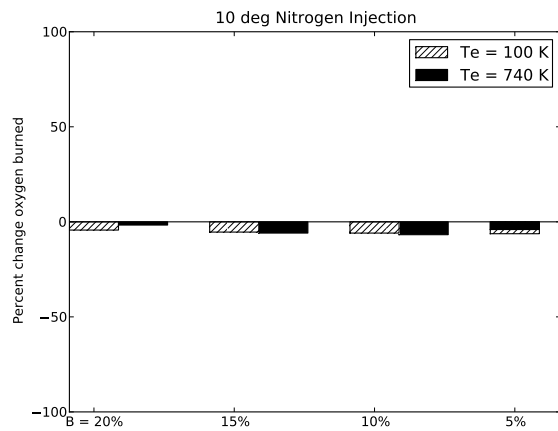
Figure 105(a) summarizes the performance of tangential nitrogen injection. Overall, only modest mitigation of wall autoignition is achieved by nitrogen injection. Nitrogen does provide some small amount of heat sink capability, which is reflected in less oxygen burning with respect to the baseline. These gains in performance were roughly constant over the blowing parameter range with only marginal difference between low- and high-temperature nitrogen temperature.

Injecting nitrogen at a  $10^\circ$  angle to the main flow resulted in worse performance relative to the tangential injection case as shown in Figure 105(b). None of the cases tested for this class of secondary injection were able to achieve over 10% reduction in the amount of oxygen burned relative to the baseline. Because of this, low-angled injection of nitrogen, while still providing marginal decreases in burned oxygen, was not a useful method of autoignition mitigation.

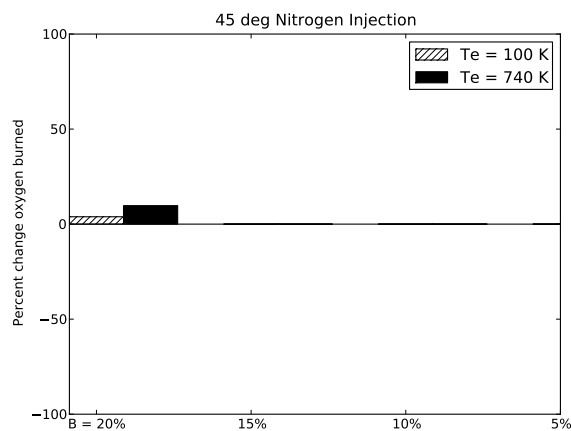
Nitrogen injected at a  $45^\circ$  angle to the main flow resulted in a net increase in oxygen burning, although like for the previous cases, the increases in burning are marginal as shown in Figure 105(c). Therefore, it was evident that high-angle injection of nitrogen was also not a feasible method for autoignition mitigation, and furthermore increases the oxygen burning that was already occurring relative to the baseline case.



(a)



(b)



(c)

**Figure 105:** Changes in mass flow of oxygen burned for secondary nitrogen injection is shown.

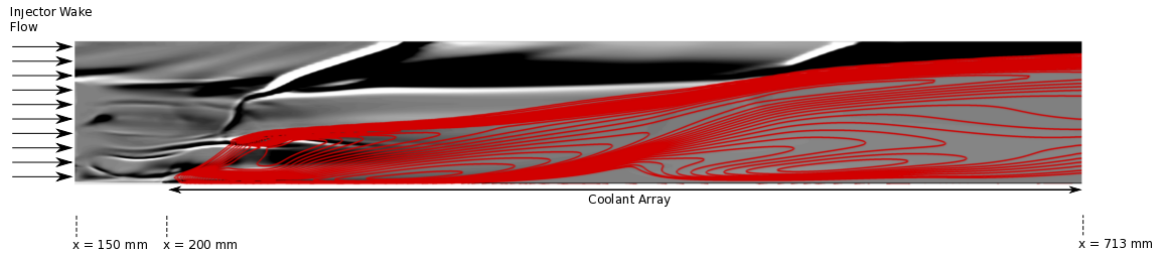


**Figure 106:** Numerical shadowgraphs overlaid with water contours  $Y_{H_2O} = 0.01, 0.02, \dots, 0.22$  for transpiration cooling with helium. Parameters  $B = 20\%$  and  $W = 25\%$  are shown.

### 3.5.3 Results of Wall Transpiration

For wall transpiration, the cases indicated by checkmarks in Table 19 were simulated to convergence with the amount of oxygen burned analyzed using the same methodology as for the film cooling case. In addition, it was decided that any cases susceptible to the bleeding of main flow into the simulated plenum, a disastrous condition that would subject the internal transpiration system to hot gases, were failure cases. In addition, the plenum pressure was tracked by the simulation in order to arrive at an idea of the system demands for transpiration cooling.

Of the cases shown in Table 19, only a subset of the helium cases were deemed to be feasible. Cases with hydrogen injection had the issue of causing autoignition near the leading edge of the transpiration patch behind the leading edge shock wave, shown in Figure 106. Injection of nitrogen as a coolant was demonstrated to be an ineffective cooling strategy in general for the same reasons of heat capacity as before, with the additional issue that the low plenum pressures associated with nitrogen tended to allow flow to bleed into the plenum.

Of the helium cases tested, only the 25% width and 50% length cases were shown to be able to mitigate the presence of autoignition by any amount. However, only high values of blowing were shown to mitigate the presence of autoignition, and even then the gains were only minimal. Figure 108 shows that the burning characteristics of the best performing transpiration cases were similar to the baseline case without

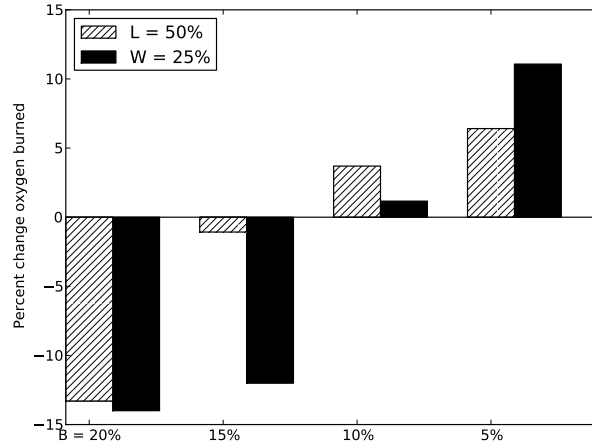


**Figure 107:** Changes in mass flow of oxygen burned for secondary helium transpiration are shown.

any cooling. This is because transpiration cooling injected fluid in the main stream at much smaller velocities relative to the main flow, severely reducing the cooling capacity of the fluid even for high specific heat species such as helium. Figure 107 shows the performance of helium injection for these cases. It was observed that a simple trend of increasing mitigation performance with increasing blowing parameter was achieved. At the highest blowing values, helium transpiration had performance only approaching that of tangential nitrogen film cooling. Because such poor performance was gained for the same amounts of mass flow as helium film cooling, it was concluded that transpiration cooling is not advantageous for autoignition mitigation for the conditions studied here.

### 3.5.4 Effect of Turbulent Schmidt Number on Autoignition

It was observed in Chapter 2 that the turbulent Schmidt number affected the diffusivity of the strut injected fuel plume into the surrounding air. While this has an effect on the mixing efficiency achieved by the strut, combustion may also be affected due to the altered region of combustible fuel. In addition, the fuel may begin to enter the boundary layer sooner and, therefore, begin to burn at locations upstream of the

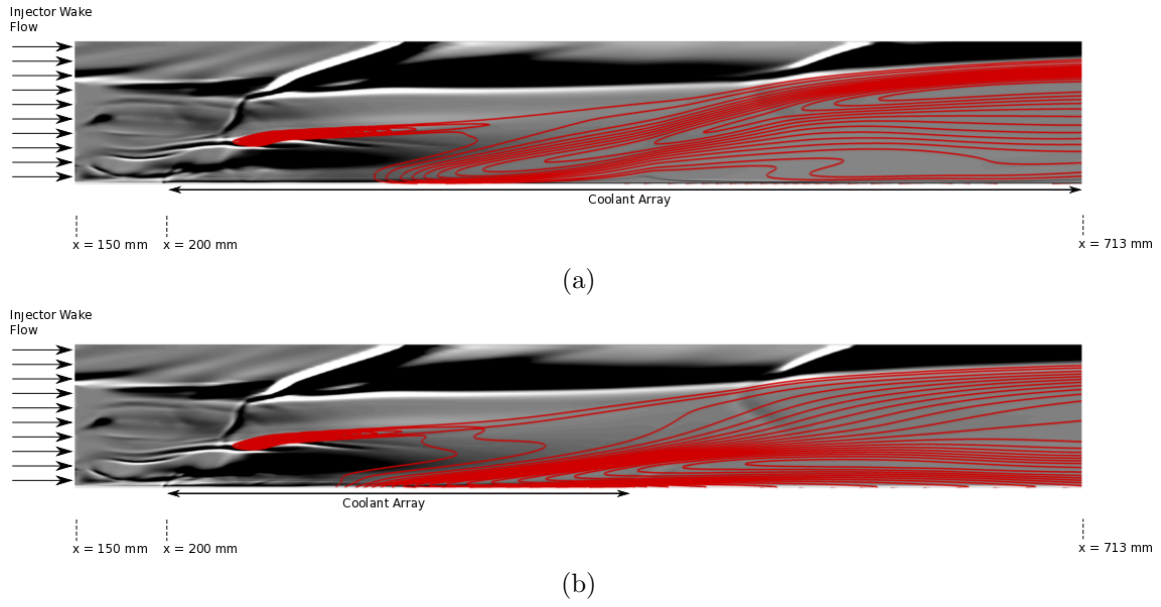


**Figure 108:** Numerical shadowgraphs overlaid with water contours  $Y_{H_2O} = 0.01, 0.02, \dots, 0.22$  for transpiration cooling with helium.  $B = 20\%$  and patch sizings of (a)  $W = 25\%$  and (b)  $L = 50\%$  are shown.

baseline  $Sc_t = 1.0$  case. With these concerns in mind, it was necessary to evaluate the effect of the selection of  $Sc_t$  on the predicted locations of autoignition and the efficacy of the implemented mitigation strategies.

A subset of the cooling cases studied in the previous sections were selected in order to evaluate the effect of turbulent Schmidt number. The selected cases were taken from the tangential film cooling geometry and consisted of hydrogen and helium at the low ( $T_e = 100$  K) static temperature condition as these cases proved to be highest-performing of the  $Sc_t = 1.0$  cases investigated in the bulk of the study. All conditions and solution methodologies were the same with the only change being the change in  $Sc_t$  to 0.25.

Before evaluating the effect of turbulent Schmidt number on film cooling results, a reacting baseline case at the lower turbulent Schmidt number was computed without any film cooling. This is because the results here are presented in terms of a relative change in oxygen burned. For a fair comparison, the change in oxygen mass burned should be relative to a baseline case run with the same turbulent Schmidt number.

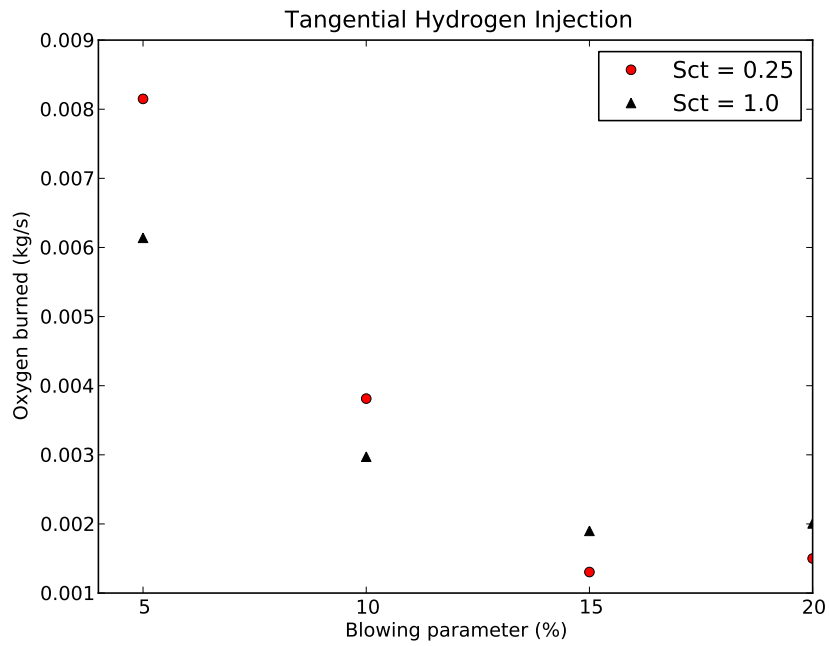
After re-running the reacting strut case (without cooling) with  $S_{ct} = 0.25$ , the oxygen mass burned changed from  $5.679\text{e-}3$  kg/s to  $8.728\text{e-}3$  kg/s, a 54% increase relative to the  $S_{ct} = 1.0$  case.

The changes in mass of oxygen burned for each Schmidt number for the selected hydrogen and helium cases are shown in Figure 110. The first comparison case was low temperature hydrogen injection. It is observed that lowering the turbulent Schmidt number overall increased the percent change in oxygen burned, but this figure is relative to the respective baselines. Figure 109 shows the actual burned mass flow rate of oxygen for each of the tested cases. It is observed that at high secondary hydrogen mass flow rates, lowering the turbulent Schmidt number slightly decreased the amount of oxygen burned while at low mass flow rates the amount of oxygen burned increased. For secondary helium injection, lowering the turbulent Schmidt number increased the oxygen burned across all blowing rates, although at 20% the values are very close. Overall, it is concluded that changing the turbulent Schmidt number did have an effect on the burning characteristics observed, but did not significantly impact the high performance of tangential film cooling of hydrogen and helium.

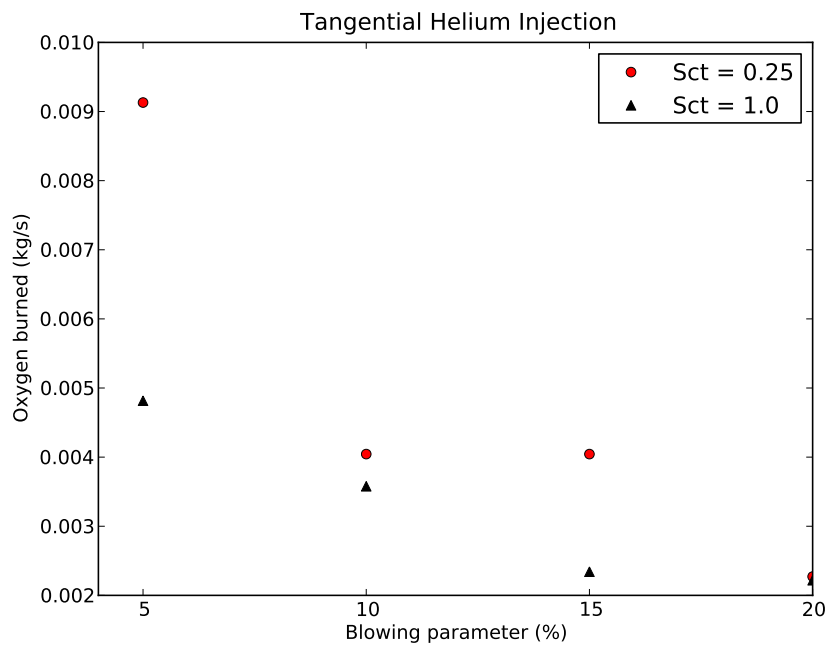
### 3.5.5 Effect of Chemical Model on Autoignition

It is useful to understand the sensitivity of the numerical simulation to the selection of chemical model in order to increase confidence in the results obtained in this study. The strut and stinger baseline autoignition cases were rerun with the Ó Conaire [92] chemistry model with and without reactions involving  $\text{H}_2\text{O}_2$ . This gives knowledge not only to the sensitivity of the problem to a different, modern mechanism, but also to the importance of hydrogen peroxide to the reacting system.

Contours of water production and mass fraction downstream of the strut and stinger injectors are shown in Figures 111 and 112, respectively. The overall morphology of the contours agree with those from the baseline simulations with Jachimowski

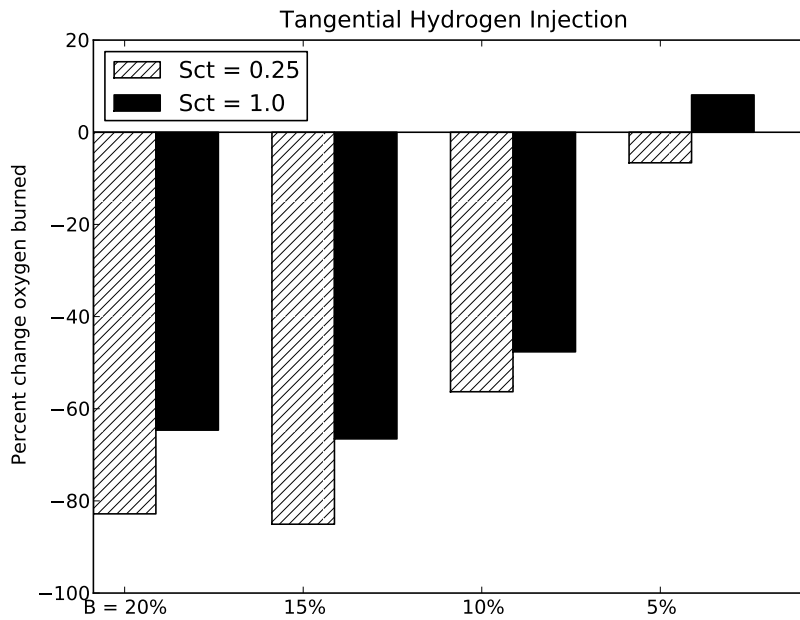


(a)

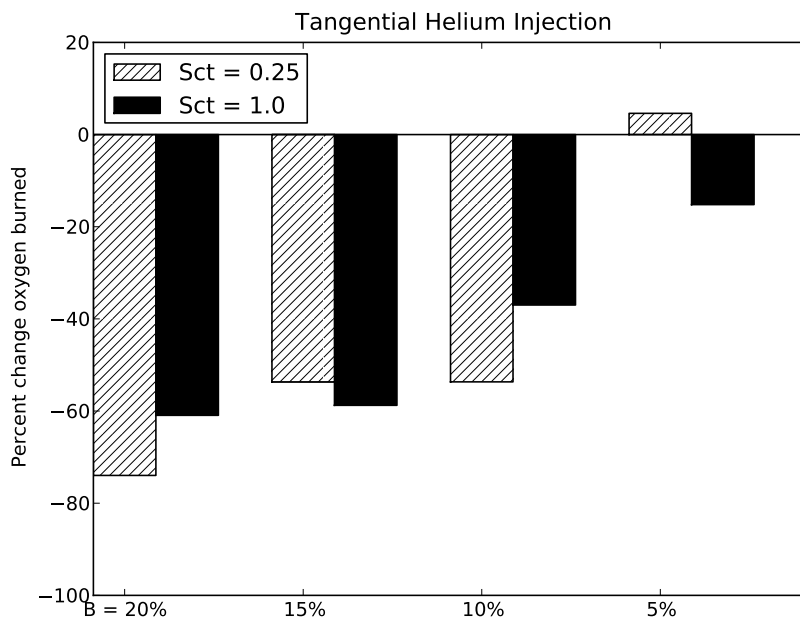


(b)

**Figure 109:** Changes in mass flow of oxygen burned for tangential, secondary hydrogen and helium injection is shown.



(a)



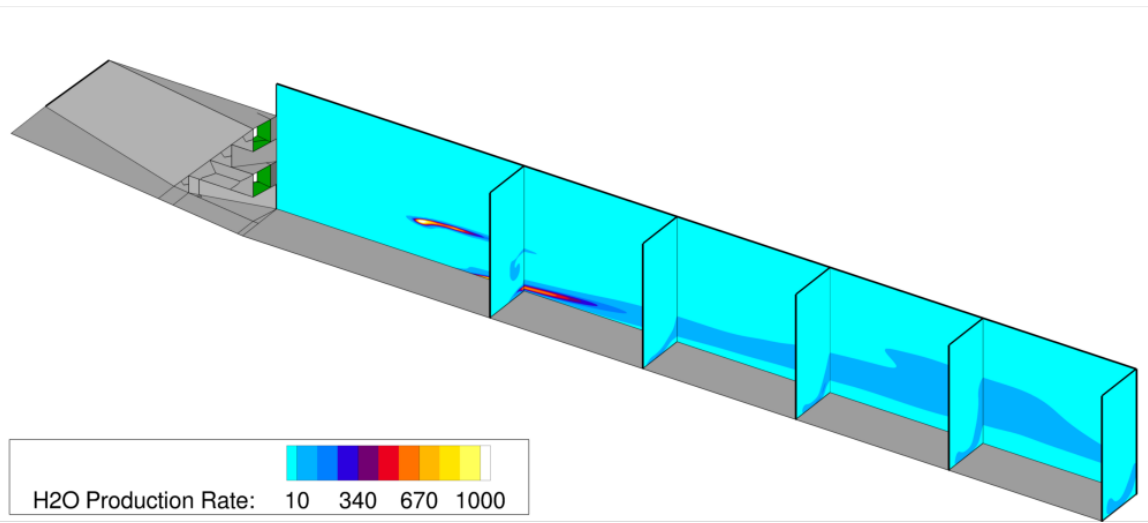
(b)

**Figure 110:** Percent changes in mass flow of oxygen burned for tangential, secondary hydrogen and helium injection is shown.

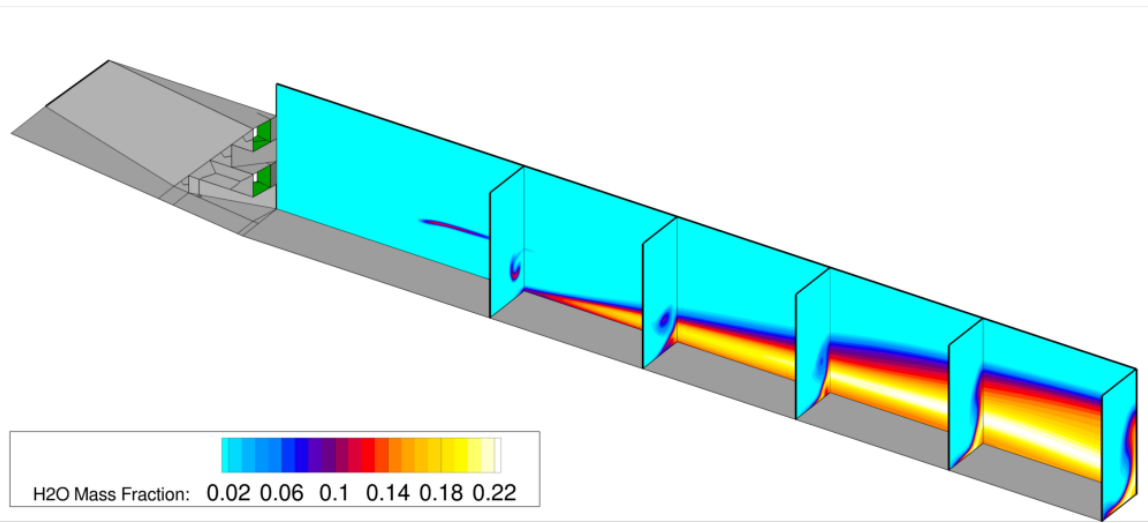
chemistry. The oxygen consumption for the strut case decreases from 0.005728 kg/s with the Jachimowski baseline to 0.005329 kg/s, a 7.2% decrease drop relative to the mean. Adding hydrogen peroxide chemistry from the Ó Conaire model affects a 6.7% decrease relative to the baseline. For the stinger case, the oxygen consumption decreases from 0.0086 kg/s with the Jachimowski baseline to 0.008415 kg/s, a 2.17% decrease drop relative to the mean. Adding hydrogen peroxide chemistry from the Ó Conaire model affects a 2.12% decrease relative to the baseline. These results indicate that while the solution is sensitive to a small degree to the selection of chemical model, it is not very sensitive to the presence of hydrogen peroxide chemistry at the simulated conditions. Therefore, it may not be worth solving for hydrogen peroxide chemistry depending on the additional number of equations (and computation time) that will be required.

### ***3.6 Chapter Summary***

The current study of the mitigation of autoignition on the forebody of a hypervelocity vehicle focused on the use of active wall cooling. Two methods of wall cooling were considered: slot injection (both parallel and angled) and wall transpiration. Both strategies were applied as boundary conditions, although the transpiration modeling used in the study allowed for physical reproductions of the presence of suction and blowing on the same region of transpiration. For each method of cooling, three species were tested: hydrogen, helium, and nitrogen. Hydrogen was chosen because of its systems benefits (by using a single fueling system) and excellent heat capacity at the cost of being a combustible coolant. Helium was chosen as an alternative because of its marginally lower heat capacity versus hydrogen with the additional benefit of being an inert species. Nitrogen was chosen as a third alternative because it is also inert and has improved storage density over helium, although its heat capacity is very low compared to the other two alternatives. Both film and transpiration cooling

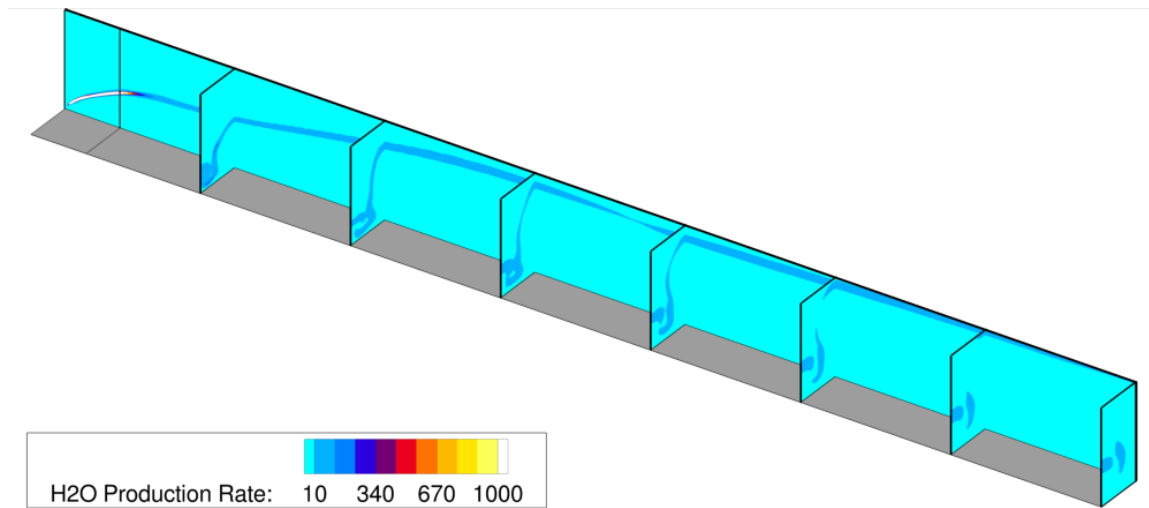


(a)

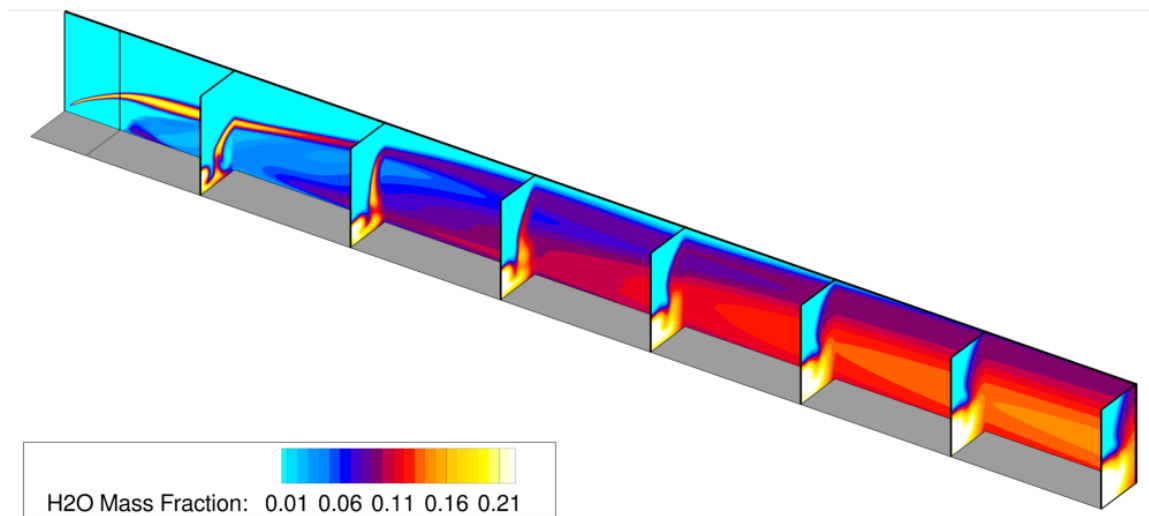


(b)

**Figure 111:** Strut injector contours of (a) water production and (b) water mass fraction in the flow domain of interest using the Ó Conaire mechanism without hydrogen peroxide. Flow is from the upper left to the lower right.



(a)



(b)

**Figure 112:** Stinger injector contours of (a) water production and (b) water mass fraction in the flow domain of interest using the Ó Conaire mechanism without hydrogen peroxide. Flow is from the upper left to the lower right.

strategies were evaluated at various levels of blowing.

Baseline reacting cases of the stinger, unswept ramp, and strut injectors from Chapter 2 were simulated without any wall cooling in order to provide a baseline case for comparison. The study of autoignition mitigation focused on the strut injector because transverse injection through a stinger proved itself to be susceptible to extensive amounts of ignition originating away from the wall while encapsulating the fuel plume. The unswept ramp injector also exhibited redundant ignition characteristics at the wall compared to the strut, just further down stream. Therefore, it was found that the strut provided an excellent geometry for study, with any solution able to potentially be applied to ramp injection.

Film cooling was tested first for hydrogen, helium, and nitrogen over blowing parameters ranging from 5% to 20%. Two exit temperatures of 100 and 740 K were tested to determine the effect of fluid total temperature on the cooling characteristics. It was found that at high blowing rates and low temperatures that hydrogen was able to eliminate all of the wall autoignition occurring for the strut case. This effect decreased in performance both as coolant temperature increased and/or blowing rate was lowered. Performance also degraded as angled injection was introduced as the coolant itself became susceptible to burning. In general, helium was able to achieve similar levels of performance as hydrogen and sustained better performance at lower levels of blowing due to its inert character. Overall, nitrogen was a poor choice in mitigating autoignition due to its diminished heat capacity with respect to mass. Therefore, it was concluded that tangential hydrogen and helium cooling are effective methods for autoignition mitigation. If high cooling mass flow rates of hydrogen are required to mitigate autoignition, fueling splits between the primary and film cooling injectors may be considered to target the optimum system global equivalence ratio.

## CHAPTER IV

### TWO-DIMENSIONAL COMBUSTOR CALCULATIONS

The intentional shocking of the premixed fuel-air mixture from the forebody flow is the primary mechanism by which ignition occurs in a scramjet concept. While wall burning can contribute to the consumption of fuel in the combustor, it is the shockwave that traverses the entire flow that produces the bulk rise in temperature ideally resulting in nearly uniform combustion. Typically the shock wave is generated by the cowl lip due to the flow turning at that location. In some concepts, however, the shock wave that raises the temperature of the flow may be generated by a wedge placed at the wall of the internal flowpath.

Depending on the point on the trajectory the vehicle is located, the separation distance between the shock and reaction fronts will vary to a large degree. Higher Mach numbers will yield correspondingly higher post-shock temperatures, thereby decreasing the ignition delay time experienced by the shocked mixture. Therefore, as the Mach number of the trajectory is increased, the shock and reaction fronts will become more closely spaced, eventually merging. As the two fronts approach each other, there is the possibility of unstable interaction with each other as the normal velocity would be subsonic, but this has not yet been observed in simulation. At low enough Mach numbers, there will either be little or no ignition or the ignition delay time will be long enough to neutralize the benefits of the scramjet due to the requirement of a long combustor. These Mach numbers will functionally define the lower limit of feasibility for a scramjet.

In this chapter, attention will be given to the simulation of premixed, shock-induced combustion in a notional combustor of arbitrary length. For this study,

it was assumed that the cowl wall provided the necessary turning of the flow in order to produce a shock wave that raised the temperature of the gas above its autoignition limit. Here the angle of turning was limited to roughly 11 degrees, a typical used total turning for such flows. This study is important in establishing quantitative performance metrics and qualitative characteristics of the combusting flow. Information gained from this study included the determination of optimum reaction length as a function of freestream conditions on a notional trajectory as well as stability characteristics along the trajectory in the vicinity of the cowl leading edge.

## ***4.1 Modeling and Simulation***

### **4.1.1 Inflow Profiles**

Evaluation of burning characteristics in the notional combustor used two types of profiles as the inflow: uniformly premixed fuel-air and profiles derived from the mixing simulations of Chapter 2. For the cases derived from the mixing simulations, the outflow plane of the simulation was saved and used as the inflow for the notional combustor simulations. This allowed the combustion characteristics of selected cases to be evaluated relatively inexpensively without needing to exhaustively simulate a notional combustor for each mixing case. The fuel-air profile of the strut from the mixing study is shown in Figure 65 of Chapter 2 for  $x = 0.713$  m. Note that nonreacting profiles were selected, so the implicit assumption is that no reaction had occurred until cowl closure, which was shown to be not true in Chapter 3. This assumption was made as a simplifying measure.

For studying uniformly premixed combustion, integer freestream Mach numbers from a Mach 10 to Mach 20, constant 71,820 Pa (1500 psf) dynamic pressure trajectory were simulated. Inflow conditions were taken from a custom-made trajectory code that takes the oncoming flow conditions at a particular trajectory point, shocks

it through two turning angles according to the notional forebody used, and then ideally mixes the airflow with the fuel while conserving mass, momentum, and energy. More details about the methodology are described in Appendix C. At each trajectory point the fuel flow supplied to the forebody air was varied in order to provide the required equivalence ratio at that point.

#### 4.1.2 Computational Domain and Methodology

The topology used in this study consisted of a short runway for grid transition from the outflow plane of the mixing studies to one that was resolved on both walls of the internal flow path. The lower wall of the topology consisted of an isothermal wall through the entire length. The upper boundary had an extrapolation boundary condition until the point of cowl closure, where an isothermal wall was defined and continued to the end of the computational domain. The sides of the computational domain are defined as symmetry boundary conditions. The cowl wall was angled at  $10.8^\circ$  to the oncoming flow in order to match the total turning experienced by the notional forebody. Figure 113 shows the topology used in this study. The number of grid points in the topology totaled 1.46 million with 1.41 million points located behind the cowl closure location.

Past the shoulder of the topology was a constant area duct that served as a notional combustor. In an actual flight vehicle the combustor walls would gradually diverge in order to combat thermal choking, but consideration is not given to that in this study. The length of the combustor was arbitrarily defined to be one meter to allow combustion to substantially complete at lower Mach numbers. The total length was chosen arbitrary because the purpose of this study was not to evaluate the performance of an actual design combustor, but rather to comparatively evaluate the performance characteristics of different inflow mixing profiles.

For simulations of premixed flow stability in the locality of the cowl leading edge,



**Figure 113:** The grid used in the combustor study is shown with every fourth grid point plotted normal to the walls.

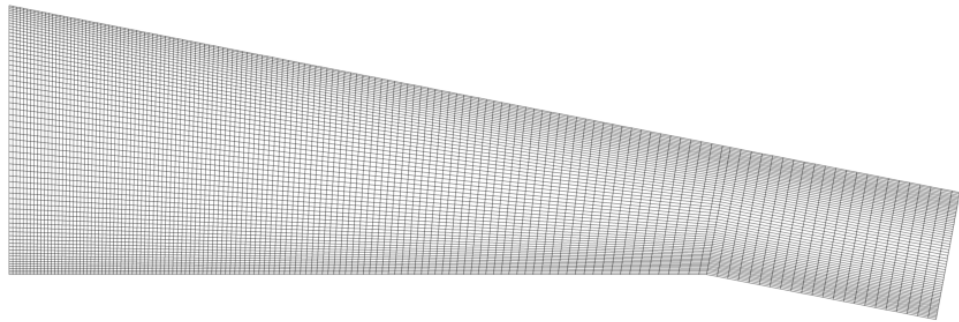


**Figure 114:** The grid used in the stability study is shown.

a refined grid was constructed using the same geometry as the full simulation, but cut off a short distance past the shoulder of the geometry. The grid had dimensions 256 x 587 points axially and transversely and is simulated in two dimensions. The topology is shown in Figure 114. The walls, as with the full simulation, were set to be at a constant temperature of 500 K.

The flow was solved using the computational methodology outlined in Section 2.1, with the chemistry using Jachimowski's reduced model described in Section 3.1.1.

#### 4.1.3 Performance Metrics

Combustion efficiency and thrust potential were the quantitative metrics used to track the performance characteristics of different inflow conditions. Combustion efficiency was used as a way to track the progress of the combustion within the notional combustion chamber by tracking the consumption of the species not in excess. As

discussed in Section 3.2.2, the definition of combustion efficiency varies. Here it was defined as the consumption of oxygen mass relative to the inflow oxygen mass. The stream thrust potential, used as a loss tracking metric in the previous study, was used here to track both the thrust benefits gained by combustion as well as the viscous and shock losses throughout the flowpath. This use case further supports the use of thrust potential throughout the flowpath as it gives an honest assessment of the balance between the beneficial and detrimental mechanisms occurring within a flow.

Using thrust potential allows the determination of optimum flowpath lengths for components such as engine modules [69] because the general thrust potential trend peaks at the point where gains due to combustion begin to lose to viscous losses near the walls of the flowpath. Figure 115 shows a notional plot of thrust potential of gas burning in a combustor as a function of distance along the flowpath. Because stream thrust potential is a measure of the stream thrust obtainable by isentropically expanding a particular cross-section to a reference nozzle exit, the optimum point on the plot represents the ideal point for geometric expansion to occur. Therefore, the distance between the beginning of the notional combustor and the local maximum is also referred to as the optimum combustor length. This length is related to the ignition delay time of the fuel-air mixture. Therefore, higher Mach numbers will demand a shorter combustor length because burning occurs relatively rapidly due to the shortened ignition delay times.

## ***4.2 Results and Discussion***

Integer points between Mach 10 and Mach 20 on a constant 71,820 Pa (1500 psf) trajectory were simulated over a one meter length constant-area duct after being shocked via turning by a notional cowl. The premixed conditions were obtained by shocking the freestream through two turns and then mixing the air with fuel at stoichiometric proportions. Figure 116 shows contours of water mass fraction overlaid

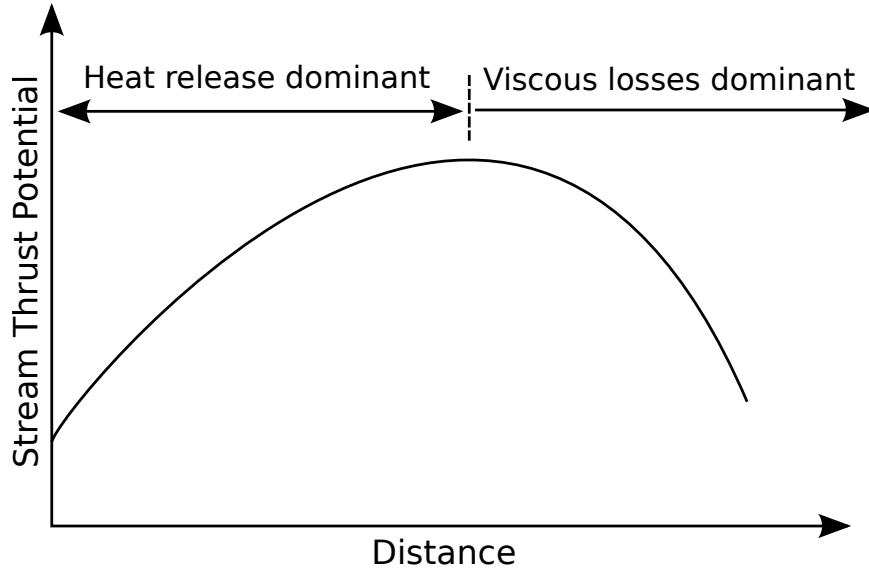
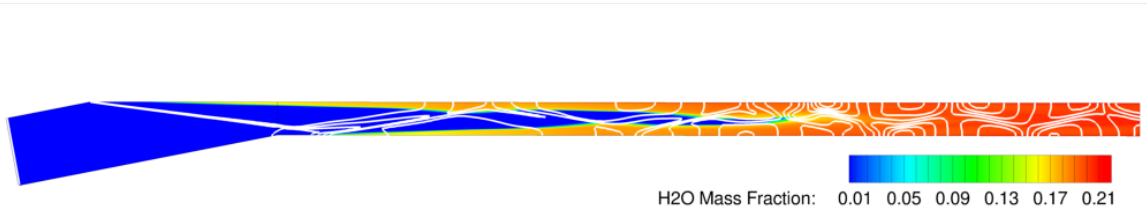


**Figure 115:** A notional trend of thrust potential versus distance in a combustor.

with lines of constant pressure for Mach numbers 11, 15, and 20. It was observed that as freestream velocity increased, the separation distance between the shock and reaction fronts decreased accordingly. This was due to the fact that larger upstream Mach numbers induce a larger temperature rise which had the effect of decreasing the induction distance through decreased ignition delay times (even though velocity increases, which would have the effect of delaying ignition for different cases having the same temperature).

The Mach 11 solution did not exhibit significant shock-induced combustion, but rather the high temperatures of the boundary layers caused the onset of combustion. This is because the temperature immediately downstream of the oblique shock wave was roughly 820 K, too low for autoignition. The combustion zones at the wall are increased in size due to the presence of expansion waves in the flow reflecting off of the walls of the flowpath, with both combustion zones eventually merging downstream. At higher Mach numbers, for example Mach 15 in Figure 116(b), a shock-induced reaction front formed due a higher temperature behind the shock wave, approximately 1180 K in this case. As freestream Mach number was increased, the shock and reaction



(a)



(b)



(c)

**Figure 116:** Contours of water mass fraction overlaid with lines of constant pressure for Mach numbers (a) 11, (b) 15, and (c) 20.

fronts eventually began to merge. Note also that as freestream Mach number was increased, the mass fraction of water in the burned flowfield is lessened mainly due to the very high temperatures in the flow. For example, the post shock temperature of the Mach 20 case is 2200 K, causing the dissociation of water.

Decreasing the distance between shock and reaction fronts generally had a beneficial effect on the overall system because it allowed for shorter optimum combustion lengths. This is because the fuel-air mixture ignited and proceeded toward completion in shorter distances. However, combustion efficiency is not an ideal metric to use for designating the optimum combustion length; stream thrust potential is a better metric for such purposes. Figure 117 shows plots of thrust potential and combustion efficiency for the Mach 12 case. The combustion efficiency curve is characterized by a shallow initial rise followed by a rapid rise as oxygen is rapidly consumed. Eventually the rise in combustion efficiency tapers off past the knee in the curve. Now examine the stream thrust potential curve, which increases in value due to combustion and reaches a maximum at the critical point where viscous losses begin to overcome the gains from further combustion.

When given only combustion efficiency, an analyst could pursue a few options for defining an “optimum” combustion length. First, he may define a “threshold” combustion efficiency, say 80%. This may not be a good idea for multiple reasons. The first is that it is unknown if this value is attainable for a given condition due to the high temperatures experienced in hypervelocity flight. Second, if this value is attainable, it may demand unreasonably long combustor lengths. This can be observed in Figure 117, which shows the combustion curve’s knee at a combustion efficiency of 0.70, past which point combustion efficiency increases slowly. Either way, the optimum point in the thrust potential is observed to coincide with a combustion efficiency value of 0.76, so designing the combustor past this point produces increasing losses anyways. Another option for defining combustor length by using the point of

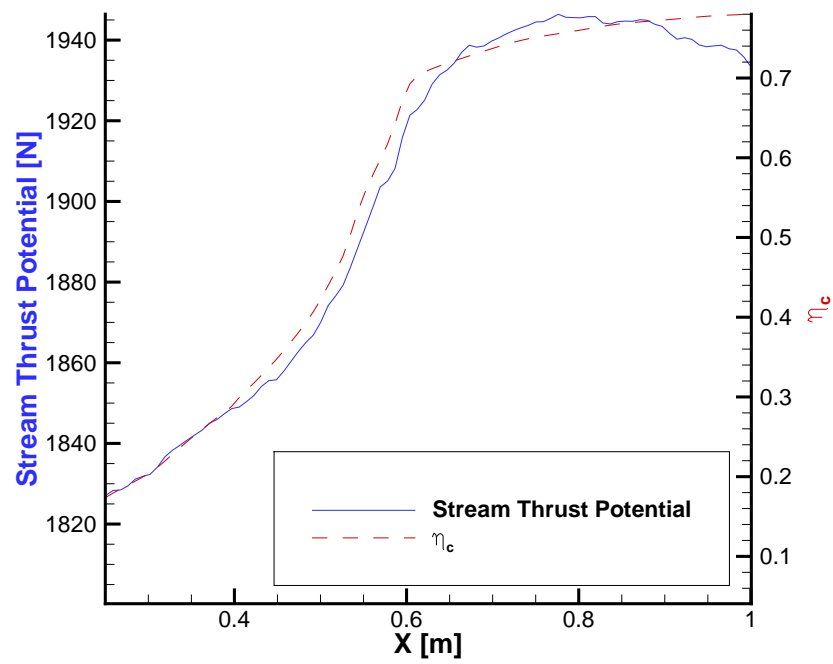


**Figure 117:** Thrust potential and combustion efficiency for the Mach 12 case. The shoulder of the geometry is where  $x = 0$ .

the knee in the curve is also not ideal because it is observed from the thrust potential curve that greater gains can be earned by a greater length.

Figure 118 plots the optimum combustion length for different points in the notional 71,820 Pa (1500 psf) trajectory. The curve of optimum combustion length can be split into three regions. The first, below Mach 13, is dominated by boundary layer burning and does not exhibit a rapid drop in optimum combustor length as a function of freestream Mach number. Between Mach 13 and Mach 17, a rapid drop in optimum combustion length occurs as a shock-induced combustion front travels upstream toward the cowl shock. Above Mach 17, the trend stops decreasing as the combustion front dwells in the vicinity of the initial shock wave. The combustion efficiency at the location of maximum stream thrust potential is also plotted and shows that in general as freestream Mach number is increased, the combustion efficiency at the optimum point decreases. This confirms the conclusion that combustion efficiency is not an ideal metric to use for finding the optimum combustion length as the “optimum” combustion efficiency changes as a function of freestream Mach number.

The trend in optimum combustor length confirms that as freestream Mach number increases, the distance required in order to extract maximum stream thrust potential decreases. For the particular notional trajectory considered, there were a wide range of optimum combustion lengths. At Mach 11, which also corresponds to the low end of feasibility for the conditions tested, the optimum combustion length is roughly 0.8 m, while at Mach 20 the length shortens significantly to 0.1 m. During the design of an actual vehicle flow path with fixed geometry, a plot like this may be used to determine the minimum required combustion length by identifying the point on the curve where scramjet concept is to begin operation. On the other hand, if a variable internal geometry is used, a plot such as this can provide a schedule for when to begin the expansion of the flow to the nozzle exit in order to extract the largest possible performance from the flow. The large variation in required combustor length

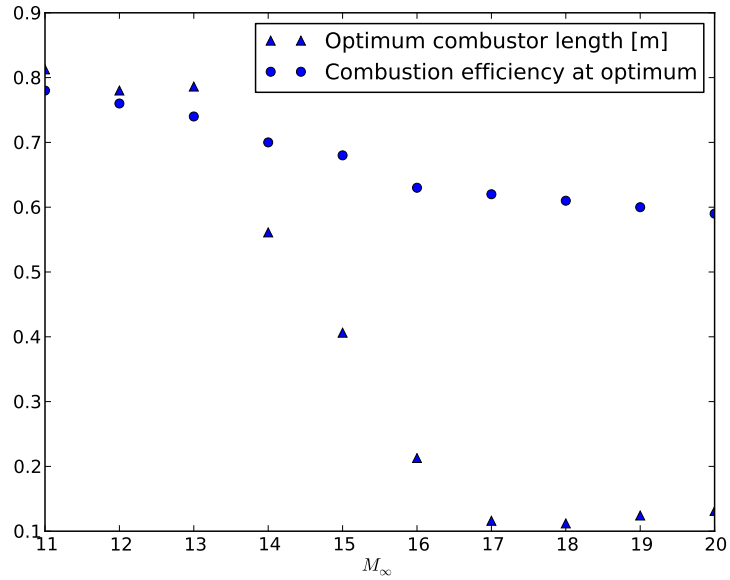


**Figure 118:** Optimum combustor length and combustion efficiency at that point at different trajectory points.

suggests that variable internal geometry will be an enabling technology for actual flight scramjets.

The flowfield input with a nonreacting strut injector cowl closure profile is shown in Figure 119. Three longitudinal slices are shown at the centerline plane, the symmetry plane between injectors, and the plane positioned between the two symmetry planes. Here it was observed that the shock-induced combustion occurs relatively rapidly compared to the Mach 12 premixed case. This was primarily due to the elevated temperatures in the strut flowfield facilitating shorter ignition delay times. It was also observed that the reaction front forms at the location of the shock reflecting away from the shoulder region of the geometry. Upon examination of the stream thrust potential and combustion efficiency trends, the stream thrust potential was observed to reach its peak at 0.681 m, a bit upstream of the premixed case, with a combustion efficiency of 0.78.

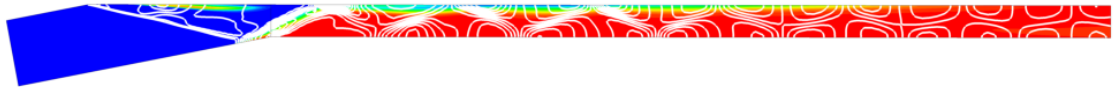
In order to determine the presence of flow instabilities, integer freestream values on



---

(a)

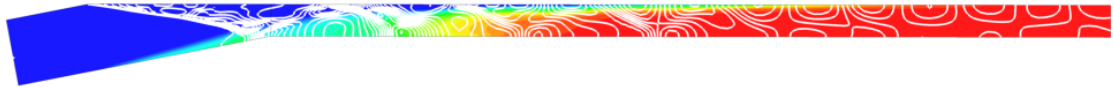
---



---

(b)

---



---

(c)

---

**Figure 119:** Filled contours of water mass fraction superimposed with lines of constant pressure for the Mach 12 strut flowfield at  $y =$  (a) 0, (b) 0.0172, and (c) 0.0345 m

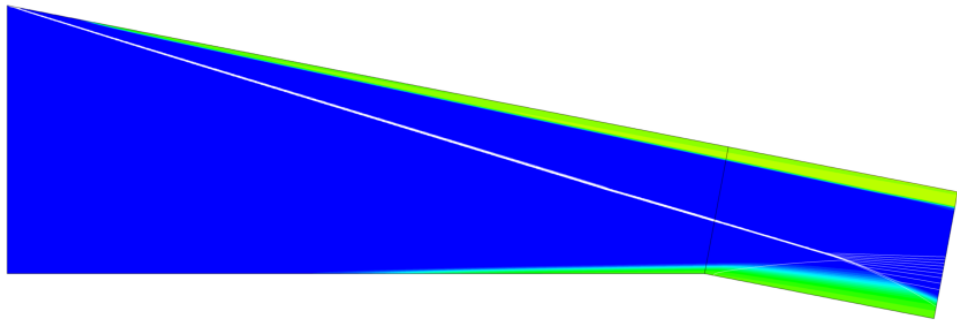
the Mach 15 to 20 trajectory were simulated in the vicinity of the cowl closure location with a refined grid. This was done because combustion instabilities occurring in a flow are sensitive to grid resolution and simply simulating the entire notional combustor flowpath at a high grid density would not be practical given where the shock-reaction front instabilities would occur (i.e. near the shock wave).

Figure 120 shows the shock-reaction front system for Mach numbers 15 through 20 for the more refined simulation in the vicinity of the cowl leading edge. For the cases shown, as the reaction front approaches the shock front no instabilities are visible in the shock layer or in the reaction zone. Some shock instabilities have been reported in the literature at higher wedge angles, but at the low turning angles characteristic of airbreathing propulsion there may be no instabilities for engineering purposes.

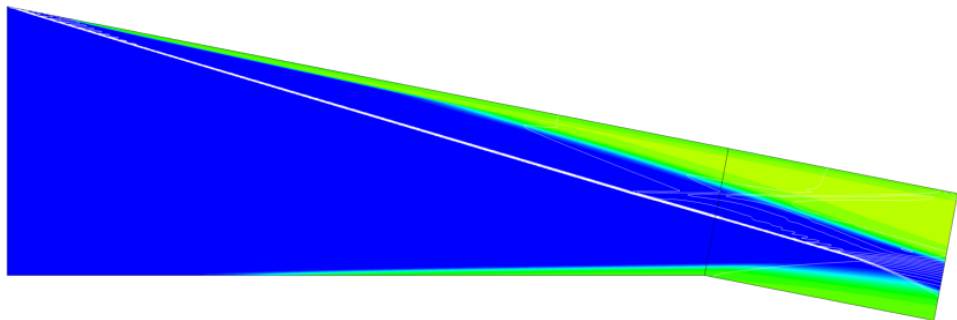
### ***4.3 Chapter Summary***

The purpose of this chapter was to examine the properties of the reacting flow system in an internal flowpath representing a notional combustor. Both ideally premixed fuel-air as well as the strut fuel-air profile as extracted from the outflow plane of the mixing study were evaluated. Two grids were used for the study, one that simulated the cowl closure shockwave as well as a constant-area duct with a length set to 1 m as well as a more refined grid in the vicinity of the cowl closure region in order to ascertain the presence of instabilities in the shock-reaction front region.

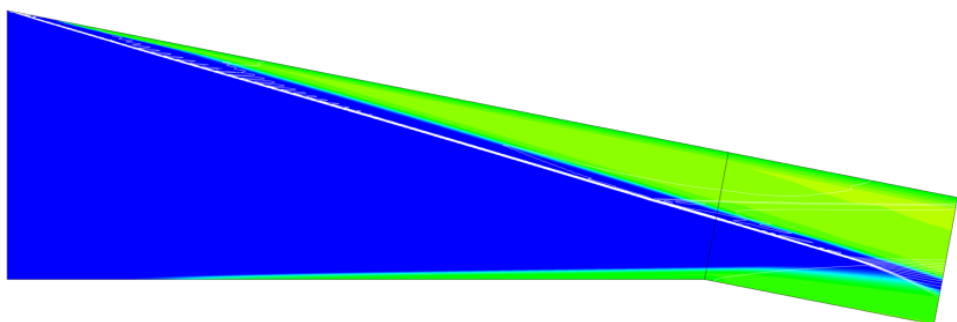
In simulating a constant area duct with reactions, the point of maximum stream thrust potential was sought. This maximum occurs at the location where gains due to the burning of the fuel and air were balanced by the losses due to viscous losses at the wall. Such a point represents the location where the flow would ideally begin to expand to the nozzle. It was noted, however, that this optimum location varied significantly depending on the point on the trajectory the vehicle is currently located. This underscores the importance of the development of variable internal geometry in



(a)



(b)



(c)

**Figure 120:** Filled contours of water mass fraction superimposed with lines of constant pressure for Mach numbers (a) 15, (a) 17, and (c) 20.

order to accommodate the maximum possible performance from the engine.

In order to evaluate the presence of instability for cases where the reaction front and shock were closely spaced, Mach numbers between 15 and 20 were simulated in the vicinity of the notional cowl leading edge with a fine grid. While the contour of the formation of  $\text{H}_2\text{O}$  closely followed the cowl shock wave at high Mach numbers, no instabilities were observed in the flow. This may be due to the low turning angle of the flow relative to other cases in the literature that show instabilities at higher turning angles.

## CHAPTER V

### QUASI-1D SHOCK & REACTION FRONT STABILITY

Instability in shock-induced combustion has been a subject of experimental attention since the early 1960's. Early classic experiments were conducted by Ruegg and Dorsey [96], Hartmuth F. Lehr [10], McVey and Toong [11], and Alpert and Toong [12] of PMSIC ahead of spherically blunted projectiles. These experiments identified three important stability regimes for such flows: stable; regular, unsteady; and large-disturbance, unsteady.

**Stable Regime** The stable regime is characterized by a reaction front and shock front with standoff distances that are invariant with time. Figure 121 shows a notional illustration of the reaction and shock front locations on the stagnation streamline as a function of time. Because combustion in this flow regime is not time varying, it is the most desirable regime for scramjet combustion.

**Regular, Unsteady Regime** The regular, unsteady regime is characterized by periodic, coupled oscillations in both the reaction and shock fronts. Figure 122 shows a notional illustration of the reaction and shock front locations on the stagnation streamline as a function of time. The currently-accepted mechanism for this behavior is as follows. First, an upstream-traveling compression wave interacts with the bow shock by pushing the shock forward and reflecting a contact discontinuity downstream. As the induction time on the upstream side of the contact discontinuity is lower due to higher temperatures compared to the downstream side, a new reaction zone forms upstream of the old reaction front. This causes compression waves to be generated and travel downstream toward the body and upstream toward the

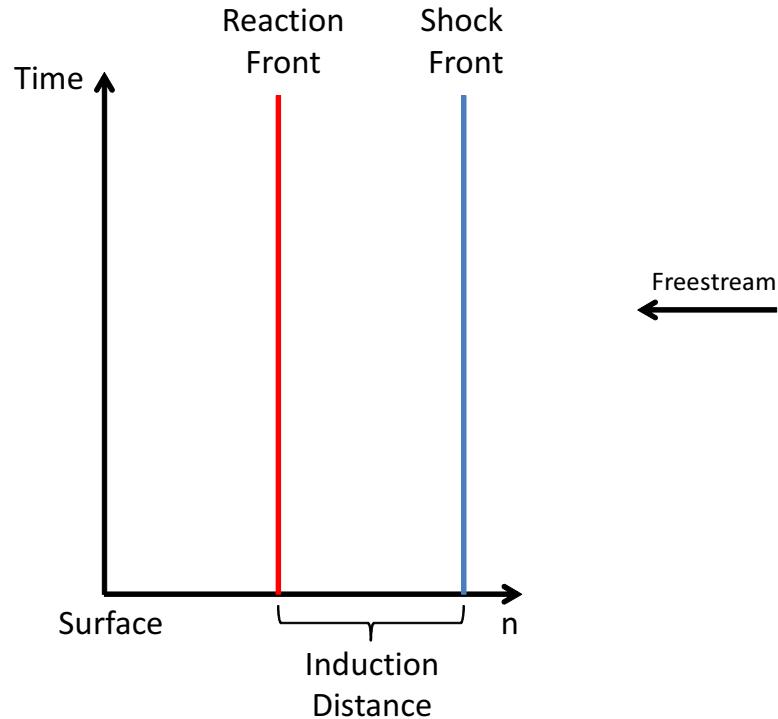


**Figure 121:** Reaction and shock front locations on the stagnation streamline as a function of time for the stable regime.

shock, eventually generating another contact discontinuity. Once the two reaction zones merge, an expansion wave travels upstream and relaxes the shock wave back downstream. This cycle repeats itself indefinitely and at regular intervals.

**Large-Disturbance, Unsteady Regime** The large-disturbance, unsteady regime is characterized by large-amplitude disturbances in the reaction zone that cause it to merge with the shock front periodically. This regime has been studied in the past by Matsuo, *et al.* [105]. Figure 123 shows a notional illustration of the reaction and shock front locations on the stagnation streamline as a function of time. In this mechanism, a deflagration-to-detonation transition (DDT) [106, 107] occurs at the point where the downstream-traveling contact discontinuity interacts with the reaction front. At this point, a retonation wave travels downstream toward the body while a detonation wave travels upstream and merges with the shock wave. Eventually the reaction and

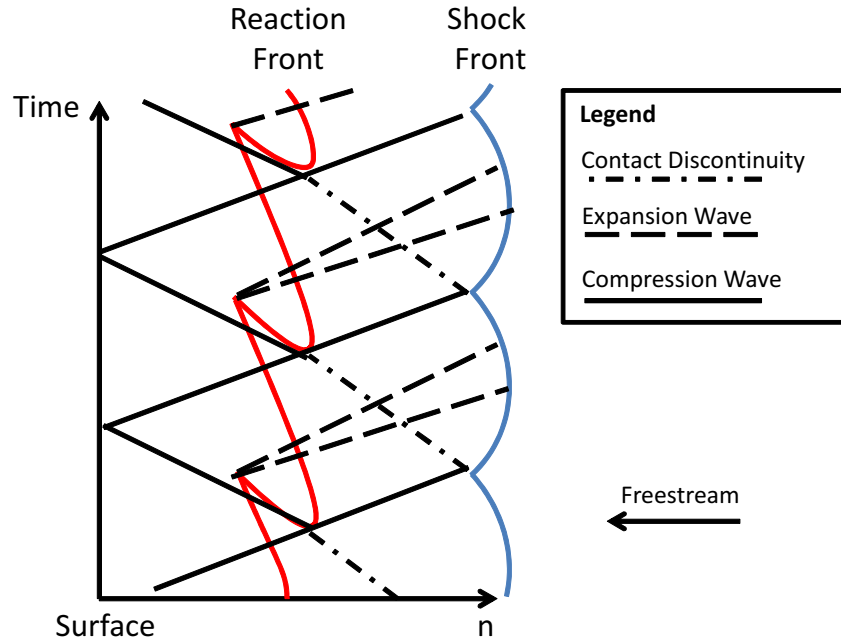


**Figure 122:** Reaction and shock front locations on the stagnation streamline as a function of time for the regular, unsteady regime.

shock fronts separate and the process repeats itself. This behavior is very large amplitude and in some cases has been observed to be non-periodic. Due to the violently unstable nature of this flow regime, it is highly undesirable for a scramjet flowpath.

Past numerical studies of PMSIC ahead of a blunted projectile [108, 105, 109, 110, 111, 112] have been carried out on two dimensional, axisymmetric grids, shown in Figure 124. Because the PMSIC phenomenon requires a reacting CFD simulation with typically high grid density, these simulations can take a very large amount of computational work to arrive at a converged solution. Because of the time-varying nature of such flows, a solution is considered to be converged when the initial, transient behaviors of the flow have passed. Due to the long clock time required for convergence and the time required at the converged condition in order to get good data for characterizing the flow, it can be difficult to understand the behavioral trends of this flow as a response to adjustments in the freestream condition (e.g. equivalence ratio, velocity, density, etc.).

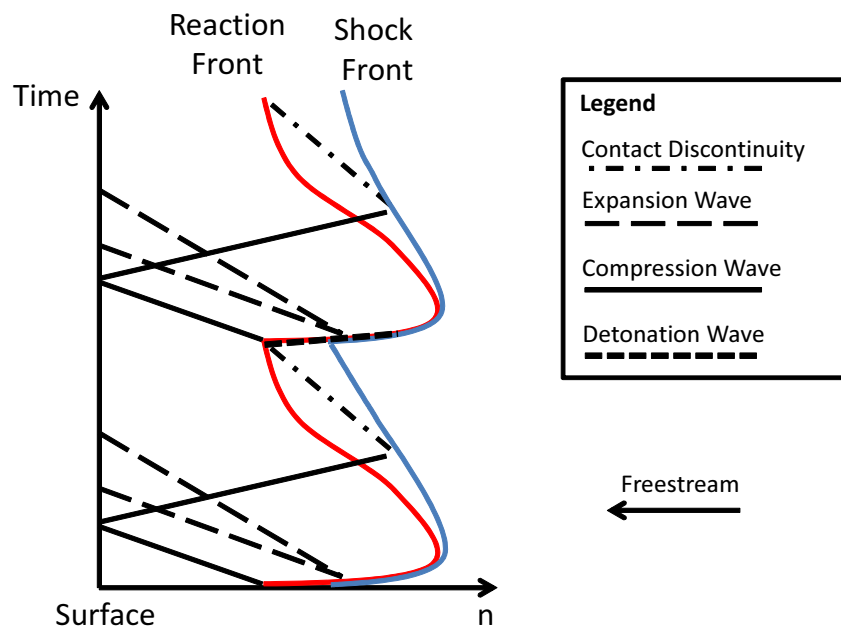


**Figure 123:** Reaction and shock front locations on the stagnation streamline as a function of time for the large-disturbance, unsteady regime.

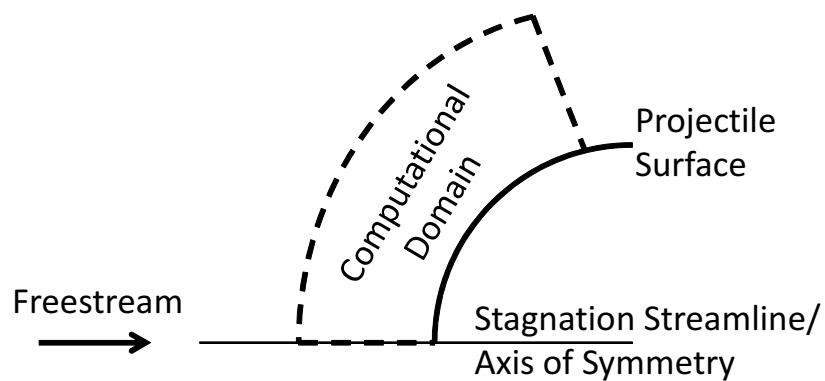


**Figure 124:** Schematic of the current state of the art for solving flow ahead of a blunt projectile.

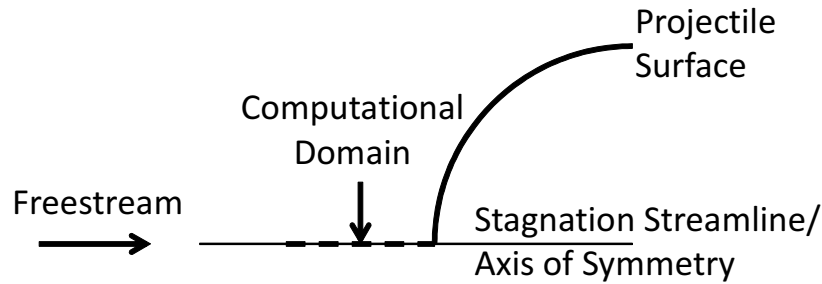


**Figure 125:** Schematic of a new way for solving flow ahead of a blunted projectile.

An advancement to the state of the art is proposed by using a quasi-1D formulation for PMSIC ahead of a blunted projectile. Previous experimental and numerical work has observed that the unsteady features of such flows are symmetric [96], suggesting that the driving mechanism is emanating around the stagnation streamline. If the flow solution is carried out only along the stagnation streamline, the computational costs associated with the multi-dimensional simulations can be greatly reduced with a minimal price paid in terms of accuracy. A schematic of such a solution domain is shown in Figure 125.

In the quasi-1D formulation, a local similarity postulation is applied to the Navier-Stokes equations. The results is a system of equations that are a function in space only as distance from the surface of the projectile. The term quasi-1D refers to the fact that the simplified governing equations account for the downstream influence by including the gradient in the tangential velocity. With the quasi-1D simulation framework in place, it is possible to rapidly determine the stability characteristics of the flow in response to variation in inflow equivalence ratio, velocity, density, fuel type, and vitiation. Variation of inflow equivalence ratio as a function of time may also be simulated in order to model the effect of vortices.

The quasi-1D formulation has high value for fundamental PMSIC research in quickly identifying the specific mechanisms of different regimes of stability with greater detail than what may be practical with multidimensional simulations. New

trends can also be quickly identified due to the ability to run many simulations in a short span of time. Large design spaces can be populated with defined regions where the different stability mechanisms exist. Beyond fundamental research, such a capability can be useful for practical engine design. For example, corridors (as a function of velocity and density) can be identified where blunt body features in the flow will not generate the instabilities seen in previous experimental and numerical work.

This purpose of this chapter will be to summarize the development, validation, and application of the quasi-1D form of the Navier Stokes equations in order to enable the rapid analysis of shock-induced combustion due to premixed fuel-air in blunt-body flow. After deriving the reduced equations, a description will follow of the physical modeling that supports the solution of the equations in a custom-built analysis tool. The tool was then validated against theory and experiment. Validating the reduced framework was a primary deliverable of the study. The framework was also be applied to conduct parameter studies previously unfeasible due to the computational demands of axisymmetric solutions.

## ***5.1 Derivation of the Quasi-1D Form of Equations***

### **5.1.1 Governing Equations**

The axisymmetric Navier-Stokes equations and species conservation equations in the body-oriented coordinate system shown in Figure 126 can be written as

$$\frac{\partial \mathbf{U}}{\partial t} + \frac{\partial \mathbf{M}}{\partial s} + \frac{\partial \mathbf{N}}{\partial n} + \mathbf{Q} = 0 \quad (12)$$

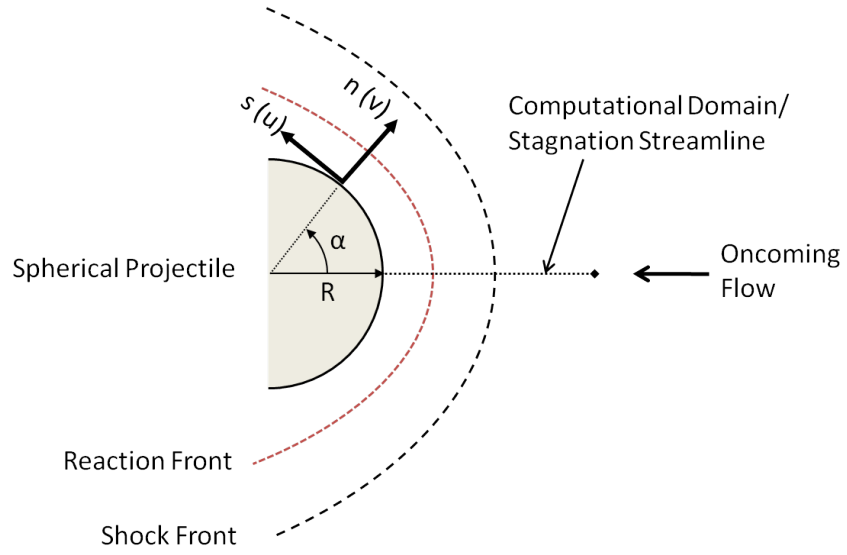


**Figure 126:** The flow schematic and coordinate system for the quasi-1D equations are shown.

The state vector ( $\mathbf{U}$ ), flux vectors ( $\mathbf{M}, \mathbf{N}$ ), and the source term vector ( $\mathbf{Q}$ ) are expressed in non-dimensional form as

$$\mathbf{U} = \lambda \begin{pmatrix} \rho \\ \rho u \\ \rho v \\ \rho E \\ \rho Y_i \end{pmatrix} \quad (13)$$

$$\mathbf{M} = \begin{pmatrix} \rho u \\ \rho u^2 - \Pi_{11} \\ \rho uv - \Pi_{12} \\ \rho Eu + q_1 - u\Pi_{11} - v\Pi_{21} \\ \rho Y_i u \end{pmatrix} \quad (14)$$

$$\mathbf{N} = \lambda \begin{pmatrix} \rho v \\ \rho uv - \Pi_{21} \\ \rho v^2 - \Pi_{22} \\ \rho Ev + q_2 - u\Pi_{12} - v\Pi_{22} \\ \rho Y_i v \end{pmatrix} \quad (15)$$

$$\mathbf{Q} = \frac{1}{\beta}(\lambda \mathbf{M} \cos \alpha + \mathbf{N} \sin \alpha) + \frac{1}{\beta} \begin{pmatrix} 0 \\ \beta k \rho uv + \lambda \Pi_{33} \cos \alpha - \beta k \Pi_{12} \\ -\beta \rho u^2 + \beta k \Pi_{11} + \lambda \Pi_{33} \sin \alpha \\ 0 \\ -\beta \lambda \dot{\omega}_i \end{pmatrix} \quad (16)$$

where  $\lambda = 1 + nk$  and  $\beta = r + n \cos \alpha$ . In these equations, variables have been non-dimensionalized with respect to free stream velocity, temperature, density, and body radius.

In order to arrive at the quasi-1D form of equations, a local similarity postulation was used in the stagnation region. Under this approach, flow variables were expanded in a series about the axis of symmetry (see Appendix A), resulting in the state equations

$$\begin{array}{l} \rho(s, n, t) = \rho_1(n, t) \\ p(s, n, t) = p_1(n, t) + p_2(n, t) \sin \alpha^2 \\ H(s, n, t) = H_1(n, t) \\ u(s, n, t) = u_1(n, t) \sin \alpha \\ v(s, n, t) = v_1(n, t) \cos \alpha \\ \text{(First Truncation)} \end{array} \left| \begin{array}{l} + \rho_2(n, t) \sin \alpha^2 + \dots \\ + p_3(n, t) \sin \alpha^4 + \dots \\ + H_2(n, t) \sin \alpha^2 + \dots \\ + u_2(n, t) \sin \alpha^3 + \dots \\ + v_2(n, t) \cos \alpha \sin \alpha + \dots \end{array} \right. \quad (17)$$

Note that the retention of the second order term in the pressure was warranted by the order of magnitude analysis. The expansions given in Equation 17 have had a small-angle approximation applied due to the result that  $s = \alpha$  for a non-dimensionalized

sphere. The solution variables in the first truncation have a simplified notation where terms in the expansion equal to zero have been removed and the remaining solution variables and their derivatives have simply been given the names of the expanded state variable with subscripts. Here  $u_1$  is actually the first derivative of velocity with respect to  $s$  and  $p_2$  is the second derivative of pressure with respect to  $s$ . All other subscripted values in the first truncation are equal to their respective state variables.

Retaining terms only to the first truncation shown in Equation 17 and substituting into Equations 13 - 16, the following set of equations is obtained for a sphere by equating the coefficients of like powers of  $\alpha$ . Note that on the stagnation streamline  $\alpha = 0$ . The governing equations are reduced to the form

$$\frac{\partial \mathbf{U}'}{\partial t} + \frac{\partial \mathbf{N}'}{\partial n} + \mathbf{Q}' = 0 \quad (18)$$

where now the solution is a function only of time and distance normal to the surface. Note that the primes have been added to indicate the quasi-1D form of the vectors. The state vector has the form

$$\mathbf{U}' = \begin{pmatrix} \rho_1 \\ \rho_1 u_1 \\ \rho_1 v_1 \\ \rho_1 H_1 - p_1 \\ \rho_1 Y_i \end{pmatrix} \quad (19)$$

The flux vector is split into contributing terms by

$$\mathbf{N}' = \mathbf{N}'_i + \mathbf{N}'_v + \mathbf{N}'_c \quad (20)$$

where each term represents the inviscid, viscous, and chemical contributions to the

flux, respectively. These terms are given by

$$\mathbf{N}'_{\mathbf{i}} = \begin{pmatrix} \rho_1 v_1 \\ \rho_1 u_1 v_1 \\ \rho_1 v_1^2 + p_1 \\ \rho_1 v_1 H_1 \\ 0 \end{pmatrix} \quad (21)$$

$$\mathbf{N}'_{\mathbf{v}} = \begin{pmatrix} 0 \\ -\frac{\mu_1}{Re_\infty} \left( \frac{\partial u_1}{\partial n} - \frac{u_1 + v_1}{1+n} \right) \\ -\frac{4}{3} \frac{\mu_1}{Re_\infty} \left( \frac{\partial v_1}{\partial n} - \frac{u_1 + v_1}{1+n} \right) \\ q_{2,visc} \\ 0 \end{pmatrix} \quad (22)$$

$$\mathbf{N}'_{\mathbf{c}} = \begin{pmatrix} 0 \\ 0 \\ 0 \\ q_{2,diff} \\ \rho_1 f_i (v_1 + \tilde{v}_1) \end{pmatrix} \quad (23)$$

In a similar fashion the source term is split up as

$$\mathbf{Q}'_{\mathbf{i}} = \frac{u_1 + v_1}{1+n} \begin{pmatrix} 2\rho_1 \\ 3\rho_1 u_1 + \frac{2}{u_1 + v_1} p_2 \\ 2\rho_1 v_1 \\ 2\rho_1 H_1 \\ 0 \end{pmatrix} \quad (24)$$

$$\mathbf{Q}'_v = \begin{pmatrix} 0 \\ \frac{\mu_1}{(1+n)Re_\infty} \left( \frac{11}{3} \frac{u_1+v_1}{1+n} - \frac{2}{3} \frac{\partial v_1}{\partial n} - 3 \frac{\partial u_1}{\partial n} \right) \\ \frac{\mu_1}{(1+n)Re_\infty} \left( 6 \frac{u_1+v_1}{1+n} - 4 \frac{\partial v_1}{\partial n} - 2 \frac{\partial u_1}{\partial n} \right) \\ \frac{2}{1+n} q_{2,visc} - \frac{\mu_1}{Re_\infty} \left[ \frac{4}{3} (u_1 + v_1) \left( \frac{u_1+v_1}{1+n} - \frac{\partial v_1}{\partial n} \right) + 2v_1 \left( \frac{\partial u_1}{\partial n} - \frac{u_1+v_1}{1+n} \right) \right] \\ 0 \end{pmatrix} \quad (25)$$

$$\mathbf{Q}'_c = \begin{pmatrix} 0 \\ 0 \\ 0 \\ \frac{2}{1+n} q_{2,diff} \\ \frac{2\rho_1 f_i (u_1+v_1+\tilde{v}_1)}{1+n} - \dot{\omega}_i \end{pmatrix} \quad (26)$$

An additional equation is required for the solution of  $p_2$ , given by

$$\frac{\partial p_2}{\partial n} = -\frac{\partial p_1}{\partial n} + \frac{\rho_1 u_1 (u_1 + v_1)}{1+n} \quad (27)$$

which comes from the  $s$ -momentum equation. This equation is decoupled from the Navier-Stokes equations and can be solved separately in a non-lagging manner.

The heat flux in the solution is composed of viscous and diffusive components, which contribute to the total heat flux according to

$$q_2 = q_{2,visc} + q_{2,diff} \quad (28)$$

where the nondimensional viscous and diffusion heat fluxes have the form

$$q_{2,visc} = -\frac{\mu_1}{Pr Re_\infty} \frac{\partial h_1}{\partial n} \quad (29)$$

$$q_{2,diff} = \rho_1 \sum_{i=1}^{species} Y_i (h_1)_i (\tilde{v}_1)_i \quad (30)$$

An additional step can be taken to convert the equations in the physical domain to the computational domain in order to streamline the handling of nonuniform grid spacing or grids that change in time. More details on this transformation can be found in Appendix B.

### 5.1.2 Boundary and Initial Conditions

The numerical solution of this problem requires the application of specific boundary conditions at the free stream wall as well as a sensible initial condition across the solution domain. The free stream boundary conditions are given by

$$u_1(\infty) = \rho_1(\infty) = T_1(\infty) = 1$$

$$v_1(\infty) = -1$$

with the boundary conditions for pressure and enthalpy given by the enthalpy and perfect gas equations. The wall conditions are set to be equal to those in the neighboring grid point with the exception of velocity. For the inviscid case  $v_1$  is set to zero at the wall and for the viscous case both  $u_1$  and  $v_1$  are set to zero.

The initial condition across the solution domain should not contain any sharp gradients in order for the solution to be convergent. Therefore, the initial condition of each variable is assumed to be monotonically increasing or decreasing depending on the initial guess for the wall conditions.

## 5.2 *Physical Modeling*

This subsection describes the thermochemical underpinnings of the tool developed to study the quasi-1D problem, the **Q**uasi-1D sol**V**er with **R**eactions (QUIVR). Although the solution domain of the problem is very simple and described elegantly by a modified form of the Navier Stokes equations, computing the thermochemical properties of each cell requires the implementation of models describing reaction rates, equilibrium constants, viscosity, conductivity, specific heat, enthalpy, entropy, and Gibbs free energy. While it is possible to leverage a computational framework to compute these quantities from first principles (e.g. statistical mechanics), it is much more practical to implement models using polynomial curve fits. Furthermore, while open source packages (i.e. CEA and Cantera) may be called upon to compute these

properties, enhanced portability and lower overhead is gained by programming these models specifically for the tool.

### 5.2.1 Nonequilibrium Chemistry

The most general description of the chemical evolution of the flow is that it is in chemical nonequilibrium. Time-accurate changes in chemical composition are addressed through the Navier-Stokes equation that conserves mass, with one equation for each species. The production rate for species  $i$  appearing in Equation 26 is given by the formula

$$\dot{\omega}_i = \frac{\partial c_i}{\partial t} m_i \quad (31)$$

here with the left hand side having the units  $kg/m^3/s$ . The concentration time rate of change of species  $i$  is given by

$$\frac{\partial c_i}{\partial t} = \sum_{j=1}^N (G_{ij} - L_{ij}) \quad (32)$$

where the right hand side is the series sum of the gain and loss terms of species  $i$  for reactions  $1, \dots, N$ . Casting the time rate of change of species concentration in terms of gain and loss terms is useful for the  $\alpha$ -QSS solution procedure outlined in Section 5.3.3. The gain and loss terms have the form

$$G_{ij} = \nu_{ij}'' q_j \quad (33)$$

$$L_{ij} = \nu_{ij}' q_j \quad (34)$$

with the rate-of-progress variable for reaction  $j$  having the form

$$q_j = k_{f,j} \prod_i c_i^{\nu_{ij}'} - k_{b,j} \prod_i c_i^{\nu_{ij}''} \quad (35)$$

for reactions not containing a third body reaction and

$$q_j = k_{f,j} \left( \sum_i e_{tb,i} c_i \right) \left( \prod_i c_i^{\nu_{ij}'} - k_{f,j} \prod_i c_i^{\nu_{ij}''} \right) \quad (36)$$

for reactions using a third body. Mechanism models using third body efficiencies typically list only species whose third body efficiencies are greater than unity for a particular reaction. All remaining unlisted species were assumed to have a third body efficiency of unity. Note that some mechanism models (e.g. Baulch, *et al.* [113]) use reactions that employ Troe parameters in order to introduce pressure dependency to certain reactions. This additional level of complexity was not accounted for in the chemistry implementation of the quasi-1D tool and was left for future work. Until then, chemistry models using Troe parameters are incompatible with the current implementation.

The forward reaction rate coefficient for each reaction was assumed to be of Arrhenius form, given by

$$k_f = C_f T^{\alpha_f} \exp\left(\frac{-b_f}{R_u T}\right) \quad (37)$$

where the reaction rate constants are generally listed in any given mechanism model along with the corresponding reaction. The backward rate coefficient is obtained simply by the relation

$$k_b = \frac{k_f}{K_c} \quad (38)$$

where the equilibrium constant in terms of concentration is calculated at a given temperature from thermodynamic data and given analytically by the equation

$$K_c = \left(\frac{R_u T}{p^0}\right)^{-\Delta n_j} \exp\left(-\frac{\Delta G_T^o}{R_u T}\right) \quad (39)$$

where

$$\Delta G_T^o = \sum_{i=1}^N \nu_{ji}'' g_{f,i}^o - \sum_{i=1}^N \nu_{ji}' g_{f,i}^o \quad (40)$$

$$\Delta n_j = \sum_{i=1}^N \nu_{ji}'' - \sum_{i=1}^N \nu_{ji}' \quad (41)$$

The presence of the reference pressure,  $p^0$ , in Equation 39 ensures that the units are consistent between the coefficient term and the exponential term.

### 5.2.2 Viscosity and Thermal Conductivity

The viscosity and thermal conductivity of the gas mixture was not computed by using a polynomial form (although such a form does exist [114]). Rather, it has been proposed that the best compromise between transport model complexity and accuracy is given by the forthcoming equations [95]. The dynamic viscosity and thermal conductivity of a monatomic species in a pure gas are given by

$$\mu_i = \frac{26.693\sqrt{m_i T}}{\sigma_i^2 \Omega^{(2,2)*}} \quad (42)$$

$$k_i = \frac{15 R_u}{4 m_i} \mu_i \quad (43)$$

The dynamic viscosity for a molecule is given by the same equation as for a monatom while the right hand side of the molecular thermal conductivity is given by

$$\frac{R_u}{m_i} \left[ \frac{15}{4} + f_{int} \left( \frac{C_{p,i}}{R_u} - \frac{5}{2} \right) \right] \mu_i \quad (44)$$

where  $f_{int} = 1.32$ , viscosity is in units of micro-Poise, and thermal conductivity is in units of cal/s/cm/K. The value of the Lennard-Jones (12-6)<sup>1</sup> collision diameter that appears in Equation 42 is species-dependent and is tabulated by Svehla [115]. The collision integral appearing in the same equation is underpinned by the bimolecular collision physics of the system and is given by

$$\Omega^{(2,2)*} = \Omega^{(1,1)*} A^* \quad (45)$$

where

$$\Omega^{(1,1)*} = a_0 + a_1 T^* + a_2 (T^*)^2 + a_3 (T^*)^3 + a_4 (T^*)^4 \quad (46)$$

$$A^* = a_0 + a_1 T^* + a_2 (T^*)^2 \quad (47)$$

The coefficients in in Equations 46 and 47 are chosen depending on the range of values in which the reduced temperature is located and are summarized in Table 20. The

---

<sup>1</sup>Twelfth-power repulsion; sixth-power attraction

coefficients are also independent of the species being considered; however, the reduced temperature in these equations is species-dependant and is given by the relation

$$T^* = \frac{T}{\epsilon/k_B} \quad (48)$$

where  $\epsilon/k_B$  is the species-dependant Lennard-Jones (12-6) energy of attraction divided by the Boltzmann constant.

For a multi-species mixture, the mixture values of dynamic viscosity and thermal conductivity must be calculated. Mixture viscosity is given by Wilke [116] as

$$\mu_{mix} = \sum_{i=1}^N \frac{\mu_i}{1 + \frac{1}{\chi_i} \sum_{j=1, j \neq i} \chi_j \psi_{ij}} \quad (49)$$

where

$$\psi_{ij} = \frac{\frac{\sqrt{2}}{4} \left[ 1 + \left( \frac{\mu_i}{\mu_j} \right)^{\frac{1}{2}} \left( \frac{m_j}{m_i} \right)^{\frac{1}{4}} \right]^2}{\left[ 1 + \frac{m_i}{m_j} \right]^{\frac{1}{2}}} \quad (50)$$

The mixture thermal conductivity is approximated by Coffee and Himerl [117] as

$$k_{mix} = \frac{1}{2} \left[ \sum_{i=1}^N \chi_i k_i + \left( \sum_{i=1}^N \frac{\chi_i}{k_i} \right)^{-1} \right] \quad (51)$$

### 5.2.3 Diffusion Velocity

The calculation of the species diffusion velocity arises in the species conservation equation. The general method for determining diffusion velocities requires the solution of systems of equations; however, a simpler method is commonly used in practice. An approximate calculation based on Fick's law of the first  $N - 1$  species velocities is given by the equation

$$\tilde{\mathbf{v}}_i = -\frac{D_{im}}{f_i} \nabla \mathbf{f}_i \quad (52)$$

while the  $N^{th}$  species diffusion velocity—typically computed for the species in excess—is given from conservation form as [118]

$$\tilde{\mathbf{v}}_N = -\frac{1}{f_N} \sum_{i=1}^{N-1} f_i \tilde{\mathbf{v}}_i \quad (53)$$

**Table 20:** Coefficients of fourth-order polynomial fits of reduced collision integrals. Integrals are expressed as  $I(T^*) = a_0 + a_1 T^* + a_2 T^{*2} + a_3 T^{*3} + a_4 T^{*4}$

$I$	$T^*$	$a_0$	$a_1$	$a_2$	$a_3$	$a_4$
$\Omega^{(1,1)*}$	< 5.0	0.23527333E+01	-0.13589968E+01	0.52202460E+00	-0.94262883E-01	0.64354629E-02
	5.0 - 10.0	0.12660308E+01	-0.16441443E+00	0.22945928E-01	-0.16324168E-02	0.45833672E-04
	> 10.0	0.85263337E+00	-0.13552911E-01	0.26162080E-03	-0.24647654E-05	0.86538568E-08
$A^*$	< 5.0	0.11077725E+01	-0.94802344E-02	0.16918277E-02		
	5.0 - 10.0	0.10871429E+01	0.31964282E-02	-0.892885689E-04		
	> 10.0	0.11059000E+01	0.65136364E-03	-0.34090910E-05		
$A^*_{H_2O}$	< 10.0	0.10764205E+01	0.46037515E-01	-0.13506975E-01	0.15404522E-02	-0.60887567E-04
	> 10.0	0.11141689E+01	0.48711959E-03	-0.44570091E-05	0.99643413E-08	0.68639118E-10

which ensures that the species diffusion fluxes sum to zero.

The effective mixture binary diffusion coefficient of species  $i$  is given by

$$D_{im} = \frac{1 - \chi_i}{\sum_{j \neq i}^N \frac{\chi_j}{D_{ij}}} \quad (54)$$

which combines the species binary diffusion coefficients. The binary diffusion coefficients are defined by collision integrals that must be approximated for a practical implementation here. The first approximation is given by [95]

$$D_{ij} = 0.002628 \frac{\sqrt{T^3/(2m_{ij})}}{p\sigma_{ij}^2\Omega^{(1,1)*}} \quad (55)$$

where the units of  $D_{ij}$  is  $cm^2/s$ ,  $p$  is atm,  $T$  is K.

The reduced mass and combined Lennard-Jones (12-6) parameters contained in the preceding equations are each computed according to the equations

$$m_{ij} = \frac{m_i m_j}{m_i + m_j} \quad (56)$$

$$\sigma_{ij} = \frac{1}{2}(\sigma_i + \sigma_j) \quad (57)$$

$$\epsilon_{ij} = \sqrt{\epsilon_i \epsilon_j} \quad (58)$$

#### 5.2.4 Specific Heat, Enthalpy, Entropy, and Gibbs free energy

The specific heat at constant pressure, enthalpy, and entropy were computed for each species in the gas mixture according to the polynomial equation used by McBride, *et al.* [119], given as

$$\frac{C_p}{R_u} = a_1 T^{-2} + a_2 T^{-1} + a_3 + a_4 T + a_5 T^2 + a_6 T^3 + a_7 T^4 \quad (59)$$

$$\frac{h}{R_u T} = -a_1 T^{-2} + a_2 T^{-1} \ln T + a_3 + a_4 \frac{T}{2} + a_5 \frac{T^2}{3} + a_6 \frac{T^3}{4} + a_7 \frac{T^4}{5} + a_8 T^{-1} \quad (60)$$

$$\frac{s}{R_u} = -a_1 \frac{T^{-2}}{2} - a_2 T^{-1} + a_3 \ln T + a_4 T + a_5 \frac{T^2}{2} + a_6 \frac{T^3}{3} + a_7 \frac{T^4}{4} + a_9 \quad (61)$$

where the coefficients for each species are given in the same reference and is the same form used by the NASA Glenn program CEA. There are two sets of coefficients

for each equation, one for the temperature ranging between 200 K and 1000 K and another for the temperature ranging between 1000 K and 6000 K. Computing the thermodynamic properties of the flow in such a matter is a simple yet accurate method to do so.

The computation of Gibbs free energy, required when computing the equilibrium constant of a reaction, uses the thermodynamic relation

$$g = h - Ts \quad (62)$$

where enthalpy and entropy are simply the values computed from Equations 60 and 61.

### 5.3 Solution Methodology

#### 5.3.1 MacCormack's Method

MacCormack's method [120] is a finite difference predictor-corrector scheme that is second-order accurate in both time and space. The method has two steps. In the first step the conserved variables in the temporal term are calculated at a temporary time step by the equation

$$\mathbf{U}_i^{\overline{t+\Delta t}} = \mathbf{U}_i^t + \Delta t \left( \frac{\partial \mathbf{U}}{\partial t} \right)_i^t \quad (63)$$

Note that the temporary time step is denoted by  $\overline{t+\Delta t}$ . The time derivative in Equation 63 is given by

$$\left( \frac{\partial \mathbf{U}}{\partial t} \right)_i^t = - \left( \frac{\partial \mathbf{N}}{\partial n} \right)_i^t - \mathbf{Q}_i^t \quad (64)$$

where the spatial derivative is given by a first-order forward difference at the initial time step. At this point the elements of the conserved vector  $\mathbf{U}_i^{\overline{t+\Delta t}}$  may be used to obtain the primitive variables for use in the corrector step.

The corrector step obtains the conserved variables at the next time step according to the equation

$$\mathbf{U}_i^{t+\Delta t} = \frac{1}{2} \left[ \mathbf{U}_i^{\overline{t+\Delta t}} + \mathbf{U}_i^t + \Delta t \left( \frac{\partial \mathbf{U}}{\partial t} \right)_i^{\overline{t+\Delta t}} \right] \quad (65)$$

Again, the time derivative at the temporary time step is given by

$$\left(\frac{\partial \mathbf{U}}{\partial t}\right)_i^{t+\Delta t} = -\left(\frac{\partial \mathbf{N}}{\partial n}\right)_i^{t+\Delta t} - \mathbf{Q}_i^{t+\Delta t} \quad (66)$$

where the spatial derivative is given by a first-order backward difference at the temporary time step. This process is repeated until a convergence criterion is satisfied.

### 5.3.2 Numerical Damping

Numerical damping is required in a shock-capturing scheme in order to dampen the Gibbs ringing phenomenon around areas of large gradient in the solution domain such as the shock wave. The term describing numerical damping at each grid point has the form

$$D_\phi = \frac{S_\phi |\phi_{i+1} - 2\phi_i + \phi_{i-1}|}{(1 - \omega_\phi)\phi_{TVD} + \omega_\phi \Phi_i} (v_i + a_i) \frac{\partial \mathbf{U}}{\partial n} \quad (67)$$

where

$$\phi_{TVD} = |\phi_{i+1} + \phi_i| + |\phi_i - \phi_{i-1}| \quad (68)$$

$$\Phi_i = \phi_{i+1} + 2\phi_i + \phi_{i-1} \quad (69)$$

$$a_1 = \sqrt{\gamma \frac{p_1}{\rho_1}} \quad (70)$$

The placeholder variable  $\phi$  represents any variable used in the damping expression, for example pressure, temperature, or species concentration. If multiple variables are used in the damping scheme simply add each to the PDE, which at spatial step  $i$  takes the form

$$\left(\frac{\partial \mathbf{U}}{\partial t}\right)_i^t + \left(\frac{\partial \mathbf{N}}{\partial n}\right)_i^t + \mathbf{Q}_i^t + (D_{\phi_1} + D_{\phi_2} + \dots)_i^t \quad (71)$$

The damping term should be updated for each step of the MacCormack method. Note that when differencing the flux vector in the damping equation, the opposite type of differencing should be used. For example, if forward differencing is currently

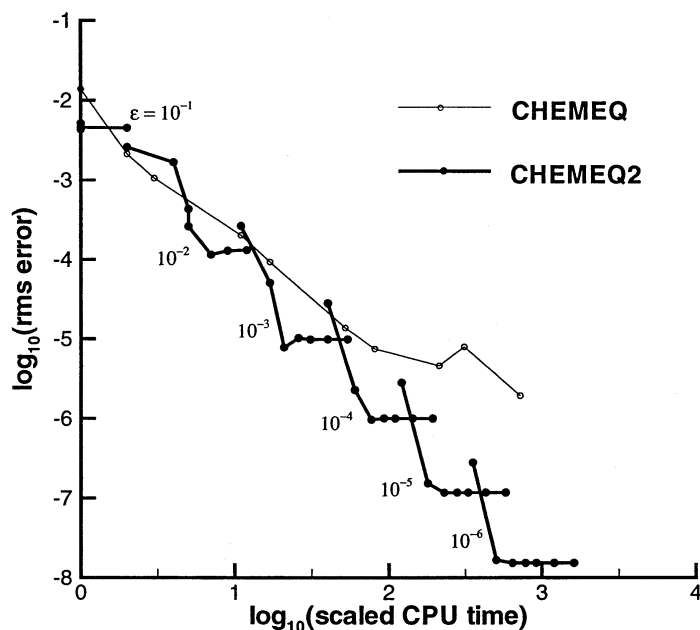


**Figure 127:** Comparison of the CHEMEQ algorithm and the CHEMEQ algorithm using  $\alpha$ -QSS. [84]

being used in the MacCormack scheme, backwards differencing should be used for the damping term and vice versa.

### 5.3.3 Finite-Rate Chemistry

The chemistry solution uses an algorithm described by Mott, *et. al* [84] known as  $\alpha$ -QSS. The  $\alpha$ -QSS algorithm is a methodology designed specifically for solving the stiff system of equations present in reacting systems. In his paper, Mott demonstrates that when the commonplace CHEMEQ algorithm's hybrid method<sup>2</sup> is replaced by the  $\alpha$ -QSS method (called CHEMEQ2), more rapid convergence is achieved over standard CHEMEQ as shown in Figure 127. The algorithm also benefits from very small overhead and storage requirements.

The method begins with the decomposition of the species rate of change term into

<sup>2</sup>A hybrid method is one that chooses stiff or non-stiff integration depending on the time scale of the equation to be integrated.

production and loss terms by the equation

$$\frac{dc_i}{dt} = G_i - p_i c_i \quad (72)$$

where  $G_i$  is the production rate of species  $i$  and  $p_i c_i$  is the loss rate. This form of the species production equation is chosen because for constant  $p$  and  $G$ , the equation has an exact solution that forms the basis of this method (and quasi-steady-state methods in general). In fact, for  $G$  and  $p$  which are slowly varying over a particular timestep, the exact solution represents an approximate, first-order version of a quasi-steady-state algorithm.

The exact solution of Equation 72 is recast in an convenient algebraic form to yield the basis for a predictor-corrector formulation upon which the algorithm depends. The predictor and corrector equations are simply

$$c_p = c_0 + \Delta t_{chem} \frac{G_0 - L_0}{1 + \alpha \Delta t_{chem} p_0} \quad (73)$$

$$c_c = c_0 + \Delta t_{chem} \frac{\bar{G} - c_0 \bar{p}}{1 + \alpha \Delta t_{chem} \bar{p}} \quad (74)$$

where the subscript 0 indicates the initial value,  $p$  the predicted value, and  $c$  the corrected value. The predictor-corrector equation set is iterated upon (with the corrected value of one iteration being used as the predicted value of the next) until convergence is achieved. Weighted parameters appearing in Equations 73 and 74 are given by

$$\bar{p} = \frac{1}{2}(p_0 + p_p) \quad (75)$$

$$\bar{G} = \bar{\alpha} G_p + (1 - \bar{\alpha}) G_0 \quad (76)$$

with

$$p_0 = \frac{L_0}{c_0 + \epsilon_m} \quad (77)$$

$$p_p = \frac{L_p}{c_p + \epsilon_m} \quad (78)$$

The inclusion of the machine epsilon terms in the denominators is a practical consideration in order to avoid divide-by-zero errors for species with no concentration.

The  $\alpha$  parameter, which arises due to the convenient algebraic form of Equation 73 and 74, is actually a function of  $p\Delta t$  and contains exponential terms. Because exponentials are not well suited to numerical computation, a polynomial approximation to  $\alpha$  is desired. Using the Pade approximation,

$$\alpha = \frac{180r^3 + 60r^2 + 11r + 1}{360r^3 + 60r^2 + 12r + 1} \quad (79)$$

$$\bar{\alpha} = \frac{180\bar{r}^3 + 60\bar{r}^2 + 11\bar{r} + 1}{360\bar{r}^3 + 60\bar{r}^2 + 12\bar{r} + 1} \quad (80)$$

where

$$r = (p_0\Delta t_{chem} + \epsilon_m)^{-1} \quad (81)$$

$$\bar{r} = (\bar{p}\Delta t_{chem} + \epsilon_m)^{-1} \quad (82)$$

If at any point during the iteration cycle  $c_c - c_p < \epsilon_m c_c$  for all species, the chemistry is converged over the chemical time step for the cell.

While it is tempting to simply run the  $\alpha$ -QSS predictor-corrector algorithm over the entire fluid dynamic time step, stability considerations dictate that the fluid dynamic time step actually be partitioned into much smaller chemical time steps with chemical integrations occurring over each partition. The initial chemical timestep is chosen to be the same as for the previous global iteration (with the initial timestep chosen to be some arbitrarily small value). If the predictor-corrector loop fails over a particular chemical timestep, the iteration is restarted by multiplying the chemical timestep by 1/3. If the predictor-corrector step is successful, the time step is allowed to grow according to the equation

$$\Delta t_{chem,new} = \Delta t_{chem,old} \left( \frac{1}{\sigma} + 0.005 \right) \quad (83)$$

where

$$\sigma = \frac{y_c - y_p}{vy_c} \quad (84)$$

with  $v = 0.001$  and  $\sigma$  chosen to be the largest among the different species.

## 5.4 Validation

The ability of QUIVR to properly predict the physics of high temperature, reacting flow along the stagnation streamline will now be summarized. Validation can be achieved by comparing the results produced by QUIVR against experimental, theoretical, and numerical results present in the literature. The validation questions can be summarized as follows:

Can QUIVR...

- ...successfully reproduce the stagnation point heat transfer experienced by stagnated flows?
- ...reproduce the space-varying thermodynamic properties in the shock layer?
- ...match the reaction front oscillation frequencies and regimes of stability observed in the literature?

### 5.4.1 Stagnation Point Heat Transfer

Comparing the wall heating computed by QUIVR to the theoretical relationship of Fay and Riddell [121] is a useful validation study to ensure the code is properly computing heating and boundary layer properties. The Fay and Riddell relation for wall heat flux without chemical dissociation is given by the equation

$$\bar{q}_w = 0.76Pr^{-0.6}(\bar{\rho}_e\bar{\mu}_e)^{0.4}(\bar{\rho}_w\bar{\mu}_w)^{0.1}\sqrt{\frac{d\bar{u}_e}{d\bar{s}}}(\bar{h}_0 - \bar{h}_w)\left[1 + (Le^{0.52} - 1)\frac{\bar{h}_D}{\bar{h}_0}\right] \quad (85)$$

where the overline above certain quantities indicate that the quantity is dimensioned. Furthermore, the subscript  $e$  denotes boundary layer edge properties and  $w$  denotes wall properties. Because the velocity vector is directed toward the body, the boundary layer edge is defined here to be the distance from the wall where the stagnation enthalpy is within 1% of the freestream value. It should also be noted that the

numerical correlation of Equation 85 is only valid for a range of parameters for  $Pr = 0.71$ , those being

- $Le = 1.0, 1.4, \text{ or } 2.0$
- $300 \text{ K} < T_w < 3000 \text{ K}$
- $1770 \text{ m/s} < v_\infty < 6950 \text{ m/s}$
- $7620 \text{ m} < h < 35,570 \text{ m}$

Because the QUIVR solution is in terms of dimensionless quantities, it is convenient to recast the Fay and Riddell relation in a nondimensional form. This is accomplished simply by substituting each dimensional term in the equation by the nondimensional version times the nondimensionalizing factor. This results in the following equation, with the dissociative enthalpy term removed because this validation study is not considering dissociation,

$$\dot{q}_w = \frac{0.76}{\sqrt{Re_\infty}} Pr^{-0.6} (\rho_e \mu_e)^{0.4} (\rho_w \mu_w)^{0.1} \sqrt{\frac{du_e}{ds}} (h_0 - h_w) \quad (86)$$

Note that the  $du_e/ds$  term references the edge velocity gradient in the direction parallel to the surface. In most applications it is typical to use the approximation  $du_e/ds \approx 1/r_n \sqrt{2(p_w - p_\infty)/\rho_w}$ , which is the modified Newtonian approximation of the edge velocity gradient. However, because the quasi-1D formulation actually solves this term directly (recall that  $u_1 = du/ds$ ), it is best in this case to simply utilize the solved value of  $u$ .

The test case used to validate the heat flux calculation was selected to lie within the valid range of the Fay and Riddell relation. A 63.5 mm diameter projectile traveling at 1770 m/s in ambient air at 35 km conditions and with a wall temperature of 3000 K was chosen as the test case. At 35 km,  $T_\infty = 237 \text{ K}$ ,  $p_\infty = 558 \text{ Pa}$ , and  $M_\infty = 5.72$  (from the velocity chosen), and  $Re_\infty = 29,470$ . The gas was chosen to be calorically

**Table 21:** Comparison of Fay and Riddell with the QUIVR solution of heat flux for the validation case.

	$(\rho_1)_e$	$(\mu_1)_e$	$(\rho_1)_w$	$(\mu_1)_w$	$(u_1)_e$	$(h_1)_0$	$(h_1)_w$	$(q_2)_w$
QUIVR Solution	5.584	4.230	3.363	5.941	0.718	0.576	0.966	0.00855
Fay and Riddell	-	-	-	-	-	-	-	0.00858
% Difference								0.34 %

perfect throughout the flow. The 401 point computational grid with  $n_{max} = 0.18$  was clustered near the wall in order to get high boundary layer resolution as heat flux is highly sensitive to spacing near the wall.

The converged heat flux as a function of distance from the projectile wall is shown in Figure 128. Note that in the freestream and behind the shock wave the heat flux remained at zero until the boundary layer is encountered. There is a nonphysical spike in the heat flux going through the shock wave which is a consequence of the shock capturing nature of the solution. The width of the spike, corresponding to the thickness of the shock wave, is of little consequence to the solution sought here where high resolution near the wall is preferred to a thinly resolved shock wave. Table 21 shows a comparison of the QUIVR solution of wall heat flux and the value obtained from Equation 86 using edge and wall values obtained from the QUIVR solution. There was observed to be only a 0.34% difference in wall heating values, thereby lending confidence to the handling of heat flux in the QUIVR code.

#### 5.4.2 Thermodynamic Properties in the Shock Layer

Tracking the variation of properties in the shock layer of a sphere in hypersonic flow is another way to validate the behavior of the QUIVR code. Freestream conditions were referenced from Kumar and Graves [122], which provides a data set against which to compare the results of QUIVR. While the reference data was computed for a spherically-blunted cone, along the stagnation streamline the solution was comparable to the spherical case. The simulated freestream conditions were  $M_\infty = 10.33$ ,  $p_\infty =$

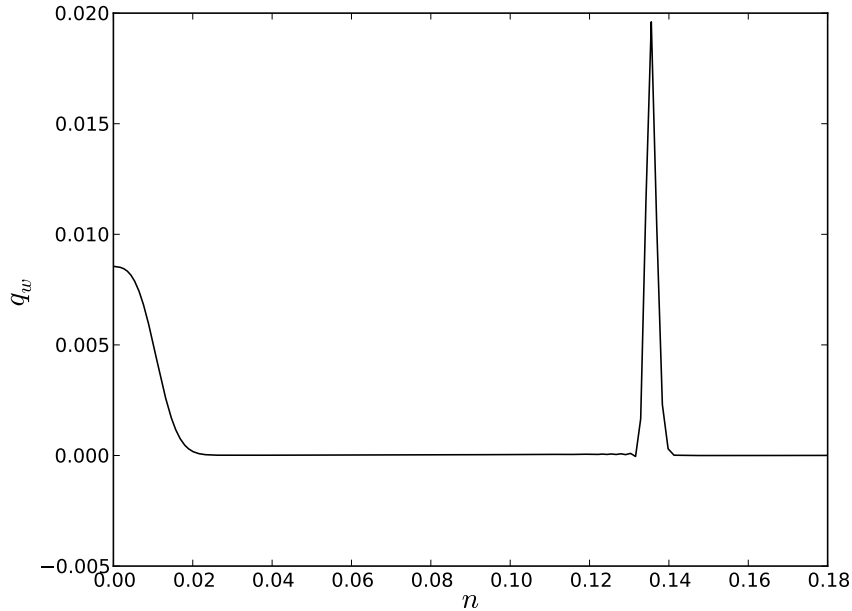


**Figure 128:** The solution of nondimensional heat flux as a function of distance from the wall is shown for a 63.5 mm projectile with  $T_w = 3000$  K and traveling at  $M_\infty = 5.72$  at an altitude of 35 km.

100.77 Pa, and  $T_\infty = 46.26$  K. These conditions approximately correspond to high-altitude, hypersonic flight. The simulation used a thermally perfect mixture of oxygen and nitrogen at atmospheric proportions. The wall temperature was set isothermally as 330.6 K. The nose radius was set to 0.03175 m. The grid consisted of 401 grid points equally spaced from the wall to  $n_{max} = 0.15$ .

The results of the analysis in Figures 129 and 130 show  $\rho/\rho_{shock}$  and  $T/T_{shock}$  as a function of distance from the wall normalized by shock standoff distance. It was observed that the numerical solution can accurately reproduce the reference density and temperature profiles from the shock to the wall. It was also observed that the boundary layer thickness was well captured by the simulation.

### 5.4.3 Qualitative Comparison to Experiment and Numerical Simulation

The experiments of Ruegg and Dorsey [96] were simulated using the quasi-1D code in order to qualitatively assess the suitability of the proposed analysis method. Ruegg

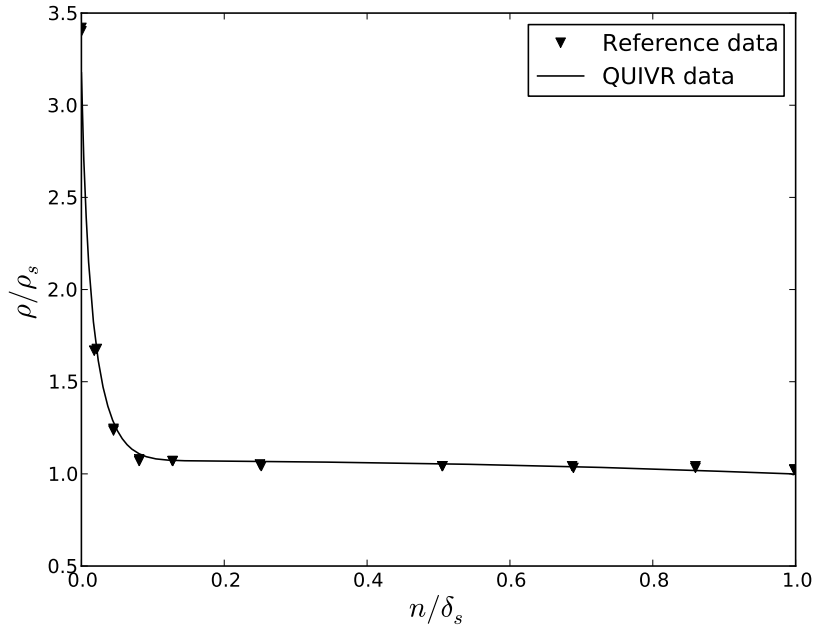


**Figure 129:** Comparison of QUIVR  $\rho/\rho_{shock}$  result in shock layer compared to reference data.

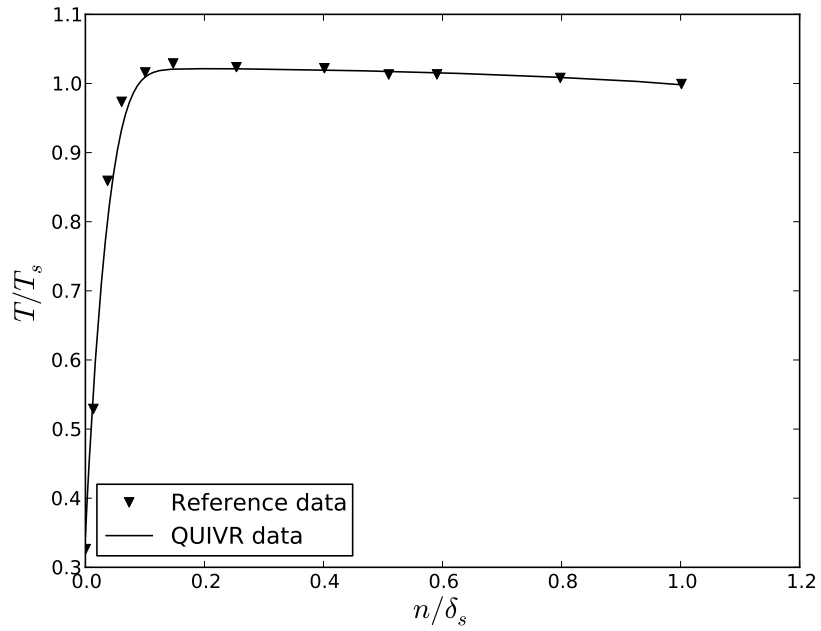


**Figure 130:** Comparison of QUIVR  $T/T_{shock}$  result in shock layer compared to reference data.

and Dorsey conducted early experiments on PMSIC by firing spherical, 20 mm diameter projectiles into a stoichiometric hydrogen-air mixture in the vicinity of Mach 5 at pressures ranging from 0.1 to 0.5 atm. Over the range of experimental conditions investigated, three distinct regimes of behavior of the reaction/shock front system were observed: stable; regular, unsteady; and large-disturbance, unsteady. A qualitative comparison between the quasi-1D simulation results and experimental shadowgraphs at the conditions in Table 22 will now be made. The simulated results consist of an evolution of water mass fraction and pressure on the stagnation streamline as a function of non-dimensionalized time and distance ( $n$ ) from the surface of the projectile.

**Table 22:** Selected Ruegg and Dorsey experimental conditions for a 20 mm diameter, spherical projectile fired into premixed, stoichiometric hydrogen/air.

Case	$M_\infty$	$p_\infty$ (atm)	$T_\infty$ (K)	Stability Regime
1	5	0.10	300	Stable
2	4.9	0.25	300	Regular, Unsteady
3	4.3	0.5	300	Large Disturbance

Figure 131 shows quasi-1D simulation and experimental results for the stable regime of oscillation. The simulated and experimental results indicate reaction and shock front locations that were invariant with time. This time independence was observed experimentally by smooth shock and reaction fronts. The reaction and shock fronts were separated by a relatively large induction distance with no direct interaction between the two beyond the shock wave raising the temperature of the hydrogen/air mixture above its autoignition limit. There was qualitative agreement between simulation and experiment for this case.

The regular instability regime is reproduced in Figure 132. The experimental shadowgraph shows a corrugated pattern in the wake of the sphere caused by an oscillation in density due to the periodic creation of new reaction fronts in the stagnation region of the flow. Between the corrugated, burned region of gas and the shock

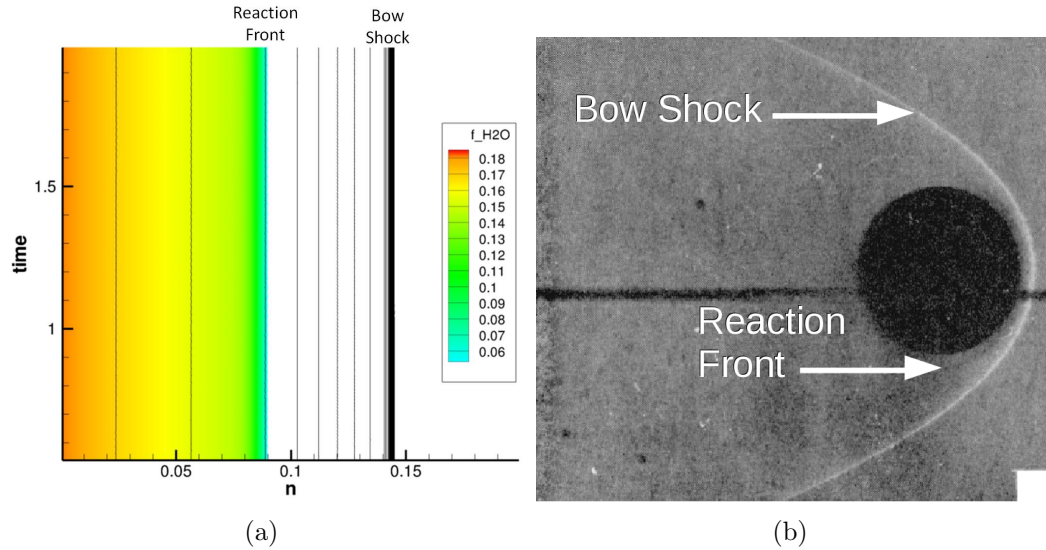


**Figure 131:** (a) Contours of water mass fraction on the stagnation streamline overlaid with contour lines of pressure as a function of non-dimensional time for Ruegg and Dorsey experiment Case 1. (b) An annotated experimental shadowgraph captured by Ruegg and Dorsey for the same conditions is shown for comparison.

wave lies a region of unburned gas. This is due to the induction time between the bow shock and the reaction front. Lines of density variation in the unburned region are due to periodic contact discontinuities traveling from the bow shock to the beginning of each new reaction zone. The contact discontinuities are not visible in the simulated results in this figure because contour lines of pressure are shown (pressure being equal on both sides of a contact discontinuity). The contact discontinuities in the computations will be visible in later figures when the computed results are compared to established 1D mechanisms. There is qualitative agreement between the experiment and the present computations because the physical mechanism observed in the simulated results match the flow features witnessed in the experimental shadowgraph.

The large-disturbance instability regime is shown in Figure 133. Experimental results of the flow at the Case 3 condition show a large-amplitude heaving of both the bow shock and the reaction front. Both the bow shock and reaction zone oscillate with a much lower frequency than that observed in the regular regime and apparently non-periodic features are visible in the shadowgraph. Although both the experiment

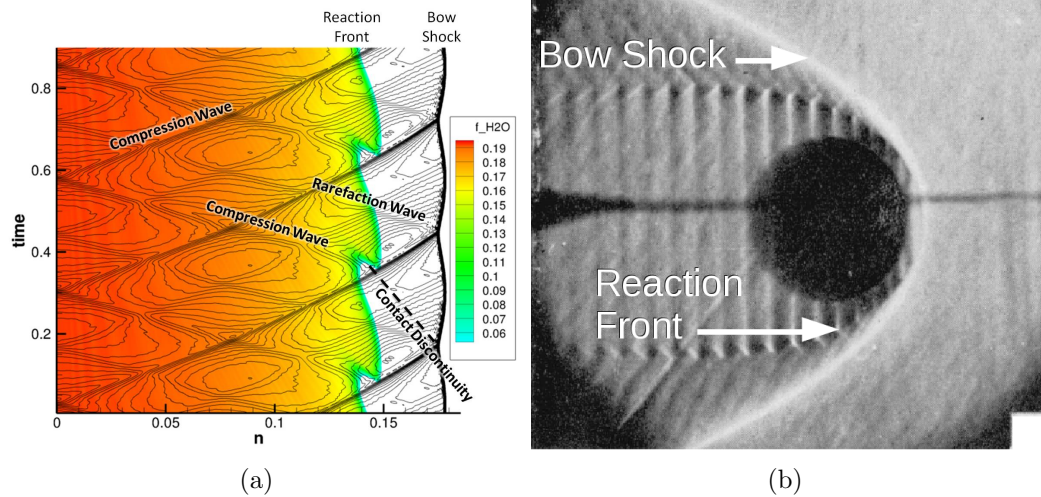


**Figure 132:** (a) Contours of water mass fraction on the stagnation streamline overlaid with contour lines of pressure as a function of non-dimensional time for Ruegg and Dorsey experiment Case 2. The drawn contact discontinuity is approximated based on separate density contours. (b) An annotated experimental shadowgraph captured by Ruegg and Dorsey for the same conditions is shown for comparison.

and the present numerical results show large amplitude behavior, it is difficult to isolate other features to determine how well the quasi-1D simulation is performing. For further comparison, the present results are compared to a higher-fidelity, 2D simulation. Figure 134 shows a zoomed-in view of a section of the present quasi-1D simulation compared to a segment of a simulation at the same conditions conducted by the author using VULCAN. These images show contours of density as a function of time and distance along the stagnation streamline. The present results show a striking agreement with the high-fidelity numerical result and clearly show coinciding features of reaction shocks, retonations, contact discontinuities, and a superdetonation as the bow shock is penetrated by the reaction front. These features will be discussed in further detail later, but for now it appears that the quasi-1D results are capable of predicting the large-disturbance instability regime.

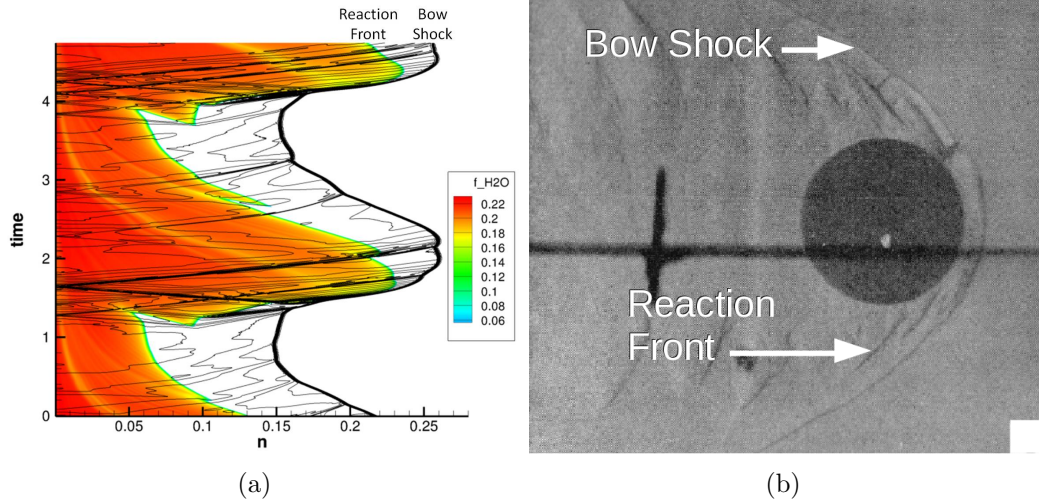


**Figure 133:** (a) Contours of water mass fraction on the stagnation streamline overlaid with contour lines of pressure as a function of non-dimensional time for Ruegg and Dorsey experiment Case 3. (b) An annotated experimental shadowgraph captured by Ruegg and Dorsey for the same conditions is shown for comparison.

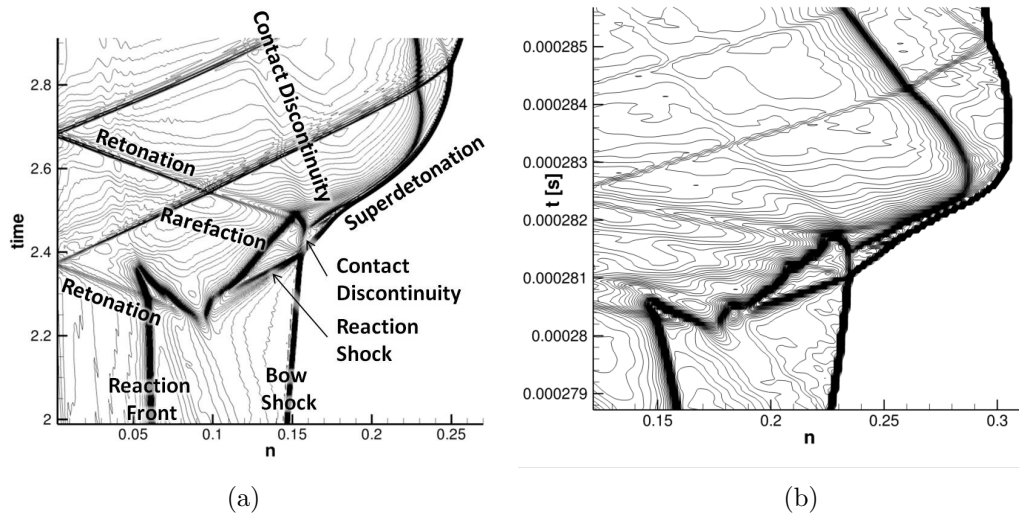


**Figure 134:** A detail view of density contours on the stagnation streamline as a function of time for Case 3 for the (a) QUIVR quasi-1D simulation and (b) high-fidelity, 2D simulation produced using VULCAN. Note that the computed results are non-dimensional in time while the high-fidelity plot is in seconds.

#### 5.4.4 Quantitative Reaction Front Oscillation Frequency

The current analysis approach has been applied to simulate the ballistic experiments conducted by H.F. Lehr [10] in which 15 mm diameter projectiles were fired into a stationary, premixed, stoichiometric hydrogen/air mixture at near-hypersonic speeds. The ambient conditions of the fuel-air mixture had a static temperature and pressure of 292 K and 0.42 atm, respectively. Before the results from the current study are discussed, some quick observations are made about Lehrs experiments and the numerical simulations by Sussman [98].

Lehr investigated the behavior of the reacting system over a wide range of velocities, 1685 to 2058 m/s. For each case, the frequency of oscillation of the reaction front was determined using shadowgraph images and considering the distance between successive striations in the wake of the sphere. Lehr found that as projectile velocity increased the frequency of oscillation increased monotonically. At high projectile velocities an overdriven detonation occurred which caused an apparently stable reaction front.

The Chapman-Jouguet detonation velocity of a stoichiometric hydrogen-air mixture with initial conditions as that of the Lehr experiments was calculated to be 1957 m/s using the Chemical Equilibrium with Applications (CEA) program developed at NASA Glenn by McBride and Gordon [123, 114]. This velocity is sensitive to species present—in this case only the species H, O, OH, H<sub>2</sub>O, HO<sub>2</sub>, H<sub>2</sub>, O<sub>2</sub>, and N<sub>2</sub> were allowed as product species. The experimental value reported by Lehr was 2030 m/s, corresponding to the velocity past which oscillations in the reaction front were no longer visible. It should be noted, however, that other analyses have established that oscillations might occur above the Chapman-Jouguet detonation velocity. For example, the experiments of Alpert and Toong [12] found oscillations in the overdriven range of flight and modern numerical analyses have also substantiated this observation [110, 111, 112].

Sussman [98] simulated the axisymmetric flow around a 15 mm diameter sphere at the same ambient conditions and freestream velocities studied by Lehr using an upwind, TVD scheme. The oncoming flow is composed of a stoichiometric hydrogen-air mixture. In general, the numerical results of Sussman matched well with the experimental results with the exception of cases near the high velocity limit. A large discrepancy was observed at 2058 m/s, which was postulated to be due to the method of interpreting the experimental frequency at that point. However, the experimental oscillation frequency at this point was successfully replicated in numerical work done around the same time by Ahuja [110, 111, 112]. At a projectile velocity of 2119 m/s, Lehr showed no oscillation although the numerical work by Ahuja showed oscillations occurring all the way to 2605 m/s; however, at this point they were of very small amplitude and located away from the stagnation streamline. Sussman was able to simulate oscillations for the 2119 m/s case but not for the 2605 m/s case.

Figure 135 and Table 23 show results from the quasi-1D simulations over the velocity range studied by Lehr and Sussman. Note that due to the reduced computing requirements of the quasi-1D simulation, a large number of cases are computed over the velocity range of the experiment versus previous numerical studies. In doing so, a better idea as to the general shape and limits of the parameter space is obtained. It is observed that, in general, the present results are in reasonable agreement with experimental results and higher-order simulations. Overall the quasi-1D simulations over-predict oscillation frequencies by approximately 20%-30%. In all cases the overall behavior of the flow is predicted (e.g. regime of instability) well.

One of the benefits of having the ability to more densely populate the projectile velocity parameter space is that transition points from one regime of stability to the next become more clear and the general morphology of the space begins to focus. In addition, transition points may be more finely interrogated by the quasi-1D simulation in order to observe the changing behavior of the flow in order to arrive at mechanisms

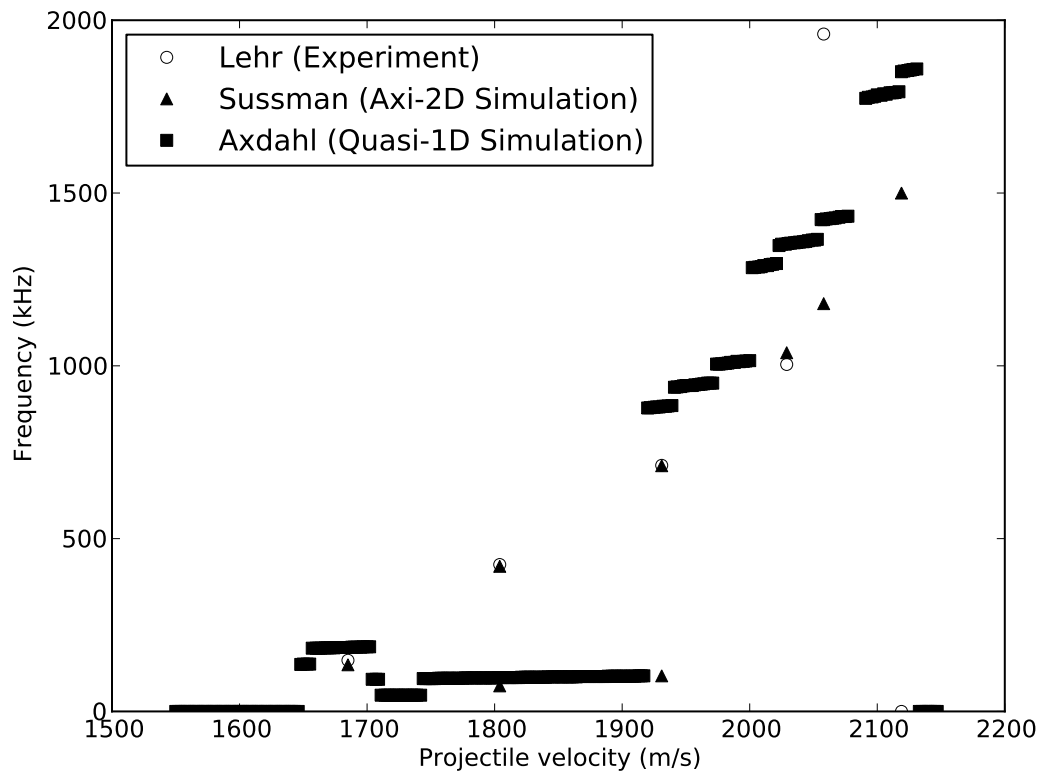


**Figure 135:** Reaction front oscillation frequency as a function of projectile velocity for experimental and numerical investigations. Note that frequencies are grouped due to FFT windowing.

**Table 23:** Oscillation frequencies from experiment and numerical investigations.

Velocity (m/s)	Lehr (kHz)	Sussman (kHz)	Present Results (kHz)
1685	148	135	185
1804	425	420/74	-/98
1931	712	711/103	881/-
2029	1040	1038	1354
2058	1960	1180	1423
2119	n/a	1500	1851
2605	n/a	n/a	n/a

for transition. With a more densely populated parameter space, trends not observed in previous work also appear. For example, the space takes on something akin to a terraced appearance where there are distinct regions of stability with rapid transitions in some locations from one dominant frequency to the next (e.g. around 2000 m/s and 2080 m/s).

The basic transition mechanism at work in the observed results is an out-of-phase behavior of pressure waves generated by the new reaction fronts. For projectile velocities below 1650 m/s, the reaction front is observed to be smooth. If new reaction fronts are being created, they are imperceptibly low in amplitude and strength at the studied grid resolution. At the beginning of the regular regime zone, there are moderate amplitude reaction front features. Increasing the projectile velocity has the effect of creating additional reaction zones along the same reaction peninsula. This is due to the pressure waves generated by new reaction zones being significantly out-of-phase with the reflected pressure waves from the projectile surface. As velocity increases, new reaction fronts are created by out-of-phase waves propagating faster than expansion waves can relax the shock front. This causes a secondary, low-frequency oscillation to appear mainly between 1730 m/s and 1960 m/s upon which the higher-frequency regular instability is superimposed. The secondary oscillation dies out around the detonation velocity of the mixture (1957 m/s), but this may be coincidental. As the projectile velocity increases past 1960 m/s, where the classic, in-phase

regular regime is re-established, a terraced trend of oscillation frequency versus projectile velocity occurs. The cause of this trend is again due to narrow velocity ranges where out-of-phase pressure wave behavior creates new reaction fronts in addition to ones already being created periodically due to the classic regular regime mechanism. The reaction front at the transition points shows mixed regular regime behavior with non-cohesive, irregular reaction fronts created by the out-of-phase pressure waves. In general, as the projectile velocity increases, the amplitude of the reaction front is found to decrease, eventually smoothing out into apparently stable behavior as it begins to couple with the shock front.

#### **5.4.5 Comparison to 1D Mechanism Models**

The simulated experiments of Ruegg and Dorsey were reexamined in order to compare the present quasi-1D numerical results to published 1D instability mechanism models in the literature. First, the quasi-1D simulation of the regular, unsteady regime was compared with the published mechanism of Matsuo [124] in Figure 136. Note that all of the major features of the mechanism proposed by Matsuo are present in the simulated result. A newly created reaction front produces pressure waves that travel downstream toward the projectile surface and upstream toward the bow shock. The upstream traveling pressure wave meets the bow shock roughly in phase with the pressure wave reflected from the projectile surface. The collision of the pressure waves and the shock front causes the shock to move upstream with a contact discontinuity reflected downstream. The contact discontinuity is visible on the density plot and is visible as a line traced from each cusp of the bow shock to the newly created reaction front. The hot gas upstream of the contact discontinuity has a lower induction time than the downstream gas, which creates a new reaction zone that eventually extinguishes the old one. This process repeats indefinitely for a projectile with constant velocity. The simulated result differs slightly from the published mechanism in that

the simulated contact discontinuity is connected to the tip of the reaction zone peninsula versus the 1D mechanism, which traces it to the point where the old reaction front is merged with the new one. In addition, the presently simulated result indicated that the reflected pressure waves skip a generation of new reaction zone before interacting with the bow shock. The published mechanism shows the reflected pressure wave interacting with the bow shock along with the upstream-traveling pressure wave of the next reaction zone generation. Finally, the present computations showed a rarefaction wave reflected at the point where the pressure wave and the bow shock meet, which is not depicted in the published model.

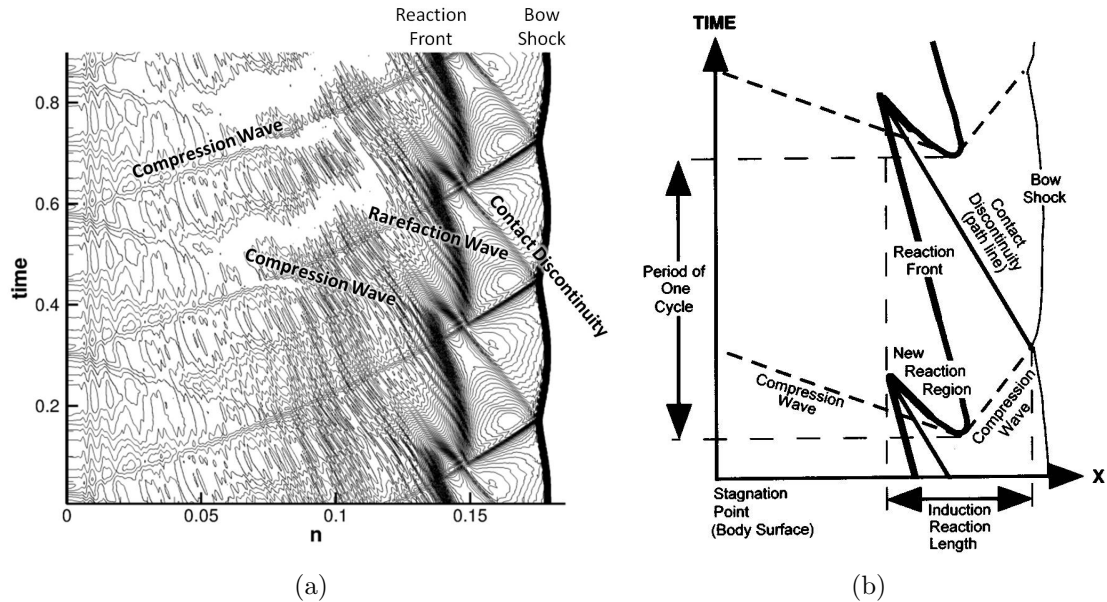


**Figure 136:** Contour lines of (a) density on the stagnation streamline as a function of time for Ruegg and Dorsey experiment Case 2 and (b) 1D mechanism for the regular, unsteady regime by Matsuo (reproduced with permission).

The quasi-1D simulation of the large-disturbance, unsteady regime, shown with a density contour plot, will now be compared with the corresponding mechanism of Matsuo and Fujii [97] in Figure 137. The large-disturbance mechanism of Matsuo and Fujii requires an energy release large enough to create a deflagration to detonation transition (DDT), noted in the figure as an explosion in an explosion (this is

discussed further in the detonation literature [106, 107]. This causes a penetration of the self-propelled reaction front through the bow shock, reflecting a rarefaction wave and contact discontinuity downstream at the point of intersection. The self-propelled reaction front, which is coupled with the bow shock for a short time, gradually separates from the shock wave and relaxes to its original position before resuming the cycle. Comparing the present results to the 1D mechanism shows that all of the essential features of the mechanism are reproduced in the quasi-1D simulation. Figure 10 shows a detailed view of the detonation region of the quasi-1D simulation to examine what is happening closer to the shock wave penetration. Here it is clearly visible that the intersection of the reaction shock wave from the first explosion with the bow shock is responsible for generating the rarefaction wave and the contact discontinuity that causes the second explosion. The second pressure wave seen in the simulated results is due to the generation of the second explosion, explaining why it doesn't appear in the general, single-explosion mechanism. After the second explosion, the pressure wave and reaction front traveling upstream merge with the bow shock and a self-sustained superdetonation is observed for a short amount of time. Overall the quasi-1D simulation shows excellent agreement with the 1D mechanism found in the literature.

### ***5.5 Effect of Equivalence Ratio on Stability***

It has been shown that QUIVR was able to reproduce the important physics occurring in blunt-body PMSIC at a much lower computational cost versus axisymmetric simulation. One benefit of this capability is the ability of the computational framework to conduct parametric simulations of the firing of a blunted projectile at different conditions. Some attempt has been made to do this in the literature, but knowledge gained is limited due to the computational time required for multidimensional simulations to converge as well as the post-processing of numerical data.

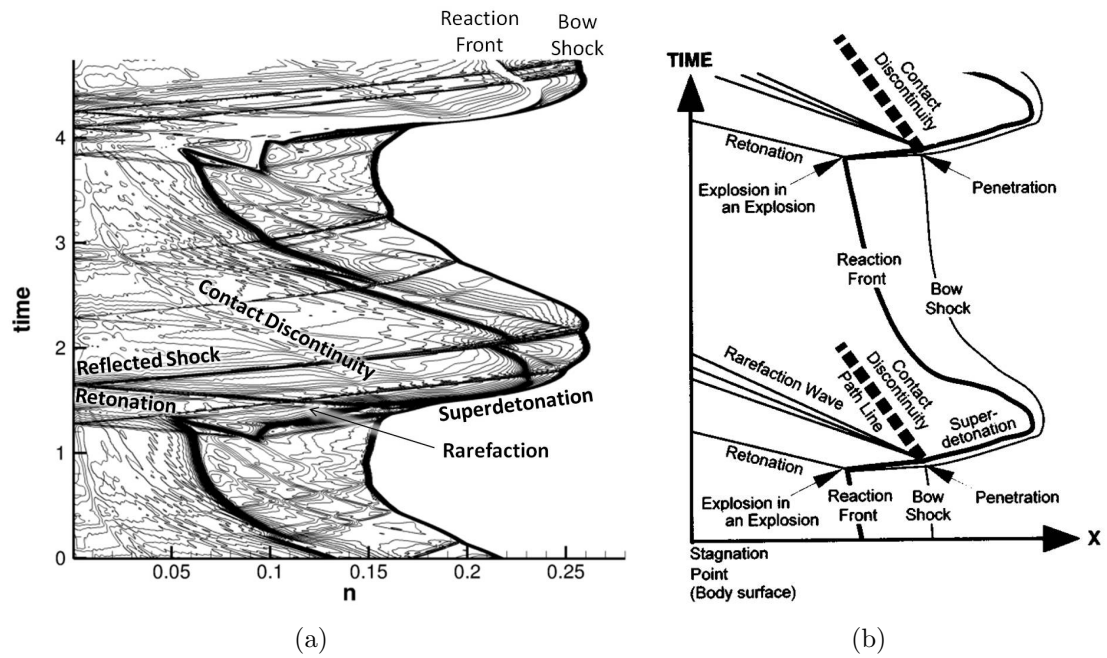


**Figure 137:** Contour lines of (a) density on the stagnation streamline as a function of time for Ruegg and Dorsey experiment Case 3 and (b) 1D mechanism for the regular, unsteady regime by Matsuo and Fujii (reproduced with permission).

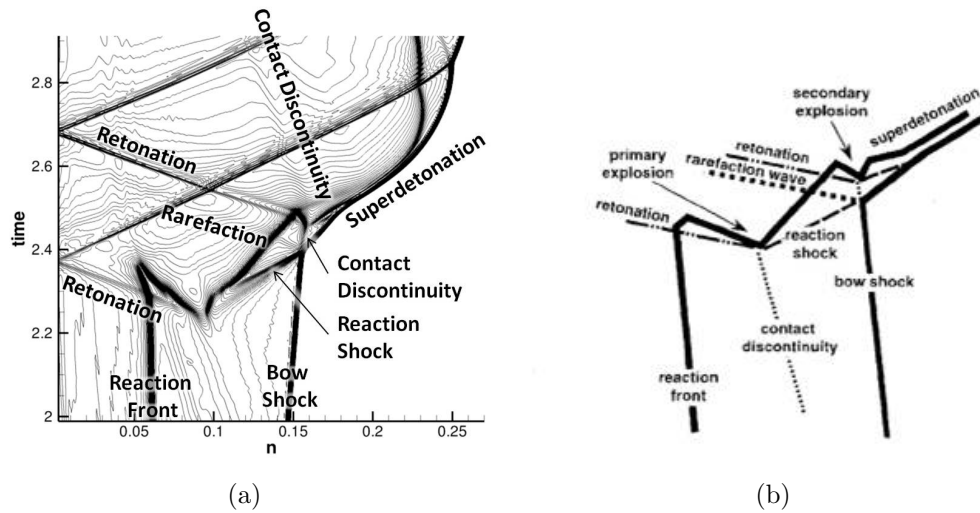


**Figure 138:** A detail view of the (a) stagnation streamline density contours from the present simulation (Case 3) compared to a (b) 1D sub-mechanism of the large-disturbance regime as proposed by Matsuo and Fujii [97] (reproduced with permission).

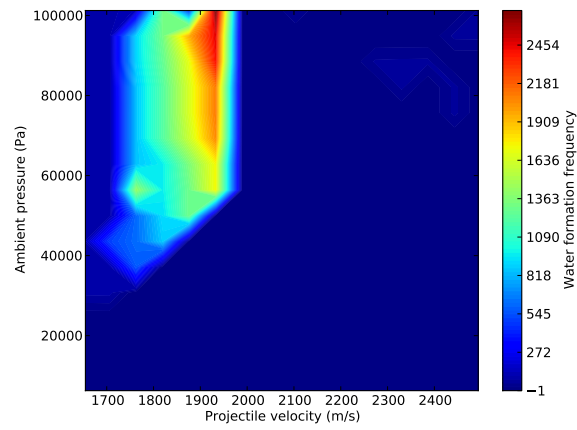
For the purposes of this study, QUIVR was integrated into DAKOTA<sup>3</sup>, an automated code execution and analysis framework, in order to allow the automated execution of the program over the design space of interest. Here the design space is bounded by projectile velocities ranging from 1650 to 2500 m/s and ambient pressures ranging from 0.05 to 1.0 atm. The design space is partitioned into 256 equally-spaced cases and the entire set of cases were run repeatedly for equivalence ratios of 0.5, 1.0, and 1.5. The ambient temperature was held constant at 292 K and the projectile diameter was set to 15 mm, equivalent to the projectile used in the Lehr study. In order to facilitate the post-processing of the data, the wall water mass fraction is tracked as a function of time and then analyzed with a discrete Fourier transform automatically at the conclusion of each simulation. The chemical model was chosen to be the Jachimowski reduced 8-species, 13-reaction model used in Chapter 3.

Figure 139 shows filled contours of reaction front frequency as a function of ambient pressure and projectile velocity for the lean, stoichiometric, and rich cases. These plots are unique contributions to the literature and are a direct result of the low computational cost to run the QUIVR code in a reacting mode. Each space is characterized by an unstable region with reaction front frequencies in excess of zero kilo-Hertz bracketed on either side by stable regimes. To the left of the unstable region are stable cases where the reaction front is detached from the shock front and to the right is a region where the reaction and shock fronts have merged into a stable detonation. The region of regular instability shows areas where the reaction front frequency decreases and then increases again. Such areas are due to the envelope regime of stability where the larger amplitude, lower frequency disturbance is detected by the FFT.

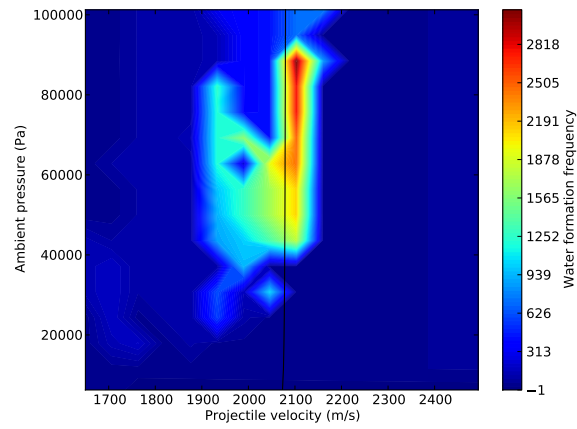
As the equivalence ratio is increased the regime of instability shifts to higher velocities. This is a Mach number effect in that increasing the equivalence ratio

---

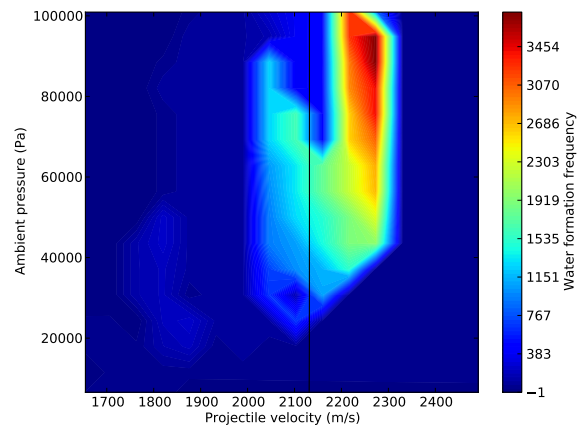
<sup>3</sup>Code obtainable from <http://dakota.sandia.gov/>



(a)



(b)



(c)

**Figure 139:** Filled contours of reaction front frequency as a function of projectile velocity and ambient pressure for (a) lean, (b) stoichiometric, and (c) rich equivalence ratios. The black line on the latter two plots indicate the Chapman-Jouget detonation velocity.

of a hydrogen-air mixture decreases the mixture molecular weight. Because for a particular case in the parameter space temperature, pressure, and velocity are being held constant, the freestream Mach number of the flow increases with decreasing gas constant. Increasing the flow Mach number caused a higher post-shock temperature that in turn decreased the induction time, shifting the behavior of the reaction front to a higher effective velocity relative to the baseline stoichiometric case. Note that these trends would presumably be reversed—increasing equivalence ratio would shift the trends to the left—for a heavier-than-air fuel as increasing equivalence ratio in that case would increase the molecular weight of the mixture.

Figures 139(b) and 139(c) both indicate the Chapman-Jouget detonation velocity through the parameter space, solved using CEA. The CJ line appears as a vertical line because it is only a weak function of pressure for the conditions considered. It was shown that instabilities may occur above the Chapman-Jouget velocity, which has been observed in experimental and numerical literature and was confirmed here.

## ***5.6 Chapter Summary***

The primary concern of this chapter was the development of a numerical methodology for the rapid solution of the premixed, shock-induced combustion ahead of blunted projectiles. Such flows are characterized by steady or unsteady physics depending on the conditions of the oncoming fuel-air stream. The current paradigm for studying such flows is an axisymmetric simulation in the vicinity of the stagnation region, but such simulations are still taxing due to the requirement for fine grids and the solution of chemical reactions using global time stepping. The currently proposed method, a quasi-1D form of the axisymmetric Navier Stokes equations, considerably reduces the computational requirements to solve such flows and makes such solutions practical on a personal computer or high performance workstation.

It was shown that the quasi-1D framework, implemented through the QUIVR

code, was able to successfully reproduce the important physics characteristic of shock-reaction front instabilities at selected conditions. This supports past experimental and numerical observation that the important physics of such flows originate in the stagnation region of blunted bodies. For the regular regime of instability, the important mechanism is the interaction of pressure waves emanating from newly created reaction zones with the bow shock, reflecting contact discontinuities that create further new reaction zones. For the large disturbance regime, the important mechanism is the creation of a deflagration-to-detonation transition that causes a rapid upstream advance of the reaction front that penetrates the bow shock. These mechanisms were captured by the quasi-1D formulation.

Past numerical studies have attempted to parametrically study PMSIC due to blunted projectiles but were limited by the computational demands of an axisymmetric simulation and the post-processing required for each case. Because of the significantly reduced demands of the current framework, such studies are able to be rapidly conducted. One example study is the effect of fuel-air equivalence ratio over given ranges of projectile velocity and ambient pressure. The current study shows results on these effects that have not existed in the literature to this point.

## CHAPTER VI

### SUMMARY AND AVENUES OF FUTURE WORK

#### *6.1 Summary of Contributions*

The application of premixed, shock-induced combustion to airbreathing engines has been identified as an enhancing technology to access the hypervelocity regime of flight. By mixing fuel with air on the forebody of a scramjet vehicle, the internal flowpath need only provide for combustion of the fuel-air mixture. This allows for significantly shortened vehicles over those that require injection, mixing, and combustion to occur internally.

Previous studies have identified three main issues with the use of PMSIC for high speed, airbreathing propulsion. The first is the ability to inject and mix fuel with a high Mach number airstream while sustaining the overall performance of the flow. The second is the prevention or mitigation of autoignition that may occur on the forebody as the fuel-air mixture accesses hot areas of the forebody flow, such as the boundary layer. The third is the possible presence of instability in the shock-reaction front at the entrance of the combustor as the literature shows that shock-reaction front interactions may give rise to either complete stable behavior or highly unstable behavior. It was the goal of this dissertation to systematically address each of these issues via studies using numerical simulation.

The study of mixing and injection at conditions relevant to Mach 12 flight yielded new analysis capabilities and contributions to knowledge. Hydrogen injector geometries within the flush-wall, ramp, and strut injector classes were simulated and compared at the same freestream conditions. A new method compared each injector on the basis of the losses incurred for any given level of mixing achieved. This allowed

the technically defensible identification of injector concepts that will best meet any given mission needs. It was shown that the strut injector was able to achieve high levels of mixing with a moderate amount of stream thrust potential loss. The ramp injector was only able to achieve modest mixing gains, but was able to preserve the highest level of stream thrust potential at cowl closure. The flush-wall injector was able to achieve similar levels of mixing as the strut but at inferior levels of stream thrust potential. The decision of what injector to use for any given flowpath is dependant on the respective system requirements on losses allowed and required level of mixing, although it appears that, from a performance standpoint, flush-wall injection is at a disadvantage for the geometries and conditions studied. The usefulness of the flush-wall injection strategy for forebody injection was further weakened after conducting reacting simulations that showed extensive burning in the shock layer ahead of the fuel plume.

The mitigation of autoignition at the wall was addressed through the use of wall cooling. After studying the parametric effect of cooling geometry, angle of injection, species, coolant temperature, and coolant mass flow rate, it was learned that hydrogen and helium coolants were both well suited for mitigating autoignition when injected tangentially to the wall through film cooling slots. The use of hydrogen as a film coolant is beneficial to a flight system due to the coolant being the same species as the fuel, although the levels of coolant mass flow rate required for substantial autoignition mitigation may pose an issue for vehicle propulsion efficiency. This drawback may be mitigated by considering a fueling split between the film cooler and the injector, however, to target a unity global equivalence ratio. It was also learned that nitrogen (and, similarly, other high molecular weight, inert species) are inappropriate for wall cooling when autoignition mitigation is required due to its poor specific heat by mass. In addition, it was found that transpiration cooling was unable to mitigate wall autoignition to any useful degree for the studied conditions and configurations.

Finally, the issue of reaction front/shock wave instability was studied through the representative problem of premixed, shock-induced combustion ahead of a sphere traveling at hypersonic speeds. It was found that the axisymmetric Navier Stokes equations were able to be reduced to a quasi-1D form valid in the stagnation region of the sphere. By verifying the solution of these reduced equations against prior experimental and numerical results, it was found that the important unstable physics found in axisymmetric simulations were successfully reproduced. This confirmed that the important physics in reaction-front, boundary layer instability originate in the stagnation region of the sphere. The quasi-1D equations were integrated into a tool and included in an automated analysis framework to enable rapid parameter studies. By doing such studies, it was possible to observe the regimes of instability in a multidimensional parameter space. This improved knowledge of the dependence of instability on velocity and pressure. For example, it was observed that there exists a single maximum for reaction front frequency and that the instability regime is encapsulated rather than extending unbounded in any given direction of pressure or velocity.

The outcomes of the research presented in this dissertation both contribute to state-of-the-art knowledge of the physics of shock-induced combustion ramjets as well as define avenues for future study and development. Key results from this research indicate that forebody injection should be limited to ramp or strut injection depending on mission requirements constraining loss and required mixing. Autoignition should be approached using tangential film cooling using a light gas such as hydrogen or helium. Furthermore, instabilities arising at conditions relevant to the inlet of such a vehicle may be predicted using the proposed quasi-1D simulation framework.

## ***6.2 Avenues of Future Numerical Work***

### **6.2.1 Forebody Injector Design and Optimization**

The work presented in this dissertation was primarily concerned with comparing different classes of injectors in the same type of forebody flow representative of hypervelocity flight and discussing the feasibility of each type of injector. The strut and ramp injectors both proved to be feasible for forebody fuel injection, although admittedly the designs used are point designs without regard to optimization. Parametrization and design space exploration of these geometries represent a future course of research with the current work forming a starting point.

Ideally numerical optimization would take place on an actual forebody and would be automated to allow for more rapid design space exploration. Systematic exploration of a design space within an automated framework brings significant benefits in time, cost, and knowledge. The current design paradigm requires an iterative process that can be time intensive and yield only point designs at each iteration. Design problems are compounded by the time issue in requiring a human in the loop at each discipline component of the design process. A paradigm shift in the current design process is obtained by integrating different codes in an automated framework. Such a shift yields significantly increased knowledge over reasonable variable ranges and allows the designer to achieve either optimized or robust designs through effective sampling of the design space and the application of state-of-the-art optimization routines.

DAKOTA would be an ideal package to design this framework around. DAKOTA can accomplish parameter studies, optimization, or uncertainty analysis either by operating directly on the design space or on surrogate models<sup>1</sup> constructed using design of experiments, an efficient sampling method also available in the toolkit.

---

<sup>1</sup>Surrogate models are polynomial equations that closely approximate the behavior of complex, time-intensive codes over a given parameter space.

A further benefit of DAKOTA has the ability to change the type of study being conducted simply by changing the input file to the toolkit without further changing the overall framework.

Figure 140 illustrates a notional  $N^2$  diagram for a CFD framework that integrates a grid generator, numerical simulator, and post-processing package. DAKOTA is placed in the framework in a position where it can direct the code execution and flow of information between nodes in the diagram through the use of shell scripting. The generality of the nodes in the diagram are to emphasize that any code that has batch processing capability may be used in the framework. Examples of each type of program are indicated below the diagram.

<b>DAKOTA</b>	Geometric and Grid Parameters	Flow Parameters	
	<b>Grid Generator</b>	Topology, Boundary Conditions	
		<b>Numerical Simulator</b>	Converged Solution
Extracted Flow Parameters, Objective Function Values			<b>Post-Processor</b>

**Grid Generator** Custom software, GridPro, Gridgen/Pointwise

**Numerical Simulator** VULCAN, Wind-US, etc.

**Post-Processor** Custom scripts, Tecplot

**Figure 140:** Notional  $N^2$  diagram for the analysis framework along with example codes to be used in each node.

A DAKOTA-enabled CFD framework has the ability to systematically and automatically sample the design space using high-fidelity codes in order to construct fast-running surrogate models. A surrogate model is a polynomial equation that closely approximates the behavior of more complex, higher fidelity analyses over a defined design space. A typical surrogate model includes an intercept term, linear terms, interaction terms, and pure quadratic terms, as shown in Equation 87.

$$R = \beta_0 + \sum_{i=1}^n \beta_i x_i + \sum_{i=1}^{n-1} \sum_{j=i+1}^n \beta_{ij} x_i x_j + \sum_{i=1}^n \beta_{ii} x_i^2 \quad (87)$$

After sampling the design space using parameter combinations defined from design of experiments in DAKOTA and constructing a surrogate model, the analyst may use the resulting model to further understand the design space through probabilistic design efforts.

Design optimization is either carried out directly on a set of codes or on a surrogate model closely approximating the behavior of the design space. Optimization strategies that may be carried out in a DAKOTA-enabled framework include

**Gradient-Based Optimization** Gradient-based optimization strategies may be carried out directly on a set of codes or on a surrogate model. In order to operate directly on a set of codes, the numerical simulator needs to be augmented with the ability to compute sensitivity derivatives in the neighborhood of a point design. In order to operate on a surrogate model, the design space needs to be representable by a polynomial equation (which may or not be the case depending on the problem being studied). Examples of gradient-based optimizers available in DAKOTA are Fletcher-Reeves conjugate gradient (CG), the method of feasible directions (MFD), sequential linear or quadratic programming (SLP or SQP), and the Broyden-Fletcher-Goldfarb-Shanno (BFGS) quasi-Newton technique.

**Nongradient-Based Optimization** For cases where the design space is not representable by a surrogate model and no derivatives are obtainable, DAKOTA may draw upon pattern search, Monte Carlo, and Solis-Wets algorithms.

**Stochastic Optimization** DAKOTA has a highly-developed capability to use evolutionary (genetic) algorithms when operating on a set of codes or surrogate model. Single- and multi-objective genetic algorithms (SOGA and MOGA) are

available for the analyst's use, with the latter representing a powerful technique as most engineering problems have multiple objectives. MOGA techniques do not require the use of weighted objective functions, instead seeking out points along the entire Pareto front of the design space.

Design problems that may be encountered by the DAKOTA-enabled CFD framework can be addressed in many different ways without changing the structure of the framework itself.

**Large design spaces** Design spaces that have a large number of parameters may be mitigated by employing a screening test before beginning higher fidelity, time-intensive analyses. A screening test is accomplished by sampling the design space using relatively few points (afforded by a two-level design of experiments) and investigating the results using an ANOVA. The ANOVA statistical technique will identify which variables produce the greatest impact on the variability of the response using the Pareto principle. Only the new, smaller subset of variables is used to define the design space with all others set at a default value.

**No derivative information** If time or technical constraints preclude the use of gradient-based optimization techniques, nongradient-based techniques may instead be used in order to analyze the design space. For example, the use of an evolutionary algorithm will allow the identification of a global optimum without the use of any derivative information at any given point.

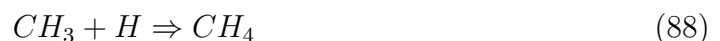
**Time-intensive codes** If optimizing directly on a set of codes proves too time intensive a task, the behavior of the design space can instead be defined using surrogate models. Surrogate models are constructed by systematically sampling the design space using design of experiments. Due to their polynomial nature,

once a surrogate model is created the design space can be explored in real-time. Assuming it has been correctly constructed, a surrogate model represents a very close approximation of the behavior of the high-fidelity analyses over a given set of parameter ranges. Therefore, design space knowledge is significantly improved.

### 6.2.2 Chemically Active Cooling

This study evaluated the use of hydrogen fuel as well as the inert species helium and nitrogen for use as coolants to be injected at the wall of the vehicle forebody. Although hydrogen would allow a single storage and cryogenic system to be used, its ability to rapidly combust presents a practical issue to its implementation. It was shown that at the right injection conditions, hydrogen is able to delay ignition significantly, but this benefit may have difficulty scaling to very large, orbital-access class flowpaths. One alternative is to use helium, which was found to have excellent mitigation properties at the expense of needing another storage system. Another expense of helium against hydrogen is that the burning of the hydrogen coolant in the combustor may contribute to thrust, whereas helium will remain inert throughout the entire flowpath.

The question then is if there is a coolant that can be used to limit autoignition while itself remaining combustible in the combustor? One possibility would be the use of cold methane ( $\text{CH}_4$ ) at the wall. When methane creates methyl ( $\text{CH}_3$ ) species through collision with OH and O species, the methyl then has a reaction pathway available to it to recombine with monatomic hydrogen to create methane. This reaction takes the form



This reaction would be called a “scavenging” reaction—removing hydrogen radicals that are important for combustion to proceed and restoring them into methane

molecules. By introducing methane chemistry into the hydrogen chemistry otherwise occurring at the wall, it may be possible to slow down the overall chemistry and delay ignition longer than would be possible with the use of hydrogen alone while still being able to ignite in the combustor. Furthermore, less methane might be needed due to its chemical activity versus simply using bulk hydrogen to act as a heat sink only.

Initial pathfinding studies could be limited to the important mechanisms, for example the methyl-creating reactions



as well as the hydrogen scavenging reaction in Equation 88. It may also be possible to use an extinguishing compound such as halon ( $CF_3Br$ ) as the coolant gas, which may only require very small amounts to mitigate autoignition compared to hydrogen or methane. The fact that it is not combustible, however, and other environmental concerns are detriments to using it.

### 6.2.3 Effect of Blunt Bodies and Non-Optimal Trajectories

The two-dimensional notional combustor studied in this work was a purely idealized case with no simulation for shock-on-lip conditions or spillage. The actual forebody geometry would possibly be subject to shock interactions and a stagnation region near the cowl lip, which would be compounded by the fact that the gas may be combustible at that point as well. Other possible stagnation regions in the flow would include areas of shock-boundary layer interaction as well as engine module walls. These regions may be susceptible to instabilities similar to those due premixed, blunt body phenomena observed in numerical and experimental literature as well as the present study.

These phenomena could be studied in the context of the entire flowpath (i.e. a complete, integrated flowpath simulation from tip-to-tail) or in more unit problems as was the strategy in the current work. For example, the cowl leading edge may be

modeled as a wedge of variable bluntness, which was studied in a premixed flow to a small degree by Matsuo. The effects of both wedge angle and leading edge radius would parameterize the study of any instabilities arising in the flow. Module walls—present in the flow whether or not the vehicle is over- or under-spiced—separating engine modules could be simulated in a similar manner. Boundary layer separation could also be modeled as a blunt body for analysis with the quasi-1D framework outlined in this dissertation.

#### **6.2.4 Integrated Analysis using Variable Geometry**

It is commonly acknowledged that a variable geometry inlet is necessary for a successful transatmospheric flight concept at the cost of greater mechanical complexity. The current study assumed a fixed inlet geometry designed for a Mach 12 point on a 1500 psf trajectory, duly penalizing geometries that spill more air or fuel than others. A variable geometry inlet can mitigate some of the issues of fuel-air spillage by actuating the cowl lip to respond undersped<sup>2</sup> conditions a flight vehicle experiences as it travels on its design trajectory. By moving the cowl closure location, air and fuel that would otherwise be spilled can be directed internally for combustion.

It was observed through the course of this study that, in addition to the injector geometries themselves, the injected gas does have some contribution to the spillage experienced in any particular case. It is hypothesized that varying the primary injection conditions to respond to changing fueling requirements as well as varying secondary injection conditions to respond to changing cooling requirements throughout a trajectory will have a substantial effect on the spillage experienced by a forebody. Therefore, a variable-geometry cowl would also need to account for not only the variation in freestream conditions but the conditions of the injectants supplied to the

---

<sup>2</sup>An undersped condition is one where the Mach number is lower than the required Mach number to cause a shock-on-lip condition that captures all of the forebody air and ideally causes shock cancellation to occur on the forebody shoulder.

forebody.

A variable geometry nozzle may also be beneficial to the operation of a vehicle. A variable geometry nozzle, besides altering the shape of the nozzle itself, could vary the location of the combustor-nozzle interface in order to begin expanding the flow at different locations depending on the trajectory point of the vehicle. This would benefit the thrust generation of the vehicle due to the fact that for some arbitrary length combustor, there is a critical location where the thrust gains from combustion are outbalanced by the growing viscous losses generated at the walls of the combustor. Beginning the nozzle expansion process at this “optimum” point would ensure that the greatest amount of thrust is generated.

### **6.2.5 Further Development and Application of Quasi-1D Framework**

A significant result of the present research was the development of a tool (QUIVR) for the study of blunt body flows of a general purpose nature. Although the current QUIVR application is the study of premixed, shock-induced combustion of premixed hydrogen-air, the code itself can simulate the stagnation region of any circular blunted-body with or without chemistry. Furthermore, the chemistry is of a general nature to allow the simulation of different chemical mechanisms. Therefore, the utility of QUIVR extends to other areas of research.

One example research area would be the study of receptivity, which analyses how acoustic disturbances in the main stream interact with boundary layers to cause their transition to turbulence. [125]. These acoustic disturbances are commonly found in wind tunnel testing, and their understanding is important in order to provide computational results that reproduce those in experiment. Furthermore, while the flight environment is typically considered to be “quiet” in terms of the generation of acoustic disturbance, facets of the flight vehicle (for example, the engine) could source some acoustic disturbance for downstream components. QUIVR could be augmented

with low-dissipation schemes to study the receptivity phenomenon rapidly.

### ***6.3 Avenues of Future Experimental Work***

#### **6.3.1 Hypervelocity Validation and Calibration Database**

The experimental simulation of high-enthalpy, hypervelocity flows is of immense performance for the purpose of providing a means of validation and calibration for numerical simulations at similar conditions. It was shown here and in previous work that, for example, the selection of turbulent Schmidt number used in RANS simulation is important to reproducing the correct physics and performance of geometries and flow phenomena. The purpose of this work was not to provide a recommendation on the correct turbulence parameters to use in RANS turbulence models, but auxiliary studies accompanying the body of work presented here show that the simulations are sensitive to the correct selection of these parameters. This is generally true, not just for cases of forebody fuel injection, mixing, and autoignition as studied here [126].

For the purposes of forebody mixing and igniting flows, experimental studies of interest would include the testing of generic transverse, ramp, and strut geometries and tracking the mixing performance using inert gases or combustible ones, if desired. The simulation of film cooling using slots or angled injectors would also yield useful information on the proper turbulence modeling of those features in high enthalpy, hypervelocity flows.

#### **6.3.2 Testing and Evaluation of Forebody Mixing Concepts**

Beyond conducting experiments for the purposes of validating simulations of hypervelocity forebody fuel injection, mixing, and autoignition, further experimental attention should be given to injectors optimized through a numerical framework like one described in Section 6.2.1. Experimentally evaluating high-potential geometries yields the maximum benefits of both numerical and experimental capabilities by identifying high performance concepts through numerical analysis and then verifying that

the performance observed actual occurs through experimental testing. Such testing would be a necessary step in proof-of-concept studies toward the development of a flight test vehicle utilizing forebody injection and mixing in the hypervelocity regime of flight.

Initial experiments on hypervelocity injection and mixing may be conducted on an open-plate in a high-enthalpy test facility. Test conditions may reproduce forebody Mach numbers while using enthalpies representative of hypervelocity flight. The use of Schlieren imaging or a laser-based method such as NO-PLIF may be used in order to observe the flow structures in the flow. Initial studies could use a pure helium or helium-air simulant to conduct non-reacting mixing studies. A traversing gas sampling system could be used to determine the concentration of injectant over a grid of cross-sectional points in order to arrive at estimates of mixing efficiency.

## APPENDIX A

### TAYLOR SERIES EXPANSION OF FLOW VARIABLES

In order to arrive at a quasi-1D formulation of the Navier Stokes equations, it is necessary to recast the flow variables in a form that allows for the expression of a system of equations that are a function of distance along the stagnation streamline only. The first step is to create a Taylor series expansion of each flow variable about the stagnation ( $s = 0$ ) streamline. Refer to Figure 126 for a schematic of the flowfield. The Taylor series expansion of a generic flow variable has the form

$$\phi(n, s) = \phi(n, 0) + \frac{\partial\phi(n, 0)}{\partial s}s + \frac{\partial^2\phi(n, 0)}{\partial s^2}s^2 + \dots \quad (91)$$

where  $\phi$  can be any flow variable (e.g. density). Because we are in a nondimensionalized system,  $s = \alpha$ . The small angle approximation further defines  $s = \sin \alpha$ . For the sake of notational brevity, define  $\phi_1 = \phi$ ,  $\phi_2 = \frac{\partial\phi(n, 0)}{\partial s}$ ,  $\phi_3 = \frac{\partial^2\phi(n, 0)}{\partial s^2}$ , and so on.

$$\phi(n, s) = \phi_1(n) + \phi_2(n) \sin \alpha + \phi_3(n) \sin^2 \alpha + \dots \quad (92)$$

#### ***A.1 Enthalpy, Pressure, and Density***

Because enthalpy, pressure, and density are scalar variables, they are symmetric about the stagnation streamline. This has the necessary effect of making odd-ordered terms in the expansion equal to zero, thereby reducing the form of these expanded variables to

$$H(n, \alpha) = H_1(n) + H_3(n) \sin^2 \alpha + H_5(n) \sin^4 \alpha + \dots \quad (93)$$

$$p(n, \alpha) = p_1(n) + p_3(n) \sin^2 \alpha + p_5(n) \sin^4 \alpha + \dots \quad (94)$$

$$\rho(n, \alpha) = \rho(n)_1 + \rho(n)_3 \sin^2 \alpha + \rho(n)_5 \sin^4 \alpha + \dots \quad (95)$$

## A.2 Velocity

The components of the velocity normal and tangential to the stagnation streamline behave differently in terms of symmetry and therefore needs to be treated separately. The normal ( $u$ ) velocity component is not symmetric in terms of sign about the stagnation streamline. As such, even-ordered terms are set to zero in the expansion. The first term (without a derivative) is also set to zero because the normal velocity must necessarily be zero along the stagnation streamline ( $\alpha = 0$ ). Therefore, the normal velocity component has the form

$$u(n, \alpha) = u_2(n) \sin \alpha + u_4(n) \sin^3 \alpha + u_6(n) \sin^5 \alpha + \dots \quad (96)$$

The tangential ( $v$ ) velocity, unlike the normal velocity, is symmetric about the stagnation streamline, thereby eliminating the odd-ordered terms in the expansion. The small angle approximation  $\cos(\alpha) \approx 1$  is also used to multiply each term by  $\cos(\alpha)$ . Therefore, the tangential velocity component has the expanded form

$$v(n, \alpha) = v_1(n) \cos \alpha + v_3(n) \cos \alpha \sin^2 \alpha + v_5(n) \cos \alpha \sin^4 \alpha + \dots \quad (97)$$

This approximation allows for the successful elimination of  $\alpha$  from the reformulated Navier Stokes equations and remains exact for  $\alpha = 0$ .

## A.3 Variable Summary

The expanded variable set is reproduced here with changed notation such that, for simplicity, sequential terms are also sequential in their numbering.

$$H(n, \alpha) = H_1(n) + H_2(n) \sin^2 \alpha + H_3(n) \sin^4 \alpha + \dots \quad (98)$$

$$p(n, \alpha) = p_1(n) + p_2(n) \sin^2 \alpha + p_3(n) \sin^4 \alpha + \dots \quad (99)$$

$$\rho(n, \alpha) = \rho_1(n) + \rho_2(n) \sin^2 \alpha + \rho_3(n) \sin^4 \alpha + \dots \quad (100)$$

$$u(n, \alpha) = u_1(n) \sin \alpha + u_2(n) \sin^3 \alpha + u_3(n) \sin^5 \alpha + \dots \quad (101)$$

$$v(n, \alpha) = v_1(n) \cos \alpha + v_2(n) \cos \alpha \sin^2 \alpha + v_3(n) \cos \alpha \sin^4 \alpha + \dots \quad (102)$$

Note that  $u_1 = \frac{\partial u}{\partial s}$  and  $p_2 = \frac{\partial^2 p}{\partial s^2}$ . This is the origin of the term “quasi-1D” when referring to this formulation, as these terms play an important role in the recast Navier-Stokes equations.

## APPENDIX B

### GRID METRICS AND COMPUTATIONAL DOMAIN

#### *B.1 Computing the Grid Metrics and Grid Jacobian*

Converting the modified Navier-Stokes equations to the computational domain is helpful when considering nonuniform grid spacing or for grids that change in time, for example in shock fitting schemes. Deriving the grid metrics and grid Jacobian for the quasi-1D equations is relatively straightforward as the only variables that must be converted are  $t$  (to  $\tau$ ) and  $n$  (to  $\xi$ ). The the grid metrics for converting the physical to computational domain can be written as

$$d\tau = dt \tag{103}$$

$$d\xi = \xi_n dn + \xi_t dt \tag{104}$$

where  $\xi_n = \partial\xi/\partial n$  and  $\xi_t = \partial\xi/\partial t$ . Writing these equations in matrix form yields

$$\begin{bmatrix} 1 & 0 \\ \xi_t & \xi_n \end{bmatrix} \begin{bmatrix} dt \\ dn \end{bmatrix} = \begin{bmatrix} d\tau \\ d\xi \end{bmatrix} \tag{105}$$

Similarly, for converting from the computational domain to the physical domain,

$$dt = d\tau \tag{106}$$

$$dn = n_\xi d\xi + n_\tau d\tau \tag{107}$$

where  $n_\xi = \partial n/\partial \xi$  and  $n_\tau = \partial n/\partial \tau$ . Writing these equations in matrix form yields

$$\begin{bmatrix} 1 & 0 \\ n_\tau & n_\xi \end{bmatrix} \begin{bmatrix} d\tau \\ d\xi \end{bmatrix} = \begin{bmatrix} dt \\ dn \end{bmatrix} \tag{108}$$

This equation can be solved using Cramer's rule to yield

$$d\tau = J \begin{vmatrix} dt & 0 \\ dn & n_\xi \end{vmatrix} = J n_\xi dt \quad (109)$$

$$d\xi = J \begin{vmatrix} 1 & dt \\ n_\tau & dn \end{vmatrix} = J dn - J n_\tau dt \quad (110)$$

where the grid Jacobian is given by

$$J = \frac{1}{\begin{vmatrix} 1 & 0 \\ n_\tau & n_\xi \end{vmatrix}} = \frac{1}{n_\xi} \quad (111)$$

Equations 109 and 110 can be compared back to Equations 103 and 104 in order to arrive at the relations

$$\begin{aligned} J n_\xi &= 1 \\ \xi_n &= J \\ \xi_t &= -J n_\tau \end{aligned} \quad (112)$$

Note that the grid metrics and grid Jacobian are computed at each grid point.

## ***B.2 Governing Equations in the Computational Domain***

Once the grid metrics and grid Jacobian have been computed, it is now possible to convert the modified Navier-Stokes equations to the computational domain. We begin with the form of the equations

$$\frac{\partial \mathbf{U}^p}{\partial t} + \frac{\partial \mathbf{M}^p}{\partial n} + \mathbf{Q}^p = 0 \quad (113)$$

where the superscript  $p$  indicates that the vectors are in the physical domain. The partial derivatives with respect to  $t$  and  $n$  can be related to the grid metrics by the relations

$$\begin{aligned} \frac{\partial}{\partial t} &= \xi_t \frac{\partial}{\partial \xi} + \mathcal{J}_t \frac{\partial}{\partial \tau} = \xi_t \frac{\partial}{\partial \xi} + \frac{\partial}{\partial \tau} \\ \frac{\partial}{\partial n} &= \xi_n \frac{\partial}{\partial \xi} + \mathcal{J}_n \frac{\partial}{\partial \tau} = \xi_n \frac{\partial}{\partial \xi} \end{aligned} \quad (114)$$

Re-expressing Equation 113 with these relations and substituting Equation 112 yields

$$-n_\tau \frac{\partial \mathbf{U}^p}{\partial \xi} + \frac{1}{J} \frac{\mathbf{U}^p}{\partial \tau} + \frac{\partial \mathbf{M}^p}{\partial \xi} + \frac{\mathbf{Q}^p}{J} = 0 \quad (115)$$

Setting  $\mathbf{U}^c = \mathbf{U}^p/J$  and  $\mathbf{Q}^c = \mathbf{Q}^p/J$ , where the superscript  $c$  indicates a vector in the computational domain, yields

$$\frac{\partial \mathbf{U}^c}{\partial \tau} + \frac{\partial \mathbf{M}^p}{\partial \xi} - n_\tau \frac{\partial \mathbf{U}^p}{\partial \xi} + \mathbf{Q}^c = 0 \quad (116)$$

It can be shown that, using the product rule,

$$-n_\tau \frac{\partial \mathbf{U}^p}{\partial \xi} = -\frac{\partial \mathbf{U}^p n_\tau}{\partial \xi} + \cancel{\mathbf{U}^p \frac{\partial n_\tau}{\partial \xi}}^0 = -\frac{\partial \mathbf{U}^p n_\tau}{\partial \xi} \quad (117)$$

which, when setting  $\mathbf{M}^c = \mathbf{M} - n_\tau \mathbf{U}^p$ , finally yields

$$\frac{\partial \mathbf{U}^c}{\partial \tau} + \frac{\partial \mathbf{M}^c}{\partial \xi} + \mathbf{Q}^c = 0 \quad (118)$$

## APPENDIX C

### IDEAL FUEL-AIR CONDITIONS ON A HYPERVELOCITY FOREBODY

The procedure by which a trajectory is defined is relatively straightforward at the top level and is summarized as follows:

- Define a range of Mach numbers and a trajectory dynamic pressure.
- Using an atmospheric model at each defined Mach number, find the corresponding altitudes whose conditions give the desired trajectory dynamic pressure.
- Model the effect of a vehicle forebody by processing the freestream flow through two subsequent turning angles.
- Using the conditions on the second vehicle ramp, mix the air stream with fuel in an ideal process that conserves mass, momentum, and energy in order to obtain a mixed gas state.

A sample hypervelocity trajectory ranging from Mach 10 to Mach 20 and obtained using the previously described process is shown in Figure 141. Hypersonic, airbreathing propulsion typically requires trajectory dynamic pressures ranging from 1000 to 2000 psf. A constant trajectory dynamic pressure of 1500 psf is chosen for this study, although a varying dynamic pressure schedule could alternatively be defined. The low end of the trajectory represents the lower limit Mach number where a engine using PMSIC would start operating while the upper limit is chosen arbitrarily. The actual Mach number where staging occurs to a self-contained rocket to reach orbit is left open.

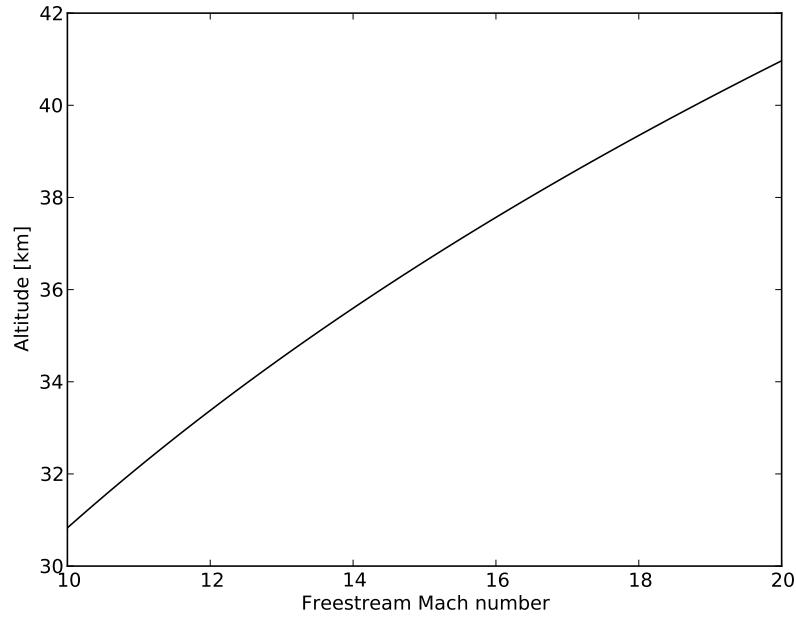


**Figure 141:** A hypervelocity trajectory at a constant dynamic pressure of 1500 psf is shown.

Once the the freestream conditions are shocked through a  $5^\circ$  followed by a  $6^\circ$  turning, the airflow is mixed with hydrogen fuel while conserving mass, momentum, and energy. The three equations to be solved are summarized respectively as

$$\sum_i^N \rho_i u_i A_i = \rho_e u_e A_e \quad (119)$$

$$\sum_i^N A_i (p_i + \rho_i u_i^2) = A_e (p_e + \rho_e u_e^2) \quad (120)$$

$$\sum_i^N \rho_i u_i A_i C_{p_i} T_i = \left( \sum_i^N \rho_i u_i A_i \right) C_{p_e} T_e \quad (121)$$

where the streamtube cross-sectional areas in Equation 120 are chosen such that the ratio of hydrogen mass flow to the mass flow of oxygen in the air is equal to 0.126 for stoichiometric flow. The value of the exit area is left to the analyst, but for the purposes of this study it was simply set to the cross-sectional area of the air streamtube. The specific heats in the energy equation are also assumed to be

**Table 24:** An example summary of the pre- and post-mixed properties are shown for stoichiometric hydrogen-air flow at the Mach 12 point on a  $q = 1500$  psf trajectory.

	Air	Hydrogen	Hydrogen-Air
$A$ [m <sup>2</sup> ]	0.002125	0.000395	0.002125
$p$ [Pa]	9111	9111	9842
$T$ [K]	541	390	496
$u$ [m/s]	3576	5815	3634

constant. The final compatibility equation given by the ideal gas law

$$p = \rho RT \tag{122}$$

The gas properties before and after mixing at the Mach 12 point on a 1500 psf trajectory are summarized in Table 24 and are chosen to be practical for an actual airbreathing system. The areas are chosen so that the final mixture is stoichiometric.

## APPENDIX D

### FINITE-RATE CHEMISTRY MODELS

**Jachimowski** ( $k_f = AT^n e^{E/RT}$ )

	Equation	A [mol/cm <sup>3</sup> /s]	n [1]	E [cal/mol]
(1)	H2 + O2 <=> OH + OH	1.70E13	0.00	48000
(2)	H + O2 <=> OH + O	2.60E14	0.00	16800
(3)	O + H2 <=> OH + H	1.80E10	1.00	8900
(4)	OH + H2 <=> H2O + H	2.20E13	0.00	5150
(5)	OH + OH <=> H2O + O	6.30E12	0.00	1090
(6)	H + OH + M <=> H2O + M	2.20E22	-2.00	0.00
(7)	H + H + M <=> H2 + M	6.40E17	-1.00	0.00
(8)	H + O + M <=> OH + M	6.00E16	-0.60	0.00
(9)	H + O2 + M <=> HO2 + M	2.10E15	0.00	-1000
(10)	HO2 + H <=> H2 + O2	1.30E13	0.00	0.00
(11)	HO2 + H <=> OH + OH	1.40E14	0.00	1080
(12)	HO2 + H <=> H2O + O	1.00E13	0.00	1080
(13)	HO2 + O <=> O2 + OH	1.50E13	0.00	950
(14)	HO2 + OH <=> H2O + O2	8.00E12	0.00	0.00
(15)	HO2 + HO2 <=> H2O2 + O2	2.00E12	0.00	0.00
(16)	H + H2O2 <=> H2 + HO2	1.40E12	0.00	3600
(17)	O + H2O2 <=> OH + HO2	1.40E13	0.00	6400
(18)	OH + H2O2 <=> H2O + HO2	6.10E12	0.00	1430
(19)	M + H2O2 <=> OH + OH + M	1.20E17	0.00	45500
(20)	O + O + M <=> O2 + M	6.00E17	0.00	-1800
(21)	N + N + M <=> N2 + M	2.80E17	-0.75	0.00
(22)	N + O2 <=> NO + O	6.40E09	1.00	6300
(23)	N + NO <=> N2 + O	1.60E13	0.00	0.00
(24)	N + OH <=> NO + H	6.30E11	0.50	0.00
(25)	H + NO + M <=> HNO + M	5.40E15	0.00	-600
(26)	H + HNO <=> NO + H2	4.80E12	0.00	0.00
(27)	O + HNO <=> NO + OH	5.00E11	0.50	0.00
(28)	OH + HNO <=> NO + H2O	3.60E13	0.00	0.00
(29)	HO2 + HNO <=> NO + H2O2	2.00E12	0.00	0.00

*continued...*

**Jachimowski (continued)**

	Equation	A [mol/cm <sup>3</sup> /s]	n [1]	E [cal/mol]
(30)	HO2 + NO <=> NO2 + OH	3.40E12	0.00	-260
(31)	H + NO2 <=> NO + OH	3.50E14	0.00	1500
(32)	O + NO2 <=> NO + O2	1.00E13	0.00	600
(33)	M + NO2 <=> NO + O + M	1.16E16	0.00	66000

Third body efficiencies:

(6): H2O = 6.0

(7): H2 = 2.0, H2O = 6.0

(8): H2O = 5.0

(9): H2 = 2.0, H2O = 16.0

(19): H2O = 15.0

Rogers and Schexnayder ( $k_f = AT^n e^{E/RT}$ )

Equation	A [mol/cm <sup>3</sup> /s]	n [1]	E [cal/mol]
(1) M + O2 <=> O + O + M	0.72E19	-1.00	117908
(2) M + H2 <=> H + H + M	0.55E19	-1.00	103298
(3) M + H2O <=> H + OH + M	0.52E22	-1.50	118000
(4) M + H + O2 <=> HO2 + M	0.23E16	0.00	-800
(5) M + NO2 <=> NO + O + M	0.11E17	0.00	64995
(6) M + NO <=> N + O + M	0.41E19	-1.00	149680
(7) M + O + CO <=> CO2 + M	0.30E15	0.00	3000
(8) M + H + NO <=> HNO + M	0.54E16	0.00	-596.1
(9) M + H2O2 <=> OH + OH + M	0.12E18	0.00	45500
(10) M + OH + NO <=> HNO2 + M	0.80E16	0.00	-1987
(11) M + OH + NO2 <=> HNO3 + M	0.13E17	0.00	-2200
(12) M + O3 <=> O2 + O + M	0.13E22	-2.00	25433
(13) M + HCO <=> CO + H + M	0.20E13	0.50	27400
(14) M + O + H <=> OH + M	0.71E19	-1.00	0
(15) H2O + O <=> OH + OH	0.58E14	0.00	18000
(16) H2 + OH <=> H2O + H	0.20E14	0.00	5166
(17) O2 + H <=> OH + O	0.22E15	0.00	16800
(18) H2 + O <=> OH + H	0.75E14	0.00	11099
(19) H2 + O2 <=> OH + OH	0.10E14	0.00	43000
(20) H + HO2 <=> H2 + O2	0.24E14	0.00	695
(21) H2 + O2 <=> H2O + O	0.41E14	0.00	50470
(22) H + HO2 <=> OH + OH	0.24E15	0.00	1887
(23) H2O + O <=> H + HO2	0.58E12	0.50	57000
(24) O + HO2 <=> OH + O2	0.50E14	0.00	1000
(25) OH + HO2 <=> O2 + H2O	0.30E14	0.00	0
(26) H2 + HO2 <=> H2O + OH	0.20E14	0.00	25000
(27) HO2 + H2 <=> H + H2O2	0.73E12	0.00	18677
(28) H2O2 + H <=> OH + H2O	0.32E15	0.00	8950
(29) HO2 + OH <=> O + H2O2	0.52E11	0.50	21062
(30) HO2 + H2O <=> OH + H2O2	0.28E14	0.00	32785
(31) HO2 + HO2 <=> H2O2 + O2	0.20E13	0.00	0
(32) O + O3 <=> O2 + O2	0.10E14	0.00	4790
(33) O3 + NO <=> NO2 + O2	0.54E12	0.00	2384

*continued...*

**Rogers and Schexnayder (continued)**

	Equation	A [mol/cm <sup>3</sup> /s]	n [1]	E [cal/mol]
(34)	O3 + H <=> OH + O2	0.70E14	0.00	1113
(35)	O3 + OH <=> O2 + HO2	0.90E12	0.00	1987
(36)	O + N2 <=> NO + N	0.50E14	0.00	75386
(37)	H + NO <=> OH + N	0.17E15	0.00	48681
(38)	O + NO <=> O2 + N	0.15E10	1.00	38746
(39)	NO2 + H <=> NO + OH	0.35E15	0.00	1470
(40)	NO2 + O <=> NO + O2	0.10E14	0.00	600
(41)	NO2 + H2 <=> HNO2 + H	0.24E14	0.00	29000
(42)	HO2 + NO <=> NO2 + OH	0.30E13	0.50	2400
(43)	NO2 + H2O <=> HNO2 + OH	0.32E13	0.00	43714
(44)	NO2 + OH <=> HNO2 + O	0.21E13	0.00	24996
(45)	CO + OH <=> CO2 + H	0.70E12	0.00	1987
(46)	CO2 + O <=> O2 + CO	0.25E12	0.50	55040
(47)	H2O + CO <=> HCO + OH	0.65E14	0.30	103026
(48)	OH + CO <=> HCO + O	0.58E13	0.32	86295
(49)	H2 + CO <=> HCO + H	0.12E14	0.29	88242
(50)	HO2 + CO <=> CO2 + OH	0.15E15	0.00	23645
(51)	HNO + H <=> H2 + NO	0.48E13	0.00	0
(52)	HNO + OH <=> H2O + NO	0.36E14	0.00	0
(53)	NO + CO <=> CO2 + N	0.46E09	0.50	23983
(54)	NO2 + CO <=> NO + CO2	0.10E13	0.00	27600
(55)	NO + HO2 <=> HNO + O2	0.72E11	0.50	10928
(56)	HNO + O <=> NO + OH	0.50E12	0.50	0
(57)	HNO3 + O <=> HO2 + NO2	0.10E12	0.00	0
(58)	HO2 + NO2 <=> HNO2 + O2	0.20E12	0.00	0
(59)	HCO + O2 <=> CO + HO2	0.10E12	0.50	5400
(60)	O3 + HO2 <=> O2 + O2 + OH	0.10E12	0.00	2800

Third body efficiencies:

- (1): O2 = 4.0, O = 10.0, H2O = 2.0
- (2): H2 = 2.0, H = 2.0, H2O = 2.0
- (3): H2O = 6.0
- (4): H2 = 2.0, H2O = 13.0
- (8): H2O = 3.0
- (9): H2O = 6.0
- (12): O2 = 1.5

### O Conaire (Using Troe Falloff Function)

	Equation	A [mol/cm <sup>3</sup> /s]	n [1]	E [cal/mol]
(1)	H + O2 <=> O + OH	1.91E14	0.00	16440
(2)	O + H2 <=> H + OH	5.08E04	2.67	6292
(3)	OH + H2 <=> H + H2O	2.16E08	1.51	3430
(4)	O + H2O <=> OH + OH	2.97E06	2.02	1340
(5)	H2 + M <=> H + H + M	4.57E19	1.40	105100
(6)	O + O + M <=> O2 + M	6.17E15	0.50	0.00
(7)	O + H + M <=> OH + M	4.72E18	1.00	0.00
(8)	H + OH + M <=> H2O + M	4.50E22	2.00	0.00
(9)	H + O2 + M <=> HO2 + M	$k_{f,0} = 3.48E16$	0.41	1120
	H + O2 <=> HO2	$k_f = 1.48E12$	0.60	0.00
(10)	HO2 + H <=> H2 + O2	1.66E13	0.00	820
(11)	HO2 + H <=> OH + OH	7.08E13	0.00	300
(12)	HO2 + O <=> OH + O2	3.25E13	0.00	0.00
(13)	HO2 + OH <=> H2O + O2	2.89E13	0.00	-500
(14a)	HO2 + HO2 <=> H2O2 + O2	4.20E14	0.00	11980
(14b)	HO2 + HO2 <=> H2O2 + O2	1.30E11	0.00	1629
(15)	H2O2 + M <=> OH + OH + M	$k_{f,0} = 1.27E17$	0.00	45500
	H2O2 <=> OH + OH	$k_f = 2.95E14$	0.00	48400
(16)	H2O2 + H <=> H2O + OH	2.41E13	0.00	3970
(17)	H2O2 + H <=> H2 + HO2	6.03E13	0.00	7950
(18)	H2O2 + O <=> OH + HO2	9.55E06	2.00	3970
(19)	H2O2 + OH <=> H2O + HO2	1.00E12	0.00	0.00
	H2O2 + OH <=> H2O + HO2	5.80E14	0.00	9560

Third body efficiencies:

(5): H2O = 12.0, H2 = 2.5

(6): H2O = 12.0, H2 = 2.5, Ar = 0.83, He = 0.83

(7): H2O = 12.0, H2 = 2.5, Ar = 0.75, He = 0.75

(8): H2O = 12.0, H2 = 0.73, Ar = 0.38, He = 0.38

(9): H2O = 14.0, H2 = 1.3, Ar = 0.67, He = 0.67

(15): H2O = 12.0, H2 = 2.5, Ar = 0.45, He = 0.45

Troe parameters:

(9): A = 0.5, T3 = 1.0E-30, T1 = 1.0E30, T2 = 1.0E100

(15): A = 0.5, T3 = 1.0E-30, T1 = 1.0E30

### San Diego Hydrogen Submechanism (Using Troe Falloff Function)

Equation	A [mol/cm <sup>3</sup> /s]	n [1]	E [cal/mol]
(1) H + O2 <=> OH + O	3.52E16	-0.70	17069.79
(2) H2 + O <=> OH + H	5.06E04	2.67	6290.63
(3) H2 + OH <=> H2O + H	1.17E09	1.30	3635.28
(4) H2O + O <=> OH + OH	7.60E00	3.84	12779.64
(5) H + H + M <=> H2 + M	1.30E18	-1.00	0.00
(6) H + OH + M <=> H2O + M	4.00E22	-2.00	0.00
(7) O + O + M <=> O2 + M	6.17E15	-0.50	0.00
(8) H + O + M <=> OH + M	4.71E18	-1.00	0.00
(9) O + OH + M <=> HO2 + M	8.00E15	0.00	0.00
(10) H + O2 + M <=> HO2 + M	$k_{f,0} = 5.75E19$	-1.40	0.00
H + O2 <=> HO2	$k_f = 4.65E12$	0.440	0.00
(11) HO2 + H <=> OH + OH	7.08E13	0.00	294.93
(12) HO2 + H <=> H2 + O2	1.66E13	0.00	822.90
(13) HO2 + H <=> H2O + O	3.10E13	0.00	1720.84
(14) HO2 + O <=> OH + O2	2.00E13	0.00	0.00
(15) HO2 + OH <=> H2O + O2	2.89E13	0.00	-497.13
(16) OH + OH + M <=> H2O2 + M	$k_{f,0} = 2.30E18$	-0.90	-1701.72
OH + OH <=> H2O2	$k_f = 7.40E13$	-0.37	0.00
(17) HO2 + HO2 <=> H2O2 + O2	3.02E12	0.00	1386.23
(18) H2O2 + H <=> HO2 + H2	2.30E13	0.00	7950.05
(19) H2O2 + H <=> H2O + OH	1.00E13	0.00	3585.09
(20) H2O2 + OH <=> H2O + HO2	7.08E12	0.00	1434.03
(21) H2O2 + O <=> HO2 + OH	9.63E06	2.00	3991.40

Third body efficiencies:

(5, 6, 7, 8, 9): H2 = 2.5, H2O = 12.0

(10): H2 = 2.5, H2O = 16.0

(16): H2 = 2.0, H2O = 6.0

Troe parameters:

(10): A = 0.5, T3 = 1.0E-30, T1 = 1.0E30

(16): A = 0.735, T3 = 94, T1 = 1756, T2 = 5182

## REFERENCES

- [1] Weidner, J. P., "A Pre-Mixed Shock-Induced-Combustion Approach to Inlet and Combustor Design for Hypersonic Applications," *Transportation Beyond 2000: Engineering Design for the Future*, Sept. 1995.
- [2] Menees, G. P., Adelman, H. G., Bowles, J. V., and Cambier, J.-L., "Wave Combustors for Trans-Atmospheric Vehicles," *Journal of Propulsion and Power*, Vol. 8, No. 3, May 1992, pp. 709–713.
- [3] Lu, F. K. and Marren, D. E., "Hypersonic Test Facility Development," *AIAA Progress in Astronautics and Aeronautics: Advanced Hypersonic Test Facilities*, Vol. 198, 2002.
- [4] Dunlap, R., Brehm, R., and Nicholls, J., "A Preliminary Study of the Application of Steady-State Detonative Combustion to a Reaction Engine," *Jet Propulsion*, Vol. 28, No. 7, July 1958, pp. 451–456.
- [5] Sargent, W. and Gross, R., "A Detonation Wave Hypersonic Ramjet," *Second Symposium on Advanced Propulsion Concepts*, AFOSR TN-59-589, Boston, MA, Oct. 1959.
- [6] Gross, R., "Exploratory Studies of Combustion in Supersonic Flow, Part I - Plane Detonation Waves," Technical Note 59-587, Air Force Office of Scientific Research, June 1959.
- [7] Gross, R., "Exploratory Studies of Combustion in Supersonic Flow, Part II - Oblique Detonation Waves," Tech. Rep. ASTIA AD 216 769, June 1959.
- [8] Rubins, P. M. and Rhodes, R. P., "Shock-Induced Combustion with Oblique Shocks, Comparison of Experiment and Kinetic Calculations," Tech. Rep. AEDC-TDR-63-103, US Air Force, June 1963.
- [9] Rubins, P. and Bauer, R., "A Hypersonic Ramjet Analysis with Premixed Fuel Combustion," *2nd Propulsion Joint Specialist Conference*, AIAA-1966-648, Colorado Springs, CO, June 1966.
- [10] Lehr, H. F., "Experiments on Shock-Induced Combustion," *Astronautica Acta*, Vol. 17, 1972, pp. 589–597.
- [11] McVey, J. B. and Toong, T. Y., "Mechanism of Instabilities of Exothermic Hypersonic Blunt-Body Flows," *Combustion Science and Technology*, Vol. 3, 1971, pp. 63–76.

- [12] Alpert, L. R. and Toong, T. Y., "Periodicity In Exothermic Hypersonic Flows About Blunt Projectiles," *Acta Astronautica*, Vol. 17, Sept. 1972, pp. 539–560.
- [13] Morrison, R. B., "Evaluation of the Oblique Detonation Wave Ramjet," Contractor Report 145358, NASA, Jan. 1978.
- [14] O'Brien, C. and Kobayashi, A., "Advanced-to-Orbit Propulsion Concepts," *22nd Joint Propulsion Conference*, AIAA 1986-1386, Huntsville, AL, June 1986.
- [15] Ostrander, M., Hyde, J., Young, M., and Kissinger, R., "Standing Oblique Detonation Wave Engine Performance," *23rd Joint Propulsion Conference*, AIAA 1987-2002, San Diego, CA, June 1987.
- [16] Fujiwara, T., Matsuo, A., and Nomoto, H., "A Two-Dimensional Detonation Supported by a Blunt Body or a Wedge," *26th Aerospace Sciences Meeting*, AIAA 1988-0098, Reno, NV, Jan. 1988.
- [17] Wang, Y.-y., Fujiwara, T., Aoki, T., Arakawa, H., and Ishiguro, T., "Three-Dimensional Standing Oblique Detonation Wave in a Hypersonic Flow," *26th Aerospace Sciences Meeting*, AIAA 1988-0478, Reno, NV, Jan. 1988.
- [18] Cambier, J.-L., Adelman, H. G., and Menees, G. P., "Numerical Simulations of Oblique Detonations in Supersonic Combustion Chambers," *Journal of Propulsion*, Vol. 5, No. 4, Aug. 1989, pp. 482–491.
- [19] Singh, D. J., Carpenter, M. H., and Kumar, A., "Numerical Simulation of Shock-Induced Combustion/Detonation in a Premixed H<sub>2</sub>-Air Mixture Using Navier-Stokes Equations," *27th Joint Propulsion Conference*, AIAA-1991-3359, June 1991.
- [20] Chinitz, W., Tamagno, J., Erdos, J. I., Singh, D., and Rogers, R., "Premixed Shock-Induced Combustion Studies in the HYPULSE Facility," *28th Joint Propulsion Conference and Exhibit*, AIAA 1992-3427, Nashville, TN, July 1992.
- [21] Adelman, H. and Cambier, J., "Transatmospheric Vehicle Research," Contractor Report NCC2-388, Eloret Institute (Sponsor: NASA), June 1990.
- [22] Gonzalez, D., "Computational Study of Inlet Injection for Pre-Mixed, Shock-Induced Combustion," *7th International Space Planes and Hypersonic Systems and Technologies Conference*, AIAA 1996-4560, Norfolk, VA, Nov. 1996.
- [23] Sislian, J. P. and Parent, B., "Hypervelocity Fuel/Air Mixing in a Shcramjet Inlet," *Journal of Propulsion and Power*, Vol. 20, No. 2, March 2004, pp. 263–272.
- [24] Schwartzenruber, T. E., Sislian, J. P., and Parent, B., "Suppression of Premature Ignition in the Pre-Mixed Inlet Flow of a Shcramjet," *39th Joint Propulsion Conference and Exhibit*, AIAA-2003-5187, Huntsville, AL, July 2003.

- [25] Billig, F., Orth, R., and Lasky, M., “A Unified Analysis Of Gaseous Jet Penetration,” *AIAA Journal*, Vol. 9, No. 6, June 1971, pp. 1048–1058.
- [26] Northam, G. B., Capriotti, D., Byington, C., and Greenberg, I., “Mach 2 and Mach 3 Mixing and Combustion in Scramjets,” *27th Joint Propulsion Conference*, AIAA 1991-2394, Sacramento, CA, June 1991.
- [27] Northam, G. B., Greenberg, I., Byington, C., and Capriotti, D., “Evaluation of Parallel Injector Configurations for Mach 2 Combustion,” *Journal of Propulsion and Power*, Vol. 8, No. 2, 1992, pp. 491–499.
- [28] Byington, C. S., Northam, G. B., and Capriotti, D. P., “Transpiration Cooling in the Locality of a Transverse Fuel Jet for Supersonic Combustors,” *26th Joint Propulsion Conference*, AIAA 1990-2341, Orlando, FL, July 1990.
- [29] Haimovitch, Y., Gartenberg, E., Jr., A. S. R., and Northam, G. B., “Effects of Internal Nozzle Geometry on Compression-Ramp Mixing in Supersonic Flow,” *AIAA Journal*, Vol. 35, No. 4, April 1997, pp. 663–670.
- [30] Hirano, K., Matsuo, A., Kouchi, T., Izumikawa, M., and Tomioka, S., “New Injector Geometry for Penetration Enhancement of Perpendicular Jet into Supersonic Flow,” *43rd Joint Propulsion Conference and Exhibit*, AIAA 2007-5028, Cincinnati, OH, July 2007.
- [31] Gutmark, E., Schadow, K., and Wilson, K., “Noncircular Jet Dynamics in Supersonic Combustion,” *Journal of Propulsion and Power*, Vol. 5, No. 5, 1989, pp. 529–533.
- [32] Quinn, J. E., Cutler, A. D., and Northam, G., “Drag Reduction of Supersonic Cavities via Mass Injection with Applications to Scramjets,” *35th Aerospace Sciences Meeting and Exhibit*, AIAA 1997-0550, Reno, NV, Jan. 1997.
- [33] Drummond, J. P., “Mixing Enhancement of Reacting Parallel Fuel Jets in a Supersonic Combustor,” *27th Joint Propulsion Conference*, AIAA 1991-1914, Sacramento, CA, June 1991.
- [34] Marble, F. E. and Hendricks, G. J., “Progress Toward Shock Enhancement of Supersonic Combustion Processes,” *23rd Joint Propulsion Conference*, AIAA 1987-1880, San Diego, CA, June 1987.
- [35] Alexander, D. C., Sislian, J. P., and Parent, B., “Hypervelocity Fuel/Air Mixing in Mixed-Compression Inlets of Scramjets,” *AIAA Journal*, Vol. 44, No. 10, Oct. 2006, pp. 2145–2155.
- [36] Sislian, J. P., Martens, R. P., Schwartzentruber, T. E., and Parent, B., “Numerical Simulation of a Real Scramjet Flowfield,” *Journal of Propulsion and Power*, Vol. 22, No. 5, Sept. 2006, pp. 1039–1048.

- [37] Sislian, J., Schirmer, H., Dudebout, R., and Schumacher, J., “Propulsive Performance of Hypersonic Oblique Detonation Wave and Shock-Induced Combustion Ramjets,” *Journal of Propulsion and Power*, Vol. 17, No. 3, 2001, pp. 599–604.
- [38] Dudebout, R., Sislian, J. P., and Oppitz, R., “Numerical Simulation of Hypersonic Shock-Induced Combustion Ramjets,” *Journal of Propulsion and Power*, Vol. 14, No. 6, Nov. 1998, pp. 869–879.
- [39] Kouchi, T., Hirano, K., Matsuo, A., Kobayashi, K., Tomioka, S., and Izumikawa, M., “Combustion Performance of Supersonic Combustor with Stinger-Shaped Fuel Injector,” *44th Joint Propulsion Conference and Exhibit*, AIAA 2008-4503, Hartford, CT, July 2008.
- [40] Riggins, D., McClinton, C., Rogers, R., and Bittner, R., “A Comparative Study of Scramjet Injection Strategies for High Mach Number Flows,” *28th Joint Propulsion Conference and Exhibit*, AIAA 1992-3287, Nashville, TN, July 1992.
- [41] NASA Langley Research Center, “VULCAN Ver. 6.2,” <http://vulcan-cfd.larc.nasa.gov>, Nov. 2010.
- [42] Drummond, J. P. and Rogers, R. C., “A Detailed Numerical Model of a Supersonic Reacting Mixing Layer,” *22nd Joint Propulsion Conference*, AIAA 1986-1427, Huntsville, AL, June 1986.
- [43] Drummond, J. P., “Development of Methods to Predict High-Speed Reacting Flows in Aerospace Propulsion Systems,” *50th Aerospace Sciences Meeting*, AIAA 2012-0112, Nashville, TN, Jan. 2012.
- [44] Eklund, D. and Gruber, M., “Study of a Supersonic Combustor Employing an Aerodynamic Ramp Pilot Injector,” *35th Joint Propulsion Conference and Exhibit*, AIAA-1999-2249, Los Angeles, CA, June 1999.
- [45] Cutler, A. and White, J., “An Experimental and CFD Study of a Supersonic Coaxial Jet,” *39th Aerospace Sciences Meeting and Exhibit*, AIAA 2001-0143, Reno, NV, Jan. 2001.
- [46] Springer, R., Cutler, A., Diskin, G., and Smith, M., “Conventional/Laser Diagnostics to Assess Flow Quality in a Combustion-Heated Facility,” *35th Joint Propulsion Conference and Exhibit*, AIAA 1999-2170, Los Angeles, CA, June 1999.
- [47] Smart, M. K., Trexler, C. A., and Goldman, A. L., “A Combined Experiment/Computational Investigation of a Rocket Based Combined Cycle Inlet,” *39th Aerospace Sciences Meeting and Exhibit*, AIAA 2001-0671, Reno, NV, Jan. 2001.
- [48] Smart, M. K. and White, J. A., “Computational Investigation of the Performance and Back-Pressure Limits of a Hypersonic Inlet,” *40th Aerospace Sciences Meeting and Exhibit*, AIAA 2002-0508, Reno, NV, Jan. 2002.

- [49] Edwards, J. R., “A Low-Diffusion Flux-Splitting Scheme for Navier-Stokes Calculations,” *Computers & Fluids*, Vol. 26, No. 6, 1997, pp. 635–659.
- [50] Pulliam, T. and Chaussee, D., “A Diagonal Form of an Implicit Approximate-Factorization Algorithm,” *Journal of Computational Physics*, Vol. 39, 1981, pp. 347–363.
- [51] Menter, F. R., “Zonal Two Equation  $k$ - $\omega$  Turbulence Models for Aerodynamic Flows,” *24th Fluid Dynamics Conference*, AIAA-1993-2906, Orlando, FL, July 1993.
- [52] Wilcox, D., “Wall Matching, a Rational Alternative to Wall Functions,” *27th Aerospace Sciences Meeting*, AIAA-1989-0611, Reno, NV, Jan. 1989.
- [53] Tannehill, J. C. and Anderson, D. A., *Computational Fluid Mechanics and Heat Transfer*, Hemisphere Pub. Corp., 2nd ed., 1984.
- [54] “Verification, Validation, and Accreditation (VV&A) Recommended Practices Guide,” Tech. rep., Defense Modeling and Simulation Office, Office of the Director of Defense Research and Engineering, Oct. 1996.
- [55] Wilkes, J., Glass, C., Danehy, P., and Nowak, R., “Fluorescence Imaging of Underexpanded Jets and Comparison with CFD,” *49th Aerospace Sciences Meeting and Exhibit*, AIAA 2006-910, Reno, NV, Jan. 2006.
- [56] Love, E. S., Grigsby, C. E., Lee, L. P., and Woodling, M. J., “Experimental and Theoretical Studies of Axisymmetric Free Jets,” Technical Report R-6, NASA, 1959.
- [57] Schetz, J. A. and Billig, F. S., “Penetration of Gaseous Jets Injected into a Supersonic Stream,” *Journal of Spacecraft and Rockets*, Vol. 3, No. 11, 1966, pp. 1658–1665.
- [58] Cohen, L. S., Coulter, L. J., and Egan, W. J., “Penetration and Mixing of Multiple Gas Jets Subjected to a Cross Flow,” *AIAA Journal*, Vol. 9, No. 4, 1971, pp. 718–724.
- [59] Schetz, J. A. and Favin, S., “The Ignition of Slot-Injected Gaseous Hydrogen in a Supersonic Air Stream,” Contractor Report 344, NASA, Jan. 1966.
- [60] Portz, R. and Segal, C., “Penetration of Gaseous Jets in Supersonic Flows,” *AIAA Journal*, Vol. 44, No. 10, Oct. 2006, pp. 2426–2429.
- [61] Waitz, I., Marble, F., and Zukoski, E., “An Investigation of a Contoured Wall Injector for Hypervelocity Mixing Augmentation,” *27th Joint Propulsion Conference*, AIAA 1991-2265, Sacramento, CA, June 1991.
- [62] Waitz, I. A., *An Investigation of Contoured Wall Injectors for Hypervelocity Mixing Augmentation*, Ph.D. thesis, California Institute of Technology, 1991.

- [63] Xiao, X., Hassan, H., and Baurle, R., “Modeling Scramjet Flows with Variable Turbulent Prandtl and Schmidt Numbers,” *44th Aersopace Science Meeting and Exhibit*, AIAA 2006-128, Reno, NV, Jan. 2012.
- [64] “Guide for the Verification and Validation of Computational Fluid Dynamics Simulations,” Guide G-077-1998, AIAA, 1998.
- [65] Mao, M., Riggins, D. W., and McClinton, C. R., “Numerical Simulation of Transverse Fuel Injection,” *NASA Lewis Research Center Computational Fluid Dynamics Symposium on Aeropropulsion*, NASA-91N21097, Cleveland, OH, Jan. 1991, pp. 635–667.
- [66] Riggins, D., “High-Speed Engine/Component Performance Assessment Using Exergy and Thrust-Based Methods,” Contractor Report 198271, NASA, Jan. 1996.
- [67] Riggins, D., McClinton, C., and Vitt, P., “Thrust Losses in Hypersonic Engines Part 1: Methodology,” *Journal of Propulsion and Power*, Vol. 13, No. 2, March–April 1997, pp. 281–287.
- [68] Riggins, D., “Thrust Losses in Hypersonic Engines Part 2: Applications,” *Journal of Propulsion and Power*, Vol. 13, No. 2, March–April 1997, pp. 288–295.
- [69] Riggins, D., “Evaluation of Performance Loss Methods for High-Speed Engines and Engine Components,” *Journal of Propulsion and Power*, Vol. 13, No. 2, March–April 1997, pp. 296–304.
- [70] Baurle, R. and Gaffney, R., “Extraction of One-Dimensional Flow Properties from Multidimensional Data Sets,” *Journal of Propulsion and Power*, Vol. 24, No. 4, July–Aug. 2008, pp. 704–714.
- [71] Schetz, J. A. and Favin, S., “An Analysis of the Ignition of Slot-Injected Gaseous Hydrogen in a Supersonic Air Stream,” *Combustion and Flame*, Vol. 11, No. 5, Oct. 1967, pp. 397–407.
- [72] Waitz, I., Marble, F., and Zukoski, E., “Vorticity Generation by Contoured Wall Injection,” *28th Joint Propulsion Conference and Exhibit*, AIAA 1992-3550, Nashville, TN, July 1992.
- [73] Terry, J. E. and Caras, G. J., “Transpiration and Film Cooling of Liquid Rocket Nozzles,” Tech. Rep. RSIC-535, U.S. Army Missile Command, Redstone Arsenal, AL, March 1966.
- [74] Slater, J. W., “Improvements in Modeling 90-Degree Bleed Holes for Supersonic Inlets,” *Journal of Propulsion and Power*, Vol. 28, No. 4, July 2012, pp. 773–781.

- [75] Andrews, G., Asere, A., Gupta, M., and Mkpadi, M., “Full Coverage Discrete Hole Film Cooling: The Influence of Hole Size,” *International Journal of Turbo and Jet Engines*, Vol. 2, 1985, pp. 213–225.
- [76] Andrews, G., Gupta, M., and Mkpadi, M., “Full Coverage Discrete Hole Film Cooling: Cooling Effectiveness,” *International Journal of Turbo and Jet Engines*, Vol. 2, 1985, pp. 199–212.
- [77] Andrews, G., Asere, A., Mkpadi, M., and Tirmahi, A., “Transpiration Cooling: Contribution of Film Cooling to the Overall Cooling Effectiveness,” *International Journal of Turbo and Jet Engines*, Vol. 3, 1986, pp. 245–256.
- [78] Brunner, M., “Active Cooling Heat Protection,” *Entry Vehicle Systems and Technology Meeting*, AIAA-1968-1154, Williamsburg, VA, Dec. 1968.
- [79] Schuster, J. R. and Lee, T. G., “Application of an Improved Transpiration Cooling Concept to Space Shuttle Type Vehicles,” *Journal of Spacecraft*, Vol. 9, No. 11, Nov. 1972, pp. 804–811.
- [80] Glass, D. E., Dille, A. D., and Kelly, H. N., “Numerical Analysis of Convection/Transpiration Cooling,” *Journal of Spacecraft and Rockets*, Vol. 38, No. 1, Jan. 2001, pp. 15–20.
- [81] Langener, T., Wolfersdorf, J., Kuhn, M., and Steelant, J., “Transpiration Cooling with Supersonic Flows and Foreign Gas Injection,” *46th Joint Propulsion Conference and Exhibit*, AIAA-2010-6794, Nashville, TN, July 2010.
- [82] Cheuret, F., Steelant, J., and Langener, T., “Numerical Investigations on Transpiration Cooling for Scramjet Applications Using Different Coolants,” *17th International Space Planes and Hypersonic Systems and Technologies Conference*, AIAA 2011-2379, San Francisco, CA, April 2011.
- [83] Takita, K. and Masuya, G., “Effects of Combustion and Shock Impingement on Supersonic Film Cooling by Hydrogen,” *AIAA Journal*, Vol. 38, No. 10, Oct. 2000, pp. 1899–1906.
- [84] Mott, D. R., Oran, E. S., and van Leer, B., “A Quasi-Steady-State Solver for the Stiff Ordinary Differential Equations of Reaction Kinetics,” *Journal of Computational Physics*, Vol. 164, No. 2, Nov. 2000, pp. 407–428.
- [85] Slack, M. and Grillo, A., “Investigation of Hydrogen-Air Ignition Sensitized by Nitric Oxide and by Nitrogen Dioxide,” Contractor Report 2896, NASA, Oct. 1977.
- [86] Rogers, R. C. and Shexnayder, C. J., “Chemical Kinetic Analysis of Hydrogen-Air Ignition and Reaction Times,” Technical Paper 1856, NASA, July 1981.

- [87] Jachimowski, C. J., "An Analytical Study of the Hydrogen-Air Reaction Mechanism With Application to Scramjet Combustion," Technical Paper 2791, NASA, 1988.
- [88] McLain, A. G. and Rao, C., "A Hybrid Computer Program for Rapidly Solving Flowing or Static Chemical Kinetic Problems Involving Many Chemical Species," Technical Memorandum X-3403, NASA, July 1976.
- [89] Warnatz, J., "Concentration-, Pressure-, and Temperature-Dependence of the Flame Velocity in Hydrogen-Oxygen-Nitrogen Mixtures," *Combustion Science and Technology*, Vol. 26, No. 5-6, 1981, pp. 203-213.
- [90] Milton, B. and Keck, J., "Laminar Burning Velocities in Stoichiometric Hydrogen and Hydrogen-Hydrocarbon Gas Mixtures," *Combustion and Flame*, Vol. 58, No. 1, Oct. 1984, pp. 13-22.
- [91] Kendall, R. M. and Kelly, J. T., "Premixed One-Dimensional Flame (*PROF*) Code User's Manual," Tech. Rep. 600/7-78-172a, Environmental Protection Agency, 1978.
- [92] O Conaire, M., Curran, H. J., Simmie, J. M., Pitz, W. J., and Westbrook, C. K., "A Comprehensive Modeling Study of Hydrogen Oxidation," *International Journal of Chemical Kinetics*, Vol. 36, No. 11, pp. 603-622.
- [93] "Chemical-Kinetic Mechanisms for Combustion Applications," Tech. rep., Mechanical and Aerospace Engineering (Combustion Research), University of California at San Diego.
- [94] Bhaskaran, K., Gupta, M., and Just, T., "Shock Tube Study of the Effect of Unsymmetric Dimethyl Hydrazine on the Ignition Characteristics of Hydrogen-Air Mixtures," *Combustion and Flame*, Vol. 21, 1973, pp. 45-48.
- [95] Gardiner, W., editor, *Combustion Chemistry*, Springer-Verlag, 1984.
- [96] Ruegg, F. W. and Dorsey, W. W., "A Missile Technique for the Study of Detonation Waves," *Journal of research of the National Bureau of Standards*, Vol. 66C, No. 1, Jan.-March 1962, pp. 51-58.
- [97] Matsuo, A. and Fujii, K., "First Damkohler Parameter for Prediction and Classification of Unsteady Combustions Around Hypersonic Projectiles," *32nd Joint Propulsion Conference*, AIAA 1996-3137, July 1996.
- [98] Sussman, M. A., "A Computational Study of Unsteady Shock Induced Combustion of Hydrogen-air Mixtures," *30th Joint Propulsion Conference*, AIAA 1994-3101, Indianapolis, IN, June 1994.
- [99] Ben-Yakar, A., Kamel, M., Morris, C., and Hanson, R. K., "Experimental Investigation of H<sub>2</sub> Transverse Jet Combustion in Hypervelocity Flows," *33rd Joint Propulsion Conference and Exhibit*, Seattle, WA, July 1997.

- [100] Axdahl, E., Kumar, A., and Wilhite, A., “Study of Unsteady, Sphere-Driven, Shock-Induced Combustion for Application to Hypervelocity Airbreathing Propulsion,” *47th Joint Propulsion Conference and Exhibit*, AIAA-2011-5790, San Diego, CA, July 2011.
- [101] Bogdanoff, D. W., “Ram Accelerator Direct Space Launch System – New Concepts,” *Journal of Propulsion and Power*, Vol. 8, No. 2, March 1992, pp. 481–490.
- [102] Doerffer, P. P. and Bohning, R., “Modelling of Perforated Plate Aerodynamics Performance,” *Aerospace Science and Technology*, Vol. 4, 2000, pp. 525–534.
- [103] Baurle, R. A. and Norris, A. T., “A Source-Term Based Boundary Layer Bleed/Effusion Model for Passive Shock Control,” *58th JANNAF Propulsion Meeting*, NF1676L-11510, April 2011.
- [104] Goyne, C., Stalker, R., Brescianini, C., and Paull, A., “Drag Reduction by Film Cooling with Hydrogen on Transatmospheric Vehicles,” *9th International Space Planes and Hypersonic Systems and Technologies Conference*, AIAA-1999-4833, Nov. 1999.
- [105] Matsuo, A., Fujii, K., and Fujiwara, T., “Computational Study of Unsteady Combustion Around Projectiles with Emphasis on the Large-Disturbance Oscillation,” *32nd Aerospace Sciences Meeting & Exhibit*, AIAA 1994-0764, Reno, NV, Jan. 1994.
- [106] Oppenheim, A. K., Manson, N., and Wagner, H. G., “Recent Progress in Detonation Research,” *AIAA Journal*, Vol. 1, No. 10, Oct. 1963, pp. 2243–2252.
- [107] Urtiew, P. A. and Oppenheim, A. K., “Experimental Observations Of The Transition To Detonation In An Explosive Gas,” *Proceedings of the Royal Society of London*, Vol. 295, Nov. 1966.
- [108] Matsuo, A. and Fujiwara, T., “Numerical Simulation of Shock-Induced Combustion Around an Axisymmetric Blunt Body,” *26th Thermophysics Conference*, AIAA-1991-1414, Honolulu, HI, June 1991.
- [109] Wilson, G. J. and Sussman, M. A., “Computation of Unsteady Shock-Induced Combustion Using Logarithmic Species Conservation Equations,” *AIAA Journal*, Vol. 31, No. 2, Feb. 1993, pp. 294–301.
- [110] Ahuja, J. K., Tiwari, S. N., and Singh, D. J., “Hypersonic Shock-Induced Combustion In a Hydrogen-Air System,” *AIAA Journal*, Vol. 33, No. 1, 1994, pp. 173–176.
- [111] Ahuja, J. and Tiwari, S., “Numerical Simulation of Shock-Induced Combustion in a Superdetonative Hydrogen-Air System,” AIAA 1993-0242, Reno, NV, Jan. 1993.

- [112] Ahuja, J. and Tiwari, S., "Investigation of Shock-Induced Combustion Past Blunt Projectiles," Contractor Report 4724, NASA, April 1996.
- [113] Baulch, D. L., Bowman, C. T., Cobos, C. J., Cox, R. A., Just, T., Kerr, J. A., Pilling, M. J., Stocker, D., Troe, J., Tsang, W., Walker, R. W., and Warnatz, J., "Evaluated Kinetic Data for Combustion Modeling: Supplement II," *Journal of Physical and Chemical Reference Data*, Vol. 34, No. 3, 2005, pp. 757–1397.
- [114] McBride, B. J. and Gordon, S., "Computer Program for Calculation of Complex Chemical Equilibrium Compositions and Applications II. User's Manual and Program Description," Reference Publication 1311, NASA, June 1996.
- [115] Svehla, R. A., "Estimated Viscosities and Thermal Conductivities of Gases at High Temperatures," Technical Report R-132, NASA, 1962.
- [116] Wilke, C. R., "A Viscosity Equation for Gas Mixtures," *The Journal of Chemical Physics*, Vol. 18, No. 4, April 1950, pp. 517–519.
- [117] Coffee, T. and Himerl, J., "Transport Algorithms for Premixed, Laminar Steady-State Flames," *Combustion and Flame*, Vol. 43, 1981, pp. 273–289.
- [118] Turns, S. R., *An Introduction To Combustion: Concepts And Applications*, McGraw-Hill series in mechanical engineering, WCB/McGraw-Hill, 2000.
- [119] McBride, B. J., Zehe, M. J., and Gordon, S., "NASA Glenn Coefficients for Calculating Thermodynamic Properties of Individual Species," Technical Paper 2002-211556, NASA, Sept. 2002.
- [120] MacCormack, R. W., "Current Status of Numerical Solutions of the Navier-Stokes Equations," *23rd Aerospace Sciences Meeting*, AIAA 1985-0032, Jan. 1985.
- [121] Fay, J. A. and Riddell, F. R., "Theory of Stagnation Point Heat Transfer in Dissociated Air," *Journal of the Aeronautical Sciences*, Vol. 25, No. 2, Feb. 1958, pp. 73–85.
- [122] Kumar, A. and Graves, R. A., "Numerical Solution of the Viscous Hypersonic Flow Past Blunted Cones at Angle of Attack," *15th Aerospace Sciences Meeting*, No. AIAA 1977-172, Jan. 1977.
- [123] Gordon, S. and McBride, B. J., "Computer Program for Calculation of Complex Chemical Equilibrium Compositions and Applications I. Analysis," Reference Publication 1311, NASA, Oct. 1994.
- [124] Matsuo, A. and Fujii, K., "Examination of the Improved Model for the Unsteady Combustion Around Hypersonic Projectiles," *31st Joint Propulsion Conference and Exhibit*, AIAA 1995-2565, San Diego, CA, July 1995.

- [125] Saric, W. S., Reed, H. L., and Kerschen, E. J., "Boundary-Layer Receptivity to Freestream Disturbances," *Annual Review of Fluid Mechanics*, Vol. 34, 2002, pp. 291–319.
- [126] Eklund, D., Baurle, R., and Gruber, M., "Numerical Study of a Scramjet Combustor Fueled by an Aerodynamic Ramp Injector in Dual-Mode Combustion," *39th Aerospace Sciences Meeting and Exhibit*, AIAA-2001-0379, Reno, NV, Jan. 2001.